Mixed harmonic azimuthal correlations in $\sqrt{s_{NN}}$=2.76 TeV Pb–Pb collisions measured by ALICE at LHC

Yasuto Hori

Dissertation for the Degree of Doctor of Science

Department of Physics
Graduate School of Science
University of Tokyo

Abstract

In 2010, $\sqrt{s_{NN}}$ =2.76 TeV Pb–Pb collision experiment was conducted at the Large Hadron Collider (LHC) at European Organization for Nuclear Research (CERN). In this thesis, a series of the mixed harmonic azimuthal correlations at mid-rapidity in Pb–Pb collisions measured with the ALICE detectors at LHC is reported.

Primary motivation of this analysis is an investigation of the Local Charge Conservation (LCC) induced effects on the charge dependent parts of the azimuthal correlations. Since any charge production mechanisms follow the law of the LCC, any charged particle has a balancing (opposite) charged particle nearby. What we want to know is a distribution of relative azimuthal angle between charge and its balancing charge denoted as $\Delta\varphi$, which is expected to have a peak around $\Delta\varphi \sim 0$ due to the LCC correlation. The charge dependent part of the correlation $\langle\cos(\varphi_\alpha - \varphi_\beta)\rangle$ is proposed to quantify an azimuthal width of this distribution, i.e. the strength of the LCC correlation. Furthermore, it is expected that this azimuthal width is possibly modulated as a function of azimuthal angle of the charge balancing pair with respect to the reaction plane because of the azimuthal anisotropic flow. A series of charge dependent parts of mixed harmonic azimuthal correlations $\langle\cos[n\varphi_\alpha + m\varphi_\beta - (n+m)\Psi_k]\rangle$ is proposed to quantify these modulations. These systematic observations, in comparison with predictions from a simple hydrodynamics-inspired model, seem to indicate that the LCC is effectively realized on the kinetic freeze-out surface, which is much later than a time of the hadron production via the hadronization of the QGP matter. The physics origin of the "effective" LCC on the kinetic freeze-out surface is not yet clear, but this phenomenological knowledge may provide some insights for the hadronization and/or hadronic dynamics in the heavy-ion collisions.

Among the various charge dependent azimuthal correlations observed in this thesis, the correlation $\langle\cos(\varphi_\alpha+\varphi_\beta-2\Psi_{RP})\rangle$ has a special interest since it was originally proposed to search the Chiral Magnetic Effect (CME). The CME is expected to be a direct evidence of the local parity P and charge-parity CP violation in QCD under the hot and dense matter. Observed result is roughly consistent with the CME. However, on the other hand, it is found that the LCC induced correlations may significantly contribute on it at the same time. Therefore, the LCC effect must be subtracted precisely for the further CME search.

Charge independent parts of the observed results are also discussed in this thesis in terms of the CME, the directed flow v_1 effect, the transverse momentum conservation effect and the jet effects. It is found that the interplay between the hydrodynamic matter and jets is a key ingredient for the comprehensive understanding of their physics origins.

Contents

Chapter 1

Introduction

The main goal of the physics of the relativistic heavy ion collisions is a discovery of the deconfined Quark Gluon Plasma (QGP) and understanding its properties such as the equation of state (EoS), temperature, order of the phase transition, transport coefficients, the chemical evolution and so on. These phenomenological knowledge about the QGP is important for the deep understanding of the fundamental theory - Quantum chromodynamics (QCD). Another physics interest which can be tested in the heavy ion collisions related to the QCD theory is the search for the possible local parity violation in QCD. In this chapter, we introduce the basic of the QGP and the measurement of the azimuthal correlations.

1.1 Quantum ChromoDynamics (QCD)

Quantum chromodynamics (QCD) is a fundamental theory of strong interactions between the quarks and gluons. QCD was developed as an extension of quantum electrodynamics (QED) via the imposition of a local SU(3) symmetry in "color" space. The most important difference between QCD and QED is that QCD is a non-Abelian gauge theory and has gluon self-interaction as a consequence. The QCD interactions among quarks and gluons become weaker at the higher energy, which is called "asymptotic freedom" while the quarks and gluons are confined inside the hadrons at the low energy, i.e. "confinement" [1]. The strong coupling constant α_s can be expressed as a function of the momentum transfer Q^2 as follows:

$$\alpha_s(Q^2) \sim \frac{12\pi}{(33-2N_f)ln(Q^2/\lambda^2_{QCD})}, \tag{1.1}$$

where N_f is the number of quark flavors and $\lambda_{QCD} \sim 0.2$ GeV is a typical QCD scale. When the momentum transfer Q^2 is much larger than λ^2_{QCD}, α_s becomes small enough to allow us to use the perturbative method for QCD calculation (pQCD) as is the case in QED. On the other hand, when the momentum transfer Q^2 is not large, QCD is in non-perturbative regime.

1.2 Quark Gluon Plasma (QGP)

It has been pointed out that the color confinement can be broken at the high temperature and/or density of many body system of hadrons. This results in a phase transition from the confined nuclear matter (ordered phase) to the deconfined state (disordered phase). The deconfined state is called "Quark Gluon Plasma (QGP)" [2].

The lattice QCD calculations predict that the phase transition to the QGP state occurs at a critical temperature, T_c, of 150-200 MeV. Figure 1.1 shows the calculated results of the entropy density s/T^3 as a function of temperature T [3]. The entropy density increases stepwise at $T_c \sim 200$ MeV due to the increase of the degree of freedom associated with the liberation of quarks and gluons from hadrons.

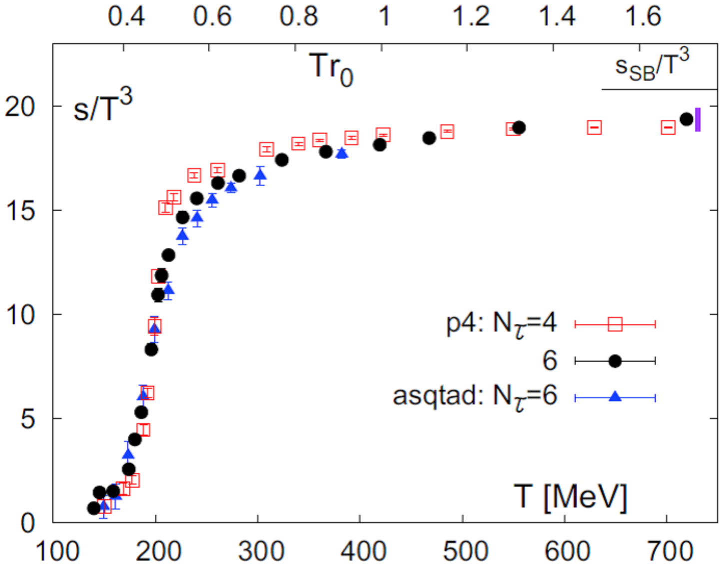

Figure 1.1: The entropy density ($s = \epsilon + p$) in units of T^3 as a function of T calculated by the lattice QCD [3].

A schematic phase diagram of hadronic matter including QGP is shown in Fig. 1.2. The horizontal axis is the baryon density normalized to the density of the normal nuclear matter (~ 0.15 GeV/fm^3) and the vertical axis is the temperature. QGP is considered to have existed in the early universe, a few micro second after the Big Bang.

1.3 Relativistic Heavy Ion Collision Experiment

In the relativistic heavy ion collisions at the top RHIC and LHC energies, the initial energy density participating in the collisions is expected to be well above the threshold for the QGP formation [5]. In a canonical picture of the collisions [6], the system undergoes six stages: (1) initial state, (2) rapid thermalization, (3) thermalized QGP phase, (4) hadronic gas phase, (5) hadronic gas phase with the chemical freeze-out and (6) hadronic

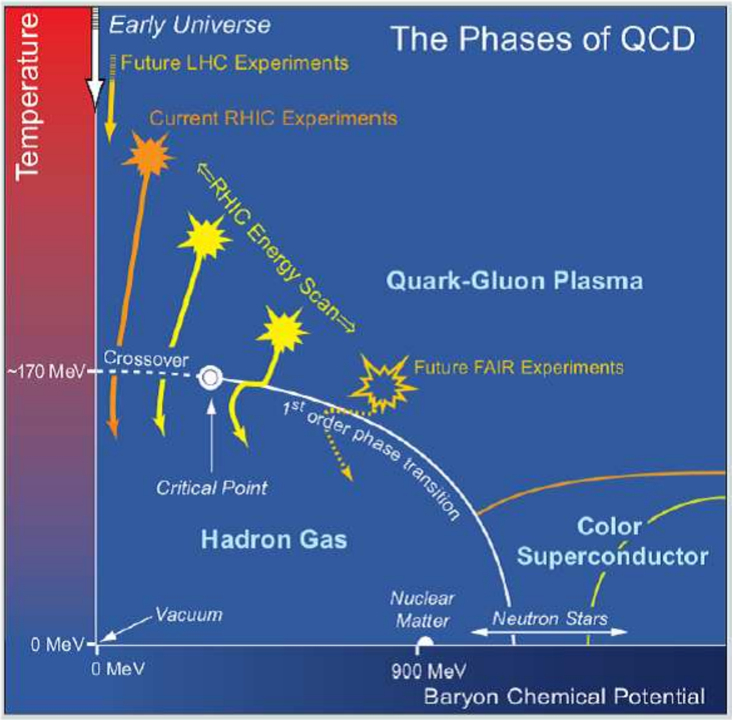

Figure 1.2: A schematic phase diagram of QCD matter [4].

gas phase with the kinetic freeze-out (free-streaming) as shown in Fig. 1.3. The nucleons taking part in the primary collisions are called as participants, and the others are spectators. A large number of the collisions between participants in target and projectile nuclei occurs. It is expected that the produced partons are strongly coupled each other and thermalized into the QGP phase rapidly within a short time of less than a few fm/c although dynamical mechanisms of this rapid thermalization is one of the most hard issues in the study of the QGP. A space-time evolution of the thermalized QGP matter can be described using the relativistic hydrodymanics with proper transport coefficients and an equation of state (EoS). The QGP matter collectively expands both in the longitudinal and the transverse directions. The latter expansion is called the radial flow. The produced particles gain the momentum and energy from the radial flow of the QGP matter and a final distribution of the transverse momentum is modified from the superposition of the independent nucleon-nucleon collisions [7]. The temperature of the matter decreases during a collective expansion of the QGP and the hadronization occurs through the phase transition from the deconfined to the hadronic matter at a time of 5-10 fm/c - this picture is called a delayed hadronization. After the phase transition, hadrons are rescattering each other and a relative number of species of the emitted particles is eventually fixed at the chemical freeze-out temperature. Finally, the kinetic freeze-out occurs and the particle momentum distribution is fixed.

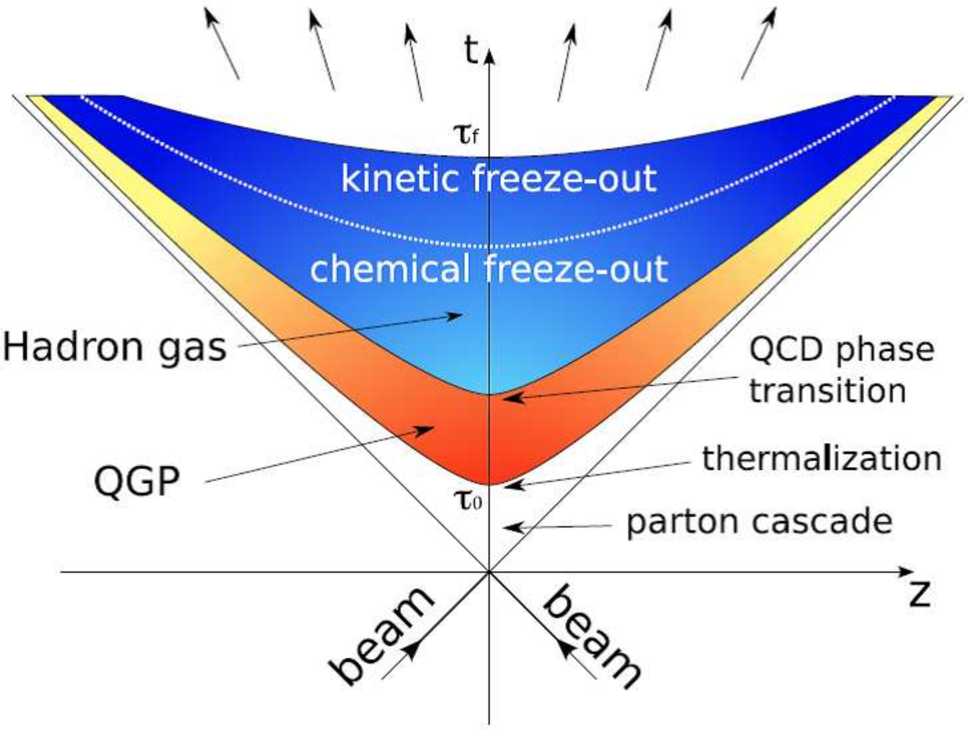

Figure 1.3: A schematic view of the dynamical evolution of a system generated after the heavy ion collision [6]. The transverse axis represents the space in the longitudinal direction.

1.4 Azimuthal Anisotropic Flow

Each collision is characterized by the collision impact parameter. Collisions with the small impact parameter are called central collisions and collisions with the large impact parameter are called peripheral collisions. A geometry of the participant region in non-central collisions has ellipticity in transverse plane as shown in Fig. 1.4 while the pseudo-rapidity invariance is expected to be hold at around mid-rapidity regions. The initial spatial anisotropy in the azimuthal direction is transformed to the anisotropy of the final particle momentum distributions due to the collective expansion of the produced system.

The reaction plane (RP) is defined as a plane between the vector between the centers of the two colliding nuclei and that of the beam direction as shown in Fig. 1.4. Ψ_{RP} represents its azimuthal angle in the laboratory frame [8, 9]. In addition, due to the event-by-event fluctuations of the nucleon positions in nuclei, the energy density profile of the system is very complex and has n-th harmonic azimuthal symmetry planes. Ψ_n represents its azimuthal angle in the laboratory frame. The 2nd harmonic symmetry plane roughly corresponds to the reaction plane, so $\Psi_2 \sim \Psi_{RP}$, but their azimuthal angles are slightly inclined event-by-event each other as shown in Fig. 1.5 (a). Figure 1.5 (b) shows the illustration of the triangle symmetry of the energy density profile [10].

The n-th harmonic spatial anisotropies ϵ_n of the hydrodynamic matter are defined as

$$\epsilon_n e^{i\Psi_n} \equiv -\frac{\{r^k e^{in\varphi}\}}{\{r^k\}}, \tag{1.2}$$

where the bracket denotes an average over the transverse plane in a single event, weighted by the energy density. An integer k is arbitrary, and it is customary set to 2 for $n \neq 1$ and 3 for $n = 1$. The origin of the coordinate (r, φ) is defined so that the center of gravity $\{re^{i\varphi}\} = 0$ at each event. This equation also defines the n-th harmonic symmetry plane angle Ψ_n. The momentum anisotropies are defined by using the energy-momentum tensor of the hydrodynamic matter [13]. Figure 1.6 shows the time evolutions of the spatial and momentum anisotropies of the hydrodynamic matter calculated numerically by the Glauber-type initial spatial anisotropy and 2+1 dimensional boost invariant ideal hydrodynamic simulation [13]. A longitudinal axis is normalized with the spatial anisotropies at the initial time τ_0. Note that the momentum anisotropies are assumed to be zero at the initial time τ_0. Dot lines in Fig. 1.6 (a) indicate that the momentum anisotropies develop in the time scale $\tau \sim \sqrt{\langle r^2 \rangle}/c_s \sim 5.4$ fm where $\sqrt{\langle r^2 \rangle}$ is the typical transverse size of the matter and c_s denotes the sound velocity. The sound velocity c_s can be derived from the Equation of State (EoS) of the matter. On the other hand, the spatial anisotropies shown in Fig. 1.6 (b) decrease with the similar time scale. These momentum anisotropies of the hydrodynamic matter lead to the anisotropic azimuthal distribution of the produced particles.

The particle azimuthal distribution with respect to the k-th harmonic azimuthal symmetry plane is customary expressed in a Fourier series:

$$E\frac{d^3N}{d^3p} = \frac{1}{2\pi}\frac{d^2N}{p_{\mathrm{T}}dp_{\mathrm{T}}dy}\Big(1 + 2\sum_{n=1}^{\infty} v_{n,k} \cdot \cos[n(\varphi - \Psi_k)]\Big), \tag{1.3}$$

where φ is an azimuthal angle in the laboratory frame and $v_{n,k} = \langle \cos[n(\varphi_i - \Psi_k)] \rangle$ (the bracket $\langle\ \rangle$ denotes an average over all particles in all events) coefficients are used to quantify the event anisotropy in the azimuthal direction. In the case of $n = k$, we sometime use the notation $v_n \equiv v_{n,n}$. The anisotropy v_2, v_3 are so-called elliptic and triangle flow respectively.

Figure A.4 shows the charged hardron p_{T} differential flow $v_{n,k}$ for each collision centrality class measured by the ALICE collaboration [15]. Since the symmetry plane angle is not known, one need to experimentally estimate it from the particle azimuthal distribution itself. $v_n\{EP, |\Delta\eta| > 2.0\}$ in this figure denotes anisotropic flow v_n measured by using the event plane method while $v_2\{4\}$ in this figure denotes the elliptic flow measured by using the four-particle correlation method. Detailed descriptions about the measurement methods are found in appendix A. The elliptic flow v_2 increases with increasing the collision centrality class, but we can roughly found $v_2 > v_3 > v_4 > v_{4,2} > 0$ in non-central collisions.

It was found that the measured azimuthal anisotropies are consistent to the collective flow signatures calculated using the hydrodynamic model with a small shear viscosity.

However, a large theoretical uncertainty exists in the initial anisotropy estimation in the hydrodynamic models even if we systematically analyze higher harmonic flow $v_{n,k}$ [10, 16, 17, 15, 18, 19, 20, 21]. Detailed descriptions about discussion with the hydrodynamic models are found in appendix A. In this thesis, the directed flow v_1 and joint correlations between the directed flow and higher harmonic flow [13, 22, 23, 24, 25, 26] are investigated as an extension of the flow analysis, which are introduced in detail at Sec.2.3. It is expected to help reducing these theoretical uncertainties.

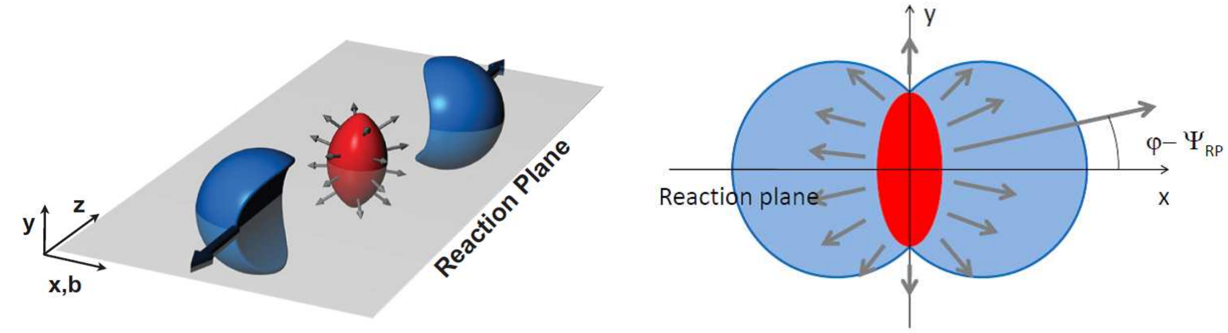

Figure 1.4: A sketch of the non-central nucleus-nucleus collision [11]. The matter created in the collision (red) is called participant region and has the azimuthal anisotropies. It collectively expands as shown by grey arrows. The nucleons in the blue region are called spectators and do not participate in the collisions. The x-axis corresponds to the vector between the centers of the two colliding nuclei. The grey plane is called the reaction plane.

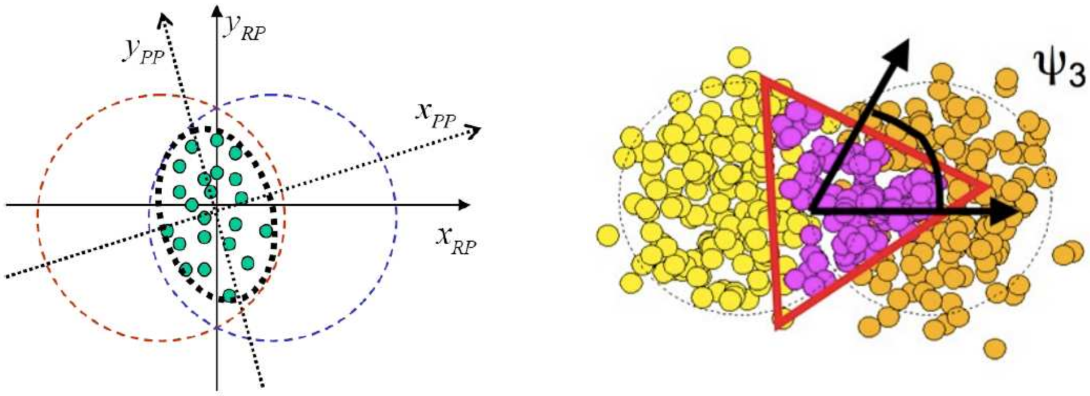

(a)

(b)

Figure 1.5: The transverse profile in a single event simulated using the Monte Carlo Glauber model [12, 8]. (a) Green circles are the positions of the nucleon-nucleon collisions. The 2nd harmonic symmetry plane is slightly inclined around the reaction plane. (b) It also has a non-zero triangle anisotropy. The azimuthal angle of the triangle anisotropy i.e. the 3rd harmonic symmetry plane angle Ψ_3 is not correlated with the reaction plane.

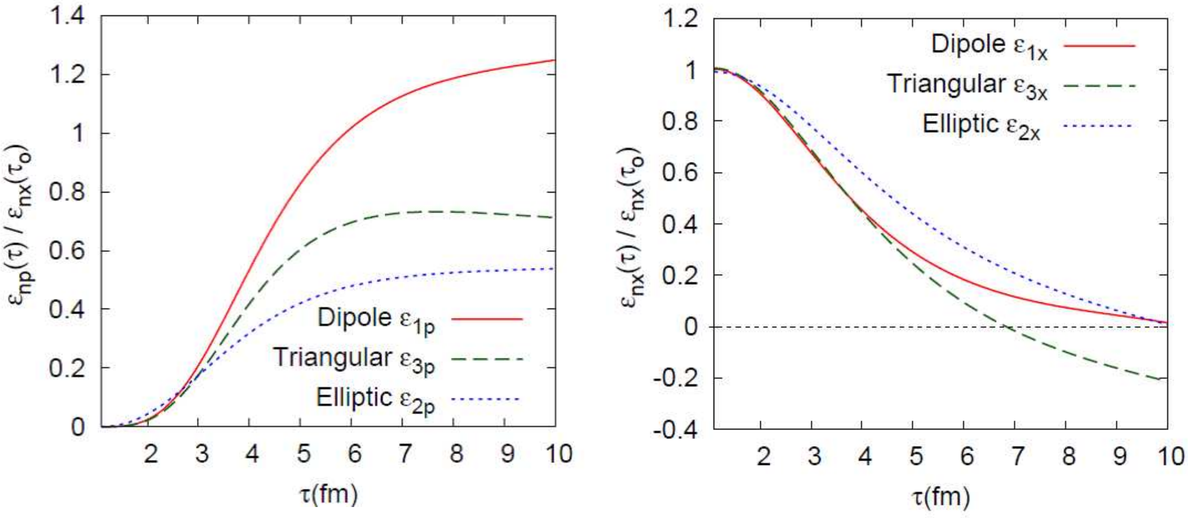

(a)

(b)

Figure 1.6: (a) The momentum anisotropy of the entropy distribution $\epsilon_{1p}, \epsilon_{2p}$ and ϵ_{3p} as a function of time for the impact parameter $b = 7.6$ fm. (b) The spatial anisotropy $\epsilon_{1x}, \epsilon_{2x}$ and ϵ_{3x} as a function of time [13]. ϵ_{nx} denotes ϵ_n in this thesis notation.

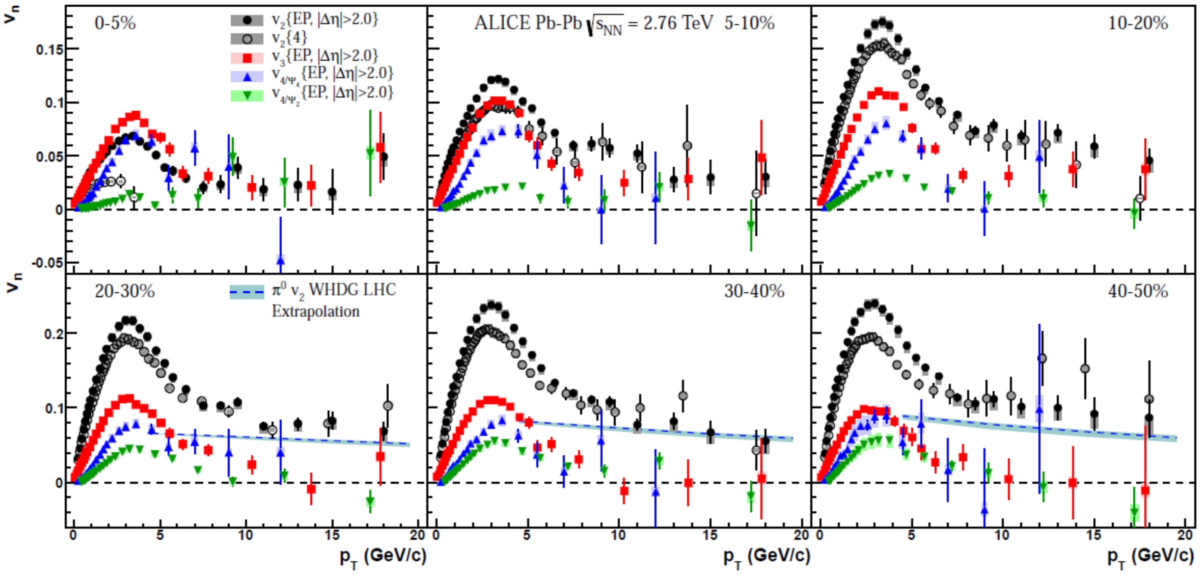

Figure 1.7: Charged hardron p_{T} differential flow v_n for each collision centrality class measured by the ALICE collaboration [14]. v_{4/Ψ_4} and v_{4/Ψ_2} in this figure notation correspond to $v_{4,4}$ and $v_{4,2}$ in this thesis notation, respectively.

1.5 Measurements of Charge dependent azimuthal correlations

Primary motivation of this thesis is to study the physics origin of the charge dependent azimuthal correlations in Pb–Pb collisions. These observables are measured by using same methods as the measurement of the azimuthal anisotropic flow.

In relativistic heavy-ion collisions a large number of charged particles is produced throughout the dynamical evolution of the system. While this is readily evident from measurements of the hadronic spectra in the final state of the evolution, the spectra provide only little insight into how and when the production of charged particles occurs. In contrast measurements of charged particle correlations contain additional information about the evolution of the system and several observables have been proposed to study in particular the chemical evolution of the system [27, 28, 29, 30, 31, 32, 33]. In this context it is important to realize, that any type of the charged particle productions at any stage are subject to microscopic conservation laws, which require local production of charge anti-charge pairs in coordinate space, i.e. the local charge conservation (LCC). The strong collective expansion of the system transforms their correlations from coordinate space to momentum space, while at the same time diffusive interactions with the medium reduce the correlations. Measuring a series of the charge dependent azimuthal correlations, we will study here to what extent experimental observations at the LHC are consistent with highly localized charge conservation on the kinetic freeze-out surface [34, 35]. This phenomenological knowledge is expected to have an information about the hadronization dynamics in heavy-ion collisions. Detail descriptions about the investigation of the LCC induced correlations are found in Sec.2.1.

Among the various mixed harmonic azimuthal correlations measured in this thesis, the correlation $\langle\cos(\varphi_\alpha+\varphi_\beta-2\Psi_{RP})\rangle$ has a special interest because it was originally proposed to search for the Chiral Magnetic Effect (CME) [36, 37, 38, 39, 40]. In the presence of the large magnetic field generated in heavy-ion collisions, the existence of the parity-odd (and topologically non-trivial) gluonic field is expected to result in the charge separation along the direction of the magnetic field. This is called Chiral Magnetic Effect. In this correlation, both the possible CME and LCC induced correlations are competing physics contributions. Therefore, if it is found that the LCC induced correlations actually contribute on the mixed harmonic azimuthal correlations, this background in the correlation $\langle\cos(\varphi_\alpha+\varphi_\beta-2\Psi_{RP})\rangle$ should be evaluated more precisely and the CME signals should be searched in the background subtracted correlation [34, 35]. Detail descriptions about the search for the CME are found in Sec.2.2.

1.6 Organization of this thesis

In Chapter 2, the physics motivations about the measurement of the mixed harmonic azimuthal correlations in the relativistic heavy ion collisions are explained. In Chapter 3, the LHC-ALICE experiment setup and the experimental conditions for $\sqrt{s_{NN}}$=2.76 TeV

Pb–Pb collisions in 2010 are described. In Chapter 4, the analysis method is explained in detail. In Chapter 5, the results of mixed harmonic azimuthal correlations are shown and the physical implication for these measurements are discussed. In Chapter 6, this thesis is concluded.

1.7 Major Contribution

The major contributions of the author as a ALICE collaborator are as follows:

- $E \times B$ calibrations of the Time Projection Chamber (TPC)
- The measurement of the charged kaon elliptic flow v_2 via kink topological identifications in $\sqrt{s_{NN}}$=2.76 TeV Pb–Pb collisions and participation in the Paper Committee (PC) for the paper "Elliptic flow of charged pions, kaons, (anti-)protons and (multi-)strange hadrons in Pb–Pb collisions at $\sqrt{s_{NN}}$=2.76 TeV" (under preparation)
- The measurement of the charge dependent azimuthal correlations in $\sqrt{s_{NN}}$=2.76 TeV Pb–Pb collisions and participation in the Paper Committee (PC) as a representative of the paper "Mixed harmonic charge dependent azimuthal correlations in $\sqrt{s_{NN}}$=2.76 TeV Pb–Pb collisions measured by the ALICE at the LHC" (under preparation)
- The measurement of the charge independent azimuthal correlations in $\sqrt{s_{NN}}$=2.76 TeV Pb–Pb collisions and participation in the Paper Committee (PC) of the paper "Non-flow and fluctuations" (under preparation)

Other works are listed below:

- Proposal of a series of mixed harmonic charge dependent azimuthal correlation measurements in order to disentangle the possible chiral magnetic effect and the local charge conservation induced correlations with the Blast Wave model calculations. (arXiv:1208.0603)
- Investigation of the directed flow v_1 and mixed harmonic correlations by using the event-by-event ideal hydrodynamics model. (a paper is under discussion)

Chapter 2

Physics Motivation

2.1 The Local Charge Conservation (LCC) induced correlations

Although the charge and balancing opposite-charge can not be identified pair by pair, the LCC can be traced statistically: *If one observes a charged particle, one can find a opposite-charged particle more closely than a same-charged particle.* Note that the concept of the LCC is different from the charge neutrality of the matter. The charge neutrality of the matter is realized statistically since the number of the particles produced in the heavy ion collisions is large enough. This just means that *If one observes a charged particle, one can find both same and opposite charged particles nearby.* In Ref. [27, 28], the observable employed in experimental studies of balancing charge correlations is the charge balance function

$$
\begin{aligned}
B_{c\bar{c}}(p_\beta|p_\alpha) \quad &= \frac{\langle N_{c\bar{c}}(p_\beta|p_\alpha) - N_{cc}(p_\beta|p_\alpha)\rangle}{\langle dM/dp_\alpha\rangle} \\
&+ \quad \frac{\langle N_{\bar{c}c}(p_\beta|p_\alpha) - N_{\bar{c}\bar{c}}(p_\beta|p_\alpha)\rangle}{\langle dM/dp_\alpha\rangle}, \qquad (2.1)
\end{aligned}
$$

which aims to identify balancing partner charges on a statistical basis. Here dM/dp_α denotes the differential charged particle multiplicity and $N_{c\bar{c}}(p_\beta|p_\alpha)$ is the number of particle pairs where the first particle has charge c and momentum p_α and the second one has charge $\bar{c}$ and momentum p_β and we denote the bracket $\langle \cdots \rangle$ as the event average. The definition of the balance function $B_{c\bar{c}}(p_\alpha|p_\beta)$ is very clear. It describes the conditional probability to observe a particle with charge $\bar{c}$ and momentum p_β, given the observation of a particle with opposite charge c and momentum p_α. Instead of considering the six-dimensional correlation function in Eq. (2.1), previous studies have focused on the integrated correlation functions $B(\Delta\varphi)$ and $B(\Delta\eta)$, which quantify the separation of balancing charges in relative azimuthal angle $\Delta\varphi \equiv \varphi_\alpha - \varphi_\beta$ and relative pseudo-rapidity $\Delta\eta \equiv \eta_\alpha - \eta_\beta$ [27, 28, 29, 30, 31, 32, 33].

In this thesis, to quantify the distribution of the balancing charge in the azimuthal direction [35], we use a set of charge dependent parts of the two-particle azimuthal correlations

$$\begin{aligned} C_n &\equiv \Delta\langle\cos[n(\varphi_\alpha-\varphi_\beta)]\rangle \\ &= \langle\cos[n(\varphi_\alpha-\varphi_\beta)]\rangle_{opp.} - \langle\cos[n(\varphi_\alpha-\varphi_\beta)]\rangle_{same}, \end{aligned} \tag{2.2}$$

where n is a natural number. In this thesis, $\Delta\langle\cdots\rangle$ denotes the difference between the opposite and same charge correlations. We assume that this subtraction plays a role of the combinatorial pair subtraction. The charge balance moments C_n simply correspond to the Fourier moments of the balance function $B(\Delta\varphi)$,

$$C_n \sim \int d\Delta\varphi B(\Delta\varphi)\cos(n\Delta\varphi). \tag{2.3}$$

The moment C_1 can be regarded as the inverse width between charge and balancing anti-charge in the azimuthal direction. A width between charge and balancing anti-charge (charge balance width) becomes smaller when the pairs are emitted from the fluid element with the larger collective velocity, which is, in other words, the focusing of the charge balance width. Hence, the charge balance width ($\propto 1/C_1$) is expected to be smaller when the larger radial flow is created as illustrated in Fig. 2.1. Note, however, HBT correlations between identical particles induce the extra (and positive) same charge correlations, which may make ΔC_1 negative. In this case, the interpretation as the inverse width completely fails. We must firstly check that this is not our case in reality.

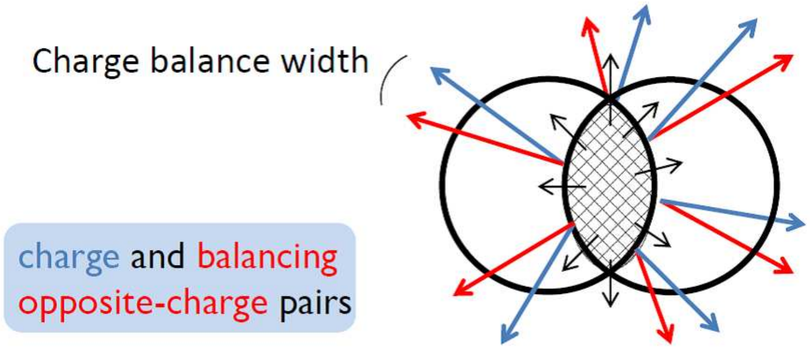

Figure 2.1: A width of balancing pairs emitted from the hydrodynamic surface with the larger radial flow (black arrows) is smaller.

A distribution of balancing charge is possibly modulated in the azimuthal direction by the azimuthal anisotropic flow at a time of the charge creation and subsequent diffusion. These azimuthal modulations can be quantified by the charge dependent parts of the mixed harmonic azimuthal correlations

$$\Delta\langle\cos[n\varphi_\alpha + m\varphi_\beta - (n+m)\Psi_k]\rangle, \tag{2.4}$$

where n, m, k are integers and $(n+m) \propto k$ since these correlations can be decomposed into the three contributions:

$$\Delta\langle\cos[n\varphi_\alpha + m\varphi_\beta - (n+m)\Psi_k]\rangle = v_{|n+m|,k}C_n + mc^{(n)}_{n+m,k} - ms^{(n)}_{n+m,k}. \tag{2.5}$$

The contribution $v_{|n+m|,k}C_n$ is the product of the n-th charge balance moments C_n defined as Eq. (2.2) and the azimuthal anisotropic flow $v_{|n+m|,k}$. The other two contributions take the form

$$mc^{(n)}_{n+m,k} = \Delta\langle\cos(n\Delta\varphi)\cos[(n+m)\tilde{\varphi}_{k,\beta}]\rangle - v_{|n+m|,k}C_n\ , \tag{2.6}$$

$$ms^{(n)}_{n+m,k} = \Delta\langle\sin(n\Delta\varphi)\sin[(n+m)\tilde{\varphi}_{k,\beta}]\rangle\ , \tag{2.7}$$

where $(\tilde{\varphi}_{k,\beta} \equiv \varphi_\beta - \Psi_k)$ and $\Delta\varphi = \varphi_\alpha - \varphi_\beta$. The contribution $mc^{(n)}_{n+m,k}$ is interpreted as the $|n+m|$-th azimuthal modulation of C_n with respect to the k-th harmonic symmetry plane. The contribution $ms^{(n)}_{n+m,k}$ is interpreted as the $|n+m|$-th azimuthal modulation of the n-th charge balance asymmetry with respect to the k-th harmonic symmetry plane.

For example, the charge balance width of the pairs in the in-plane region is expected to be smaller than that in the out-of-plane region because of the elliptic flow $v_{2,2}$. This 2nd azimuthal modulation of C_1 can be quantified by $mc^{(1)}_{2,2}$. Similarly, although the correlation $\Delta\langle\sin(\varphi_\alpha - \varphi_\beta)\rangle$, which is called charge balance asymmetry, is zero due to the symmetry of the matter, its 2nd azimuthal modulation can be nonzero. The 2nd azimuthal modulation of the charge balance asymmetry can be quantified as $ms^{(1)}_{2,2}$. These 2nd azimuthal modulations of the charge balance width and asymmetry are illustrated in the left and right pictures of Fig. 2.2 respectively and can contribute the correlations $\Delta\langle\cos(\varphi_\alpha + \varphi_\beta - 2\Psi_2)\rangle$ and $\Delta\langle\cos(\varphi_\alpha - 3\varphi_\beta + 2\Psi_2)\rangle$.

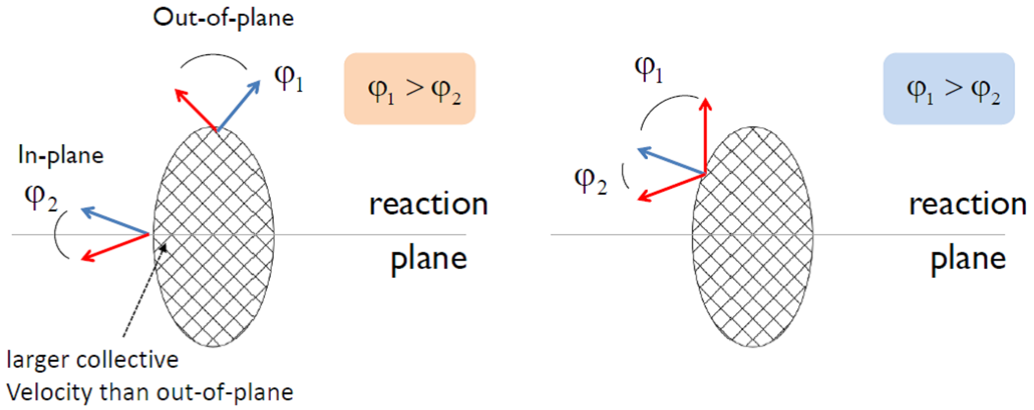

Figure 2.2: The illustrations of (left) the 2nd azimuthal modulation of C_1 and (right) the 2nd azimuthal modulation of the charge balance asymmetry due to the elliptic flow.

In the conventional Blast Wave model, the spatial geometry of the kinetic freeze-out surface is simply parametrised so as to mimic the shape of the kinetic freeze-out surface calculated using the full hydrodynamic simulations. Then the hadrons are emitted from the parametrized kinetic freeze-out surface according to the Boltzmann distribution with the freeze-out temperature T_{kin}. In the model developed in Ref. [34, 41], when one hadron is emitted from a space-point on the freeze-out surface, it is imposed that balancing anti-hadron is also emitted from nearby. The model parameter σ_φ describes how near the balancing anti-hadron are emitted and in the case of $\sigma_\varphi = 0$ the perfect LCC is effectively realized on the freeze-out surface. Here we use the word "effective" since the particle production occurs not on the kinetic freeze-out surface but at an earlier time. Detailed description of this model is found in Sec.5.1.1.

As shown in Fig. 2.3, this Blast Wave model incorporating with the LCC roughly reproduce the observed $\Delta\langle\cos(\varphi_\alpha + \varphi_\beta - 2\Psi_{RP})\rangle$ by the STAR collaboration, which is written as $\gamma_{\mathrm{OS}} - \gamma_{\mathrm{SS}}$ in this plot's notation. In this plot, M denotes the non-corrected number of track used in the experimental measurement of $\Delta\langle\cos(\varphi_\alpha + \varphi_\beta - 2\Psi_{RP})\rangle$ and the longitudinal axis is scaled by M for the sake of visibility. Blue symbols are results calculated by the model with the perfect local charge conservation on the kinetic freeze-out surface. Red symbols are the model calculation tuned the model parameter σ_φ to reproduce the experimental results (black symbols). Furthermore, in this plot, the centrality dependencies of each three contributions $mc^{(1)}_{2,2}$, $ms^{(1)}_{2,2}$ and $v_{2,2}C_1$ are also shown (in this plot's notation, v_{2c}, v_{2s} and v_2C_B).

Although the Blast Wave model incorporating with the LCC can reproduce the correlation $\Delta\langle\cos(\varphi_\alpha + \varphi_\beta - 2\Psi_{RP})\rangle$ measured by the STAR collaboration, the physics origin of the "effective" LCC on the kinetic freeze-out surface is not trivial. Rather, the "effective" LCC on the kinetic freeze-out surface should be tested experimentally. If the "effective" LCC is realized on the freeze-out surface and the freeze-out surface has a large radial and anisotropic flow $v_{|n+m|,k}$, one expects the naive scaling that the correlations $\Delta\langle\cos[n\varphi_\alpha + m\varphi_\beta - (n+m)\Psi_k]\rangle$ are roughly proportional to the corresponding flow $v_{|n+m|,k}$. The significant anisotropic flow created in the heavy ion collisions are the elliptic flow quantified by $v_{2,2}$ and the fourth harmonic flow with respect to the 2nd harmonic symmetry plane quantified by $v_{4,2}$. Therefore, the corresponding correlations with $n = 1$ are $\Delta\langle\cos(\varphi_\alpha + \varphi_\beta - 2\Psi_2)\rangle$, $\Delta\langle\cos(\varphi_\alpha - 3\varphi_\beta + 2\Psi_2)\rangle$, $\Delta\langle\cos(\varphi_\alpha + 3\varphi_\beta - 4\Psi_2)\rangle$ and $\Delta\langle\cos(\varphi_\alpha - 5\varphi_\beta + 4\Psi_2)\rangle$. The triangle flow $v_{3,3}$ and the fourth harmonic flow $v_{4,4}$ are also generated in the heavy ion collisions. They will lead the modulation of C_1, which can be quantified using $\Delta\langle\cos(\varphi_\alpha + 2\varphi_\beta - 3\Psi_3)\rangle$ and $\Delta\langle\cos(\varphi_\alpha + 3\varphi_\beta - 4\Psi_4)\rangle$ and so on.

Theoretical calculations of these correlations will be conducted using the Blast Wave model incorporating with the LCC described in Sec.5.1.1. They are compared with the experimental observations at the LHC energy which are described in Sec.5.1.2 to test whether or not the "effective" LCC is realized on the anisotropically radial expanding kinetic freeze-out surface [35].

The correlation $\Delta\langle\cos[n\varphi_\alpha + m\varphi_\beta - (n+m)\Psi_k]\rangle$ corresponds to different moments of

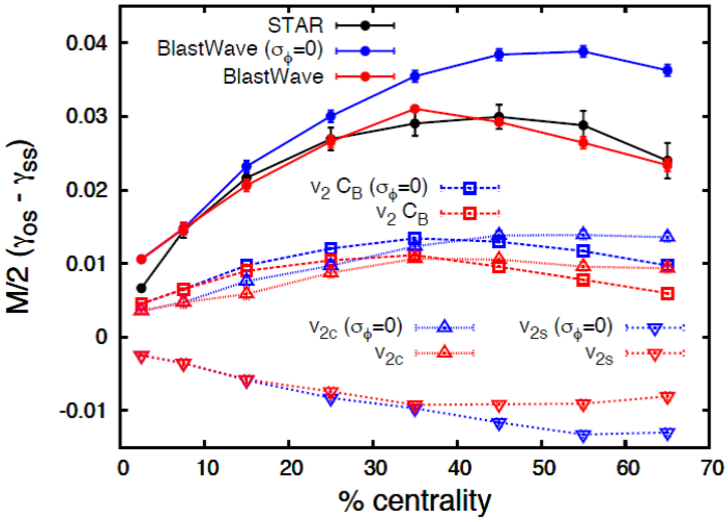

Figure 2.3: The centrality dependence of the correlation $M/2(\gamma_{\mathrm{OS}}-\gamma_{\mathrm{SS}})$ measured by the STAR collaboration in comparison with the results calculated using the Blast Wave model incorporating with the LCC [34, 41]. Here γ_{OS} and γ_{SS} denote the opposite and same charge correlation $\langle\cos(\varphi_\alpha+\varphi_\beta-2\Psi_{RP})\rangle$ respectively, so $(\gamma_{\mathrm{OS}}-\gamma_{\mathrm{SS}})=\Delta\langle\cos(\varphi_\alpha+\varphi_\beta-2\Psi_{RP})\rangle$. M denotes the non-corrected number of track used in the experimental measurement of $\gamma_{\mathrm{OS/SS}}$. v_{2c}, v_{2s} and v_2C_B in this thesis notation are $mc^{(1)}_{2,2}$, $ms^{(1)}_{2,2}$ and $v_{2,2}C_1$ respectively in this thesis notation. Blue symbols are results calculated by the model with the perfect local charge conservation on the kinetic freeze-out surface. Red symbols are the model calculation tuned the model parameter σ_ϕ (σ_φ in this thesis notation) to reproduce the experimental results (black symbols). The model parameter σ_ϕ represents how locally the charge conservation is realized.

the balance function with respect to the k-th harmonic symmetry plane Ψ_k - $B(\tilde{\varphi}_k,\Delta\varphi)$

$$\begin{aligned}\frac{\Delta\langle M^2\cos[n\varphi_\alpha+m\varphi_\beta-(n+m)\Psi_k]\rangle}{\langle M\rangle} &= \frac{4}{\langle M\rangle}\int d\tilde{\varphi}_k\, d\Delta\varphi\, \langle\frac{dM}{d\tilde{\varphi}_k}\rangle B(\tilde{\varphi}_k,\Delta\varphi)\\ &\quad\times\cos[n\Delta\varphi+(n+m)\tilde{\varphi}_k], \qquad (2.8)\end{aligned}$$

where M is the total number of the charged particles used for the correlation measurement and

$$\begin{aligned}B(\tilde{\varphi}_k,\Delta\varphi) &\equiv \frac{1}{\langle dM/d\tilde{\varphi}_k\rangle}\int dp_\beta \left\langle\frac{dM}{dp_\alpha}\right\rangle dp_\alpha\, B(p_\beta|p_\alpha)\\ &\quad\times\,\delta(\Delta\varphi-(\varphi_\alpha-\varphi_\beta))\,\delta(\tilde{\varphi}_k-\tilde{\varphi}_{\beta,k}). \qquad (2.9)\end{aligned}$$

Figure 2.4 shows the results of $B(\tilde{\varphi}_2,\Delta\varphi)$ measured by the STAR collaboration [42]. Indeed, these balance functions have a single peak at $\Delta\varphi\sim 0$ and can be regarded as a distribution of the balancing charge. Furthermore, the 2nd azimuthal modulation of

C_1 with respect to the 2nd harmonic symmetry plane (the reaction plane) are observed. However, the detailed shape of the balance function is sensitive to the detector effect but irrelevant to the physics while the most detector effects cancel out in the azimuthal correlations. What is worse about the balance function is that there is no clear way to correct for the detector effect on the experimental estimation of $B(\tilde{\varphi}_k, \Delta\varphi)$. So the balance function itself is not measured in this thesis. Instead, a series of charge dependent azimuthal correlations is used to investigate the distribution of the balancing charge.

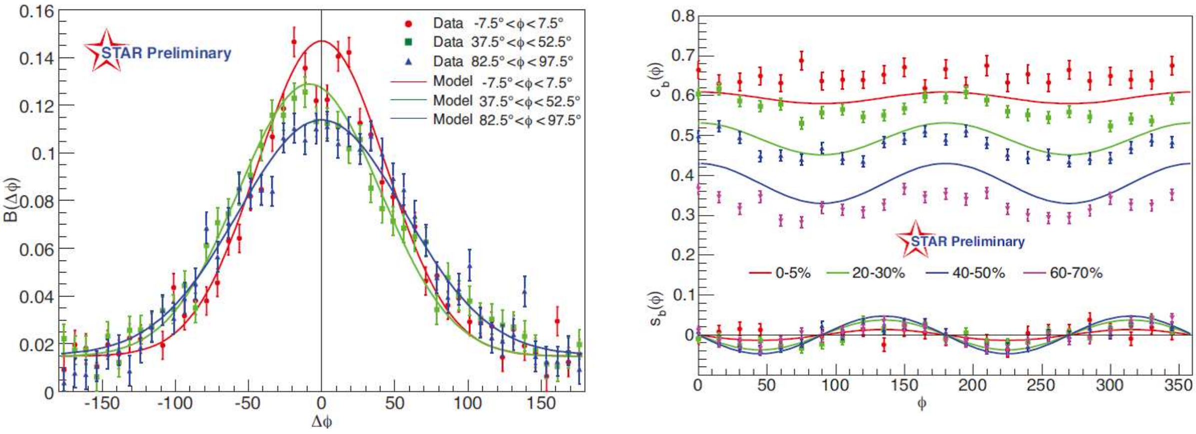

(a)

(b)

Figure 2.4: (a) Charge balance function $B(\tilde{\varphi}_2, \Delta\varphi)$ measured by the STAR collaboration. (b) The azimuthal modulation of the charge balance moments. Here $\phi \rightarrow \tilde{\varphi}_2$, $\Delta\phi \rightarrow \Delta\varphi$, $c_b(\phi) \rightarrow mc^1_{2,2} + v_{2,2}C_1$ and $s_b(\phi) \rightarrow ms^1_{2,2}$ in this thesis notations [42].

2.2 Chiral Magnetic Effect (CME) search

The possibility to observe local parity violation in the strong interaction using relativistic heavy-ion collisions has been discussed for many years. In high temperature QCD, this symmetry violation originates in the interaction between quarks and gluonic fields, instantons, and sphalerons which carry non-zero topological charge. A typical size of such gluonic fields is expected to be ~ 0.3 fm while typical transverse size of the participant regions in the heavy ion collisions is a few tens fm. Hence, a few hundreds of such fields are created like bubbles in a single heavy ion collision. The experimental search of this effect has intensified recently, following the realisation that, in the presence of the magnetic field generated perpendicularly to the reaction plane in non-central collisions, the existence of such parity-odd bubbles results in a charge separation along this magnetic field direction as shown in Fig. 2.5. This phenomenon is called the Chiral Magnetic Effect (CME). Theoretical details of the CME are found in appendix B. The charge dependent azimuthal correlations $\langle \cos(\varphi_\alpha + \varphi_\beta - 2\Psi_{RP}) \rangle$ measured by the STAR Collaboration was originally proposed for the CME search and is consistent with the qualitative expectations for the CME, and has triggered an intense discussion.

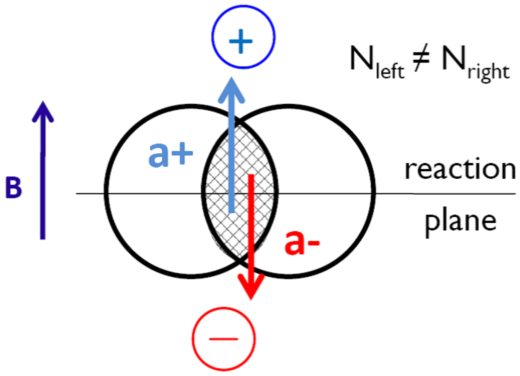

Figure 2.5: The charge dependent coefficient $a_{1,\alpha}$ in Fourier expansion Eq. (2.10) of the particle azimuthal distribution with respect to the reaction plane.

Phenomenologically, the charge separation with respect to the reaction plane due to the CME can be described by adding P-odd sine terms to the Fourier decomposition of the charge dependent particle azimuthal distribution in a single event [43]:

$$\frac{dN_\alpha}{d\tilde{\varphi}_{2,\alpha}} \propto 1 + 2\sum_n \Big(v_{n,2,\alpha} \cos(n\tilde{\varphi}_{2,\alpha}) + a_{n,\alpha} \sin(n\tilde{\varphi}_{2,\alpha}) \Big), \tag{2.10}$$

where the index α refers to the charge of the particles. The $a_{n,\alpha}$ parameters represent the P-violating effect and in particular $a_{1,\alpha}$ represents the charge separation with respect to the reaction plane as shown in Fig. 2.5. The event averaged $v_{n,k,\alpha}$ parameters, $\langle v_{n,k,\alpha} \rangle$ do not vanish in general but they are P-even observables (As similar to $v_{n,k,\alpha}$, the coefficient of the sine term should be written as $a_{n,k,\alpha}$. However it is obvious that we only think about $k = 2$ case, so we omit k and define as $a_{n,\alpha}$). We know that the reaction plane differs from the 2nd harmonic symmetry plane due to the fluctuations of the initial conditions, but here we roughly regard them as identical ones $\Psi_{RP} \sim \Psi_2$. The effects of local parity violation can not be significantly observed in a single event because of the statistical fluctuations in the large number of particles, which are irrelevant to the P-violating fields. However, the average of $a_{n,\alpha}$ over many evens, $\langle a_{n,\alpha} \rangle$ is zero. Even in a single event, $\langle a_{1,\alpha} \rangle$ is expected to be small because the large number of the parity-odd bubbles with both positive and negative topological charge is created in a single event. The observation of the effect is possible only via measuring charge distribution fluctuations, e.g. $\langle a_{1,\alpha} a_{1,\beta} \rangle$ with the average taken over all events in a given event sample. The correlation $\langle a_{1,\alpha} a_{1,\beta} \rangle$ is, however, a P-even quantity, and an experimental measurement of this quantity may contain contributions from effects unrelated to parity violations.

Based on the current theoretical understanding of the CME, one might expect the following features for the correlation $\langle a_{1,\alpha} a_{1,\beta} \rangle$ [39] :

Magnitude

A signal of the order of $|a_1| \sim Q_w/N_\pi \sim 10^{-2}$ is predicted for mid-central collisions.

Charge combinations

If the particles experience no medium effects (re-interaction with other particles in the system) after leaving the domain, one would expect $a_{1,+} = -a_{1,-}$ as shown in Fig. 2.5. Thus, in the absence of medium effects, one expects $\langle a_{1,+} a_{1,+} \rangle = \langle a_{1,-} a_{1,-} \rangle = -\langle a_{1,+} a_{1,-} \rangle > 0$. If the process occurs in a dense medium one needs to account for correlation modifications due to the interactions with the medium and the parity-odd bubbles. The effect of these modifications is similar to the modification of the jet-like two-particle correlations which experience strong suppression of the back-to-back correlations: $\langle a_{1,+} a_{1,+} \rangle = \langle a_{1,-} a_{1,-} \rangle \gg -\langle a_{1,+} a_{1,-} \rangle$. In the CME view, this is a suppression of the back-to-back opposite charge correlations [37]. The effect of strong radial flow can further modify this relation such that the opposite charge correlations can even become positive.

Centrality dependence

Under the assumption that the average size of the P-violating domain does not change with centrality, the correlation should follow a $1/M$ dependence multiplied by a factor accounting for the variation of the magnetic field. Here M is a total multiplicity. The latter is difficult to predict reliably at present. In the most central collisions, where the magnetic field is zero, the CME signal should vanish.

Beam species dependence

The effect may be roughly proportional to the square of the nuclear charge Z^2 because the magnetic field does, but the atomic number A dependence is not well understood. One qualitative prediction is that the suppression of the back-to-back opposite charge correlations should be smaller in collisions of lighter nuclei because the collisions between the lighter nuclei generate the smaller medium.

A event averaged $\langle a_{1,\alpha}a_{1,\beta}\rangle$ is simply estimated using the charge dependent azimuthal correlation $\langle \sin(\tilde{\varphi}_{2,\alpha})\sin(\tilde{\varphi}_{2,\beta})\rangle$. However, this correlation may has other contributions from the background correlations in the out-of-plane region ($\tilde{\varphi}_{2,\alpha} \sim \pi/2$ and $\tilde{\varphi}_{2,\beta} \sim \pi/2$) denoted by B_{out}:

$$\langle \sin(\tilde{\varphi}_{2,\alpha})\sin(\tilde{\varphi}_{2,\beta})\rangle = \langle a_{1,\alpha}a_{1,\beta}\rangle + B_{out}. \tag{2.11}$$

Only when the both particles are in the out-of-plane region, correlations between them can contribute on the background B_{out} since the cosine term results in non-zero. Therefore, the background B_{out} is considered to be produced mainly by clusters, like jets and resonances, in the out-of-plane region.

In Ref. [40], it was proposed that the correlation $\langle \cos(\varphi_\alpha + \varphi_\beta - 2\Psi_{RP})\rangle$ is a best observable to search for the CME since the background is expected to be suppressed with the following decomposition

$$\begin{aligned}\langle \cos(\varphi_\alpha + \varphi_\beta - 2\Psi_{RP})\rangle &= \langle \cos(\tilde{\varphi}_{2,\alpha})\cos(\tilde{\varphi}_{2,\beta})\rangle - \langle \sin(\tilde{\varphi}_{2,\alpha})\sin(\tilde{\varphi}_{2,\beta})\rangle \\ &= (\langle v_{1,2,\alpha}v_{1,2,\beta}\rangle + B_{in}) - (\langle a_{1,\alpha}a_{1,\beta}\rangle + B_{out}) \\ &= \langle v_{1,2,\alpha}v_{1,2,\beta}\rangle - \langle a_{1,\alpha}a_{1,\beta}\rangle + B_{in} - B_{out}, \end{aligned} \tag{2.12}$$

where B_{in} describes the background contributions of the particles for the in-plane region ($\tilde{\varphi}_{2,\alpha} \sim 0$ and $\tilde{\varphi}_{2,\beta} \sim 0$) in the correlation $\langle \cos(\tilde{\varphi}_{2,\alpha})\cos(\tilde{\varphi}_{2,\beta})\rangle$ and $v_{1,2,\alpha/\beta}$ denotes the dipole component with respect to the reaction plane, which comes from the first P-even Fourier coefficient of the single particle azimuthal distribution in a single event Eq. (2.10). Although both the charge dependent and independent parts of B_{in} and B_{out} are not known, it is naively expected that the backgrounds B_{in} and B_{out} may cancel out in the correlation $\langle \cos(\varphi_\alpha + \varphi_\beta - 2\Psi_{RP})\rangle$ and the reaction plane dependent background $[B_{in} - B_{out}]$ remains. The background of the term $\langle v_{1,2,\alpha}v_{1,2,\beta}\rangle$ is ignored in this thesis since the correlation $\langle v_{1,2,\alpha}\rangle$ is less than $O(10^{-3})$. Note that this term is expected to be non-zero and have an interesting physics in the asymmetric heavy-ion collisions like Au–Cu collisions [44].

If the dipole components $\langle v_{1,2,\alpha}v_{1,2,\beta}\rangle$ and the reaction plane dependent background $[B_{in} - B_{out}]$ can be negligible, the correlation $\langle \cos(\varphi_\alpha + \varphi_\beta - 2\Psi_{RP})\rangle$ is expected to be positive for the opposite charge combination and negative for the same charge combinations. The correlation $\langle \cos(\varphi_\alpha + \varphi_\beta - 2\Psi_{RP})\rangle$ can be measured both by using the three-particle cumulant method and the event plane method, which are described in detail in Sec.4.4 and Sec.4.5.

Figure 2.6 (a) shows the results of the correlation $\langle \cos(\varphi_\alpha + \varphi_\beta - 2\Psi_{RP})\rangle$ for same and opposite charge combinations in $\sqrt{s_{NN}}$ =200 GeV Au–Au and Cu–Cu collisions at RHIC measured by the STAR collaboration [39]. A transverse axis represents the collision centraliy percentile. Same charge correlation is negative while the opposite charge correlation is positive. Their magnitudes are roughly same as the expectation from the CME if the dipole component $\langle v_{1,2,\alpha}v_{1,2,\beta}\rangle$ and the reaction plane dependent background $[B_{in} - B_{out}]$ can be negligible. Magnitudes of both the same and opposite charge correlations decrease with decreasing event centrality percentage and are very small in the

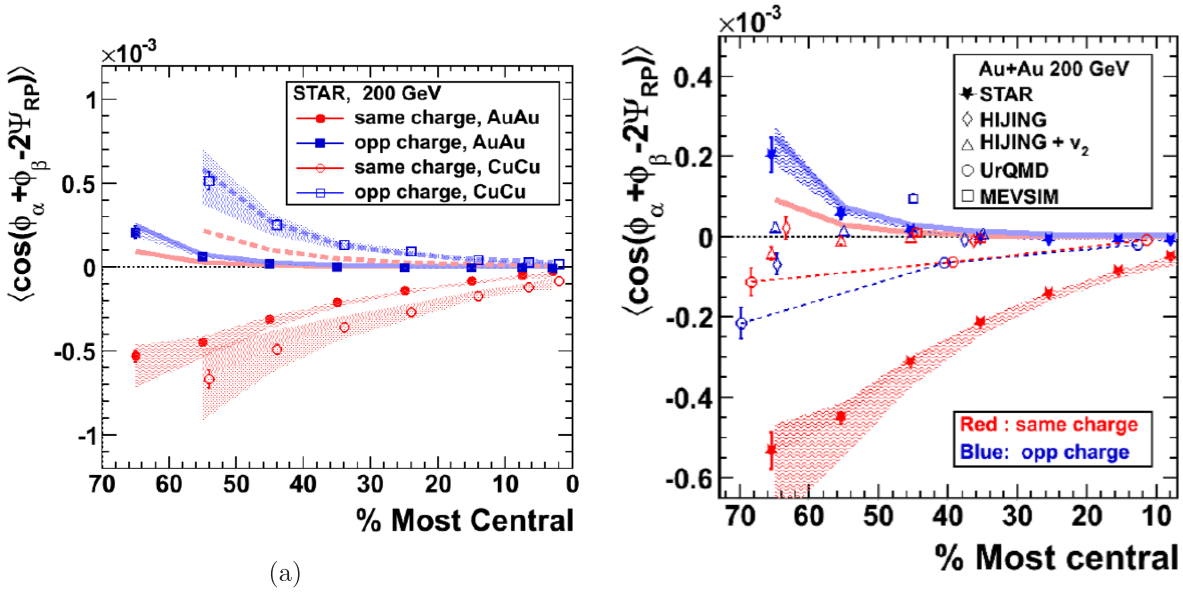

(a)

(b)

Figure 2.6: (a) The centrality dependence of the correlation $\langle \cos(\varphi_\alpha + \varphi_\beta - 2\Psi_{RP}) \rangle$ in $\sqrt{s_{NN}}$ =200 GeV Au–Au and Cu–Cu collisions at RHIC measured by the STAR collaboration. The thick solid (Au–Au) and dashed (Cu–Cu) lines represent the HIJING model expectations for the reaction plane independent background estimated by the correlation $\langle \cos(\varphi_\alpha + \varphi_\beta - 2\varphi_\gamma) \rangle / v_2^{measured}$. (b) $\langle \cos(\varphi_\alpha + \varphi_\beta - 2\Psi_{RP}) \rangle$ calculated by event generator HIJING (with and without an elliptic flow afterburner), UrQMD and MEVSIM. Blue symbols mark opposite charge correlation, and red are same charge correlation. For the event generator, the true reaction plane from the generated event was used for Ψ_{RP} in order to estimate the reaction plane dependent backgrounds [39].

most central collisions. These centrality dependencies also roughly agree with the CME expectation.

However, both same and opposite charge correlations in Cu–Cu collisions are larger in magnitude than those in Au–Au collisions. This beam species dependence conflicts with the naive CME expectations, where it is roughly proportional to the square of the nuclear charge Z^2 because the generated magnetic field does.

The magnitude of the opposite charge correlation is smaller than that of the same charge correlation, which agree with the expectation that the back-to-back opposite charge correlation is suppressed in comparison with the same charge correlation due to the interactions between the medium and parity-odd bubbles, i.e. $\langle a_{1,+} a_{1,+} \rangle = \langle a_{1,-} a_{1,-} \rangle \gg -\langle a_{1,+} a_{1,-} \rangle$ [37]. Furthermore, the opposite charge correlation in Cu–Cu collision is less suppressed than in Au–Au collision, which can be explained in the CME context by the smaller medium in the Cu–Cu collision than in the Au–Au collision.

The CME might be stronger at lower energies since the time integral of the magnetic field is larger. At the same time, the charge separation effect is expected to depend strongly on deconfinement and chiral symmetry restoration. The signal might be greatly suppressed in the lower energy collisions where the QGP is not formed. Measurements in the lower energy collisions were conducted by the STAR collaboration and are described in appendix B. In this thesis, we will discuss at the LHC energy. Some theories predict the signals in the LHC energy is smaller than that in the RHIC top energy. Others predict little collision energy dependence between LHC and RHIC top energies. Detailed discussion is found in Sec.5.1.2.

One ignores the reaction plane dependent background $[B_{in} - B_{out}]$ in the correlation $\langle\cos(\varphi_\alpha + \varphi_\beta - 2\Psi_{RP})\rangle$ so far. As already discussed, both the backgrounds B_{in} and B_{out} originate from the correlations between two particles, which are products of a cluster decay such as jets and resonances. If such cluster properties are different between in the in-plane and out-of-plane regions due to the interaction with the anisotropic medium, nonzero reaction plane dependent background $[B_{in} - B_{out}]$ remains. This is called the flowing cluster effect. If flowing cluster is the only contribution to these correlations, we can write:

$$\begin{aligned}\langle\cos(\varphi_\alpha + \varphi_\beta - 2\Psi_{RP})\rangle &= A_{clust}\langle\cos[(\varphi_\alpha + \varphi_\beta - 2\varphi_{clust}) + 2(\varphi_{clust} - \Psi_{RP})]\rangle_{clust} \\ &\sim A_{clust}\langle\cos(\varphi_\alpha + \varphi_\beta - 2\varphi_{clust})\rangle_{clust} \times v_{2,clust}\{RP\}, \quad (2.13)\end{aligned}$$

where $\langle\cdots\rangle_{clust}$ indicates that the average is performed only over pairs consisting of two daughters from the same cluster and the resulting normalization factor is $A_{clust} = N_{\frac{clust}{event}} N_{\frac{pairs}{clust}} / N_{\frac{pairs}{event}}$. This equation assumes the small reaction plane dependence of $\langle\cos(\varphi_\alpha + \varphi_\beta - 2\varphi_{clust})\rangle_{clust}$. The term $\langle\cos(\varphi_\alpha + \varphi_\beta - 2\varphi_{clust})\rangle_{clust}$ is a measure of the azimuthal correlations of decay products with respect to the cluster azimuth, while $v_{2,clust}\{RP\}$ is the elliptic flow of the cluster. In case of jets as a flowing cluster, their properties may vary with respect to the reaction plane due to the interaction between the medium and jets. Figure 2.6 (b) shows the comparison with the event generator HIJING (with and without an elliptic flow afterburner) [45], UrQMD [46] and MEVSIM [47]. For the moment, any realistic models can not reproduce observed large charge dependence.

In Ref. [34], it was pointed out that the observed charge dependence of the correlation $\langle\cos(\varphi_\alpha + \varphi_\beta - 2\Psi_{RP})\rangle$ used for the CME search by the STAR collaboration can be explained almost solely by the charge dependent parts of the reaction plane dependent background $[B_{in} - B_{out}]$, which are originated from the effects combined with the "effective" LCC and the elliptic flow $v_{2,2}$ on the kinetic freeze-out surface as already discussed at the previous section. If the LCC is imposed on the switching procedure from the hydrodynamic to the hadronic particle picture in the hydro model, the hadron and anti-hadron are spatially correlated and virtually form the cluster. In the conventional hydrodynamic model, the switching procedure from the hydrodynamic to the hadronic particle picture implements on the kinetic freeze-out surface. Since the kinetic freeze-out surface is expected to already have large ellipticity, the virtual clusters formed by the hadron and anti-hadron are affected by the elliptic flow and hence can be regarded as the flowing cluster backgrounds for the CME signals. Note however that the LCC induced correlations affect only on the difference between the same and opposite charge correlations while the CME predicts both the same and opposite charge correlations. So the other mechanism for the charge independent parts of the mixed harmonic azimuthal correlations introduced in the next section (Sec. 2.3), is necessary for a complete understanding of the observed signals. This argument has triggered intensive discussion on the interpretation of experimental results of the CME search [34, 35, 42, 48, 49, 50].

Finally, for the completeness, we need to discuss that the correlation $\langle \cos(\varphi_\alpha - \varphi_\beta) \rangle$ can be decomposed as

$$\begin{aligned}
\langle \cos(\varphi_\alpha - \varphi_\beta) \rangle &= \langle \cos(\tilde{\varphi}_{2,\alpha}) \cos(\tilde{\varphi}_{2,\beta}) \rangle + \langle \sin(\tilde{\varphi}_{2,\alpha}) \sin(\tilde{\varphi}_{2,\beta}) \rangle \\
&= (\langle v_{1,2,\alpha} v_{1,2,\beta} \rangle + B_{in}) + (\langle a_{1,\alpha} a_{1,\beta} \rangle + B_{out}) \\
&= \langle v_{1,2,\alpha} v_{1,2,\beta} \rangle + \langle a_{1,\alpha} a_{1,\beta} \rangle + 2B, \qquad (2.14)
\end{aligned}$$

where B denotes the reaction plane independent background $B = [B_{in} + B_{out}]/2$. So the charge balance moment C_1 also has the possible contribution from the CME denoted as $\langle a_{1,\alpha} a_{1,\beta} \rangle$, but the magnitude of the correlation $\Delta \langle a_{1,\alpha} a_{1,\beta} \rangle$ is a few order smaller than the expected charge balance width from the LCC induced correlations.

2.3 Directed flow and Mixed harmonic azimuthal correlation

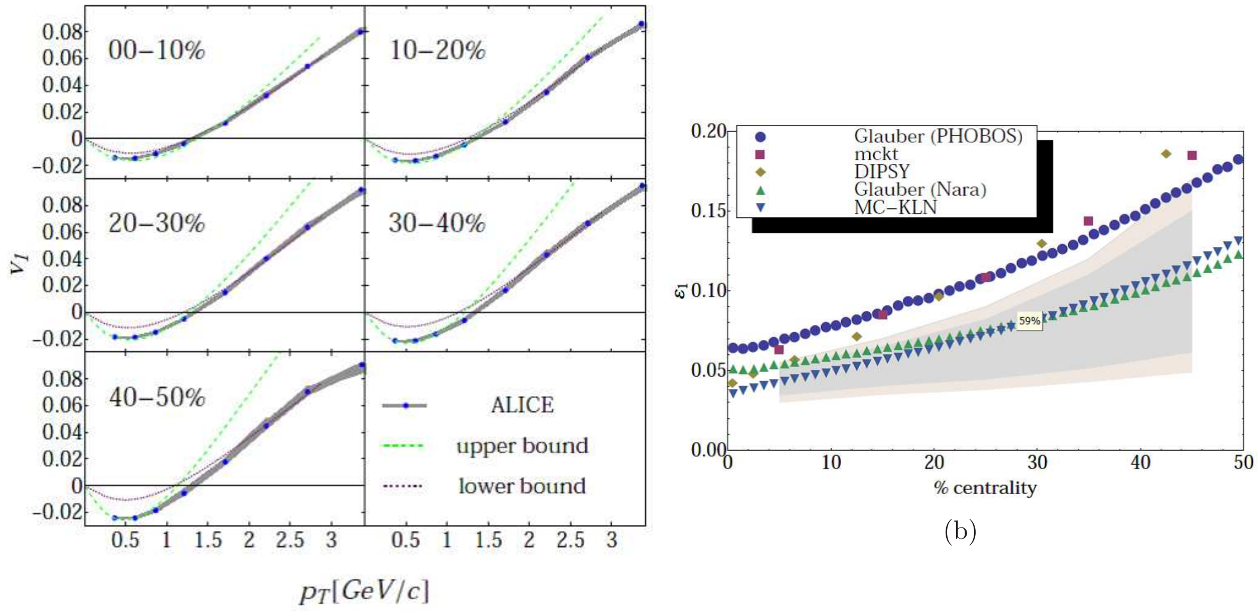

(a)

(b)

Figure 2.7: (a) $v_1(p_\mathrm{T})$ in Pb–Pb collisions at 2.76 TeV extracted from correlation data measured by the ALICE collaboration in comparison with the viscous hydrodynamic simulations with $0 < \eta/s < 0.24$ and the value of ϵ_1 adjusted so as to match the data. (b) The centrality dependence of ϵ_1 with various models. The shaded bands indicate the allowed regions using ALICE data in combination with the viscous hydrodynamics, assuming either $0 < \eta/s < 0.24$ (lighter shade) or $0.08 < \eta/s < 0.16$ (darker shade)[26].

It has been pointed out that the correlation $\langle\cos(\varphi_\alpha + \varphi_\beta - 2\Psi_{RP})\rangle$ used for the CME search has a charge independent part which may be originated from the effect of the transverse momentum conservation [51] and the joint correlation between the directed flow v_1 and the elliptic flow v_2 [13]. Here we introduce the possible signature of the directed flow v_1 and the joint correlations between the different harmonic azimuthal flow.

In Ref. [13], it was pointed out that the fluctuations of the initial density profile can create dipole components. This dipole asymmetry possibly develops through the hydrodynamical evolution of the system with high p_T particles flowing in the direction of the steepest gradient and low p_T particles flowing in the opposite direction because of the global momentum conservation rule, which results in the directed flow v_1 as shown by red lines in Fig. 1.6. When the sign of v_1 at the low p_T region is assigned to be negative, then the sign of v_1 at the high p_T region is expected to be positive. Assuming the boost invariance of the initial density at the mid-rapidity, this directed flow should be rapidity even. With the consideration of the p_{T} conservation effect on the two-particle correlation [22, 23, 24, 25], the two-particle correlation $V_{1\Delta} \equiv \langle \cos(\varphi_\alpha - \varphi_\beta)\rangle$ is expected to be factorized as

$$V_{1\Delta} = v_{1,\alpha} v_{1,\beta} - \frac{p_{T,\alpha} p_{T,\beta}}{\langle \sum p_{\mathrm{T}}^2 \rangle}, \tag{2.15}$$

where rapidity range of particle α and β must be even and the $\sum$ goes over all particles in the events. Recent experimental results on $V_{1\Delta}$ from the ALICE collaboration reasonably agree with the event-by-event ideal hydrodynamic calculations and the viscous hydrodynamic calculations as shown by green dot lines in Fig. 2.7 (a) [26] at the low p_{T} region where the p_{T} conservation effect is rather small. Figure 2.7 (b) shows the centrality dependence of the dipole eccentricities calculated by using various models. The shaded bands indicate the allowed regions using ALICE data in combination with the viscous hydrodynamics, assuming either $0 < \eta/s < 0.24$ (lighter shade) or $0.08 < \eta/s < 0.16$ (darker shade)

Furthermore, the mixed harmonic azimuthal correlations $\langle \cos(\varphi_\alpha + \varphi_\beta - 2\Psi_2)\rangle$ and $\langle \cos(\varphi_\alpha - 3\varphi_\beta + 2\Psi_2)\rangle$ were proposed to measure the directed flow v_1 and joint correlations between v_1 and higher harmonic flow in Ref. [13]. Following their works, the mixed harmonic correlations in Monte Carlo initial models were investigated in detail in Ref. [52] as shown in Fig. 2.8. Generally, a k-particle mixed harmonic azimuthal correlation is defined as:

$$\begin{aligned} v_{n_1,n_2,\cdots,n_k} &\equiv \langle \cos(n_1\varphi_1 + \cdots + n_k\varphi_k)\rangle \\ &= \langle v_{n_1} ... v_{n_k} \cos(n_1\Psi_{n_1} + \cdots + n_k\Psi_{n_k})\rangle, \end{aligned} \tag{2.16}$$

where $n_1, .., n_k$ are integers and $n_1 + \cdots + n_k = 0$. The eccentricity ϵ_n represents the magnitude of the n-th harmonic anisotropy and Φ_n is an azimuthal angle of the n-th harmonic symmetry plane in the initial density profile. Anisotropic flow during the hydrodynamic evolution scales like ϵ_n and develops along Φ_n, so we approximately have $v_n \sim K_n \epsilon_n$ and $\Psi_n \sim \Phi_n$ where K_n is a constant which contains the information of the hydrodynamic response to the initial deformations. The constant K_n depends on the measured p_{T} and η ranges. In case of the integrated measurement, the constant K_1 is expected to be negative and others are positive constant. With the assumption of the boost invariance of the system, we can speculate the following generalization:

$$v_{n_1,n_2,\cdots,n_k} \sim K_{n_1} \cdots K_{n_k} \epsilon_{n_1,n_2,\cdots,n_k}, \tag{2.17}$$

where

$$\epsilon_{n_1,n_2,\cdots,n_k} \equiv \langle \epsilon_{n_1} ... \epsilon_{n_k} \cos(n_1\Phi_{n_1} + \cdots + n_k\Phi_{n_k})\rangle. \tag{2.18}$$

This factorization conjectures are attractive simplifications since we can investigate the detailed geometry of the initial condition, in particular, by the following version of the formula:

$$\frac{v_{n_1,n_2,\cdots,n_k}}{v_{n_1}\{2\} ... v_{n_k}\{2\}} \sim \frac{\epsilon_{n_1,n_2,\cdots,n_k}}{\epsilon_{n_1}\{2\} ... \epsilon_{n_k}\{2\}}, \tag{2.19}$$

where we remove the uncertainty of the factor K_n and $\epsilon_n\{2\} \equiv \langle \epsilon_n^2 \rangle^{1/2}$ corresponds to the n-th harmonic flow $v_n\{2\}$ measured by the two-particle cumulant method. The left-hand side of this equation can be observed experimentally and the right-hand side can be calculated by theoretical models such as MC-CGC and MC-Glauber model. Figure 2.8 shows the calculation of the left-hand side of this equation for various mixed harmonics.

If we believe the above factorization, the mixed harmonic correlation $\langle \cos(\varphi_\alpha - 3\varphi_\beta + 2\Psi_2) \rangle$ has a special interest related to the directed flow v_1. This correlation is expected to be factorized as:

$$\begin{aligned} \langle \cos(\varphi_\alpha - 3\varphi_\beta + 2\Psi_2) \rangle &\sim v_{1,\alpha} \cdot v_{3,\beta} \cdot \langle \cos(\Psi_1 - 3\Psi_3 + 2\Psi_2) \rangle \\ &\sim v_{1,\alpha} \cdot v_{3,\beta} \cdot \frac{\epsilon_{123}}{\epsilon_1\{2\}\epsilon_2\{2\}\epsilon_3\{2\}}. \end{aligned} \tag{2.20}$$

Therefore, the $p_{T,\alpha}$ dependence of this correlation is expected to reflect the p_T dependence of the directed flow $v_1(p_\mathrm{T})$ and its magnitude is expected to be proportional to the initial correlations ϵ_{123} as shown in Fig. 2.9 (a). In this model, the factorization is assumed and ϵ_{123} calculated with the Glauber model, v_1 and v_3 calculated with the ideal hydrodynamic simulations are used. Experimental measurement of the p_T differential correlation $\langle \cos(\varphi_\alpha - 3\varphi_\beta + 2\Psi_2) \rangle$ can be used to test the factorization conjecture, measure the initial correlation ϵ_{123}, and provide another measurement of the directed flow v_1.

Figure 2.9 (b) shows the centrality dependence of the integrated correlation $\langle \cos(\varphi_\alpha + \varphi_\beta - 2\Psi_2) \rangle$, whose sign is negative and originated from a sign of ϵ_{12} shown in Fig. 2.8. Note that this prediction is compatible to the observed charge independent part of the correlation $\langle \cos(\varphi_\alpha + \varphi_\beta - 2\Psi_2) \rangle$ as shown in Fig. 2.6.

In this thesis, the extension of the flow analysis described above is conducted, especially in terms of the directed flow v_1 and the mixed harmonic correlations. These observables are expected to be useful for the better understanding of the initial state of the heavy-ion collisions and the hydrodynamic properties as well as for the understanding of the CME backgrounds.

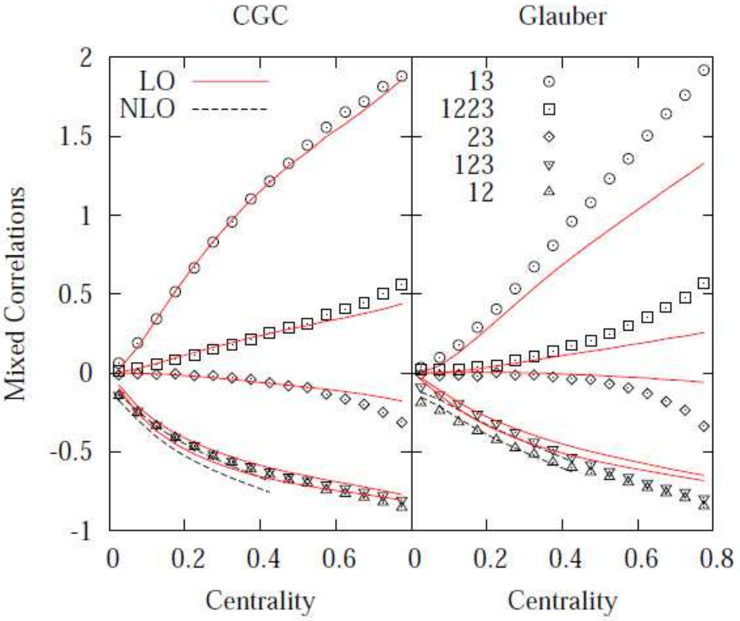

Figure 2.8: Mixed harmonic azimuthal correlations in (left) the CGC-type and (right) the Glauber-type initial density profile versus the event centrality. From top to the bottom: $\epsilon_{13}/(\epsilon_1\{2\}^3\epsilon_3\{2\})$ (labeled 13), $\epsilon_{1223}/(\epsilon_1\{2\}\epsilon_2\{2\}^2\epsilon_3\{2\})$ (labeled 1223), $\epsilon_{23}/(\epsilon_2\{2\}^3\epsilon_3\{2\}^2)$ (labeled 23), $\epsilon_{123}/(\epsilon_1\{2\}\epsilon_2\{2\}\epsilon_3\{2\})$ (labeled 123), $\epsilon_{12}/(\epsilon_1\{2\}^2\epsilon_2\{2\})$ (labeled 12). Symbols are Monte Carlo results. Full and dashed lines are analytic results [52].

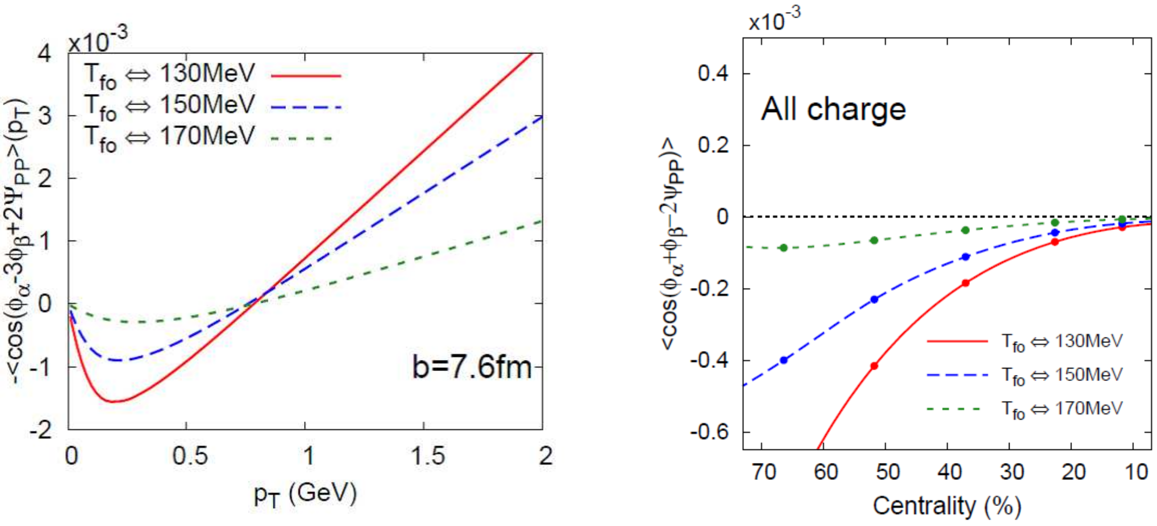

(a)

(b)

Figure 2.9: Theoretical expectations of (a) the $p_{T,\alpha}$ differential correlation $\langle\cos(\varphi_\alpha - 3\varphi_\beta + 2\Psi_{RP})\rangle$ and (b) the integrated correlation $\langle\cos(\varphi_\alpha + \varphi_\beta - 2\Psi_{RP})\rangle$ with various freeze-out temperatures [13].

Chapter 3

Experimental Setup

3.1 The Large Hadron Collider

The Large Hadron Collider (LHC) was constructed between 2002 and 2009 at the CERN laboratory. It is the largest and most powerful particle accelerator ever built. It was installed in the 27 km long circular underground tunnel across the border between France and Switzerland that hosted its predecessor the Large Electron-Positron (LEP collider). The LHC has 16 radio-frequency (RF) accelerating cavities and over 1600 superconducting magnets and can accelerate, store and collide protons with a centre-of mass energy up to 14 TeV and Pb ions with a centre-of mass energy per nucleon up to 5.5 TeV [53].

The protons are firstly accelerated in linear accelerator LINAC 2 and injected into the BOOSTER at an energy of 50 MeV. The BOOSTER accelerates them to 1.4 GeV before they are sent to the Proton Synchrotron (PS), which further accelerates the protons to 25 GeV. From the PS they are sent to the Super Proton Synchrotron (SPS), where they yet again are accelerated, this time to 450 GeV. And finally they are transferred to the LHC ring. At maximum the 2808 bunches of the protons travel the ring either clockwise or counter-clockwise.

For running the LHC with lead ions the procedure is similar, but with some differences. The lead ions are produced by heating a highly purified lead sample up to around 550°. This creates a number of charge states, with Pb^{27+} being the dominant one. The ions are accelerated in LINAC 3 to 4.2 MeV per nucleon. Afterwards they are sent through a carbon foil, which strips them to Pb^{54+} . The Pb^{54+} beam is lead to the Low Energy Ion Ring (LEIR), where it is accelerated to 72 MeV per nucleon, before being transferred to the PS. At the PS, the ions are accelerated up to 5.9 GeV per nucleon. The ions once again are sent through the foil, stripping them to Pb^{82+}, which is the final ionisation used for collisions. After the PS the now fully stripped ions arrive at the SPS, where they are accelerated to 177 GeV per nucleon, before being sent into the LHC ring for acceleration to their collision energy. Like in the proton case, the ion bunches are sent either clockwise or counter-clockwise around the ring. The collision of lead ions only occur at 3 of the experiment sites, namely ALICE, ATLAS and CMS.

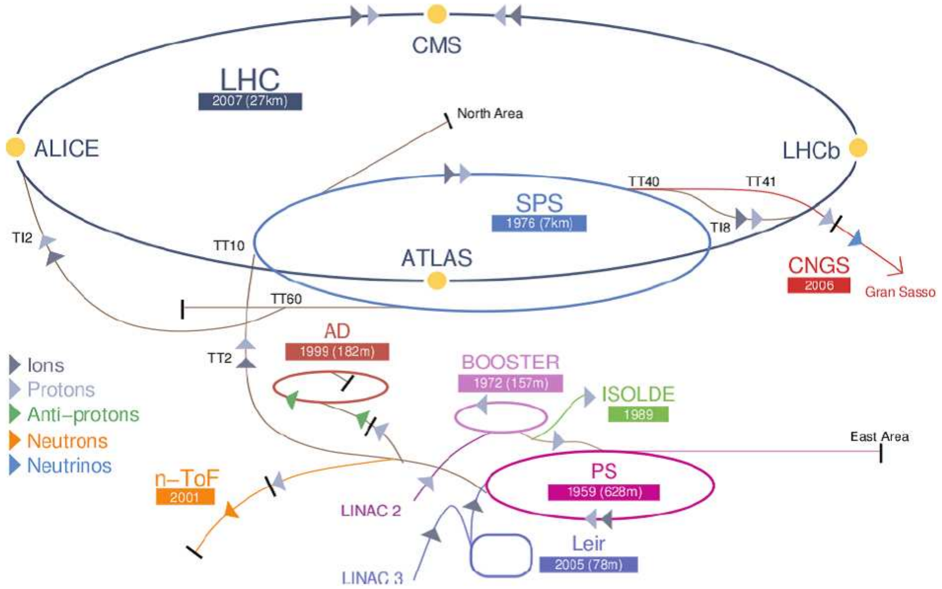

Figure 3.1: The LHC layout [53].

3.2 The ALICE Experiment

A Large Ion Collider Experiment (ALICE) is a large experiment placed at one of the four collision points of LHC. The collaboration involves over a thousand scientists and engineers from 116 institutes in 33 countries. It was designed to study the properties of QCD and to characterize the Quark-Gluon Plasma (QGP). It is the only experiment at LHC which was optimized for the heavy ions collisions.

The detector is placed in the solenoid magnet from the L3 experiment. This provides a relatively low magnetic field of 0.5 T, which allows to measure low momentum particles corresponding to the so-called soft QCD, as well as more energetic particles form hard processes. Because of the extremely high multiplicity expected in central nucleus-nucleus collisions at LHC energies, the design of ALICE was optimized for a multiplicity $dN_{ch}/dy = 8000$. ALICE has an efficient and robust tracking system over a large momentum range, from tens of MeV/c (soft physics) to over 100 GeV/c (jet physics). As some of the tracking detectors are based on drift technologies, they are slower then the detectors operated by the other LHC experiments but can work at the nominal LHC ion beam rate of 10 kHz. A specificity of the ALICE detector over the other LHC experiments is its emphasis on hadron and lepton identification (PID). It is achieved over much of the momentum range using most known PID techniques: specific ionization energy loss dE/dx, time-of-flight, transition and Cherenkov radiation, electromagnetic calorimetry, muon filters, and topological decay reconstruction.

The detectors in the ALICE experiment are arranged in a classical layered structure around the interaction point as shown on Fig. 3.2. Here is a short description of the main detectors [54, 55, 56]:

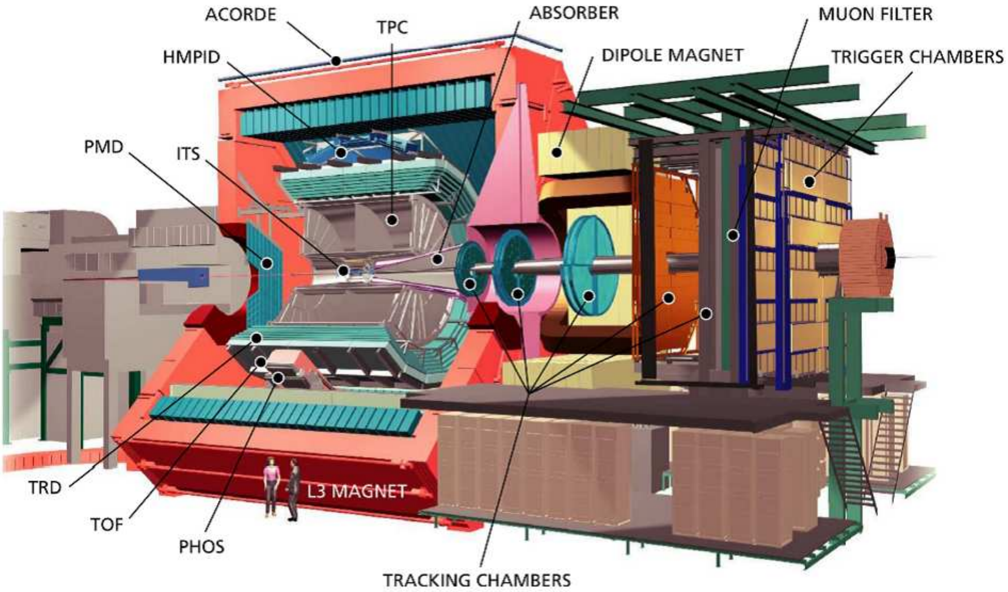

Figure 3.2: The ALICE detector setup [55].

Inner Tracking System (ITS)

It consists in 6 cylindrical layers of silicon detectors at radii from 3.9 to 43 cm, and covering the pseudo-rapidity region $|y| < 0.9$. It allows tracking and identification of low momentum particles, detection of secondary vertexes, and provides a reference to improve the tracking resolution of the TPC. Combined with the TPC, it can identify vertexes with a 14 μm resolution in the transverse plane. It is described in detail in the subsection 3.3.1.

Time Projection Chamber (TPC)

It is a large cylindrical gas detector, and has an inner and outer radius of about 85 cm and 250 cm, respectively, and covers $|\eta| < 0.9$. It is described in detail in the subsection 3.3.2.

Transition Radiation Detector (TRD)

It is placed from 2.9 to 3.8 m from the interaction point, $|\eta| < 0.84$. It discriminates electrons from pions with high efficiency for momenta about 1 GeV/c by the identification of the transition radiation photons from electrons. Thanks to its fast response time, it can provide a trigger for electrons.

Time Of Flight (TOF)

It is placed from 3.99 to 7.41 m from the interaction point, $|\eta| < 0.9$. The detector is made of Multigap Resistive Plate Chamber strips (MRPC), which is made by a ten layer double-stack detector with a time resolution of about 40 ps. By measuring the time particles take to reach it, and combined with the tracking information of the TPC, it allows to identify pions, kaons and protons at low and intermediate momentum ($p_{\mathrm{T}} < 2.5$ GeV/c).

High Momentum Particle Identification Detector (HMPID)

The HMPID consists of an array of proximity-focusing Ring Imaging CHerenkov counters (RICH) and covers a pseudo-rapidity range of $|\eta| < 0.6$ and 58° of azimuthal angle. The HMPID discriminates pions and kaons in the range $1 < p < 3$ GeV/c and protons and kaons in the range $2 < p < 5$ GeV/c by means of their Cherenkov rings.

PHOton Spectrometer (PHOS)

The PHOS is placed partially opposite to the EMCAL and covering a rapidity range $|\eta| < 0.14$ and an azimuthal angle of 110°, made of highly segmented electromagnetic calorimeter of lead-tungstenate ($PbWO_4$, PbWO) crystals with a radiation length of $20X_0$. It is used for neutral mesons and direct photon measurements.

ElectroMagnetic Calorimeter (EMCAL)

The EMCAL is a lead scintillator sampling calorimeter that covers an azimuthal angle range of 107° in the rapidity interval $|\eta| < 0.7$ at a radial distance of about 4.5 m from the vacuum tube. The EMCAL is designed for the study of jet-physics and can provide trigger signals for hard jets, photons and electrons.

Muon Spectrometer

It is situated in the forward region ($-4 < \eta < -2.5$), on one side of the experiment. It offers tracking of muons with high momentum ($p > 4$ GeV/c, having passed the large concrete absorber). It provides measurement of the different quarkonia ($J/\psi, \psi', \Upsilon, \Upsilon', \Upsilon''$) decaying into the $\mu\mu$ channel.

T0 Detector

The T0 detector is designed to determine the collision time with 50 ps resolution and to determine the collision vertex with 1.5 cm resolution. T0 consists of two units, one on each side of the interaction point. Each T0 unit is comprised of quartz Cherenkov radiators glued to photo multiplier tubes. A coincidence between signals in both sides is used for both vertex and time determination. T0 furthermore acts as a early wake-up signal to other detectors. Due to the low acceptance of T0, it is only reliable for Pb–Pb collisions.

Zero Degree Calorimeter (ZDC)

The Zero Degree Calorimeters (ZDC) are positioned at very forward angles. Their role is to measure the spectator nucleons from heavy ion collisions, in order to estimate the number of participants, and hence the centrality. Furthermore it is also used to determine the event plane.

The two ZDC themselves are positioned on each side of the interaction point, 116 meters away from it. Counted as part of the ZDC system are also two electromagnetic calorimeters (ZEM). These are placed on either side of the beam pipe, but only 7 meters away from the interaction point on the opposite side of the muon absorber.

The ZEM measures the photons from particles emitted at forward rapidity, which is used for determining the centrality of very central collisions where few spectators escape to the ZDCs. Similarly they are also used for very peripheral collisions. For very peripheral collisions, the spectators resemble the incoming nuclei (both in amount and direction), and thus might continue inside the beam pipe, avoiding detection in the ZDCs.

VZERO Detector

VZERO detector consists of two units of scintillator counters (V0A and V0C) located on each side of the interaction point. It is described in detail in the subsection 3.4.1.

Forward Multiplicity Detector (FMD)

It consists of silicon strip detectors and covers the forward regions ($-3.4 < \eta < -1.7$ and $1.7 < \eta < 5$) in order to measure the charged particle multiplicity in the forward region. It is described in detail in the subsection 3.4.2.

The pseudo-rapidity acceptances of the subdetectors in the ALICE are shown in Fig. 3.3. A z-axis of global coordinate is defined as an axis parallel to the mean beam direction, pointing towards the “A-Side” or “Shaft-Side”, away from the muon arm. The opposite side (negative z values) is called “C-Side” or “Muon-Side”. The x-axis is lying in the local horizontal accelerator plane, pointing towards the centre of the LHC ring. the side with positive x values is called “I-Side” (inner), the opposite side correspondingly “O-Side” (outer). The y-axis is chosen to define a right handed system, thus pointing upwards.

The azimuthal angle ϕ is increasing counterclockwise, starting from the x-axis (ϕ-0) and looking from the “A-Side” towards the “C-Side”. The polor angle θ is increasing from the z-axis towards the xy-plane.

3.3 Tracking System in ALICE Detectors

3.3.1 The Inner Tracking System (ITS)

The ITS consists of six layers of silicon detectors with radii from 3.9 cm to 43 cm as shown in Fig. 3.4 [57]. The tasks of the ITS are the reconstruction of the primary vertex of the collision as well as the reconstruction of secondary vertexes with a resolution better than 100 μm in transverse direction. The ITS stand-alone tracking can provide the tracking information for low-momentum particles that do not reach the TPC. The p_{T} cut-off at nominal field for the two innermost layers is about 35 MeV/c.

The two innermost layers, Silicon Pixel Detector (SPD), are based on hybrid silicon pixels which consist of silicon detector diodes with a thickness of 200 μm. The first layer and the second layer are placed at 3.9 cm and 7.6 cm with an acceptance of $|\eta| < 2.0$ and $|\eta| < 1.4$, respectively. The SPD has approximately 9.8 million channels. The average material traversed by a straight track perpendicular to the beam line crossing the SPD

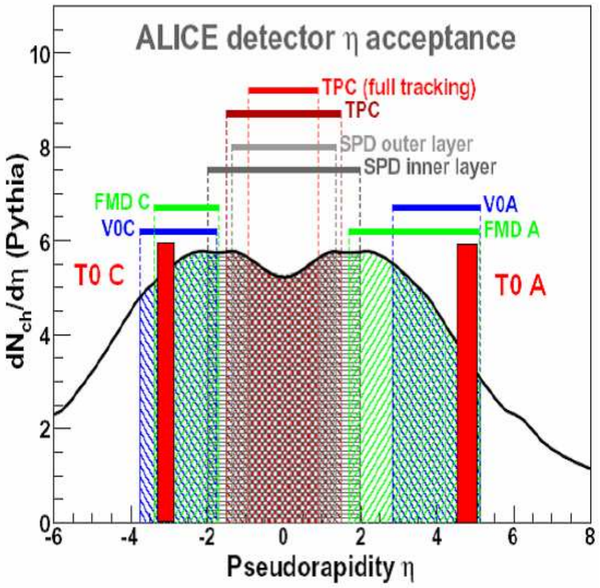

Figure 3.3: The pseudo-rapidity acceptance of the subdetectors in the ALICE [55].

barrel corresponds to about 2% X_0. The pixel readout chip (ALICE1LHCb) is a mixed-signal ASIC for the readout of 8192 pixels. Each pixel cell contains a preamplifier-shaper with leakage current compensation, followed by a discriminator. A signal above threshold results in a logical 1 which is propagated through a delay line during the 6 μs latency time until the arrival of the L1 trigger signal. A four-hit-deep front-end buffer on each cell allows derandomization of the event arrival times. Upon arrival of the L1 trigger, the logical level present at the end of the delay line is stored in the first available buffer location. The outputs of the discriminators in the pixel cells of the ALICE1LHCb chip provide a fast-OR digital pulse when one or more pixels are hit on the chip. The fast-OR is an invaluable tool in testing and allows implementing a unique triggering capability in the SPD. Upon arrival of the second level trigger (L2), the data contained in the front-end buffer locations corresponding to the first (oldest) L1 trigger are loaded onto the output shift registers. One pixel chip is read out in 25.6 μs. The 10 chips of two ladders (one half-stave) are read out sequentially in a total time of about 256 μs.

The third and forth layer, Silicon Drift Detector (SDD), consist of a 300 μm thick layer of homogeneous high-resistivity silicon. The readout of the SDD is analog, therefore particle identification can be conducted using the information of energy-loss. The SDD has 133,000 channels.

The two outermost layers, Silicon Strip Detector (SSD), consist of sensors equipped on both sides with silicon micro-strips. These are arranged under a stereo angle of 35 mrad allowing for a two-dimensional measurement of the track position together with an energy-loss measurement for particle identification. The SSD has approximately 2.6 million channels.

The information for ITS is summarized in Table 3.1.

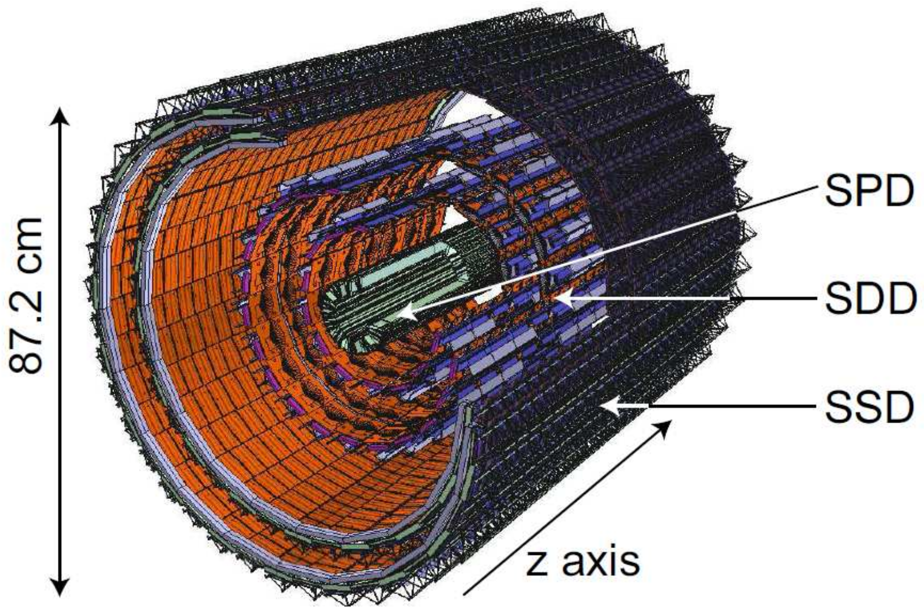

Figure 3.4: Schematic view of the ITS [57].

3.3.2 The Time Projection Chamber (TPC)

The main tracking device of the ALICE experiment is a large volume (~88 m^3), cylindrical Time Projection Chamber (TPC) operated in 0.5 T solenoidal B field parallel to the E field axis as shown in Fig. 3.5 [58, 59]. The main performance goals considered in the design are a dE/dx resolution better than 5%, a relative p_{T} resolution better than 1% for momenta of $\sim$ 1 GeV/c and better than 2.5% for momenta of 4 GeV/c, and two track resolution capable fo separating tracks with a relative momentum difference of $<$ 5 MeV.

The TPC is separated into two volumes with the Central Electrode (CE) made of single stretched Mylar foil, and secondary electrons drift toward the end-caps. The drift gas Ne-CO_2-N_2 is optimized for drift speed, large ion mobility, low diffusion of electrons, low radiation length and hence low multiple scattering, small space-charge effect, and ageing properties. The drawback of Ne-CO_2-N_2 is that this mixture is a cold gas, with a steep dependence of drift velocity on temperature. For this reason, the TPC is aiming for a thermal stability with $\Delta T < 0.1$ K in the drift volume over the running period. Because of the Ne-CO_2-N_2 (90%-10%-5%) gas mixture used in the TPC, the field cage will have to be operated at very high-voltage gradients, of about 400 V/cm , with a high voltage of 100 kV at the central electrode which results in a maximum drift time of about 90 μs.

The readout chambers are at the two end-caps of the TPC cylinder. The chambers are multi-wire proportional chambers (gain $\sim 10^4$) with cathode pad readout as shown in Fig. 3.6. The readout chambers are made of standard wire planes, i.e. they consist of a grid of anode wires above the pad plane, a cathode wire plane, and a gating grid. The readout pad size is 4×7.5 mm^2 in the inner region and the pad occupancy for Pb–Pb collisions is 15 $\sim$ 40 %. Space-point resolution depends on the drift length, the track inclination angle, the charge deposit on the anode wire, and so on. Its typical value is $\sim$ 1 mm in $r\phi$

Layer	Technology	Radius (cm)	±z (cm)	Special resolution (μm)	
				$r\phi$	z
1	Pixel	4.0	14.1	12	100
2	Pixel	7.2	14.1	12	100
3	Drift	15.0	22.2	38	28
4	Drift	23.9	29.7	38	28
5	Strip	38.5	43.2	20	830
6	Strip	43.6	48.9	20	830

Table 3.1: Geometrical information of the ITS and the design values for the resolutions [57].

and z direction. The readout chambers are normally closed by a gating grid for electrons coming from the drift volume and they are opened only by the L1 trigger (6.5 μs after the collision) for the duration of one drift-time interval, i.e. of about 90 μs. This helps to prevent space charge due to positive ions from drifting back from the multiplication region for non-triggered interactions and background.

The charge collected on the TPC pads is amplified and integrated by a low-input impedance amplifier. It is based on a Charge Sensitive Amplifier (CSA) followed by a semi-Gaussian pulse shaper of the fourth order. These analogue functions are realized by a custom integrated circuit (PASA), implemented in a CMOS technology 0.35 μm, which will contain 16 channels with a power consumption/channel of 12 mW. The circuit has a conversion gain of 12 mV/fC and an output dynamic range of 2 V with a linearity of 1%. It produces a pulse with a rise time of 120 ns and a shaping time (FWHM) of 190 ns. The single channel has a noise value (r.m.s.) below 1000e and a channel-to-channel cross-talk below 60 dB. Immediately after the PASA, a 10-bit pipelined ADC (one per channel) samples the signal at a rate of 5-6 MHz. The digitized signal is then processed by a set of circuits that perform the baseline subtraction, tail cancellation, zero-suppression, formatting and buffering. The ADC and the digital circuits are contained in a single chip named ALTRO (ALice Tpc ReadOut). The ALTRO chip integrates 16 channels, each of them consisting of a 10-bit, 30-MSPS ADC, a pipelined Digital Processor and a multi-acquisition Data Memory. When a L1 trigger is received, a predefined number of samples (acquisition) are temporarily stored in a data memory. Upon L2 trigger arrival the latest acquisition is frozen, otherwise it will be overwritten by the next acquisition.

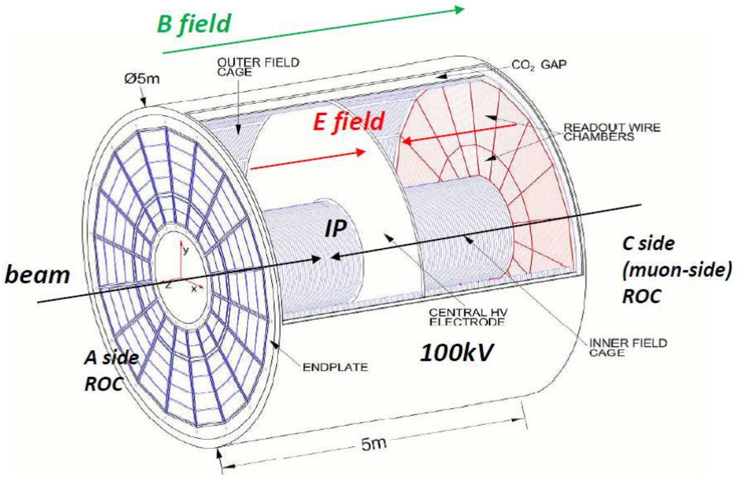

Figure 3.5: Schematic view of the TPC [58].

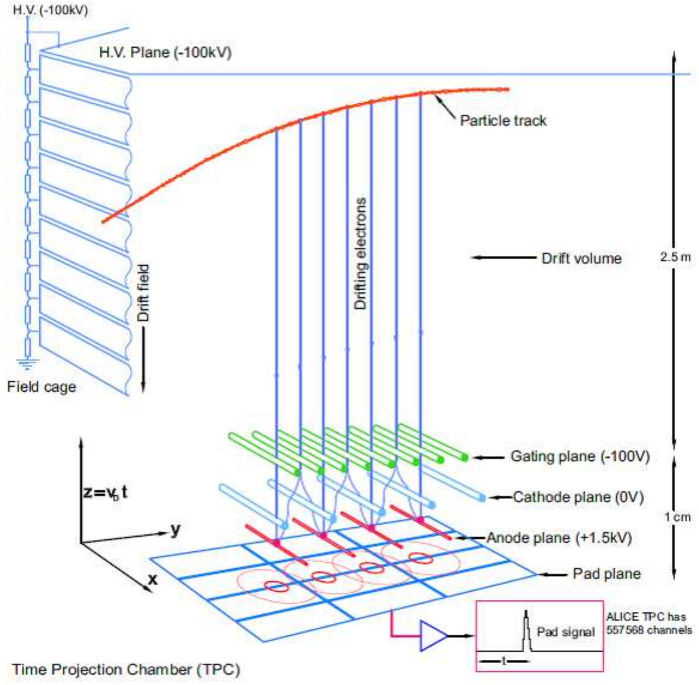

Figure 3.6: Schematic view of a multiwire proportional chamber used in the ALICE-TPC [58].

3.4 Forward detectors

3.4.1 VZERO detectors

The VZERO detectors are designed with a much larger acceptance, in order to perform as a minimum bias trigger in both proton-proton and Pb–Pb collisions. Furthermore, it is also used, together with the timing information of the collision, for the rejection of beam-gas interactions. The VZERO is also used to determine the event centrality as discussed in Sec.4.1.2 and the event plane as discussed in Sec.4.5.

The V0A/V0C are segmented into 32 elementary counters distributed in four rings as shown in Fig. 3.7 (a). Each ring covers 0.4-0.6 unit of pseudo-rapidity. The rings are divided into eight sectors of 45°. The elementary counter consists of scintillator material with embedded WaveLength Shifting (WLS) fibres. The light from the WLS is collected by clear fibres and transported to PhotoMultiplier (PM) installed at 3-5 m from the detectors, inside the L3 magnet. The time resolution of each individual counter will be better than 1 ns.

Signals from each PMT are sent to an electronics circuit, which delivers two signals. The first one is sent to a threshold discriminator for the generation of the V0 event triggers. It is amplified by a factor of about 10. If at least one duscriminator is fired during the time window around the timing of the beam crossing (after 3 ns for V0A, 11 ns for V0C), the V0 event trigger is issued. Figure 3.7 (b) shows correlation between the arrival time of particles on the V0A and V0C disks in proton-proton collisions measured in November 23, 2009. A peak around [80,80] corresponds to the beam-beam collisions while the other two peaks are due to the beam-gas collisions. The second one, not amplified, is used for the measurement of the charge given by the counter. The multiplicity of Minimum Ionizing Particles (MIPs) can be measured using this second signals in two different ways. In a one way, the charges from PMT anode are integrated and digitized by ADCs. Figure 3.7 (c) shows the distribution of PMT charges. In the other way, the pulse legnth are measured. Figure 3.7 (d) shows the distribution of PMT signal width, which shows a three bump structure revealing the presence of one, two and three MIPs more clearly than Figure 3.7 (c).

Note that the significant fraction of secondray particles are produced from inner materials such as the beam pipe, but their azimuthal distribution is proportional to that of the primary particles. Therefore, in order to calculate the event plane from the VZERO hits, non-corrected ADC values for each PMT channels are used.

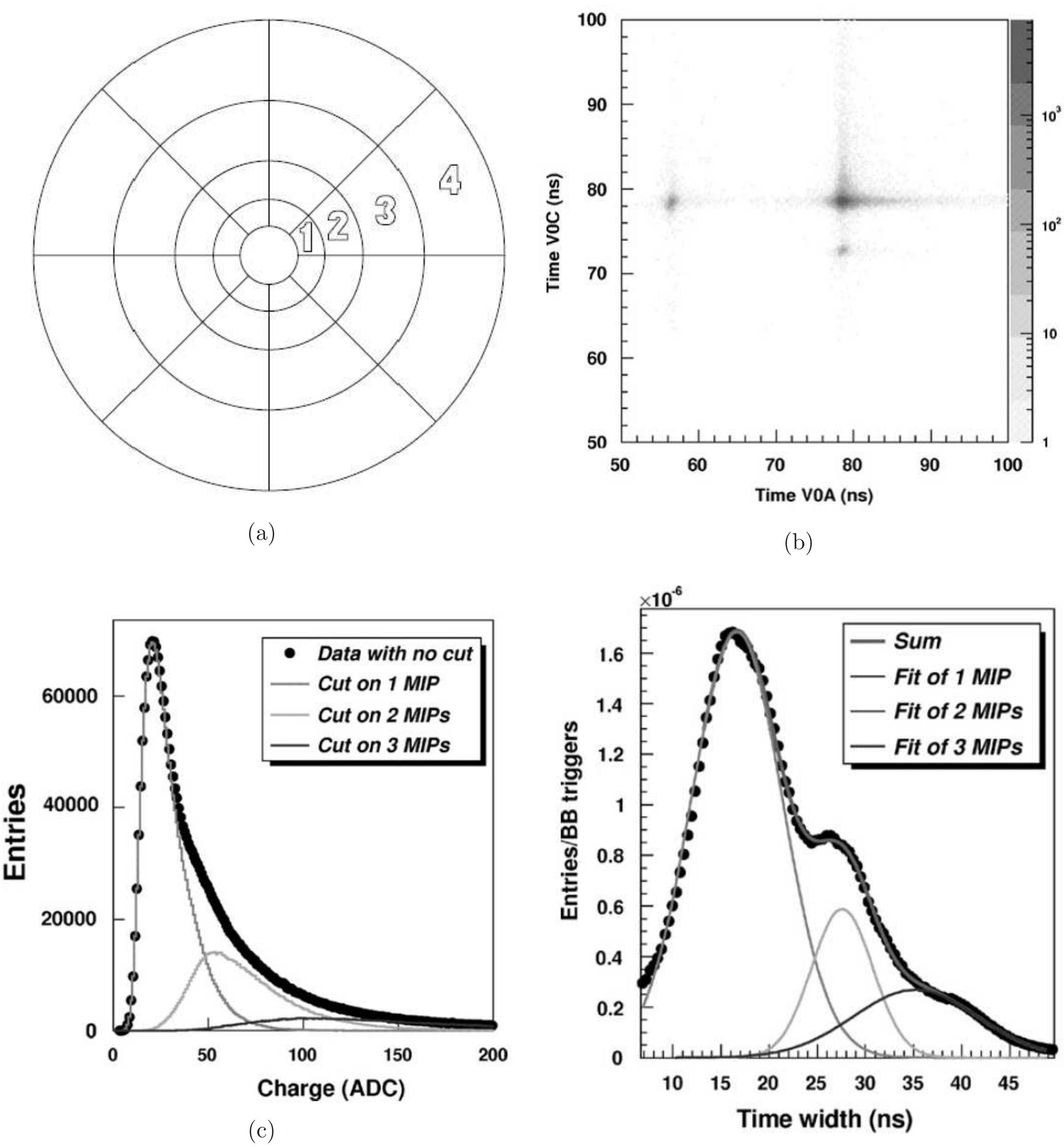

(a)

(b)

(c)

(d)

Figure 3.7: (a) Schematic view of the VZERO detectors [55]. (b) Correlation between the arrival time of particles in the V0A and V0C disks. (c) Distributions of the photomultiplier signal widths and (d) charges from V0A channels. [61].

3.4.2 Forward Multiplicity Detector (FMD)

The FMD consists of 51200 silicon strip channels distributed over five ring counters of two types with each 20 or 40 sectors in azimuthal angle, respectively as shown in Fig. 3.8. Each sector will be read out independently and contains 512 or 256 detector strips at constant radius. The choice of segmentation of the FMD is driven by the requirement to keep the average number of hits per strip well below 2-3 particles for most strips in order to enable an accurate multiplicity reconstruction based on total energy deposition.

The individual Si sensors are manufactured out of 300 μm thick 15 cm diameter n-type Si wafers with p+ type implants (strips). Each p+ implant is connected through a bias resistor to a bias ring. During operation, high voltage (greater than 70V) is applied to an aluminum surface on the back of the silicon bulk (where no p+ implants exist) and the bias ring is left grounded. This depletes the silicon bulk of thermal electron-hole pairs that would dominate the readout noise in an unbiased sensor. Readout lines are capacitively coupled to the p+ implants. The front-end electronics are highly integrated circuits mounted on a hybrid board onto which the Si sensor itself is firmly attached. Strips are bonded to the hybrid. In addition to the electrical functions, the hybrid substrate serves as mechanical support for the Si sensor and the corresponding front-end amplifier chips. The preamplifier-shaper integrated circuit that was chosen is the VA1 chip which is a low-noise amplifier (r.m.s. noise of 1.5% MIP for 25 pF input capacitance) with a 1-2 μs speaking time and a dynamic range of 0-20 MIPS. The chip incorporates a sample-and-hold circuit for each of the 128 channels and a multiplexed readout at a speed of 10 MHz, resulting in a full readout time of 12.8 μs.

Figure 3.9 (a) shows a sample of the data taken in that test beam for a single strip using high energy (680 MeV) electron beam at the ASTRID facility at the University of Arhus in Denmark [62]. A minimum ionizing signal peak can be seen in the raw signal. However, a large number of signals are observed with energies between the noise level and the 1 MIP peak. Figure 3.9 (b) shows the correlation between the energy deposited in two adjacent silicon strips. The sharing of energy from a single particle among the two strips can be clearly seen. If the signal in both pads is required to be above the noise level (0.4 fC in this case), the resultant distribution of summed energy from the adjacent pads fits a Landau distribution well. If signals which could have been shared with neighboring channels are excluded by requiring that only small amounts of energy (on the order of the noise level) are recorded in adjacent strips, the number of signals between the noise peak and the 1 MIP peak is drastically reduced. After this cut, a clear signal peak is evident and the signal to noise of the detector can be calculated. A resultant signal to noise ratio of 60:1 is measured. This signal peak also displays properties of a Landau distribution, but retains some features of residual sharing.

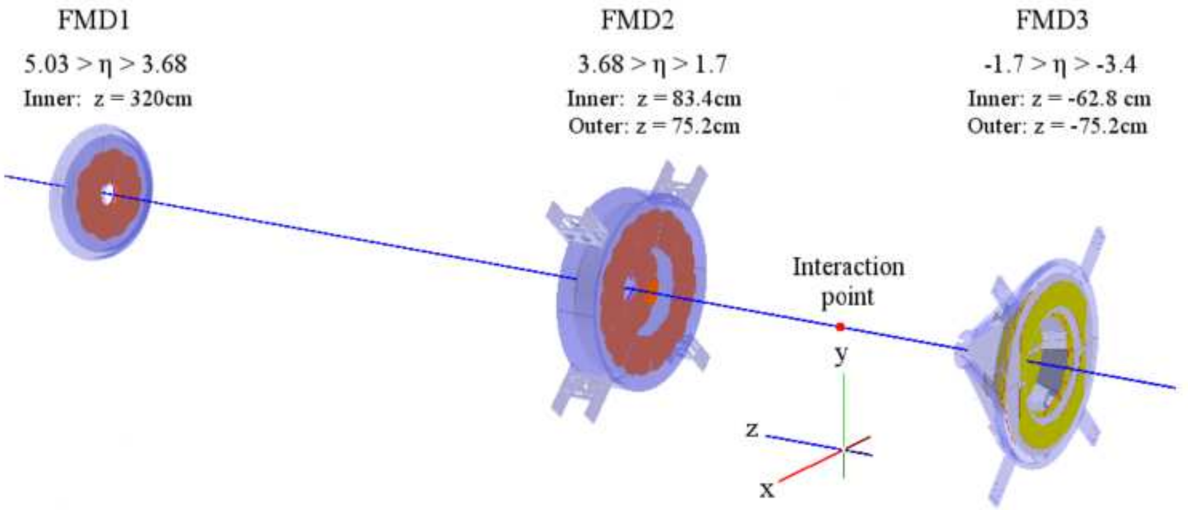

Figure 3.8: Schematic view of the FMD [60]. The FMD consists of 5 rings (FMD1, FMD2 inner, FMD2 outer, FMD3 inner and FMD outer).

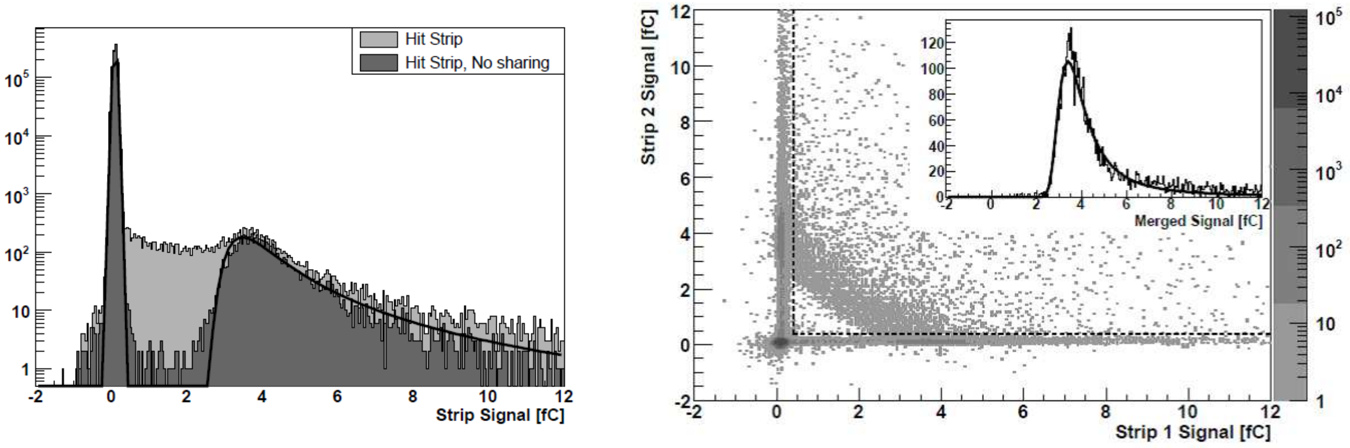

(a)

(b)

Figure 3.9: (a) Distribution of the silicon strip signals using 680 MeV electron beam. (b) Correlation between energies deposited in 2 adjacent silicon strips. A clear band of shared energy representing E1 + E2 = 1 MIP can be seen. [62].

3.5 DAQ and Trigger System

The trigger input signals from the detectors are collected and managed by the ALICE Central Trigger Processor (CTP), designed to select events having a variety of different features and rates and to manage these rates with bandwidth requirements of the Data AcQuisition system (DAQ).

The ALICE trigger system is subdivided in three levels:

The Level-Zero Trigger (L0)

is issued according to the L0 input signals from the fastest detectors, such as the SPD, VZERO, T0 and the muon trigger. The trigger is distributed with a fast fan-out to all the front-end cards. The trigger latency with respect to the time of the interaction is fixed at 1.2 μs. The detectors respond to the L0 with Detector BUSY signals. The front-end is held on L0 and the logic waits for a first-level trigger L1 or for a timeout in the case of a missing L1. In 2010 runs, L0 rate for Pb–Pb ($p + p$) minimum bias collisions is $\sim$ 500 Hz (1 kHz).

The Level-One Trigger (L1)

is issued at a fixed latency of around 6 μs (still to be precisely specified) with respect to the interaction time. A positive L1 trigger causes the event number to be distributed to the detectors and starts the transfer of the data from the front-end event registers to the multievent buffers.

The Level-Two Trigger (L2)

causes, after data reduction and packing, the data transfer to the ALICE data acquisition. The L2 reject signal (L2r) can be issued at any time before the fixed latency corresponding to a level-2 accept (L2a) trigger at around 90 μs (that still needs to be precisely specified).

Once the CTP has decided to acquire a particular event, the trigger signal is dispatched to the front-end read-out electronics (FERO) of the involved detectors. The data are then injected in the Detector Data Link (DDL, an ALICE-standard, in ALICE there are more than 450 optical DDLs) and sent to a farm of computers, called Local Data Concentrators (LDC), that do sub-event building from the event fragments they receive from the front-end electronics. The sub-events are than shipped through an event building network to the Global Data Collectors (GDC) that take all the sub-events from the various LDCs and build the full event and, depending on the High Level Trigger decision, send it to the storage facilities. The rate of data collected by the different ALICE detectors can reach the impressive amount of 25 GB/s, where the data size of the single Pb–Pb ($p + p$) event is 50 (2) MB. The bandwidth of the DAQ system is limited to 4 GB/s. The High Level Trigger (HLT) is responsible of the acceptance or rejection of an event on the basis of an online analysis and, in case of positive decision, compress the amount of collected data (without any loss of physical information) using specific algorithms in order to reduce the data rate to a value acceptable by the DAQ and by the storage elements.

3.6 The ALICE Offline Analysis Framework

3.6.1 Dataflow

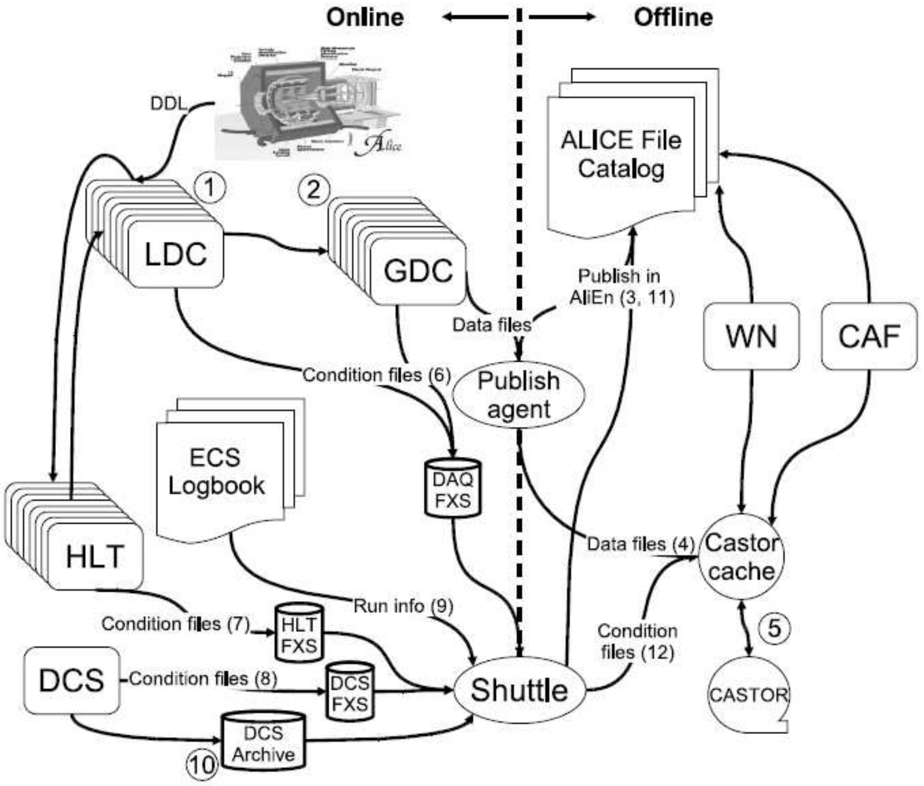

Figure 3.10: Schematic view of ALICE's data flow [63].

The raw data taken by the subdetectors has to be processed before it is available in the form of reconstructed events for further analysis. This happens in several stages and is illustrated in Fig. 3.10. Data originating from the subdetectors (denoted by 1 in Fig. 3.10) is processed by LDCs, global events are built by GDCs (2). The publish agent registers the assembled events into the AliEn system (3) and ships them to the CERN computing center where they are stored first on disks (4) and then permanently on tapes (5) by the CASTOR system.

During data-taking the subdetectors also produce "conditions data" which are relevant for the calibration of individual detector signals. Conditions data provide information about the detector status and environmental variables during data-taking. Examples are inactive and noisy channel maps, distributions that describe the response of a channel, temperatures and pressure in a detector, and detector configuration. Many of the conditions data could in principle be calculated from the raw data and extracted offline after data-taking. However, such an approach would require an additional pass over the raw data before the reconstruction which is not feasible due to the limited computing resources. Therefore, conditions data are already extracted during data-taking.

Conditions data are produced by special programs that process the raw data stream and extract the needed values. These programs work in the realm of DAQ, DCS (Detector Control System), and HLT and store their output on so-called "File eXchange Servers"(FXS) (6-8 in Fig. 3.10). A dedicated program called "Shuttle collects" collects these outputs and makes them available to the reconstruction. Furthermore, it retrieves information about the run from the ECS logbook (9) and collects continuously monitored values that are written by DCS into the "DCS Archive" (10). After processing the data, the Shuttle registers the produced condition files in AliEn (11) and stores the data in CASTOR (12).

With the registration of the raw and conditions data the transition from the online to the offline would has taken place. Online denotes all actions and programs that have to run in real time. Offline processing is the subsequent step, like for example event reconstruction, which is executed on worker nodes (WN) of Grid sites located around the Grid.

3.6.2 AliRoot

AliRoot is the offline framework for simulation, alignment, calibration, reconstruction, visualization, quality assurance, and analysis of experimental and simulated data. It is based on the ROOT framework. Most of the code is written in C++ with some parts in Fortran that are wrapped inside C++ code [64, 65].

3.6.3 GRID

The GRID paradigm implies the unification of resources of distributed computing centers, in particular computing power and storage, to provide them to users all over the world. It allows computing centers to oer their resources to a wider community. This allows resources in large collaborations to be shared. The huge amount of data produce by the ALICE detector (∼2 PB per year) makes almost unavoidable the necessity of automatized procedures for the (software) reconstruction of the events and for the first steps of the analysis, with the consequent employ of a large mass of computing resources. The world-wide distributed GRID facilities were designed to provide both the computing power and the disk space needed to face the LHC software challenge. Hence the need of a GRID-oriented analysis code. One of the main advantages in using the GRID is the possibility to analyze a large set of data by splitting a job analysis into many "clone" subjobs running in parallel on different computing nodes. The ALICE VO (Virtual Organization) is made of more than 80 sites distributed worldwide.

Each site is composed of many WN, which are the physical machines where the software programs can be run. The Storage Element (SE) is responsible for managing physical data in the site and for providing an interface to mass storage. The Computing Element (CE) service is an interface to the local (WN) batch system and manages the computing resources in the site. The ALICE Collaboration has developed AliEn [66] as an implementation of distributed computing infrastructure needed to simulate, reconstruct and analyze data from the experiment. AliEn provides the two key elements needed for large-scale distributed data processing: catalogue for data storage and the possibility to execute the jobs in a distributed environment. The analysis software, the user code and the AliRoot libraries needed by each subjob to run must be specified in a JDL (Job Description Language), together with the data sample and the way to split it. The data sample is specified through a XML (eXecutable Machine Language) collection which contains a list of the Logical File Names (LFN, the entries in the catalogue).

3.6.4 Reconstruction

The data reconstruction is divided into two steps: local and global. The local reconstruction is done individually for each sub-detector using only data collected by this sub-detector.

The first step of the global reconstruction is finding the primary vertex using the SPD clusters. This is done by connecting reconstructed clusters from two layers of SPD to build tracklets. Many of the tracklets are constructed from two clusters produced by different particles. Each tracklet is propagated to the beam line. The crossing points of the tracklets originating from real particles coming from the primary vertex with the beam line are very close. Those crossing points are used to estimate the position of the SPD primary vertex.

Before reconstructing the tracks, two-dimensional clusters in the TPC pad row-time planes are found. The reconstructed positions of the clusters are interpreted as the crossing points of the tracks and the centres of the pad rows. We investigate the region of 5×5 bins in z (drift) and y (pad) directions around the central bin with maximum amplitude. This is bigger than the typical size of a cluster, which is $\sigma \sim 0.75$ bins in both directions. The position of a cluster is reconstructed as its centre of gravity (COG). The track reconstruction is performed with these clusters using the Kalman filter approach. This approach was developed to measure dynamic system parameters or predict the system behaviour. It was adopted for reconstruction of tracks in high-energy experiments by changing the time steps to space points. Detailed description of the Kalman filter is in appendix.

In the end, each reconstructed track has a list of parameters (e.g. number of clusters in the TPC or the ITS, χ^2 per cluster), which describes its quality. The reconstructed tracks are used to improve the reconstruction of the primary vertex. The improved vertex is called a global vertex. The resolution of the z-coordinate is ~ 10 μm in Pb–Pb events.

The output of the reconstruction is stored in the Event Summary Data (ESD), a file containing all the physical information needed for the analysis both at track and event level plus information relevant for checking the quality of the reconstruction for each detector. Since the ESD contains more information than what is needed for the analysis, further event and track cuts are applied in the analysis procedure.

3.7 Run Conditions

The data of $\sqrt{s_{NN}}$=2.76 TeV Pb–Pb collisions used in this analysis were taken by the ALICE experiment in December 2010. Table 3.2 shows typical parameters for $\sqrt{s_{NN}}$=2.76 TeV Pb–Pb collisions at ALICE in 2010. The recorded integrated luminosity for ALICE rose up to 10 μb^{-1} which corresponds to about 13 M events with the minimum bias (MB) trigger. A peak luminosity at ALICE reached $\sim 30 \times 10^{24}$ cm^{2}s^{-1}. Figure 3.11 shows the integrated and peak luminosities as a function of day of year 2010.

Parameters	Values
$\sqrt{s_{NN}}$ [TeV]	2.76
Initial ion-ion Luminosity [cm^{-2}s^{-1}]	0.7 $\times 10^{25}$
Number of bunches	62
Minimum bunch spacing [ns]	1350
β^* [m]	3.5
Pb ions per bunch	7×10^7
Transv. norm. RMS emittance [μm]	1.5
Longitudinal emittance [eV·s/charge]	2.5
Luminosity half-life (when 1,2,3 experiments are conducted) [h]	14, 7.5, 5.5

Table 3.2: Typical parameters for $\sqrt{s_{NN}}$=2.76 TeV Pb–Pb collisions at ALICE in 2010.

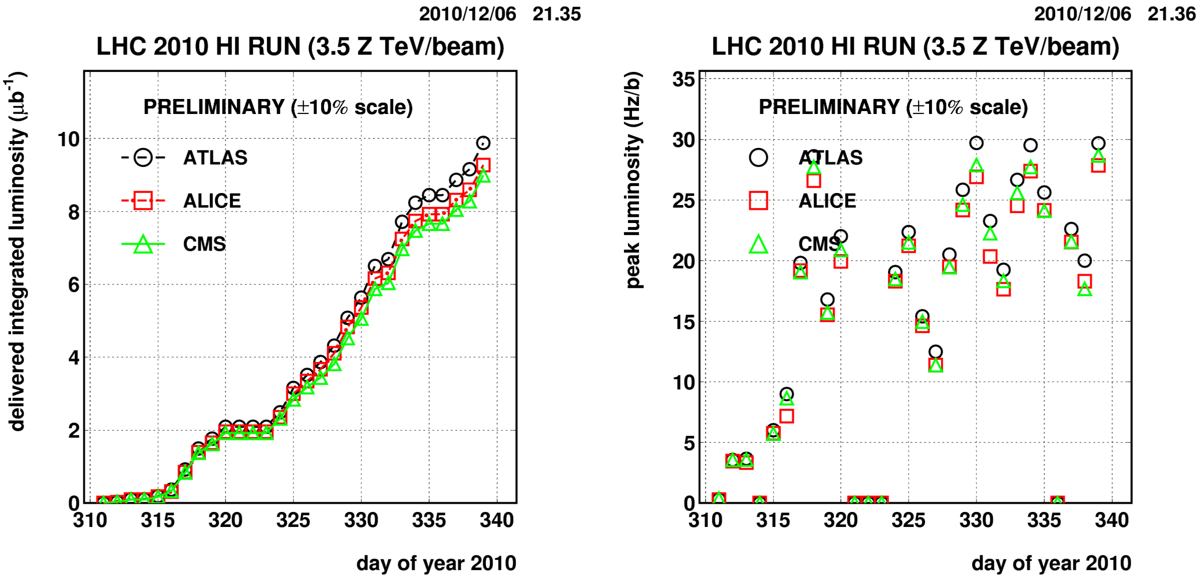

Figure 3.11: The delivered integrated luminosities (left) and the peak luminosities (right) of $\sqrt{s_{NN}}$=2.76 TeV Pb–Pb collisions at the LHC in 2010 [67].

Chapter 4

Data Analysis

4.1 Event selections

4.1.1 Minimum-bias event selection

The first step of the event selection is the online trigger selection. The Minimum-Bias (MB) samples are the hadronic collision candidates with the least strict selection criteria in order to get a sample with the least possible bias [68]. The VZERO detector and the SPD are used for the minimum-bias online trigger. The minimum-bias online trigger requires at least two out of three (2-out-of-3) conditions listed below to be satisfied:

- two pixel chips hit in the outer layer of the SPD
- signal in the VZERO-A detector
- signal in the VZERO-C detector

The trigger efficiency as a function of the VZERO amplitudes with three kinds of the trigger configurations are studied by Monte Carlo full simulations using the GEANT3 detector simulation program for events generated with the HIJING and AMPT model events and proton-proton high multiplicity events shown in Fig. 4.1 (a) [69, 45, 70, 71, 72]. Further selections are carried out in the offline analysis. In order to remove the beam background events caused by beam-gas and beam-halo collisions, the VZERO and ZDC timing information are used and the cut for the position of the primary vertex in the beam direction estimated by the SPD tracks $|Vz| < 7$ cm is required as shown in Fig. 4.1 (b). Electromagnetic interactions are removed by requiring an energy deposition above 500 GeV in each of the ZDCs. The combined trigger and selection efficiency estimated from a variety of Monte Carlo simulations is $97 \sim 99$ % with a purity of 100 % for the centrality range 0-80 %.

4.1.2 Centrality determination

For the heavy ion collisions, we need to divide the events into the centrality classes to make a correspondence to the collision impact parameter b to characterize the collision geometry. Several methods of centrality determination are used in the ALICE setup. The centrality is determined using the both VZERO-A and VZERO-C detectors in this analysis as shown in Fig. 4.2 (a) [68]. The VZERO amplitude distribution is fitted using a phenomenological approach based on the Glauber Monte Carlo plus a convolution of a model for the particle production and a negative binomial distribution (NBD). It is assumed that the number of independently decaying precursor particles ("ancestors") is given by a 2 component model $N_{ancestors} = f \cdot N_{part} + (1 - f) \cdot N_{coll}$, where N_{part} is the number of participating nucleons and N_{coll} is the number of binary nucleon-nucleon collisions. With the former term, the soft particle production mechanism is taken into consideration. With the latter term, the hard particle production mechanism is taken into consideration. The parameter f controls their relative contributions and $f \sim 80$ %. Other ancestor dependences have been tested, using power-law functions of N_{part} or N_{coll}. The number of particles produced per precursor source was assumed to follow a NBD distribution. The fit is performed in a region corresponding to 88% of the total cross section to avoid the peak of contamination and inefficiency. Extracting the number of participants from the Glauber fit gives accesses directly to the N_{part}, nearly identical to the geometrical one. However it is important to remember that we use the Glauber model and the ancestor assumptions only to determine the fraction of total cross section that we see, confirming the results obtained with the data-based analysis.

Figure 4.2 (b) shows the resolutions of the centrality determination with various methods [69]. A longitudinal axis is the RMS of the distribution of $\sigma_i = cent_i - \langle cent \rangle_i$, where subscript i denotes the centrality estimation method, e.g. VZERO-A and -C, and $cent_i$ is the estimated centrality percentile with the method i. The estimation of the centrality percentile by averaging the results with the other detectors ($\neq i$), $\langle cent \rangle_i$, is calculated iteratively as

$$\langle cent \rangle_i = \frac{\sum_{j \neq i} cent_j / \sigma_j^2}{\sum_{j \neq i} 1/\sigma_j^2}. \tag{4.1}$$

This iteration converges rapidity. The resolutions with the various methods are roughly scaled by the square root of the number of particles detected in each detectors. The resolution of the centrality determination by using the VZERO-A and -C detectors is best as shown by blue symbols. The resolution is good enough to divide the events with the width of 10 % centrality bins for all events and 5 % centrality bins for the most central events.

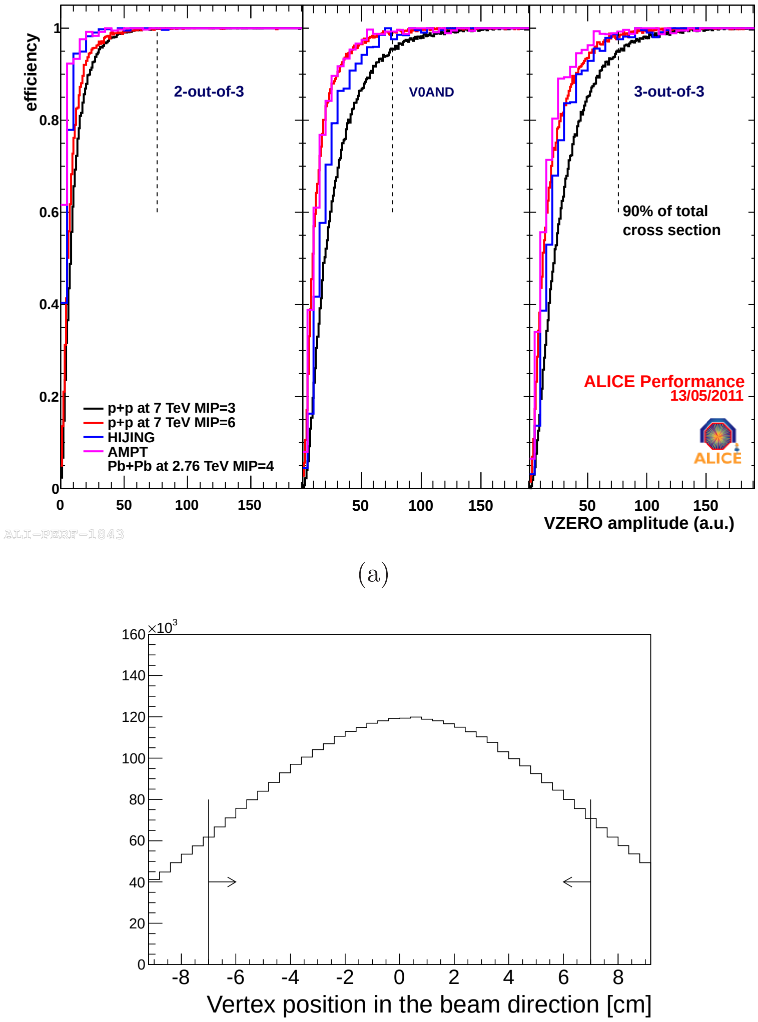

(a)

(b)

Figure 4.1: (a) Trigger efficiency as a function of VZERO amplitude investigated by Monte Carlo full simulations of the HIJING and AMPT model events using a GEANT3 detector simulation and event reconstruction with the trigger configuration (left) 2-out-of-3, (center) VZERO-A and VZERO-C signals, (right) the requirement of all three conditions [69]. (b) The distribution of the vertex position in the beam direction.

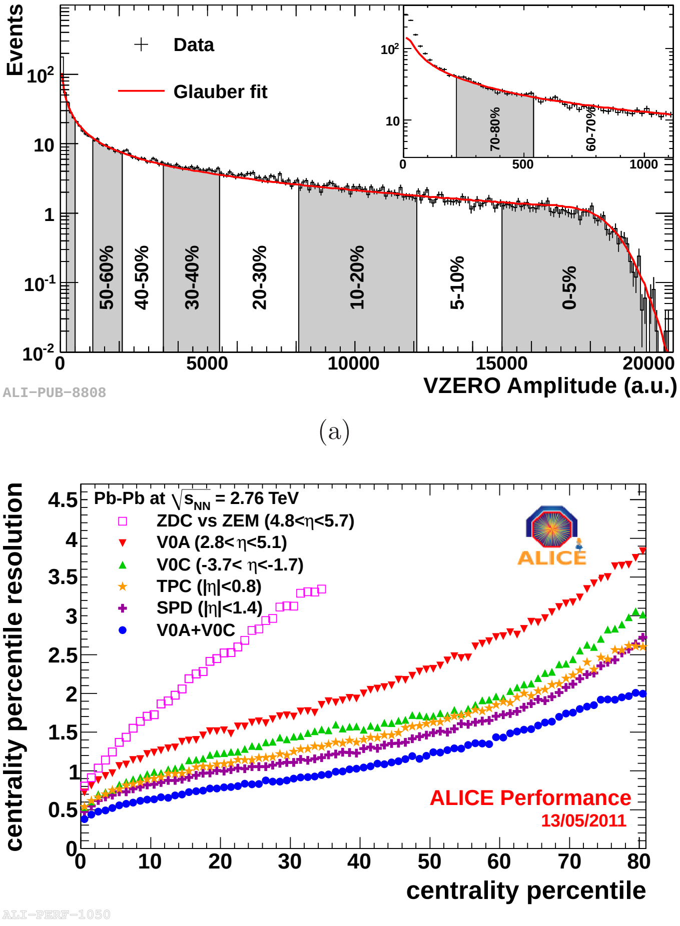

(a)

(b)

Figure 4.2: (a) The selection of the event centrality classes by the VZERO amplitude with Glauber model fitting (red line) [68]. (b) The resolutions of the centrality percentile determinations with various methods. The resolution of the centrality determination by the VZERO detectors is best as shown by blue symbols [69].

4.2 Track selections

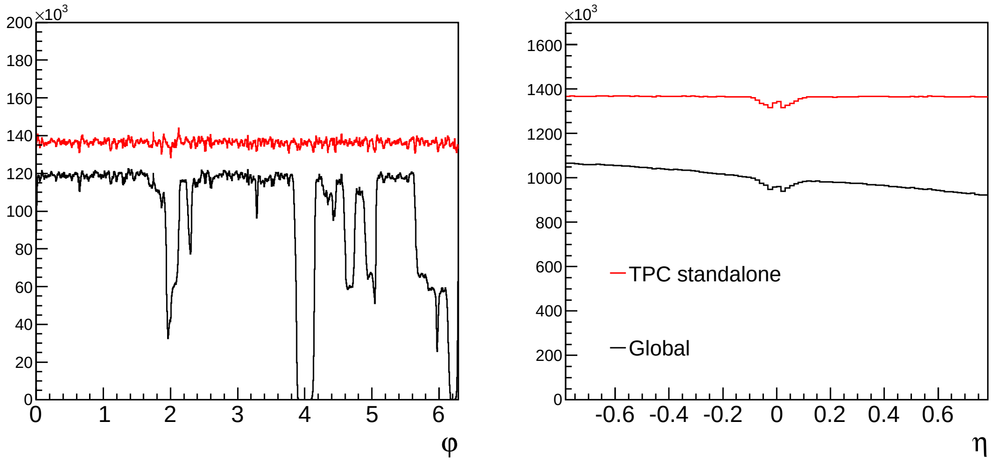

Figure 4.3: Distribution of the global and TPC standalone tracks in the (left) azimuthal and (right) pseudo-rapidity direction.

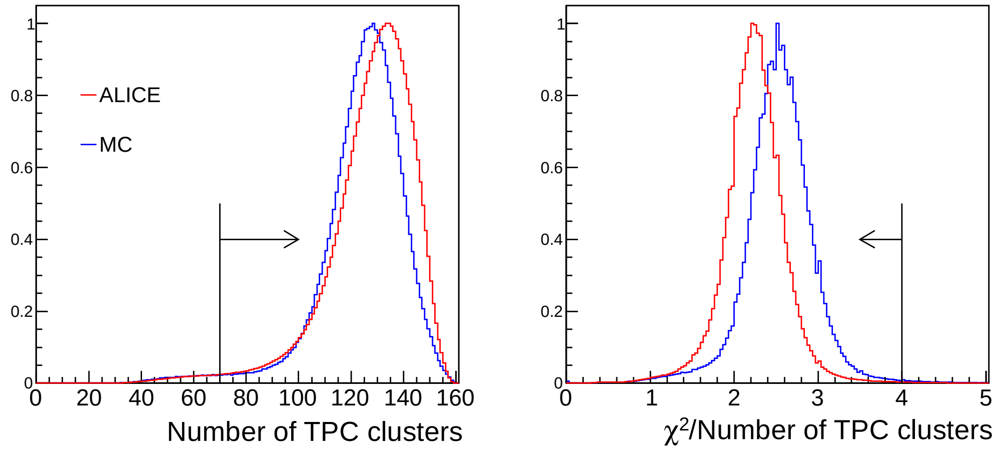

Figure 4.4: Distribution of (left) the number of TPC cluster and (right) χ^2 divided by the number of TPC clusters for the TPC standalone tracks with Monte Carlo full simulations.

Detailed descriptions of the track reconstruction and calibrations for the tracking are found in App.B and App.C.

To select charged particles with high efficiency and to minimize the contribution from secondary charged particles produced in the detector material and the weak decays, further track requirements in the analysis are applied for tracks reconstructed with the TPC (TPC standalone tracks) [73, 68]. Both azimuthal and pseudo-rapidity distributions of the TPC standalone track are quite flat as shown by red lines in Fig. 4.3 since the TPC uniformly covers the full azimuth and the pseudo-rapidity range $|\eta| < 0.9$. Note that the azimuthal angle φ of tracks is estimated by an azimuthal angle of the track vector at the collisions vertex, which can be calculated with the extrapolation of the TPC trajectories to the measured (global) primary vertex. Resolutions of various track parameters e.g. the transverse momentum are significantly improved by associating with the ITS hits. A track with additional requirement of at least two hits of the six ITS layers is called a global track. However, since the the ITS does not have uniform acceptance both in azimuthal and pseudo-rapidity directions because of the relatively large dead area as shown by black lines in Fig. 4.3, the TPC standalone track is used in this analysis. The tracks are required to have at least 70 reconstructed space points out of the maximum 159 in the TPC and a χ^2 per TPC cluster 4 (with 2 degrees of freedom per cluster). The definition of the χ^2 is given as Eq. (B.6). Figure 4.4 shows the distributions of the number of TPC clusters and χ^2 per TPC cluster in comparison with the Monte Carlo full simulations. Some parts of the detector simulations, e.g. the motion of the drift electrons in the TPC, are not conducted in the GEANT3 simulation but the simple parametrization are used, e.g. the space-point resolutions, the drift distortions in $x - y$ plane, and so on. There are clear difference between the measured and simulated results in the distributions of the number of TPC clusters and χ^2 per TPC cluster, but the criteria of the cuts are chosen so that the integrated efficiency is similar between measured and simulated results. Tracks are rejected if their distances of closest approach to the primary vertex in the transverse plane and longitudinal direction (dca_{xy} and dca_z) are larger than 3 cm. For the selected tracks the reconstruction efficiency and remaining contamination are estimated by the full simulations as shown in Fig. 4.5. The reconstruction efficiency for tracks with 0.2 $< p_{\mathrm{T}} <$ 1.0 GeV/c increases from 70% to 90% after which it stays constant at 90 ± 5%. The contamination from secondary interactions and photon conversions is less than 17% at $p_{\mathrm{T}} = 0.2$ GeV/c and less than 13% at $p_{\mathrm{T}} > 1$ GeV/c. Both the efficiency and contamination as a function of transverse momentum do not change significantly as a function of multiplicity and are therefore the same for all centrality classes.

To reduce the contamination, TPC standalone tracks with $dca_{xy,z} < 0.3$ cm are also used in this analysis. The reconstruction efficiency does not change significantly while the contamination is less than 7% at p_{T} =0.2 GeV/c and drops below 5% at $p_{\mathrm{T}} >$ 1GeV/c as shown in Fig. 4.5.

The contamination from the weak decays and detector materials are also estimated by fitting the measured dca_{xy} distributions with the Monte Carlo dca_{xy} distributions for each components as shown in Fig. 4.6. The shapes of the dca_{xy} distributions for the primary particles (brown), the secondary particles from the weak decays (green) and from the detector material (blue) are extracted from the full simulations. Then, the magnitude of each components are obtained by the fitting the measured dca_{xy} distributions (black points). Fitting works very well and estimated fractions of the contamination from the weak decays and the material are 13% and 6%, respectively for the TPC standalone track with $dca_{xy,z} < 3$ cm and 5.6% and 2.9% respectively for the TPC standalone track with $dca_{xy,z} < 0.3$ cm at $0.2 < p_{\mathrm{T}} < 0.4$ GeV/c. These results are roughly consistent to the simulated results in Fig. 4.5 (b).

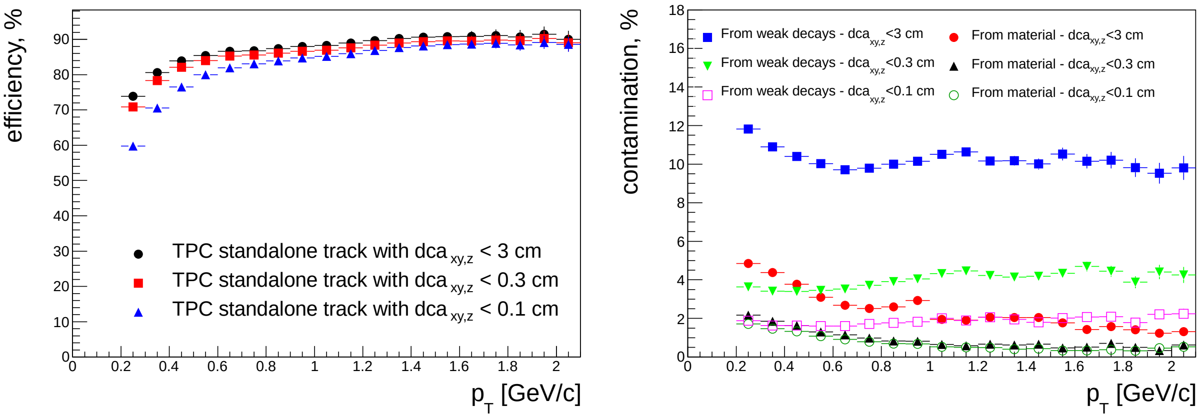

(a)

(b)

Figure 4.5: (a) Efficiency and (b) contamination as a function of p_{T} for the TPC standalone tracks with $dca_{xy,z} < 3$, 0.3 and 0.1 cm estimated with Monte Carlo full simulations for the AMPT model events.

In the analysis of the p_{T}-integrated correlations, it is impossible to correct the effects of the efficiency and contamination as a function of p_{T}. It is confirmed by using the model dependent simulations that the p_{T}-integrated elliptic flow is insensitive to these effects [74]. However, in general, we need to be careful for these effects on the correlation measurements when the measured results are compared with the theoretical calculations and the results from other experiments. It is confirmed that the variations of the efficiency and contamination by changing the track cuts do not change the observables measured in this thesis as described in the Sec.4.6.

Note that the transverse momentum resolution at $p_T = 0.2$ and 5 GeV/c are estimated to be below 1% and $\sim 5\%$ respectively. The performance of the estimation for the various track parameters as well as p_{T} is described in detail in Ref. [55, 56, 54, 59]. We assume that the transverse momentum resolution is good enough to ignore them even in the p_T differential correlation measurements. In any case, the p_{T} resolution effect can not be corrected in the correlation measurements.

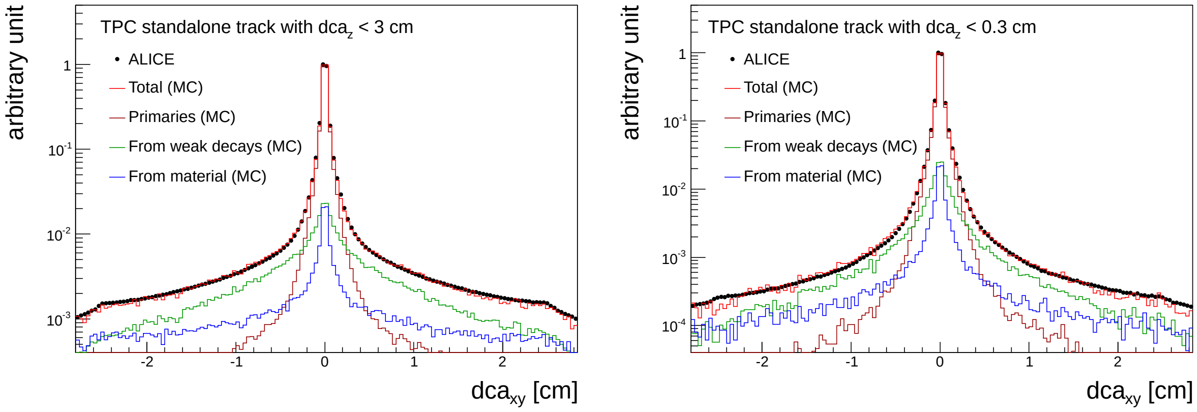

(a) (b)

Figure 4.6: dca_{xy} distributions for the TPC standalone tracks with (a) $dca_z < 3$ cm and (b) $dca_z < 0.3$ cm fitting with the Monte Carlo full simulations in order to estimate fractions of the contamination into the selected tracks.

4.3 Definition of observables

The main observables in this thesis are listed below for the remainder:

Two-particle correlations

> $\langle\cos[n(\varphi_\alpha - \varphi_\beta)]\rangle$ with $n = 1, 2, 3, 4$ measured by using the two-particle cumulant method. A method of the measurement is explained in the next section.

Two-particle correlations with respect to the symmetry plane

> $\langle\cos[n\varphi_\alpha + m\varphi_\beta - (n+m)\Psi_k]\rangle$ with $(n+m) \propto k$ measured by using the two independent methods: the multi-particle cumulant method and the event plane method. Methods of the measurement are explained in the next section and Sec.4.5. Correlations with $(n, m, k) = (1, 1, 2), (1, -3, 2), (1, 3, 2), (1, -5, 2), (1, -4, 3)$ and $(1, -5, 4)$ are presented in this thesis.

Kinematical regions of particles are $0.2 < p_{\mathrm{T}} < 5$ GeV/c and $|\eta| < 0.8$.

4.4 Multi-particle cumulant method

In the multi- and two-particle cumulant methods [75], we are interested in the connected parts of the multi- and two-particle correlations. Two particle correlation of the two random variables X_1 and X_2 can be decomposed as follows:

$$\langle X_1 X_2\rangle_r = \langle X_1\rangle_r \langle X_2\rangle_r + \langle X_1 X_2\rangle_c, \tag{4.2}$$

where the bracket $\langle\cdots\rangle_r$ denotes the average over all particles or all pairs of the particles. The bracket $\langle X_1 X_2\rangle_c$ is the genuine two particle correlation which can not be decomposed further. By definition this term is the two particle cumulant [76]. If two random variables are statistically independent,

$$\langle X_1 X_2\rangle_r = \langle X_1\rangle_r \langle X_2\rangle_r, \quad \text{when } X_1 \text{ and } X_2 \text{ are independent.} \tag{4.3}$$

The correlations $\langle\cos[n(\varphi_\alpha - \varphi_\beta)]\rangle$ with $n = 1, 2, 3, 4$ are measured as the two-particle cumulant

$$\langle\cos[n(\varphi_\alpha - \varphi_\beta)]\rangle_c = \langle\cos[n(\varphi_\alpha - \varphi_\beta)]\rangle_r - \langle\cos(n\varphi_\alpha)\rangle_r \langle\cos(n\varphi_\beta)\rangle_r. \tag{4.4}$$

The ALICE TPC has quite uniform azimuthal acceptance. Nevertheless, TPC sector boundaries may cause biases on the azimuthal correlations, in particular, the moments $\langle\cos(n\varphi)\rangle_r$ and $\langle\sin(n\varphi)\rangle_r$. We can eliminate such detector effects by using cumulants.

In the multi-particle cumulant method [75], the azimuthal angle of the k-th harmonic symmetry plane Ψ_k is not explicitly determined. Instead, the role of the symmetry plane is played by another particles entering the correlation, which are called Reference Particles (RPs) while the particles α and β are called Particles Of Interest (POIs). Under the assumption that RPs are correlated with POIs only via common correlation to the symmetry plane, we have

$$\langle \cos[n\varphi_\alpha + m\varphi_\beta - (n+m)\Psi_k] \rangle \sim \frac{\langle \cos[n\varphi_\alpha + m\varphi_\beta \cdots - k\varphi_{\gamma_{(n+m)/k}}] \rangle_c}{v_{k,\gamma_1} \times \cdots \times v_{k,\gamma_{(n+m)/k}}}, \tag{4.5}$$

where the bracket $\langle\ \rangle_c$ in the numerator of the right side of the equation denotes the multi-particle cumulant.In the denominator, the average of $v_k\{2\}$ and $v_k\{4\}$ is used to estimate v_k without nonflow and flow fluctuation effects as shown in Fig. 4.7 and Fig. 4.8 [73, 15], where $v_k\{2\}$ and $v_k\{4\}$ denotes the $k-$th harmonic flow v_k measured with the two- and four-particle method respectively. The discussion about the flow measurement method and flow flucutation effects are found in appendix A. While both $v_k\{2\}$ and $v_k\{4\}$ with $k = 2, 3$ are available with small statistical errors, stable results for v_3 at centrality 50-60% and v_4 are obtained only by the Scalar Product method (SP) with eta gap $|\Delta\eta| > 1$ between the POIs and RPs because of the lack of statistics. The SP method is described in detail in App.D.

Here comes the three particle correlations,

$$\begin{aligned} \langle X_1X_2X_3\rangle_r &= \langle X_1\rangle_r\langle X_2\rangle_r\langle X_3\rangle_r \\ &+ \langle X_1X_2\rangle_c\langle X_3\rangle_r + \langle X_1X_3\rangle_c\langle X_2\rangle_r + \langle X_2X_3\rangle_c\langle X_1\rangle_r \\ &+ \langle X_1X_2X_3\rangle_c \end{aligned} \tag{4.6}$$

$$\begin{aligned} \Leftrightarrow \langle X_1X_2X_3\rangle_c &= \langle X_1X_2X_3\rangle_r \\ &- \langle X_1X_2\rangle_r\langle X_3\rangle_r - \langle X_1X_3\rangle_r\langle X_2\rangle_r - \langle X_2X_3\rangle_r\langle X_1\rangle_r \\ &+ 2\langle X_1\rangle_r\langle X_2\rangle_r\langle X_3\rangle_r. \end{aligned} \tag{4.7}$$

In case of the four particle correlations,

$$\begin{aligned}
\langle X_1X_2X_3X_4\rangle_r &= \langle X_1\rangle_r\langle X_2\rangle_r\langle X_3\rangle_r\langle X_4\rangle_r \\
&+ \langle X_1X_2X_3\rangle_c\langle X_4\rangle_r + \langle X_1X_2X_4\rangle_c\langle X_3\rangle_r \\
&+ \langle X_1X_3X_4\rangle_c\langle X_2\rangle_r + \langle X_2X_3X_4\rangle_c\langle X_1\rangle_r \\
&+ \langle X_1X_2\rangle_c\langle X_3X_4\rangle_c + \langle X_1X_3\rangle_c\langle X_2X_4\rangle_c + \langle X_1X_4\rangle_c\langle X_2X_3\rangle_c \\
&+ \langle X_1X_2\rangle_c\langle X_3\rangle_r\langle X_4\rangle_r + \langle X_1X_3\rangle_c\langle X_2\rangle_r\langle X_4\rangle_r + \langle X_1X_4\rangle_c\langle X_2\rangle_r\langle X_3\rangle_r \\
&+ \langle X_1\rangle_r\langle X_2\rangle_r\langle X_3X_4\rangle_c + \langle X_1\rangle_r\langle X_3\rangle_r\langle X_2X_4\rangle_c + \langle X_1\rangle_r\langle X_4\rangle_r\langle X_2X_3\rangle_c \\
&+ \langle X_1X_2X_3X_4\rangle_c \qquad (4.8)
\end{aligned}$$

$$\begin{aligned}
\Leftrightarrow \langle X_1X_2X_3X_4\rangle_c &= \langle X_1X_2X_3X_4\rangle_r \\
&- \langle X_1X_2X_3\rangle_r\langle X_4\rangle_r - \langle X_1X_2X_4\rangle_r\langle X_3\rangle_r \\
&- \langle X_1X_3X_4\rangle_r\langle X_2\rangle_r - \langle X_2X_3X_4\rangle_r\langle X_1\rangle_r \\
&- \langle X_1X_2\rangle_r\langle X_3X_4\rangle_r - \langle X_1X_3\rangle_r\langle X_2X_4\rangle_r - \langle X_1X_4\rangle_r\langle X_2X_3\rangle_r \\
&+ 2\langle X_1X_2\rangle_r\langle X_3\rangle_r\langle X_4\rangle_r + 2\langle X_1X_3\rangle_r\langle X_2\rangle_r\langle X_4\rangle_r + 2\langle X_1X_4\rangle_r\langle X_2\rangle_r\langle X_3\rangle_r \\
&+ 2\langle X_1\rangle_r\langle X_2\rangle_r\langle X_3X_4\rangle_r + 2\langle X_1\rangle_r\langle X_3\rangle_r\langle X_2X_4\rangle_r + 2\langle X_1\rangle_r\langle X_4\rangle_r\langle X_2X_3\rangle_r \\
&- 6\langle X_1\rangle_r\langle X_2\rangle_r\langle X_3\rangle_r\langle X_4\rangle_r. \qquad (4.9)
\end{aligned}$$

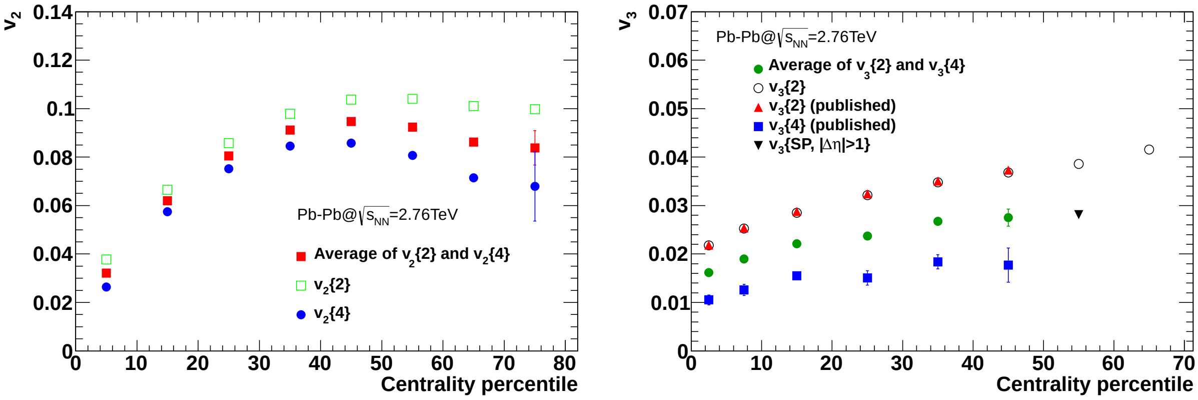

(a) (b)

Figure 4.7: (a) The centrality dependence of the integrated v_2 for the RPs by the two-particle and four-particle cumulant methods [73]. (b) The centrality dependence of the integrated v_3 for the RPs by the SP with $|\Delta\eta| > 1$, the two-particle and four-particle cumulant methods [15].

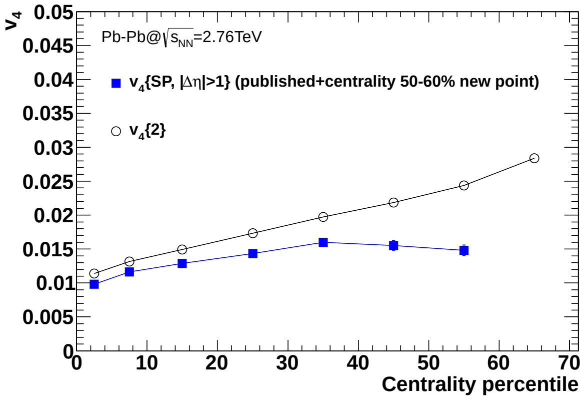

Figure 4.8: The centrality dependence of the integrated v_4 for the RPs by the SP with $|\Delta\eta| > 1$ and the two-particle cumulant methods [15].

Therefore, to estimate the correlation $\langle\cos[n\varphi_\alpha + m\varphi_\beta \cdots - k\varphi_{\gamma_{(n+m)/k}}]\rangle_c$ in Eq. (4.5), one need to calculate all its descendants. For example, the correlation $\langle\cos(\varphi_\alpha+\varphi_\beta-2\varphi_\gamma)\rangle_c$ can be calculated by

$$\begin{aligned}
\langle\cos(\varphi_\alpha + \varphi_\beta - 2\varphi_\gamma)\rangle_c &= \langle\cos(\varphi_\alpha + \varphi_\beta - 2\varphi_\gamma)\rangle_r \\
&- \langle\cos(\varphi_\alpha)\rangle_r\langle\cos(\varphi_\beta - 2\varphi_\gamma)\rangle_r \\
&- \langle\cos(\varphi_\beta)\rangle_r\langle\cos(\varphi_\alpha - 2\varphi_\gamma)\rangle_r \\
&- \langle\cos(\varphi_\alpha + \varphi_\beta)\rangle_r\langle\cos(-2\varphi_\gamma)\rangle_r \\
&+ 2\langle\cos(\varphi_\alpha)\rangle_r\langle\cos(\varphi_\beta)\rangle_r\langle\cos(-2\varphi_\gamma)\rangle_r. \qquad (4.10)
\end{aligned}$$

In the first step for the calculation of the correlation $\langle\cos(n_1\varphi_1 + \cdots + n_k\varphi_k)\rangle_r$, we define the *single event* k-particle correlation $\{\cos(n_1\varphi_1 + \cdots + n_k\varphi_k)\}$ in the following way:

$$\{\cos(n_1\varphi_1 + \cdots + n_k\varphi_k)\} \equiv \frac{1}{M(M-1)\cdots(M-k+1)} Re \sum_{\substack{i_1,\cdots i_k=1 \\ i_1\neq\cdots\neq i_k}}^{M} e^{i(n_1\varphi_{i_1}+\cdots+n_k\varphi_{i_k})} \quad (4.11)$$

The sum goes over all combinations of M-particles in a single event. In order to avoid a trivial and strong contribution coming from auto-correlations, we have enforced the constraints $i_1 \neq \cdots \neq i_k$. In the second step we define the *all event* average correlation $\langle\cos(n_1\varphi_1 + \cdots + n_k\varphi_k)\rangle_r$;

$$\langle\cos(n_1\varphi_1 + \cdots + n_k\varphi_k)\rangle_r \equiv \frac{\sum_{i=1}^{N} M_i(M_i-1)\cdots(M_i-k+1)\{\cos(n_1\varphi_1 + \cdots + n_k\varphi_k)\}}{\sum_{i=1}^{N} M_i(M_i-1)\cdots(M_i-k+1)}. \quad (4.12)$$

One of the problems in using multi-particle cumulant method is the computing power needed to go over all possible particle multiplets $\sum_{\substack{i_1,\cdots i_k=1 \\ i_1\neq\cdots\neq i_k}}^{M}$, which practically prohibits calculations of correlations of order larger than three. To avoid this problem, Q-cumulant method is proposed in Ref. [77]. In this approach, one can express analytically all multi-particle azimuthal correlations in terms of Q-vectors, $Q_n \equiv \sum_i e^{in\varphi_i}$.

$$\{\cos(\varphi_\alpha + \varphi_\beta - 2\varphi_\gamma)\} = \frac{Q_1^2 Q_2^* - |Q_2|^2 - 2|Q_1|^2 + 2M}{M(M-1)(M-2)}, \quad (4.13)$$

$$\{\cos(\varphi_\alpha - 3\varphi_\beta + 2\varphi_\gamma)\} = \frac{Q_1 Q_2 Q_3^* - |Q_3|^2 - |Q_2|^2 - |Q_1|^2 + 2M}{M(M-1)(M-2)}, \quad (4.14)$$

$$\begin{aligned}
\{\cos(\varphi_\alpha + 3\varphi_\beta - 2\varphi_{\gamma_1} - 2\varphi_{\gamma_2})\} &= \Big(Q_1 Q_3 (Q_2^*)^2 - Q_1 Q_3 Q_4^* - Q_4 (Q_2^*)^2 \\
&- 2Q_1^* Q_3 Q_2^* - 2(Q_1)^2 Q_2^* \\
&+ |Q_4|^2 + 2|Q_3|^2 + 4|Q_2|^2 + 4|Q_1|^2 \\
&- 6M\Big)/(M(M-1)(M-2)(M-3)), \quad (4.15)
\end{aligned}$$

$$\begin{aligned}\{\cos(\varphi_\alpha - 5\varphi_\beta + 2\varphi_{\gamma_1} + 2\varphi_{\gamma_2})\} &= \Big(Q_1 Q_5^*(Q_2)^2 - Q_1 Q_5^* Q_4 - Q_4^*(Q_2)^2 \\ &- 2Q_5^* Q_3 Q_2 - 2Q_1 Q_3^* Q_2 + 2|Q_5|^2 \\ &+ |Q_4|^2 + 2|Q_3|^2 + 4|Q_2|^2 + 2|Q_1|^2 \\ &- 6M\Big)/(M(M-1)(M-2)(M-3)), \quad (4.16)\end{aligned}$$

and so on. Since the Q_n-vectors can be calculated by scanning the tracks at only one time, the computing speed becomes faster than that with the calculation of the multi-particle sum by its definition.

Statistical Errors

Strictly speaking, there may exist non-zero covariance between a numerator and a denominators of Eq. (4.5). But we ignore this covariance because correlations between the mixed harmonic azimuthal correlations and the n-th harmonic flow are in general small. The total statistical error is defined as the quadratic sum of the statistical error of denominator and numerator. Here we will discuss about the calculation of the statistical error of the numerator.

Consider the random observable x sampled from some probability density function (p.d.f) $f(x)$ [78]. The *mean* of x is denoted by μ_x and the *variance* of x is denoted by σ_x (or equivalently by $V[x]$). Mean and variance of x are given by the following expressions:

$$\mu_x = E[x] = \int_{-\infty}^{\infty} x f(x) dx, \quad (4.17)$$

$$\sigma_x^2 = V[x] = E[(x - E(x))^2] = \int_{-\infty}^{\infty} (x - \mu_x)^2 f(x) dx, \quad (4.18)$$

where $E[x]$ stands for the *expectation value* of a random variable x. We denote by x_i the measured random observable x in the i-th event and by $(w_x)_i$ the observable weight in that event. Even if the p.d.f $f(x)$ is completely unknown, we can still use measured values x_i to estimate mean μ_x and variance σ_x of the random variable x. In particular, the unbiased estimator for the variance σ_x^2, which is denoted by s_x^2, is given by

$$s_x^2 \equiv \left[\frac{\sum_{i=1}^{N} (w_x)_i (x_i - \langle x \rangle)^2}{\sum_{i=1}^{N} (w_x)_i}\right] \times \left[\frac{1}{1 - \frac{\sum_{i=1}^{N} (w_x)_i^2}{[\sum_{i=1}^{N} (w_x)_i]^2}}\right], \quad (4.19)$$

where we have introduced also $\langle x \rangle$ as the unbiased estimator for the mean μ_x,

$$\langle x \rangle \equiv \frac{\sum_{i=1}^{N} (w_x)_i x_i}{\sum_{i=1}^{N} (w_x)_i}. \quad (4.20)$$

In above two equations N is the number of the independent measurements, which in our context corresponds to the number of events. Since the sample mean $\langle x \rangle$ is an unbiased estimator for the mean of x, μ_x, we will report the final results and the statistical errors as

$$\langle x \rangle \pm V[\langle x \rangle]^{1/2}. \tag{4.21}$$

One can easily show that the variance of the sample mean, $V[\langle x \rangle]$, can be written as

$$V[\langle x \rangle] = \frac{\sum_{i=1}^{N} (w_x)_i^2}{[\sum_{i=1}^{N} (w_x)_i]^2} V[x], \tag{4.22}$$

i.e.

$$V[\langle x \rangle] = \frac{\sum_{i=1}^{N} (w_x)_i^2}{[\sum_{i=1}^{N} (w_x)_i]^2} \sigma_x^2. \tag{4.23}$$

Taking into account the unbiased estimator s_x^2 for the variance σ_x^2, we can now write down the expression which we will use to report the final results and statistical errors of the random variable x:

$$\langle x \rangle \pm \frac{\sqrt{\sum_{i=1}^{N} (w_x)_i^2}}{\sum_{i=1}^{N} (w_x)_i} s_x. \tag{4.24}$$

In our case, x_i corresponds to the *single event* average correlation $\{\cos(n_1\varphi_1 + \cdots + n_k\varphi_k)\}$ and the weight w_i corresponds to $M_i(M_i - 1)\cdots(M_i - k + 1)$. We can calculate the event averages of multi-particle correlations (i.e. the unbiased estimator for their true mean values) $\langle\cos(n_1\varphi_1 + \cdots + n_k\varphi_k)\rangle_r$ and also the unbiased estimators for their variances $s^2_{\{\cos(n_1\varphi_1+\cdots+n_k\varphi_k)\}}$ straightforwardly from the data by making use of the definitions Eq. (4.20) and Eq. (4.19), respectively. Since the unbiased estimator for the variance is used for the statistical error calculation, the statistical error becomes large if the intrinsic spread of the event-by-event observables is large because of any reasons including the physical reasons (e.g. the flow fluctuations), detector effects, and imperfect event cuts.

4.5 Event Plane method

In the event plane method [9], one first estimates the symmetry plane with the so-called event plane determined from particle azimuthal distributions for the each event. In this analysis, the FMD and VZERO detector are used for the event plane determination. The azimuthal angle of the k-th harmonic event plane $\Psi_{k,EP}$ is defined as

$$\begin{aligned} \Psi_{k,EP} &\equiv \tan^{-1}\left(\frac{Q_{k,y}}{Q_{k,x}}\right)/k, \text{ with} \\ (Q_{k,x}, Q_{k,y}) &= (\sum_i w_i \cos k\varphi_i, \sum_i w_i \sin k\varphi_i), \end{aligned} \tag{4.25}$$

where φ_i is the azimuthal angle of each cell of the FMD or VZERO detector and w_i is the weight, which is non-corrected multiplicity measured at each cell in this analysis. The event plane angle is defined by the azimuthal angle of Q-vector.

The correlation $\langle \cos[n\varphi_\alpha + m\varphi_\beta - (n+m)\Psi_{k,EP}]\rangle$ can be decomposed as the following:

$$\begin{aligned}
&\langle \cos[n\varphi_\alpha + m\varphi_\beta - (n+m)\Psi_{k,EP}]\rangle \\
&= \langle \cos[n\varphi_\alpha + m\varphi_\beta - (n+m)\Psi_k + (n+m)(\Psi_{k,EP} - \Psi_k)]\rangle \\
&= \langle \cos[n\varphi_\alpha + m\varphi_\beta - (n+m)\Psi_k]\cos[(n+m)(\Psi_{k,EP} - \Psi_k)]\rangle \\
&\quad -\langle \sin[n\varphi_\alpha + m\varphi_\beta - (n+m)\Psi_k]\sin[(n+m)(\Psi_{k,EP} - \Psi_k)]\rangle \\
&\sim \langle \cos[n\varphi_\alpha + m\varphi_\beta - (n+m)\Psi_k]\rangle\langle \cos[(n+m)(\Psi_{k,EP} - \Psi_k)]\rangle,
\end{aligned} \tag{4.26}$$

where $\langle \cos[(n+m)(\Psi_{k,EP} - \Psi_k)]\rangle (\equiv R_{n+m,k})$ is the event plane resolution factor which is determined from the correlation between the event plane vectors of two or three independent subevents. $\langle \sin[(n+m)(\Psi_{k,EP} - \Psi_k)]\rangle$ can be ignored when the effect of non-uniform acceptance on the event plane angle determination is corrected properly. The estimate of the correlation $\langle \cos[n\varphi_\alpha + m\varphi_\beta - (n+m)\Psi_k]\rangle$ with the event plane method is then defined as

$$\langle \cos[n\varphi_\alpha + m\varphi_\beta - (n+m)\Psi_k]\rangle \sim \frac{\langle \cos[n\varphi_\alpha + m\varphi_\beta - (n+m)\Psi_{k,EP}]\rangle}{R_{n+m,k}}. \tag{4.27}$$

In this analysis, tracks at $|\eta| < 0.8$ and $0.2 < p_{\mathrm{T}} < 5\mathrm{GeV}/c$ are used for the POIs and tracks at forward rapidity are used for the RPs so that auto-correlation between the POIs and the RPs is removed.

4.5.1 Event Plane calibration

In order to take account of the imperfect acceptance effects on the event plane determination [79], we introduce the single particle production probability density with respect to the k-th harmonic symmetry plane $\rho(\varphi - \Psi_k)$ and the acceptance function $A(\varphi)$ which are normalized to unity:

$$\rho(\varphi - \Psi_k) = \frac{1}{2\pi}\left(1 + 2\sum_{n=1}^{\infty} v_n \cos\left[n\left(\varphi - \Psi_k\right)\right]\right), \tag{4.28}$$

$$\int \frac{d\varphi}{2\pi} A(\varphi) = 1. \tag{4.29}$$

where v_n is the n-th harmonic flow with respect to k-th harmonic symmetry plane. Then the average of some function $f(\varphi)$, which depends on particle azimuthal angle φ, over events with the fixed symmetry plane orientation is given by the integral:

$$\begin{aligned}
\langle f\rangle_{\Psi_k} &= \int d\varphi A(\varphi) f(\varphi) \rho(\varphi - \Psi_k) \\
&= \bar{f} + 2\sum_{m=1}^{\infty} v_m [\overline{f\cos m\varphi} \times \cos m\Psi_k + \overline{f\sin m\varphi} \times \sin m\Psi_k],
\end{aligned} \tag{4.30}$$

where $\bar{f}$ means the average over the detector acceptance:

$$\bar{f} = \int \frac{d\varphi}{2\pi} A(\varphi) f(\varphi). \tag{4.31}$$

An important observation is that the acceptance average of f, $\bar{f}$, coincides with the event average, $\langle f \rangle$:

$$\langle f \rangle = \frac{\int d\Psi_k d\varphi A(\varphi) f(\varphi) \rho(\varphi - \Psi_k)}{\int d\Psi_k d\varphi A(\varphi) \rho(\varphi - \Psi_k)} = \bar{f}. \tag{4.32}$$

We assume here that the distribution of the symmetry plane angle is uniform within a given centrality event sample. Now we consider the imperfect acceptance effects on the Q_x and Q_y.

$$\begin{aligned} \langle Q_{k,x} \rangle_{\Psi_k} &= \overline{Q_{k,x}} + M v_k \times (1 + \overline{\mathrm{cos} 2k\varphi}) \times \mathrm{cos} k\Psi_k \\ &+ M v_k \times \overline{\mathrm{sin} 2k\varphi} \times \mathrm{sin} k\Psi_k \\ &+ \sum_{m \neq 2}^{\infty} v_m [\overline{Q_{k,x} \mathrm{cos} m\varphi} \times \mathrm{cos} m\Psi_k + \overline{Q_{k,x} \mathrm{sin} m\varphi} \times \mathrm{sin} m\Psi_k] \\ &\sim \overline{Q_{k,x}} + M v_k (1 + \overline{\mathrm{cos} 2k\varphi}) \mathrm{cos} k\Psi_k, \end{aligned} \tag{4.33}$$

where M is the number of track used for Q-vector calculation. Term at the second line can be ignored as long as $\overline{\mathrm{sin} 2k\varphi} \ll 1$. Terms at the third line can be ignored since v_m $(m \neq k)$ is small enough. $\langle Q_{k,x} \rangle_{\Psi_k}$ can be regarded as the estimate of $Q_{k,x}$ in a single event with the symmetry plane Ψ_k because $\rho(\varphi - \Psi_k)$ can be also regarded as the particle azimuthal distribution in a single event. Then $\overline{Q_{k,x}} (\neq 0)$ and $M v_k (1 + \overline{\mathrm{cos} 2k\varphi}) (\neq 1)$ in front of $\mathrm{cos} k\Psi_k$ come from detector effects. The latter can be measured by the width of $Q_{k,x}$ distribution:

$$\begin{aligned} \langle Q_{k,x}^2 \rangle - \langle Q_{k,x} \rangle^2 &\sim \frac{1}{2\pi} \int d\Psi_k \langle Q_{k,x}^2 \rangle_{\Psi_k} - \overline{Q_{k,x}}^2 \\ &\sim \frac{1}{2\pi} \int d\Psi_k \Big(\overline{Q_{k,x}}^2 + 2\overline{Q_{k,x}} M v_k \left(1 + \overline{\mathrm{cos} 2k\varphi}\right) \mathrm{cos} k\Psi_k \\ &+ \left(M v_k \left(1 + \overline{\mathrm{cos} 2k\varphi}\right) \mathrm{cos} k\Psi_k \right)^2 \Big) - \overline{Q_{k,x}}^2 \\ &= \left(M v_k \left(1 + \overline{\mathrm{cos} 2k\varphi}\right) \right)^2. \end{aligned} \tag{4.34}$$

So-called re-centering calibration is defined as

$$\begin{aligned} Q_{k,x}^{re} &\equiv \frac{Q_{k,x} - \langle Q_{k,x} \rangle}{\sqrt{\langle Q_{k,x}^2 \rangle - \langle Q_{k,x} \rangle^2}} \sim \frac{\langle Q_{k,x} \rangle_{\Psi_k} - \langle Q_{k,x} \rangle}{\sqrt{\langle Q_{k,x}^2 \rangle - \langle Q_{k,x} \rangle^2}} \sim \mathrm{cos} k\Psi_k, \\ Q_{k,y}^{re} &\equiv \frac{Q_{k,y} - \langle Q_{k,y} \rangle}{\sqrt{\langle Q_{k,y}^2 \rangle - \langle Q_{k,y} \rangle^2}}, \\ \Psi_{k,EP}^{re} &\equiv \tan^{-1} \left(\frac{Q_{k,y}^{re}}{Q_{k,x}^{re}} \right) / k. \end{aligned} \tag{4.35}$$

In case of the VZERO detector, a gain for each VZERO cell must be corrected before re-centering calibration. Figure 4.9 shows that the corrected multiplicity in each cell is same among each VZERO rings. The corrected multiplicity for each VZERO cell is used for the weight w_i in Eq. (4.25). Figure 4.10 shows the FMD hit map on (η, φ). The azimuthal acceptance of FMD is roughly flat although the FMD cell at $\eta \sim 4.75$ and $\varphi \sim 4.25$ is a dead area.

Figure 4.11 shows the event plane distribution measured with the FMD and VZERO detectors. In the central collisions, the event plane distributions are flat enough after the re-centereing calibration. The event plane distributions are not flat enough in the peripheral collisions, so we perform the flattening calibration which is defined as

$$\begin{aligned} k\Delta\Psi_k &\equiv \sum_{m=1}^{m_{max}} [A_m \cos(mk\Psi^{re}_{k,EP}) + B_m \sin(mk\Psi^{re}_{k,EP})], && (4.36) \\ \Psi^{flat}_{k,EP} &\equiv \Psi^{re}_{k,EP} + \Delta\Psi_k. && (4.37) \end{aligned}$$

The coefficients A_m and B_m can be obtained by requiring that m-th Fourier moment of the $\Psi^{flat}_{k,EP}$ distribution is vanished, i.e., requiring isotropic distribution of $\Psi^{flat}_{k,EP}$. Assuming that the correction $\Delta\Psi_k$ is small,

$$\begin{aligned} \langle\cos(mk\Psi^{flat}_{k,EP})\rangle &= \langle\cos(mk\Psi^{re}_{k,EP} + mk\Delta\Psi_k)\rangle \\ &= \langle\cos(mk\Psi^{re}_{k,EP}) \times \cos(mk\Delta\Psi_k)\rangle - \langle\sin(mk\Psi^{re}_{k,EP}) \times \sin(mk\Delta\Psi_k)\rangle \\ &\sim \langle\cos(mk\Psi^{re}_{k,EP})\rangle - \langle\sin(mk\Psi^{re}_{k,EP}) \times (mk\Delta\Psi_k)\rangle \\ &= \langle\cos(mk\Psi^{re}_{k,EP})\rangle - mB_m\langle\sin^2(mk\Psi^{re}_{k,EP})\rangle \\ &= \langle\cos(mk\Psi^{re}_{k,EP})\rangle - \frac{mB_m}{2} \\ &= 0 && (4.38) \\ \Leftrightarrow B_m &= \frac{2}{m}\langle\cos(mk\Psi^{re}_{k,EP})\rangle, && (4.39) \end{aligned}$$

and similarly,

$$\begin{aligned} \langle\sin(mk\Psi_{k,EP})\rangle &= \langle\sin(mk\Psi^{re}_{k,EP} + mk\Delta\Psi_k)\rangle \\ &= \langle\sin(mk\Psi^{re}_{k,EP}) \times \cos(mk\Delta\Psi_k)\rangle + \langle\cos(mk\Psi^{re}_{k,EP}) \times \sin(mk\Delta\Psi_k)\rangle \\ &\sim \langle\sin(mk\Psi^{re}_{k,EP})\rangle + \langle\cos(mk\Psi^{re}_{k,EP}) \times (mk\Delta\Psi_k)\rangle \\ &= \langle\sin(mk\Psi^{re}_{k,EP})\rangle + mA_m\langle\cos^2(mk\Psi^{re}_{k,EP})\rangle \\ &= \langle\sin(mk\Psi^{re}_{k,EP})\rangle + \frac{mA_m}{2} \\ &= 0 && (4.40) \\ \Leftrightarrow A_m &= -\frac{2}{m}\langle\sin(mk\Psi^{re}_{k,EP})\rangle, && (4.41) \end{aligned}$$

in our case, $m_{max} = 5$ is enough.

The flattering calibration is a necessary condition but not the sufficient conditions. In case of the event plane calculated with the VZERO and FMD, the distributions of $\Psi^{re}_{k,EP}$ are roughly flat as shown in Fig. 4.11 so that the correction $\Delta\Psi_k$ is small and the approximation used above is satisfied.

4.5.2 Event Plane resolution

The event plane resolution with subevent i can be calculated in the three subevent method by the following formula [80]:

$$\begin{aligned} R_{n+m,k} &\equiv \langle \cos[(n+m)(\Psi_{k,EP,i} - \Psi_k)] \rangle \\ &= \sqrt{\frac{\langle \cos[(n+m)(\Psi_{k,EP,i} - \Psi_{k,EP,j})] \rangle \langle \cos[(n+m)(\Psi_{k,EP,i} - \Psi_{k,EP,l})] \rangle}{\langle \cos[(n+m)(\Psi_{k,EP,j} - \Psi_{k,EP,l})] \rangle}}, \end{aligned} \tag{4.42}$$

where subscripts j and l represent other two subevents. In this analysis, in order to calculate the VZERO and the FMD event plane resolutions, TPC standalone tracks at $0.2 < \eta < 0.8$ and at $-0.8 < \eta < -0.2$ are used as other two subevents. Figure 4.12 shows the centrality dependence of the correction factor for the event plane resolution.

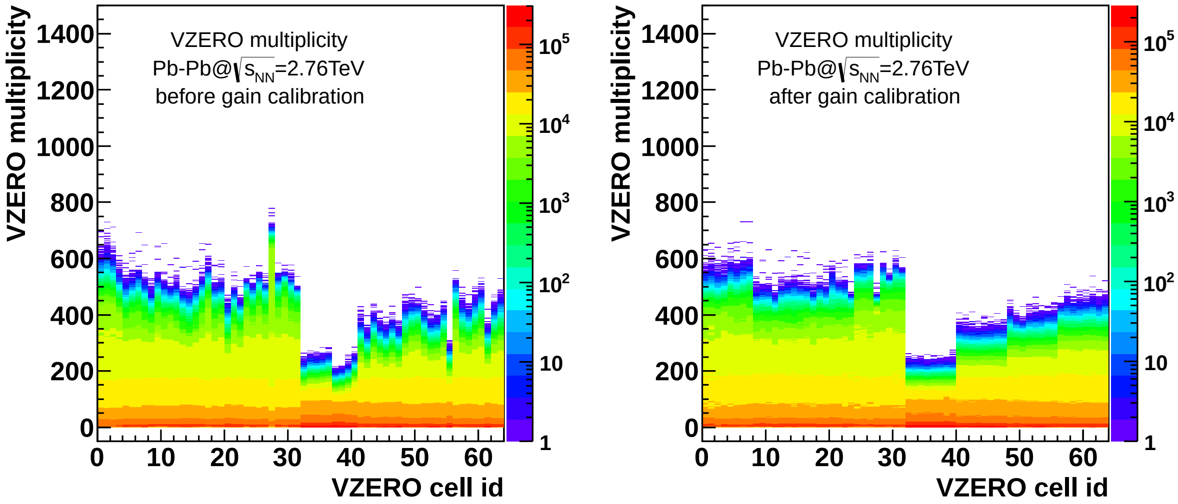

Figure 4.9: VZERO multiplicities for each VZERO cell (left) before and (right) after the gain calibration. The VZERO consists of eight rings, which correspond to cell id 0-8, 8-16, 16-24, 24-36, 36-48, 48-56 and 56-64.

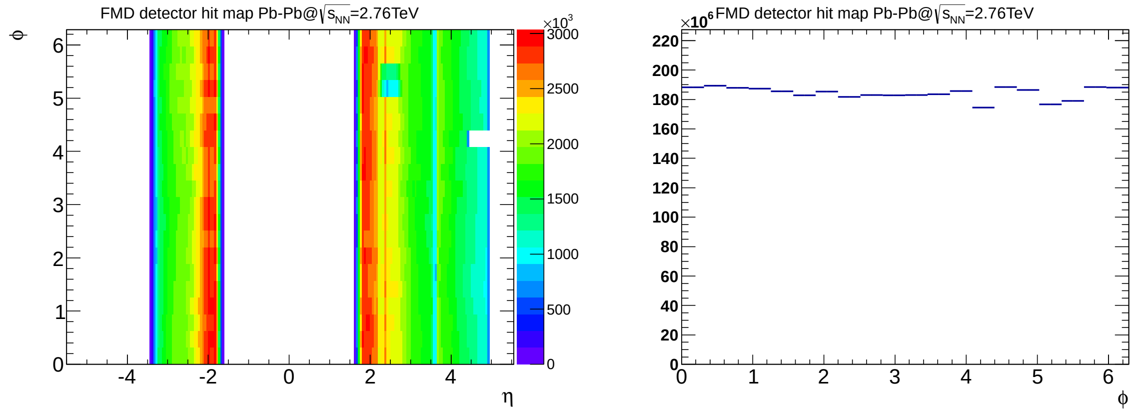

(a)

(b)

Figure 4.10: (a) The FMD detector hit map on (φ, η). (b) Particle azimuthal distribution measured by the FMD.

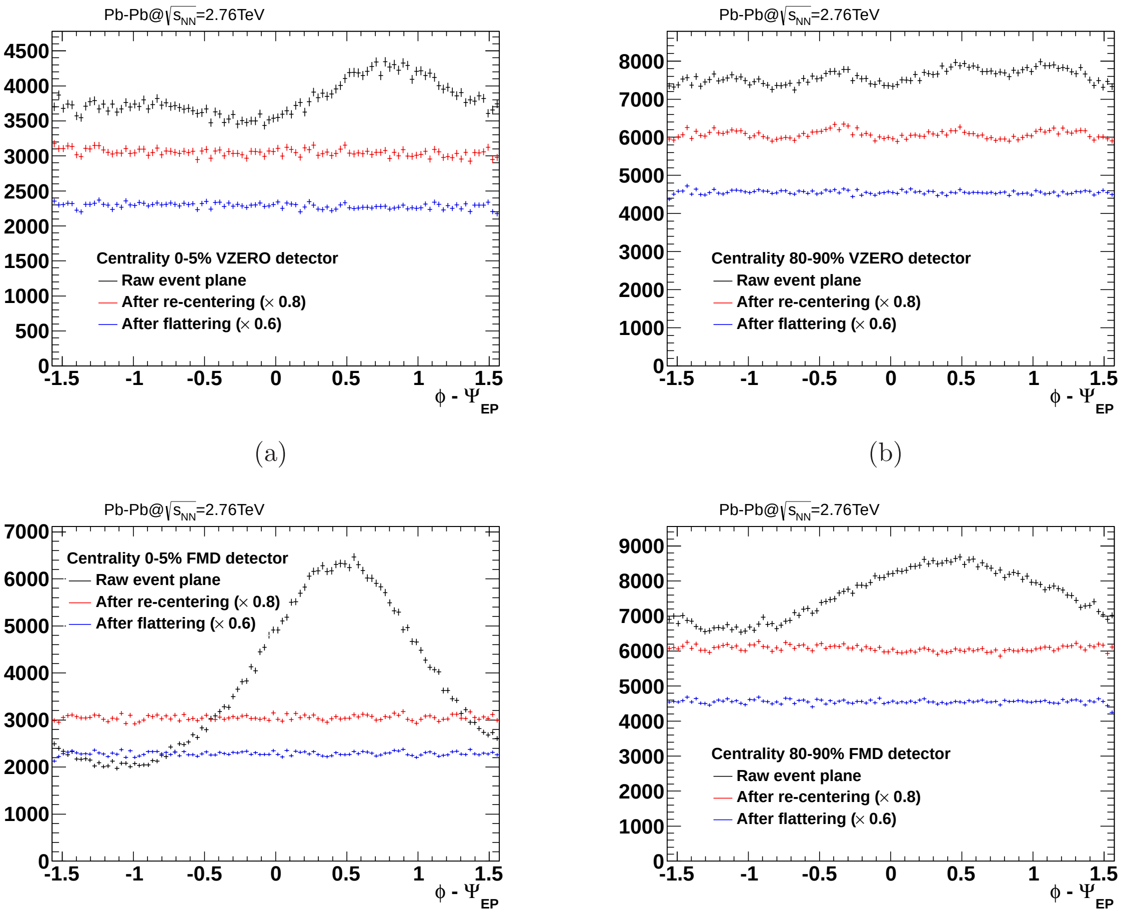

(a) (b)

(c) (d)

Figure 4.11: Event plane distribution; (a) with the VZERO at centrality 0-5%, (b) with the VZERO at centrality 80-90%, (c) with the FMD at centrality 0-5%, (d) with the FMD at centrality 80-90%.

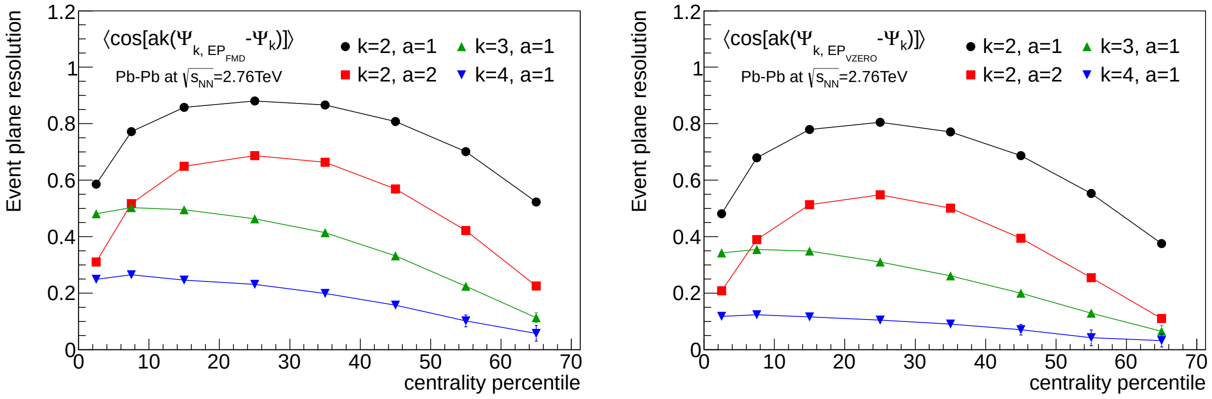

(a) (b)

Figure 4.12: The centrality dependence of the event plane resolution with (a) the FMD and (b) the VZERO detector.

4.6 Systematic uncertainty study

Figure 4.13 shows the results of the integrated correlation $\langle\cos[n(\varphi_\alpha - \varphi_\beta)]\rangle$ measured by the two-particle cumulant method. Figure 4.14 shows the results of the integrated correlation with respect to the symmetry planes measured by the multi-particle cumulant method. Since the relations $\langle\cos[n\varphi_+ + m\varphi_+ - (n+m)\Psi_k]\rangle \sim \langle\cos[n\varphi_- + m\varphi_- - (n+m)\Psi_k]\rangle$, $\langle\cos[n\varphi_+ + m\varphi_- - (n+m)\Psi_k]\rangle \sim \langle\cos[n\varphi_- + m\varphi_+ - (n+m)\Psi_k]\rangle$ and $\langle\cos[n(\varphi_+ - \varphi_+)]\rangle \sim \langle\cos[n(\varphi_- - \varphi_-)]\rangle$ hold for all correlations within statistical uncertainties, we can safely combine them into two sets of points, labelled *same* and *opposite* charge combinations. A difference between same and opposite charge correlations is found to be non-zero. Systematic uncertainties are studied as shown in Fig. 4.15 and Fig. 4.16. Evaluated items are summarized below:

- Magnetic field polarities
  The event sample analyzed, was recorded with two setting of the magnetic field polarities, namely the (++) and the (−−) ones.

- Centrality estimation
  The centrality of the given collision can be evaluated by various detectors. By the default setting, the multiplicity of the VZERO detector is used. Another method uses the multiplicity of tracks evaluated by the standalone TPC tracking.

- Variation of the cut on the position of the z-coordinate of the primary vertex
  The variation of the cut on the position of the primary vertex allows one to accept or reject events that in general are considered in the analysis. The default cut is set to $|V_z| < 7$ cm.

- Variation of the cut on the number of TPC clusters
  By varying the accepted values for this parameters, we accept tracks with worst or better quality. The default cut is set to 70 clusters.

- Variation of the cut on the *dca* of track
  By varying this cuts, one can change the fraction of non-primary tracks. The default cut is set to 3 cm for both xy plane and z coordinate.

Dominant systematic errors of the correlation $\langle\cos[n(\varphi_\alpha - \varphi_\beta)]\rangle$ come from the variation of *dca* cuts. Other systematic errors are negligible. There is a rather large discrepancy between the results with the small *dca* cuts and the default results in the correlation $\langle\cos[n(\varphi_\alpha - \varphi_\beta)]\rangle$ for $n = 2, 3, 4$ as shown in Fig. 4.15. One possible reason is that the higher charge balance moments are sensitive to the short range correlation induced by the resonance decays. However, these correlations may be affected also by the variations of the efficiency and contamination by changing this cut as shown in Fig. 4.5. We can not distinguish these two possible reasons, so the systematic error is assigned to be $5.6 \cdot 10^{-5}$, $7.5 \cdot 10^{-5}$, $9.2 \cdot 10^{-5}$ and $1.1 \cdot 10^{-4}$ for $n = 1, 2, 3$ and 4 respectively at centrality 30-40% according to the difference between the results with $dca_{xy,z} < 0.1, 0.3$ and 3 cm cuts.

	(1) $[10^6]$	(2) $[10^6]$	(3) $[10^6]$	(4) $[10^6]$	(5) $[10^6]$	(6) $[10^6]$	(7) $[10^6]$
$\Delta\langle\cos(\varphi_\alpha + \varphi_\beta - 2\Psi_2)\rangle$	25.1	1.4	15	4.0	0.76	1.6	1.3
$\Delta\langle\cos(\varphi_\alpha - 3\varphi_\beta + 2\Psi_2)\rangle$	15.5	1.8	5.2	3.4	0.54	0.99	3.2
$\Delta\langle\cos(\varphi_\alpha + 3\varphi_\beta - 4\Psi_2)\rangle$	7.22	1.4	4.2	0.61	1.8	3.1	4.6
$\Delta\langle\cos(\varphi_\alpha - 5\varphi_\beta + 4\Psi_2)\rangle$	7.89	2.4	2.6	1.3	1.3	2.2	3.4
$\Delta\langle\cos(\varphi_\alpha - 4\varphi_\beta + 3\Psi_3)\rangle$	14.3	2.0	4.4	1.2	1.7	2.2	5.1
$\Delta\langle\cos(\varphi_\alpha - 5\varphi_\beta + 4\Psi_4)\rangle$	15.0	2.0	8.0	0.40	1.3	5.7	7.0

Table 4.1: Table of the systematic errors on the correlation $\Delta\langle\cos[\varphi_\alpha - (m+1)\varphi_\beta + m\Psi_k]\rangle$ at centrality 30-40% events: (1) Comparison between different methods, (2) Centrality estimation cuts, (3) *dca* cuts, (4) Number of TPC cluster cuts, (5) Vz cuts, (6) Magnetic polarities, (7) statistical errors

Figure. 4.17 shows the comparison between the results of the correlations with respect to the symmetry planes with four different methods; multi-particle cumulant method (TPC), multi-particle cumulant method with $v_k\{2\}$ denominators (TPC $v_k\{2\}$), VZERO event plane method (VZERO EP) and FMD event plane method (FMD EP). There are three possible reasons for the small discrepancy between the different methods. The first possible reason is that the v_k estimation by the average of $v_k\{2\}$ and $v_k\{4\}$ may not be proper or the multi-particle factorization Eq. (4.5) is not precise enough in the multi-particle cumulant method. The second possible reason is that event plane determination is not correct due to the mis-calibration in the event plane method. The third possible reason is that there are charge sensitive correlations between the POIs and the RPs, which differently contribute on the observables for different methods. We can not distinguish these possible reasons, so the systematic errors are assigned according to the comparison of the different methods shown as grey bands in these figures. In fact, these are dominant systematic errors. Table 5.1 shows the typical systematic errors on the correlation $\Delta\langle\cos[\varphi_\alpha - (m+1)\varphi_\beta + m\Psi_k]\rangle$ at centrality 30-40% events.

4.7 Pair differential azimuthal correlations

Dependencies of the correlations $\langle\cos(\varphi_\alpha - \varphi_\beta)\rangle$, $\langle\cos(\varphi_\alpha + \varphi_\beta - 2\Psi_{RP})\rangle$ and $\langle\cos(\varphi_\alpha - 3\varphi_\beta + 2\Psi_{RP})\rangle$ on the transverse momentum difference $|p_{T,\alpha} - p_{T,\beta}|$, the average transverse momentum $(p_{T,\alpha} + p_{T,\beta})/2$ and the rapidity separation $\Delta\eta = |\eta_\alpha - \eta_\beta|$ of two charged particles are measured as a same way to the results by the STAR collaboration shown in Fig. B.6. The Q-cumulant method can be used also for the measurements of these pair differential correlations as described in detail in App.D.4. The systematic uncertainty study was also conducted as a same way as that for the integrated correlations shown in Fig. C.1∼C.10.

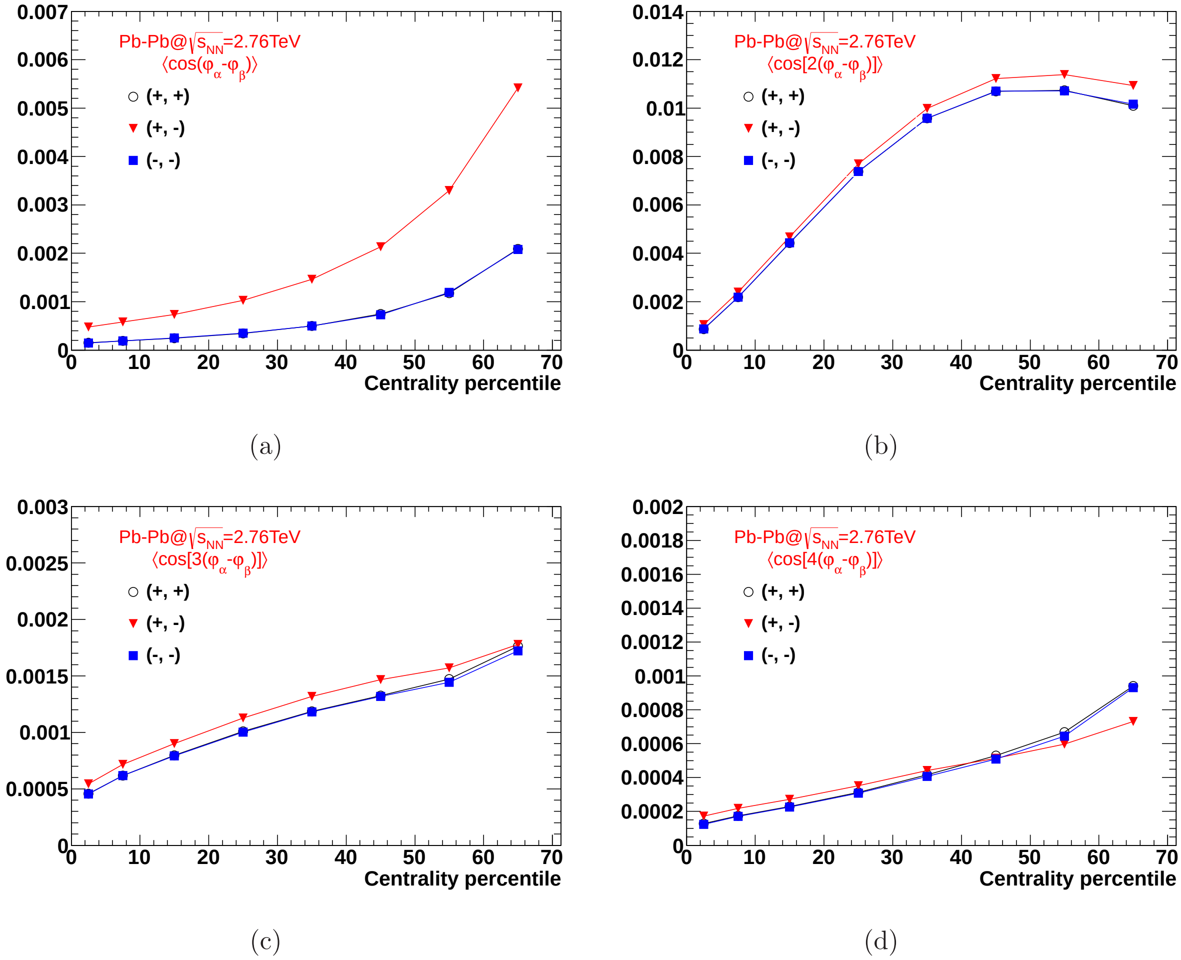

(a)

(b)

(c)

(d)

Figure 4.13: The centrality dependence of the integrated 2-particle correlation by the two-particle cumulant method. The legend indicates the charge combinations for particle α and β: (a) $\langle\cos(\varphi_\alpha-\varphi_\beta)\rangle$, (b) $\langle\cos[2(\varphi_\alpha-\varphi_\beta)]\rangle$, (c) $\langle\cos[3(\varphi_\alpha-\varphi_\beta)]\rangle$, (d) $\langle\cos[4(\varphi_\alpha-\varphi_\beta)]\rangle$.

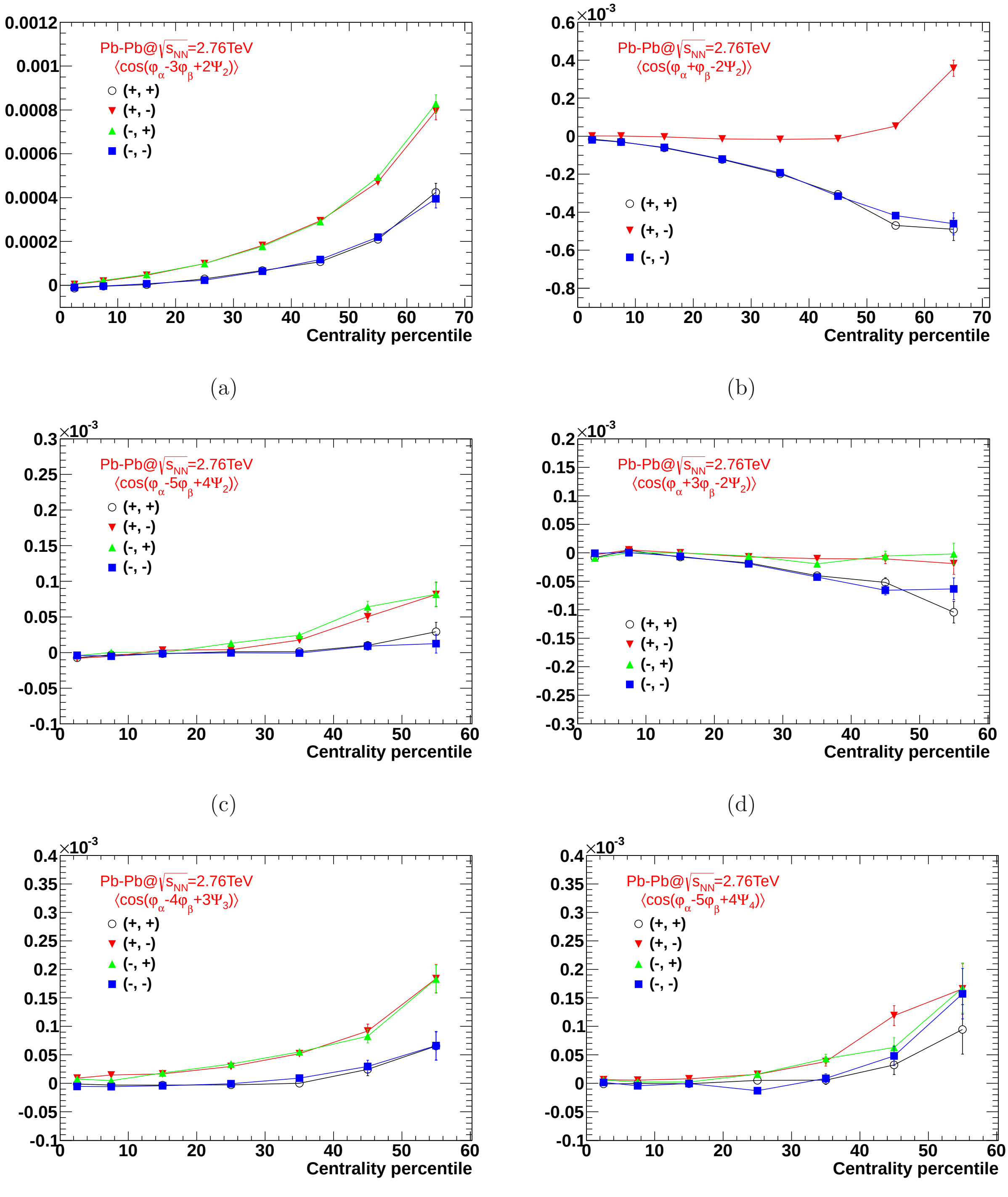

(a)

(b)

(c)

(d)

(e)

(f)

Figure 4.14: The centrality dependence of the integrated two-particle correlation with respect to the symmetry planes measured by the multi-particle cumulant method. The legend indicates the charge combinations for particle α and β. (a) $\langle\cos(\varphi_\alpha - 3\varphi_\beta + 2\Psi_2)\rangle$, (b) $\langle\cos(\varphi_\alpha + \varphi_\beta - 2\Psi_2)\rangle$, (c) $\langle\cos(\varphi_\alpha - 5\varphi_\beta + 4\Psi_2)\rangle$, (d) $\langle\cos(\varphi_\alpha + 3\varphi_\beta - 4\Psi_2)\rangle$, (e) $\langle\cos(\varphi_\alpha - 4\varphi_\beta + 3\Psi_3)\rangle$, (f) $\langle\cos(\varphi_\alpha - 5\varphi_\beta + 4\Psi_4)\rangle$.

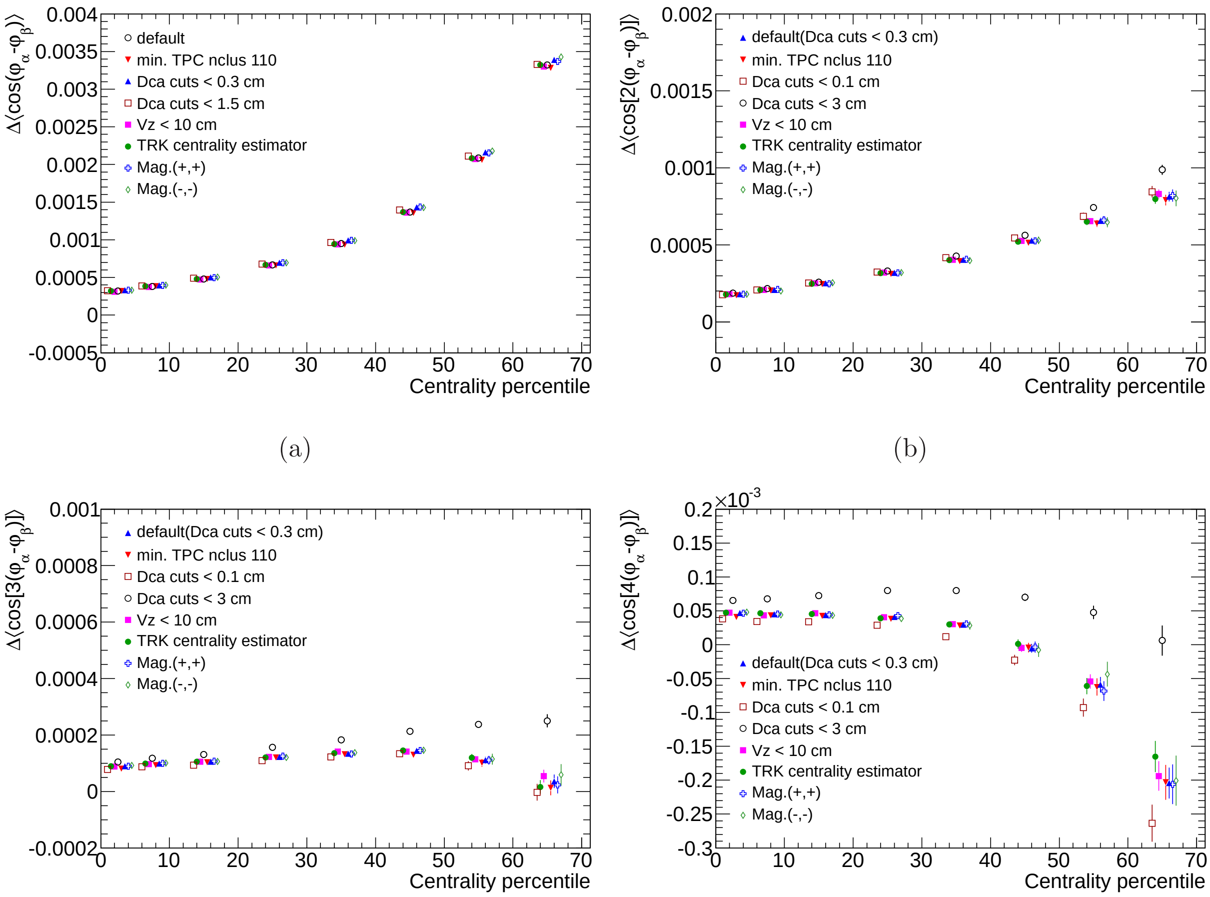

(a)

(b)

(c)

(d)

Figure 4.15: The centrality dependence of the charge dependent parts of the two-particle correlations measured by using the two-particle cumulant method with the various event and track cuts.

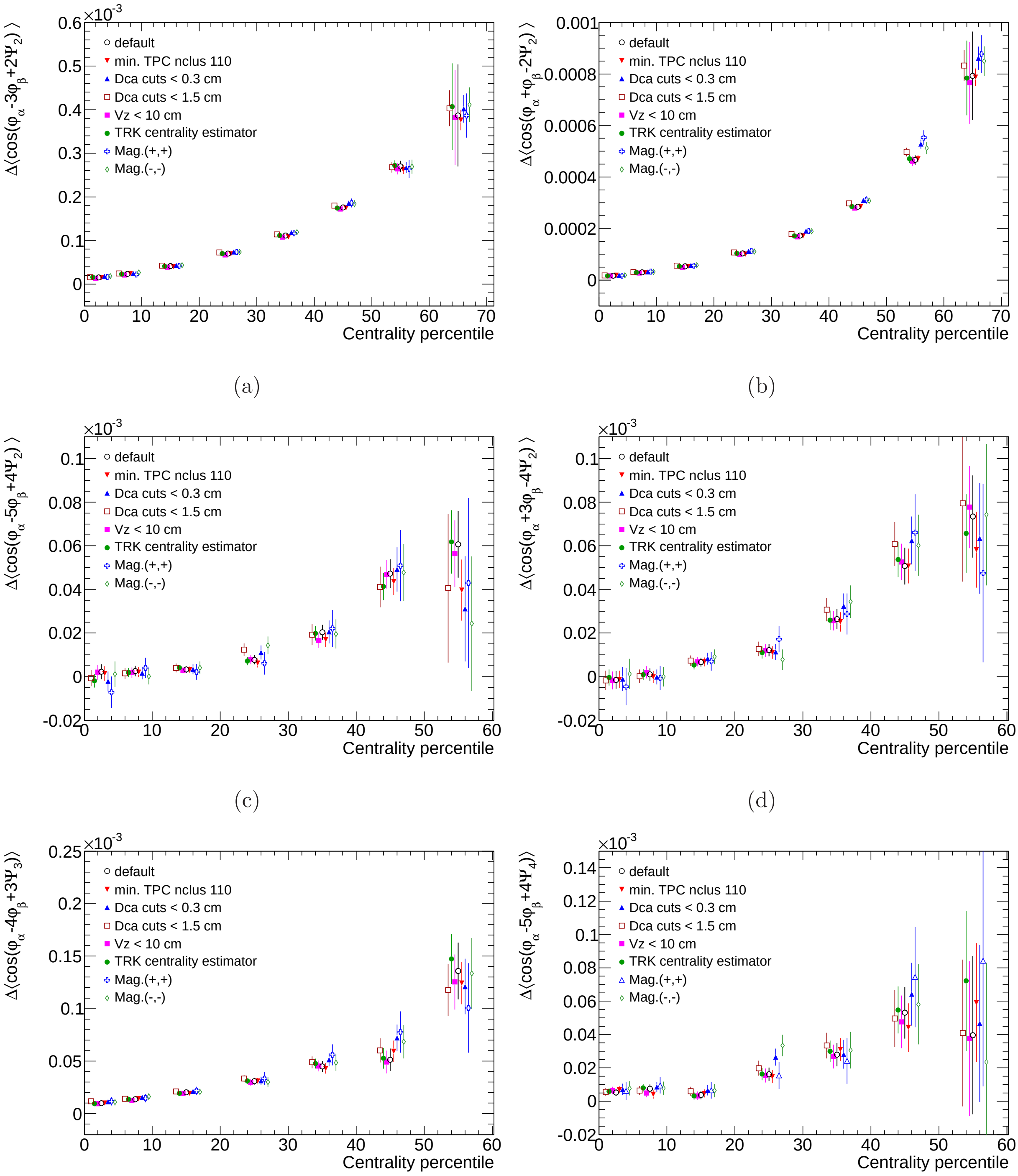

(a) (b)

(c) (d)

(e) (f)

Figure 4.16: The centrality dependence of the charge dependent parts of the two-particle correlations with respect to the symmetry plane measured by using the multi-particle cumulant method with the various event and track cuts.

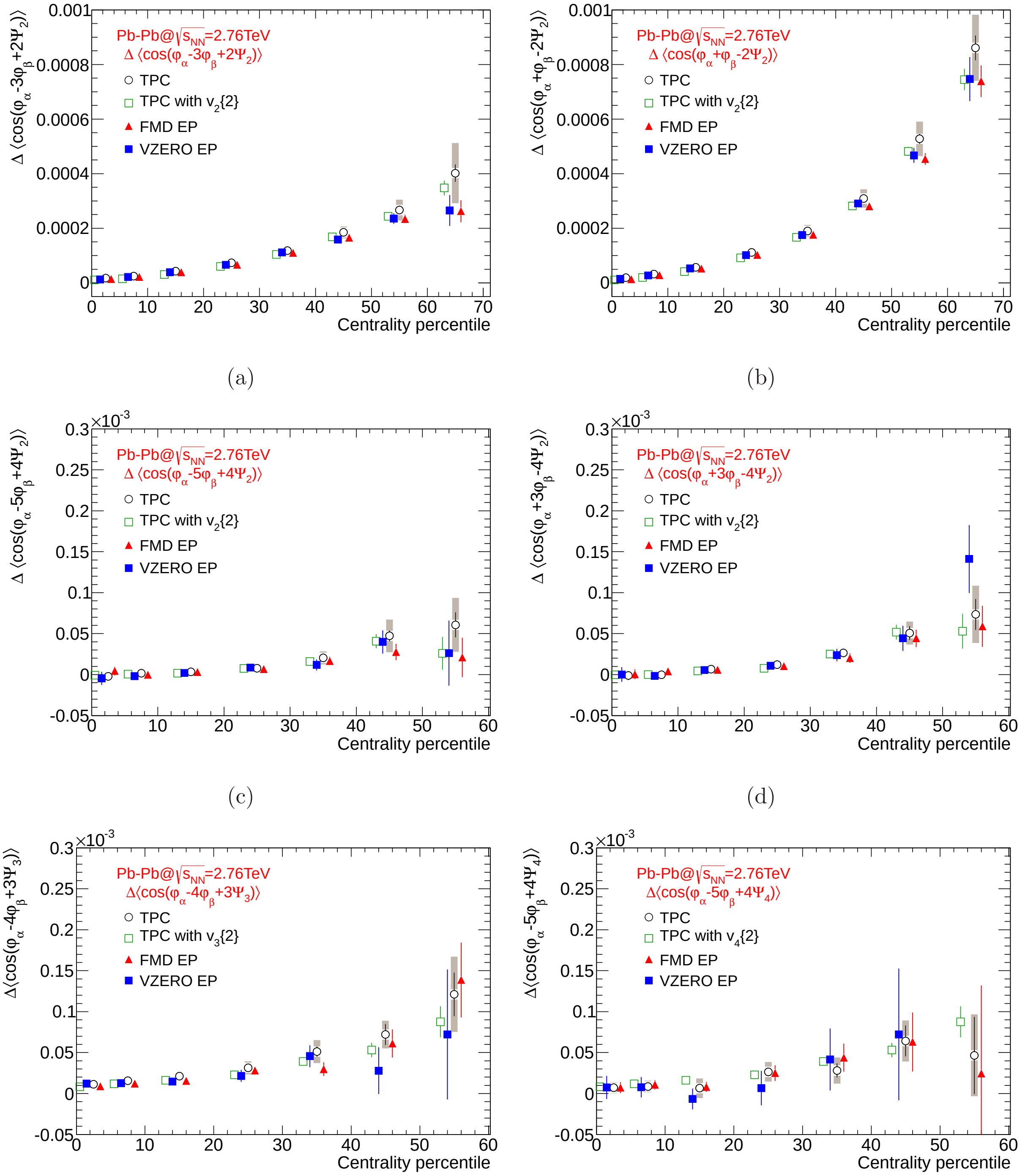

(a) (b)

(c) (d)

(e) (f)

Figure 4.17: The centrality dependence of the charge dependent parts of the two-particle correlations with respect to the symmetry plane measured by using the multi-particle cumulant and the event plane methods.

Chapter 5

Results and Discussions

5.1 Charge dependent azimuthal correlations

In this section, we firstly describe the model in detail used to investigate the LCC induced correlations [34, 35], which may be the reaction plane dependent backgrounds for the CME search. Then the measured results are compared with the model results [81, 82].

5.1.1 Blast Wave model incorporating effects of the LCC

The model used in this thesis is based on Monte Carlo Blast Wave model. The Blast Wave model parametrizes the coordinate and momentum configuration at the kinetic freeze-out generated by hydrodynamic evolution [83]. In the Blast Wave model, it is assumed that a geometry of freeze-out configuration in the transverse direction is set to a filled ellipse with a major axis aligned with the reaction plane as shown in Fig. 5.1 while the boost invariant is assumed in the beam direction. Each fluid element of the system is boosted outward by a collective velocity field $u_\mu(x)$ superimposed on a randomly directed component quantified by a kinetic freeze-out temperature T_{kin}. Here outward indicates the direction normal to the surface of the elliptical shell on which the element sits. The boost azimuthal direction (φ_b) is assumed to be perpendicular to the freeze-out surface, which leads to a relationship between the space and boost azimuthal angles of the emitted particles as follows:

$$\tan(\varphi_s) = \frac{R_y^2}{R_x^2}\tan(\varphi_b), \tag{5.1}$$

where the x direction is in the reaction plane and φ_s denotes the space azimuthal angles of the source fluid element. R_x and R_y denote the in-plane and out-of-plane radii, respectively. R_y sets to unit here since $R = \sqrt{R_x^2 + R_y^2}$ is an arbitrary radius for the azimuthal flow analysis. The ellipticity is defined by:

$$\epsilon \equiv \frac{R_y^2 - R_x^2}{R_y^2 + R_x^2}. \tag{5.2}$$

The system is bounded within a ellipse such as $\Omega(r, \varphi_s) = \theta[\tilde{r}(\varphi_s)]$ with θ the step function and

$$\tilde{r}(\varphi_s) = \sqrt{[r\cos(\varphi_s)/R_x]^2 + [r\sin(\varphi_s)/R_y]^2}. \tag{5.3}$$

The magnitude of flow velocity vanishes at the center of the system and grows monotonically with the distance from the center, reaching the maximum at the transverse edge of the system. A collective flow velocity is parametrized as

$$\begin{aligned} u_\mu(x) &= (\cosh\rho,\ \sinh\rho\,\cos\varphi_b,\ \sinh\rho\,\sin\varphi_b,\ 0), &(5.4)\\ \rho(r,\varphi_s) &= \tanh^{-1}\beta(r,\varphi_s), &(5.5)\\ \beta(r,\varphi_s) &= \tilde{r}^n(\varphi_b)(\beta_0 + \beta_2\cos(2\varphi_b) + \beta_4\cos(4\varphi_b)). &(5.6)\end{aligned}$$

The conventional way to apply such the Blast Wave model is then to choose a point on the freeze-out surface, create a particle with momentum according to T_{kin} and $u_\mu(x)$ assuming the local thermal equilibrium, calculate the observable of interest and then repeat for several particles until sufficient statistics is achieved. With regard to charge-balance correlations one needs to additionally incorporate the local charge conservation. This can be achieved in the following way: Instead of generating a single particle at a time, we generate a canonical ensemble of particles at a chemical freeze-out temperature of T_{chem} = 148 MeV [84] and fixed volume 100 fm^3 with exactly conserved charges by using a dilute description of the hadron resonance gas. The details of the implementation of the canonical ensemble can be found in Ref. [28]. For a given ensemble every particle is then assigned a collective velocity v_i such that all the v_i follow the single particle Blast Wave parametrization with the additional constraint of being emitted within a certain angle distance σ_φ in the direction $\bar{\varphi} = \text{atan}[(R_x/R_y)(y/x)]$ of each others. The illustration of the definition of $\bar{\varphi}$ is shown by green lines in Fig. 5.1. In the limit where the charge conservation at the kinetic freeze-out is perfectly local, this distance is zero $\sigma_\varphi = 0$ and all particles within a given ensemble are emitted as if their sources had the same collective velocity. The details of the implementation of the local charge conservation can be found in Ref. [34]. Charge dependent correlations can be calculated separately for each array as particles from different arrays are assumed to be uncorrelated in our model. We note that in reality, charge dependent correlations are sensitive also to the correlations induced by the final-state interactions and the identical particle interference [85]. When incorporated in the model, these have been shown to explain distortions of the balance function [34, 85]. However, for our purpose of estimating the magnitude of the local charge conservation signal, we expect these effects to be less relevant and we will neglect them in the following.

Analytic expressions of the transverse momentum spectrum and n-th harmonic azimuthal flow are given as

$$\frac{dN}{p_\mathrm{T}dp_\mathrm{T}} = \frac{2m_\mathrm{T}\tau e^{\mu/T}}{(2\pi)^3}\int_0^1 rdr\int_0^{2\pi} d\varphi_s I_0(\alpha(r,\varphi_s))K_1(\beta(r,\varphi_s))\Sigma(r,\varphi_s), \tag{5.7}$$

$$v_n(p_\mathrm{T}) = \frac{\int_0^1 rdr\int_0^{2\pi} d\varphi_s K_1(\beta(r,\varphi_s))I_n(\alpha(r,\varphi_s))\cos(n\varphi_s)\Sigma(r,\varphi_s)}{\int_0^1 rdr\int_0^{2\pi} d\varphi_s K_1(\beta(r,\varphi_s))I_0(\alpha(r,\varphi_s))\Sigma(r,\varphi_s)}, \tag{5.8}$$

where I_n and K_1 are the modified Bessel functions. $\alpha(r, \varphi_s)$ and $\beta(r, \varphi_s)$ are defined as

$$\begin{aligned}\alpha(r, \varphi_s) &= \frac{p_{\mathrm{T}}}{T} \sinh\rho(r, \varphi_s), \\ \beta(r, \varphi_s) &= \frac{m_{\mathrm{T}}}{T} \cosh\rho(r, \varphi_s).\end{aligned} \tag{5.9}$$

The six free parameters T_{kin}, n, β_0, β_2, β_4 and ϵ were extracted by fitting the measured dN/dp_{T}, p_{T} differential $v_2\{EP_2\} \sim v_2$ and $v_4\{EP_2\} \sim v_{4,2}$ as shown in table 5.1 below, Fig. 5.2 [73, 84, 86].

In order to compare the model results to ALICE data, we account for the detector efficiency and acceptance by using the same kinematic cuts as the ALICE experiment ($|\eta| < 0.8$, $0.2 < p_{\mathrm{T}} < 5$ GeV/c) and rescaling the model results to reproduce the experimental uncorrected multiplicities [87] and the overall normalization $Z = \langle N_{--} - N_{++} \rangle / \langle M_+ \rangle + \langle N_{-+} - N_{+-} \rangle / \langle M_- \rangle$ [88], which corresponds to the probability of observing the balancing charge in the detector. The correction factor would be $Z = 1$ for a perfect detector with full acceptance and equal number of positive and negative charged particles in each event. Note that the calculated magnitudes of the azimuthal correlations may change at most 20% due to the systematic uncertainty of Z and M, but the ratios of the azimuthal correlations are insensitive to them.

Figure 5.3 shows the balance function with respect to the reaction plane $B(\tilde{\varphi}_2, \Delta\varphi)$ calculated by this model. One observes that the balance function in the in-plane region ($\tilde{\varphi}_2 \sim 0°$) is significantly narrower compared to the balance function in the out-of-plane region ($\tilde{\varphi}_2 \sim 90°$). This is a consequence of the larger collective velocities in the in-plane region, which lead to a focusing in azimuthal angle as illustrated in the left picture in Fig. 2.2. At intermediate angles ($\tilde{\varphi}_2 \sim 45°$) the balance function shows an asymmetry towards the in-plane direction. This can be attributed to the fact that the balancing partner charge is statistically more likely to be found in the in-plane region than to in the out-of-plane region as illustrated in the right picture in Fig. 2.2.

This model uses the simple parametrization of the freeze-out surface. In reality, the geometry of the freeze-out surface is considered to be more complicated as shown in Fig. 5.4 (a) [89]. The freeze-out hypersurfaces have the *volume emission* parts (with time-like normal vectors, i.e. running approximately flat in Fig. 5.4 (a)), which are similar to the Blast Wave parametrization. However, they also contain the *surface emission* parts (with space-like normal vectors, i.e. running more-or-less vertical in Fig. 5.4 (a). In order to avoid confusion with the freeze-out surface or hypersurfaces, italic letters are used for this *surface emission* parts), absent in the usual Blast Wave parametrization. The *surface emission* parts have the higher transverse flow than the *volume emission* parts. Both the spatial and momentum ellipticities of the *surface emission* parts change its sign at $t \sim 9$ fm. The high p_{T} particles are likely to come from the fluid with higher transverse flow and it was found that about half of the produced particles comes from the *volume emission* parts and about half from the *surface emission* parts. Therefore, the model used in this thesis may overestimate the ellipticity of high p_{T} particles. In addition, it would be interesting to study the effects of the LCC in event-by-event fully

centrality	T_{kin} [GeV]	n	β_0	β_2	β_4	ϵ
5-10%	0.086	1.10	0.930	0.00831	0.00021	0.0962
10-20%	0.085	1.17	0.935	0.0129	0.000237	0.135
20-30%	0.083	1.24	0.938	0.0154	0.000255	0.172
30-40%	0.080	1.35	0.940	0.0160	0.00029	0.204
40-50%	0.080	1.46	0.943	0.0151	0.00033	0.224
50-60%	0.079	1.50	0.944	0.0136	0.00033	0.226

Table 5.1: Table of the Blast Wave parameters for each centrality bins for Pb–Pb $\sqrt{s_{NN}} =$ 2.76 TeV collisions.

hydrodynamic simulations in order to obtain complete pictures of the charge dependent azimuthal correlations.

Moreover, the separation between hadrons and anti-hadrons on the freeze-out surface is parametrized not in the spatial but in the $\bar{\varphi}$ angle space because it is easy to implement. The separation width with $\sigma_\varphi = 0.5$ roughly corresponds to the spatial separation width of $6 \times \sin(0.5) \sim 3$ fm on the freeze-out surface since the measured Hanbury-Brown-Twiss (HBT) radius R_{side} [89, 90] at the LHC energy is ~ 6 fm as shown in Fig. 5.4 (b). This is compatible to a few fm/c of the hadron formation time [91].

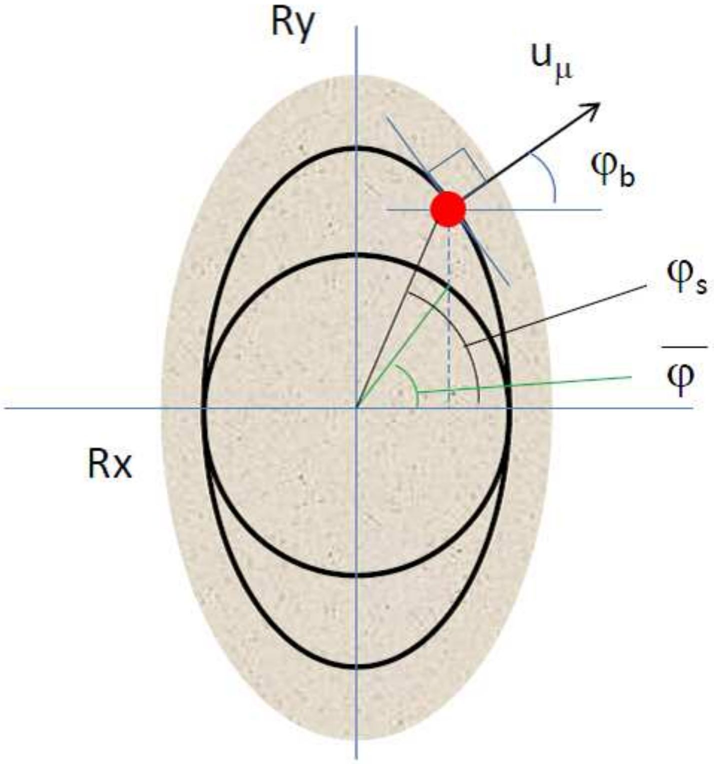

Figure 5.1: Visualization of the Blast Wave parametrization in the transverse plane. At a point (x, y) in the transverse plane the associated collective velocity is perpendicular to the surface of the ellipse. The magnitude of the transverse collective rapidity increases linearly with the reduced radius and has a second order harmonic component w.r.t the boost angle φ_b. The relative distribution of the balance charges in the transverse plane is a Gaussian in $\Delta\bar{\varphi}$ with the width σ_φ.

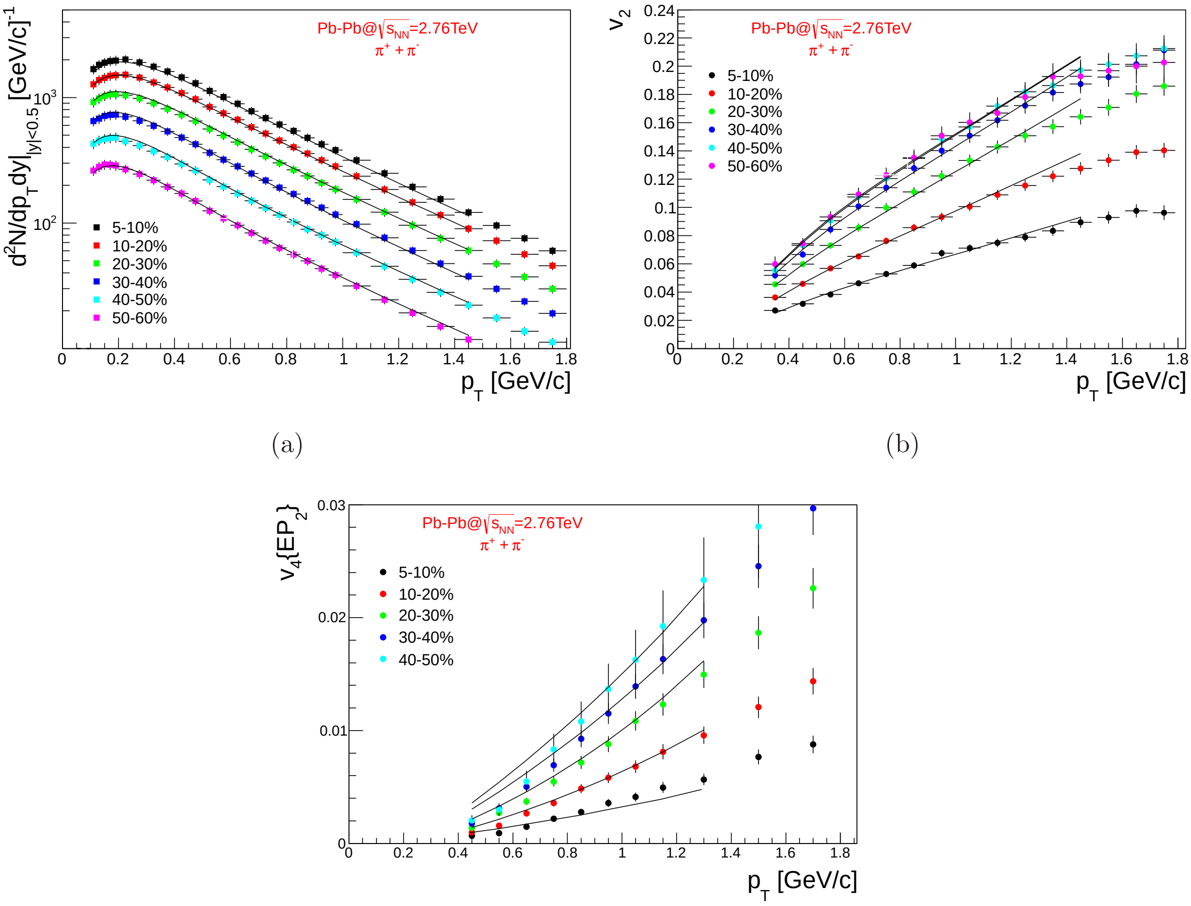

(a)

(b)

(c)

Figure 5.2: (a) Charged pion $d^2N/dp_{\mathrm{T}}dy|_{|y|<0.5}$ as a function of p_{T}, (b) p_{T} differential elliptic flow v_2, (c) p_{T} differential elliptic flow $v_4\{EP_2\}$ measured by the ALICE collaboration for each centrality events in comparison with the Blast Wave model fitting [73, 84].

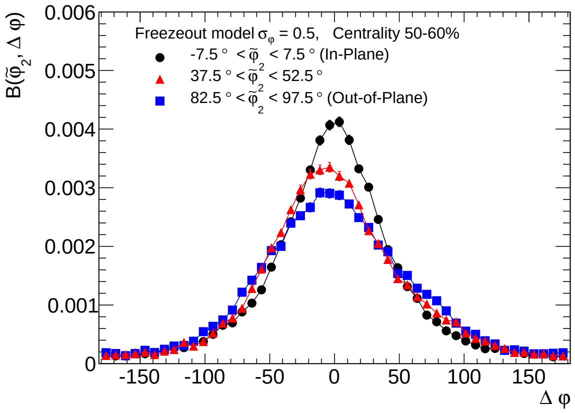

Figure 5.3: The balance function with respect to the reaction plane $B(\tilde{\varphi}_2, \Delta\varphi)$ calculated from the Blast Wave model incorporating effects of the LCC. One observes that the balance function is narrower for in-plane pairs than out-of plane pairs. The balance function at intermediate angles shows an asymmetry in $\Delta\varphi$ towards the reaction plane.

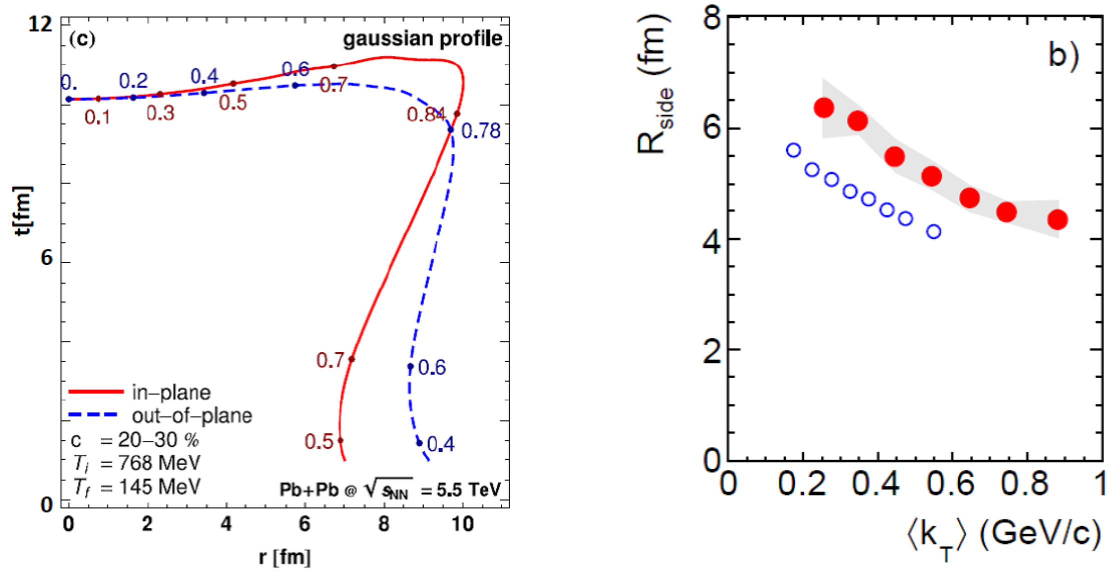

(a)

(b)

Figure 5.4: (a) Sections of the freeze-out hypersurfaces for the gaussian-type initial condition for centrality 20-30% at the LHC. The dots with numbers indicate the values of the transverse velocity at the freeze-out. The hydrodynamic evolution proceeds until the freeze-out occurs, where the assumed condition for the universal freeze-out temperature is $T_f = 145$ TeV [89]. (b) Pion HBT radii R_{side} as a function of $\langle k_{\mathrm{T}} \rangle \equiv \langle |\mathbf{p}_{\mathrm{T},1} + \mathbf{p}_{\mathrm{T},2}| \rangle / 2$. Red closed circles are experimental results at the 5% most central Pb–Pb collisions measured by the ALICE collaboration. Blue open circles are experimental results at the 5% most central Au–Au collisions measured by the STAR collaboration [90].

5.1.2 Experimental Results

(i) Charge balance moments

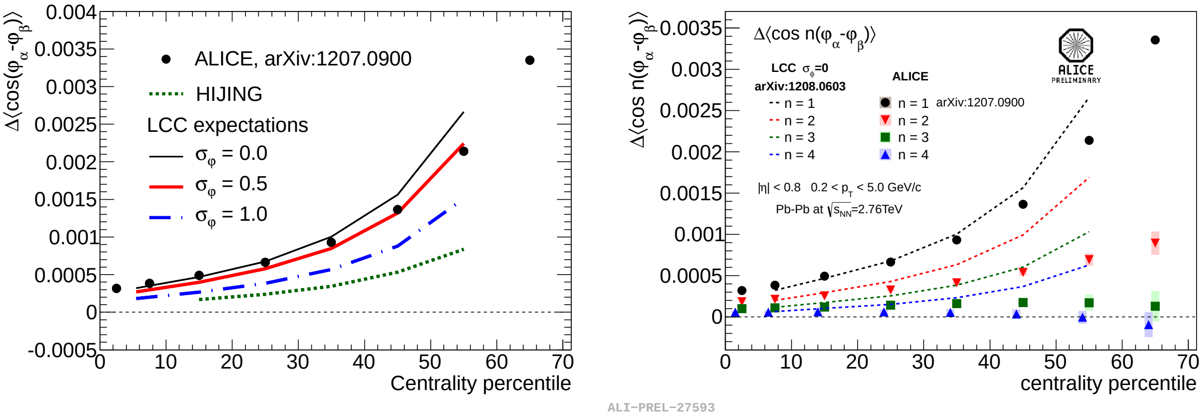

(a)

(b)

Figure 5.5: Centrality dependence of the correlation (a) $C_1 = \Delta\langle\cos(\varphi_\alpha - \varphi_\beta)\rangle$ in comparison with the HIJING model and the Blast Wave model incorporating effects of the LCC $\sigma_\varphi = 0.0, 0.5, 1.0$ and (b) the higher charge balance moments $C_n = \Delta\cos[n(\varphi_\alpha - \varphi_\beta)]\rangle$ in comparison with the Blast Wave model incorporating effects of the LCC $\sigma_\varphi = 0.0$ [35, 81].

As discussed in Sec.4.6, since relation $\langle\cos[n(\varphi_+ - \varphi_+)]\rangle \sim \langle\cos[n(\varphi_- - \varphi_-)]\rangle$ is found to hold with $n = 1 - 4$, they are safely combined into one set labelled *same* charge combinations. Then, we can define the charge balance moments C_n as the difference between the opposite and same charge correlations.

Figure 5.5 (a) shows the centrality dependence of the 1st charge balance moment $C_1 = \Delta\langle\cos(\varphi_\alpha - \varphi_\beta)\rangle$ compared with the results of the HIJING model and the Blast Wave model incorporating effects of the LCC. The statistical and systematic uncertainties are smaller than the symbol size. The measured results are positive for all the centrality class, which is consisient with the interpretation as the inverse width of the charge balancing pairs and opposite to the CME expectation discussed as Eq. (2.14). Furthermore, $|C_1|$ is much larger than the possible CME contributions $|\Delta\langle a_{1,\alpha}a_{1,\beta}\rangle|$, so we can safely ignore the possible CME on this correlation.

The HIJING model underestimates this strong charge dependence as shown by a green dot line. On the other hand, the Blast Wave model reproduces the ALICE result well. The model parameter σ_φ is the separation width between hadrons and anti-hadrons on the kinetic freeze-out surface. The parameter σ_φ is found to be small by the comparison of the correlation C_1. observed large positive C_1 can be regarded as an evidence of the combined effect of the LCC and the large radial flow on the kinetic freeze-out surface while the HIJING model fails to describe it because it does not have a large radial flow in the final state.

Figure 5.5 (b) shows the centrality dependence of the charge balance moments $C_n = \Delta\langle\cos[n(\varphi_\alpha - \varphi_\beta)]\rangle$ with $n = 1 - 4$ compared with the results of the Blast Wave model incorporating effects of the LCC. Higher charge balance moments ($C_n, n > 1$) have smaller magnitudes and 4th charge balance moments are negative for peripheral collisions, which however can not be described by the Blast Wave model with $\sigma_\varphi = 0$. For the higher charge balance moments, charge dependent near side correlations (e.g. HBT) may be relevant and is not taken into consideration in this simple Blast Wave model. In this thesis, the most of the correlations investigated are the 1st charge balance moment C_1 and its azimuthal modulations discussed below.

(ii) Azimuthal Modulation w.r.t. the 2nd harmonic symmetry plane

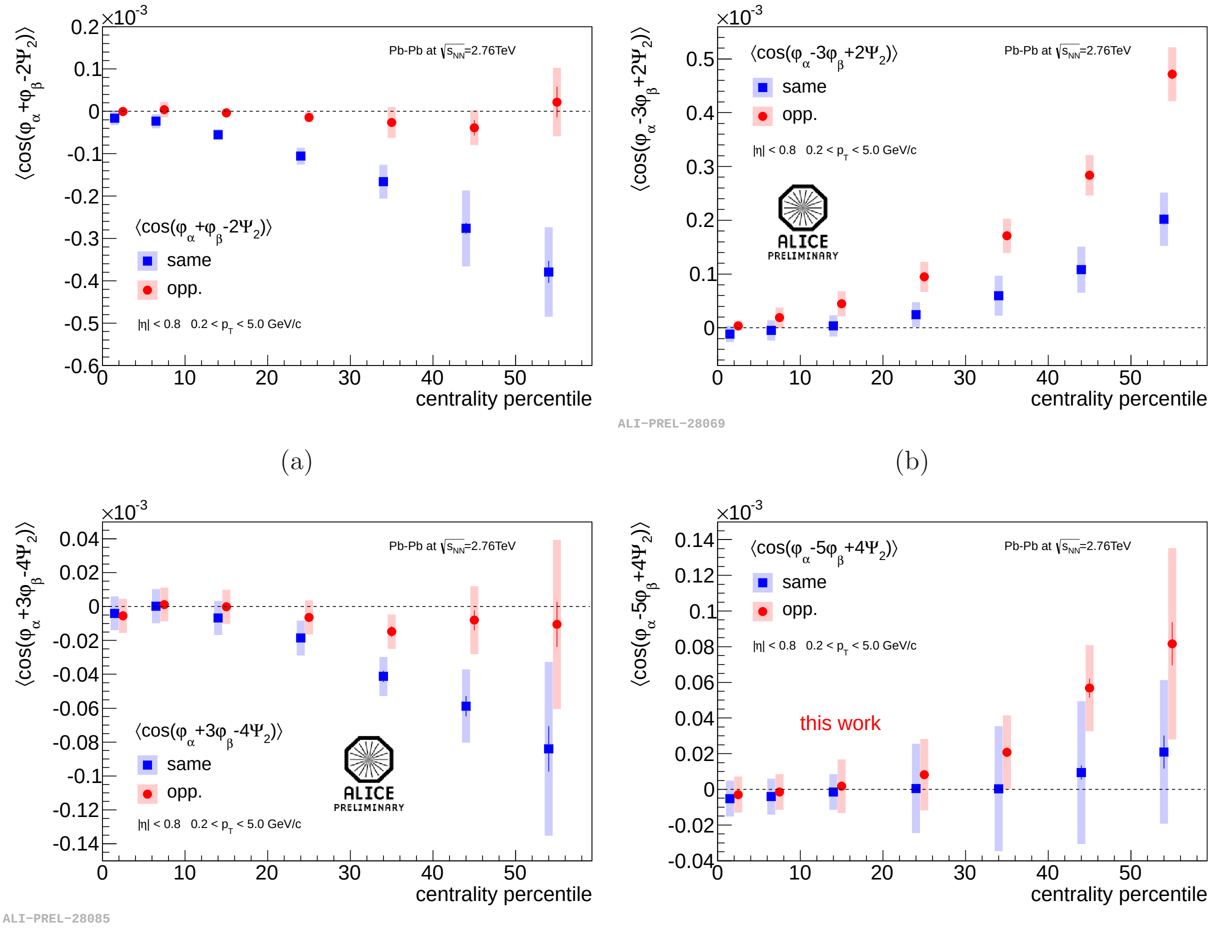

(a)

(b)

(c)

(d)

Figure 5.6: Centrality dependence of the charge dependent two particle azimuthal correlations with respect to the 2nd harmonic symmetry plane: (a) $\langle\cos(\varphi_\alpha + \varphi_\beta - 2\Psi_2)\rangle$ [92], (b) $\langle\cos(\varphi_\alpha - 3\varphi_\beta + 2\Psi_2)\rangle$ [81], (c) $\langle\cos(\varphi_\alpha + 3\varphi_\beta - 4\Psi_2)\rangle$ [81], (d) $\langle\cos(\varphi_\alpha - 5\varphi_\beta + 4\Psi_2)\rangle$.

As discussed in Sec.5.6, since relations $\langle\cos[n\varphi_+ + m\varphi_+ - (n+m)\Psi_k]\rangle \sim \langle\cos[n\varphi_- +$

$m\varphi_- - (n+m)\Psi_k]\rangle$ and $\langle\cos[n\varphi_+ + m\varphi_- - (n+m)\Psi_k]\rangle \sim \langle\cos[n\varphi_- + m\varphi_+ - (n+m)\Psi_k]\rangle$ are found to hold with $(n,m,k) = (1,1,2), (1,-3,2), (1,3,2)$ and $(1,-5,2)$, they are safely combined into two sets of points, labelled *same* and *opposite* charge combinations. Figure 5.6 shows the centrality dependence of the charge dependent two particle azimuthal correlations with respect to the 2nd harmonic symmetry plane: $\langle\cos(\varphi_\alpha + \varphi_\beta - 2\Psi_2)\rangle$, $\langle\cos(\varphi_\alpha - 3\varphi_\beta + 2\Psi_2)\rangle$, $\langle\cos(\varphi_\alpha + 3\varphi_\beta - 4\Psi_2)\rangle$ and $\langle\cos(\varphi_\alpha - 5\varphi_\beta + 4\Psi_2)\rangle$ for the same and opposite charge combinations. Similar to the correlation $\langle\cos(\varphi_\alpha + \varphi_\beta - 2\Psi_2)\rangle$ used for the CME search, all the additional three correlations of the opposite charge pairs are significantly larger than that of the same charge pairs. Here we discuss these nonzero charge dependent parts (The charge independent parts of these correlations are discussed in Sec.6.2.3). Figure 5.7 shows the centrality dependent parts of the correlation $\Delta\langle\cos[\varphi_\alpha - (m+1)\varphi_\beta + m\Psi_k]\rangle$ for $m = 2, -2, 4, -4$ which corresponds to the $|m|$-th azimuthal modulation of C_1 with respect to the 2nd harmonic symmetry plane (the reaction plane). The correlations $\Delta\langle\cos(\varphi_\alpha + \varphi_\beta - 2\Psi_{RP})\rangle$ and $\Delta\langle\cos(\varphi_\alpha - 3\varphi_\beta + 2\Psi_{RP})\rangle$ are categorized into the 2nd azimuthal modulation by the elliptic flow v_2 while the correlations $\Delta\langle\cos(\varphi_\alpha + 3\varphi_\beta - 4\Psi_2)\rangle$ and $\Delta\langle\cos(\varphi_\alpha - 5\varphi_\beta + 4\Psi_2)\rangle$ are categorized into the 4th azimuthal modulation by the 4th harmonic flow $v_{4,2}$. The formers (red symbols) are larger than the latter (blue symbols) as same ordering of $v_2 > v_{4,2}$. Open symbols are larger than closed ones for both red and blue symbols and the difference between open and closed symbols comes from a sign in front of the term $ms^n_{n+m,k}$ in Eq. (2.5), which represents the modulation of the charge balance asymmetry.

Since the HIJING model do not have the collective flow, the three-particle correlation $\langle\cos[n\varphi_\alpha + m\varphi_\beta - k\varphi_{\gamma_1} \cdots - k\varphi_{(n+m)/k}]\rangle$ calculated by using the HIJING are divided by the experimentally measured values of elliptic flow $v_2\{2\}^{(n+m)/k}$ for the estimation of contributions from jets, resonances, and other trivial processes by the HIJING model. The HIJING model gives negligible charge dependent parts of all the correlations as shown in Fig. 5.7 (a), while the Blast Wave model can reproduce the main features of the charge dependent parts of all the correlations very well as shown in Fig. 5.7 (b). The observed charge dependent parts of a series of the mixed harmonic azimuthal correlations including the correlation $\langle\cos(\varphi_\alpha + \varphi_\beta - 2\Psi_{RP})\rangle$ can be systematically explained due to mostly the correlations induced by the “effective” LCC on the kinetic freezeout surface.

Although it is found that the LCC seems to be realized on the kinetic freezeout surface and induces the significant contribution on the charge dependent azimuthal correlations as discussed above, we discuss the CME search via the charge dependent azimuthal correlation $\langle\cos(\varphi_\alpha + \varphi_\beta - 2\Psi_{RP})\rangle$ ignoring the LCC effects. Observed charge dependence shown in Fig. 5.6 (a) (Fig. 5.7 (c)) is roughly consistent with the CME expectation that the opposite charge correlation is larger than the same charge correlation. Its centrality dependence is also consistent with the CME expectation that the charge dependent part is smaller in central collisions than in peripheral collision because of the dilution of correlations with the increasing number of participants in the collisions and the decrease of the magnetic field. It is also found that there is a difference in magnitude between the same and opposite charge combinations of the correlation $\langle \cos(\varphi_\alpha + \varphi_\beta - 2\Psi_{RP}) \rangle$. In the view of the CME, this can be explained by the quenching effect of the back-to-back opposite charge correlation by the interactions with the parity-odd bubbles and medium [37]. Alternative explanations will be discussed in detail at Sec.6.2. The shaded blue band in Fig. 5.7 (c) is the result for the charge independent correlation.

A large source of uncertainty in the theoretical model of the CME can be reduced by studying the colliding energy dependence [38, 93, 94, 95, 96]. Some authors argued that the magnitude of the effect should decrease with increasing collision energy [38, 96] while others predicts little collision energy dependence [95]. A red line in Fig. 5.7 (c) is a model prediction for the same charge correlation by the authors in Ref. [38]. The opposite charge correlation in this model has a positive sign and the same magnitude as the same charge correlation (not shown in plot). In this model, it is expected that the quantity $\langle a_\alpha a_\beta \rangle$ depends on the collision energy $\sqrt{s_{NN}}$ and the lifetime of the strong magnetic field and the deconfined matter τ_B as $\propto (\sqrt{s_{NN}})^{-1/8} \cdot \tau_B$. The normalization of the signals are tuned at the reference data obtained by the STAR collaboration at the RHIC top energy $\sqrt{s_{NN}} = 200$ GeV. Observed correlation $\langle \cos(\varphi_\alpha + \varphi_\beta - 2\Psi_{RP}) \rangle$ is much larger than this model prediction and compatible to the results at the RHIC top energy, which may provide further insights for the CME.

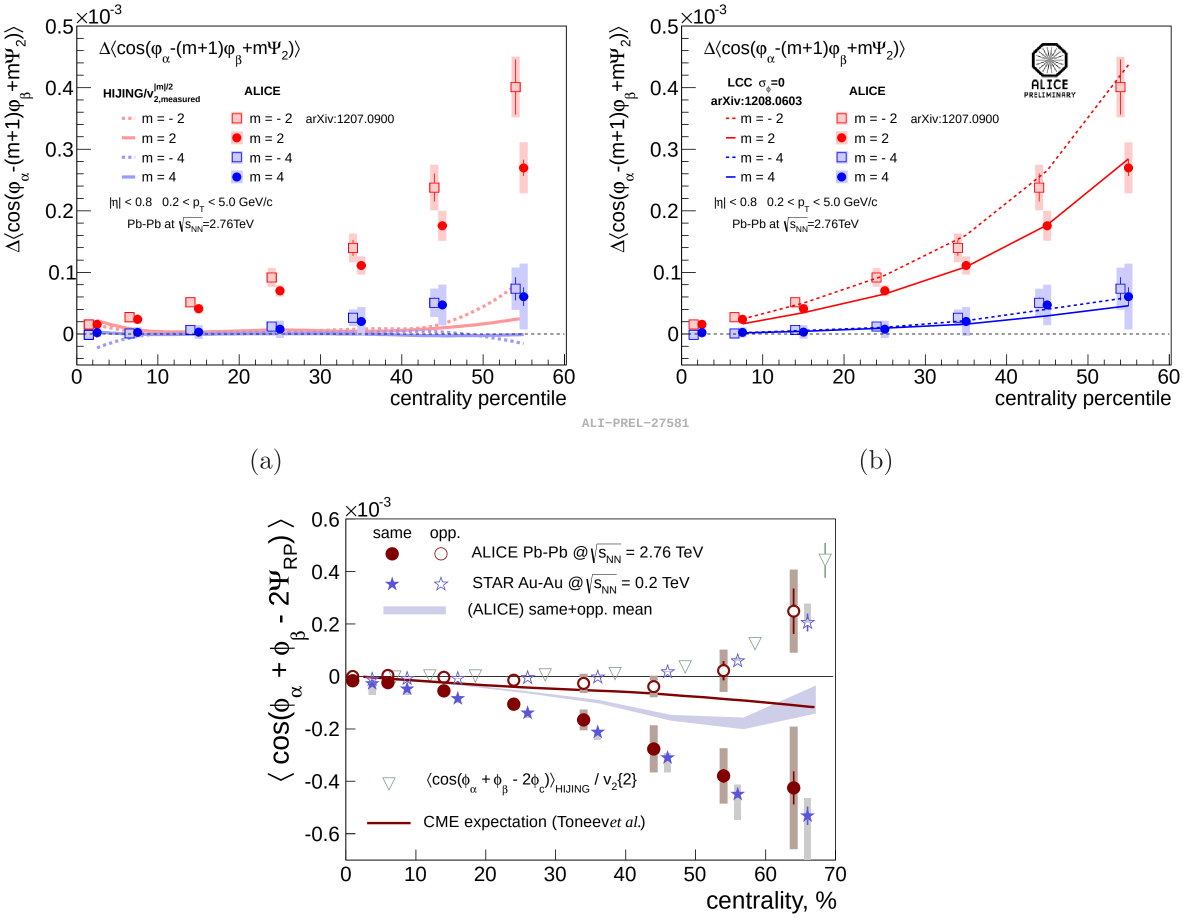

(a)

(b)

(c)

Figure 5.7: Centrality dependence of the correlation $\Delta\langle\cos[\varphi_\alpha - (m+1)\varphi_\beta + m\Psi_2]\rangle$ in comparison with (a) the HIJING model and (b) the Blast Wave model incorporating effects of the LCC $\sigma_\varphi = 0.0$ [45, 35, 81]. (c) Centrality dependence of the correlation $\langle\cos(\varphi_\alpha + \varphi_\beta - 2\Psi_{RP})\rangle$ measured by the ALICE in comparison with the results by STAR collaboration and theoretical calculations [92].

(iii) Azimuthal Modulation w.r.t. the higher harmonic symmetry planes

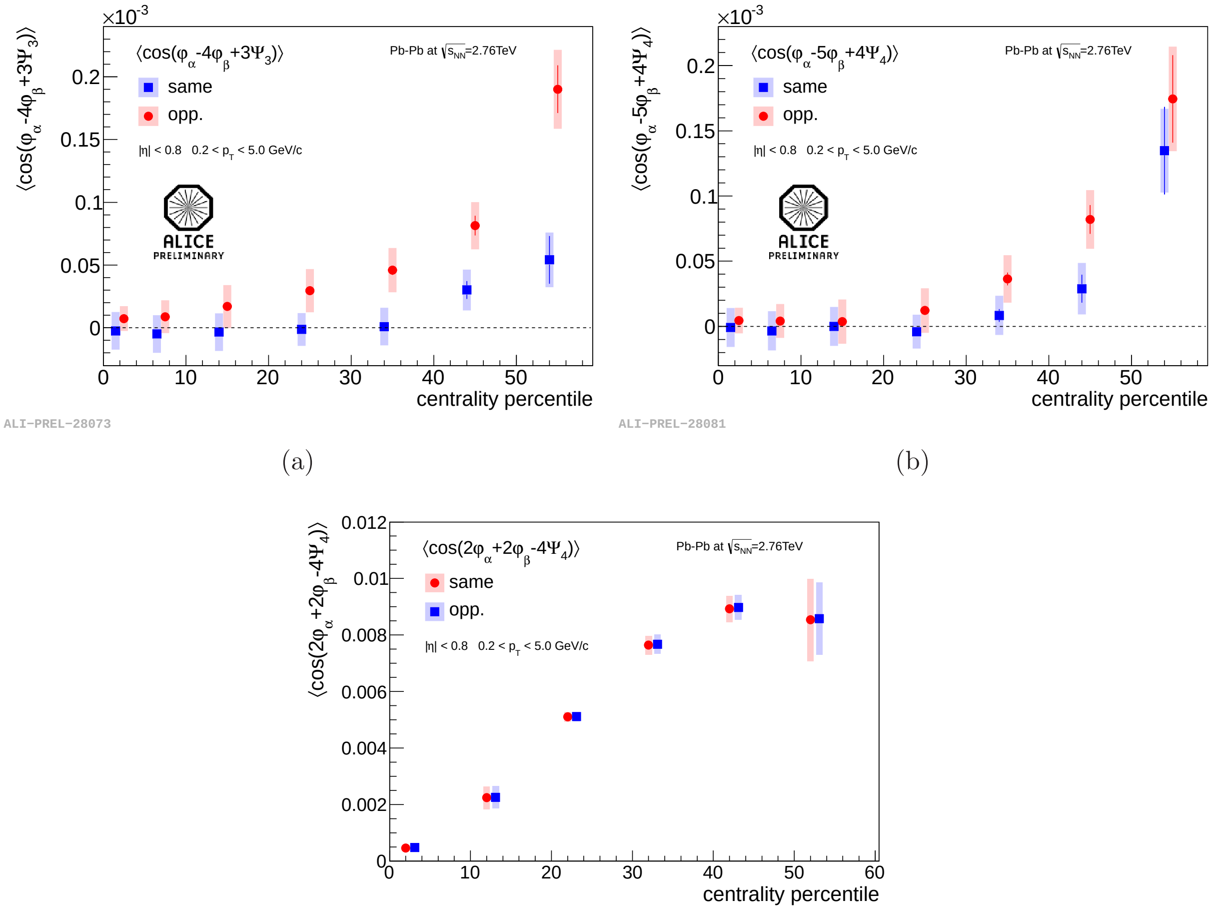

(a)

(b)

(c)

Figure 5.8: Centrality dependence of the charge dependent two particle azimuthal correlations with respect to the 3rd and 4th harmonic symmetry planes: (a) $\langle\cos(\varphi_\alpha - 4\varphi_\beta + 3\Psi_3)\rangle$ [81], (b) $\langle\cos(\varphi_\alpha - 5\varphi_\beta + 4\Psi_4)\rangle$ [81], (c) $\langle\cos(2\varphi_\alpha + 2\varphi_\beta - 4\Psi_4)\rangle$ [82].

Furthermore, the azimuthal modulations of C_1 (and C_2) with respect to the higher harmonic symmetry planes are investigated. Figure 5.8 shows the centrality dependence of the charge dependent two particle azimuthal correlations with respect to the 3rd and 4th harmonic symmetry plane angles: $\langle\cos(\varphi_\alpha - 4\varphi_\beta + 3\Psi_3)\rangle$, $\langle\cos(\varphi_\alpha - 5\varphi_\beta + 4\Psi_3)\rangle$ and $\langle\cos(2\varphi_\alpha + 2\varphi_\beta - 4\Psi_4)\rangle$ for the same and opposite charge combinations. The first two correlations $\langle\cos(\varphi_\alpha - 4\varphi_\beta + 3\Psi_3)\rangle$ and $\langle\cos(\varphi_\alpha - 5\varphi_\beta + 4\Psi_3)\rangle$ show a similar centrality and charge dependence as the correlations in Fig. 5.6 (a). The correlation $\langle\cos(2\varphi_\alpha + 2\varphi_\beta - 4\Psi_4)\rangle$ is often used to measure the 4th harmonic flow $v_{4,2}$ [97] and was also proposed in Ref. [98] to study the physics backgrounds for the CME search. Indeed, magnitudes of the both same and opposite charge correlations are rather large as expected by $\sim v_{2,\alpha}v_{2,\beta}v_{4,2}$. On the other hand, its charge dependent part is zero consistent within the statistical error even when the Pb–Pb data collected by the ALICE detectors both at 2010 and 2011 are used in the analysis of this correlation.

Figure 5.9 shows the differences between the same and opposite charge combinations for these correlations. The correlation $\Delta\langle\cos(\varphi_\alpha - 4\varphi_\beta + 3\Psi_3)\rangle$ corresponds to the 3rd azimuthal modulation of C_1 with respect to the 3rd harmonic symmetry plane and is expected to be proportional to the triangle flow v_3 in the LCC scenario. Similarly, the correlation $\Delta\langle\cos(\varphi_\alpha - 5\varphi_\beta + 4\Psi_4)\rangle$ corresponds to the 4th azimuthal modulation of C_1 with respect to the 4th harmonic symmetry plane and is expected to be proportional to the 4th harmonic flow v_4 in the LCC scenario. Combined with the results in Fig. 5.7, the charge dependent parts of the correlations with respect to the higher harmonic symmetry plane is smaller than that of the correlations with respect to the 2nd harmonic symmetry plane as expected by the the ordering of $v_2 > v_3 > v_4 \sim v_{4,2}$.

Figure 5.9 (b) shows the centrality dependence of the correlation $\Delta\langle\cos(2\varphi_\alpha + 2\varphi_\beta - 4\Psi_4)\rangle$, which corresponds to the 4th azimuthal modulation of C_2 with respect to the 4th harmonic symmetry plane. It is natural to expect the small correlation $\Delta\langle\cos(2\varphi_\alpha + 2\varphi_\beta - 4\Psi_4)\rangle$ in the LCC scenario because both the 2nd charge balance moments $C_2 = \Delta\langle\cos[2(\varphi_\alpha - \varphi_\beta)]\rangle$ in Fig. 5.5 (b) and the 4th harmonic flow v_4 are small.

A event-by-event hydrodynamic models with the LCC are mandatory for quantitative discussions, especially about the physics origin of the charge dependent azimuthal correlations with respect to the higher harmonic symmetry plane.

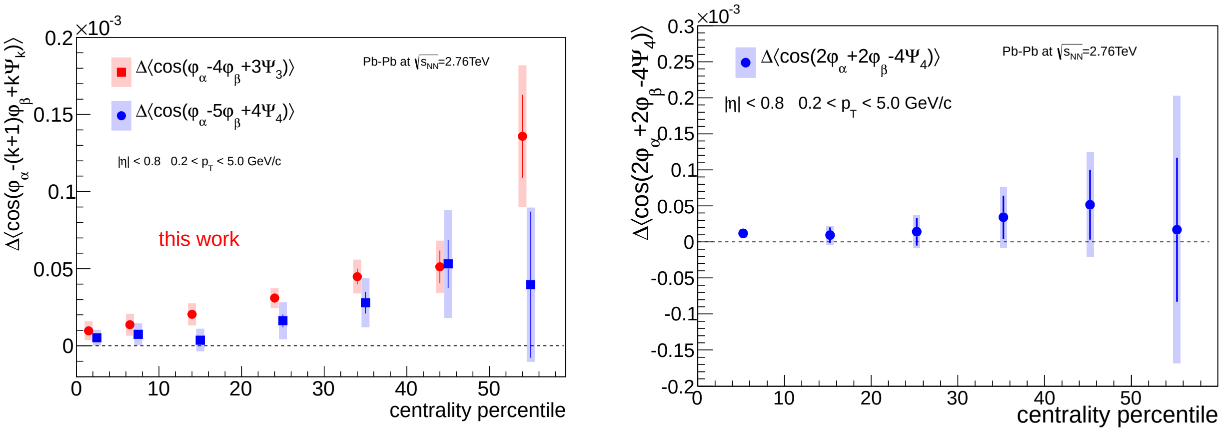

(a)

(b)

Figure 5.9: Centrality dependence of the correlation (a) $\Delta\langle\cos(\varphi_\alpha - 4\varphi_\beta + 3\Psi_3)\rangle$, $\Delta\langle\cos(\varphi_\alpha - 5\varphi_\beta + 4\Psi_4)\rangle$ and (b) $\Delta\langle\cos(2\varphi_\alpha + 2\varphi_\beta - 4\Psi_4)\rangle$ [82].

(iv) Pair differential correlations

Figure 5.10 shows the differential dependencies of the correlations $\langle\cos(\varphi_\alpha - \varphi_\beta)\rangle$, $\langle\cos(\varphi_\alpha + \varphi_\beta - 2\Psi_{RP})\rangle$ and $\langle\cos(\varphi_\alpha - 3\varphi_\beta + 2\Psi_{RP})\rangle$ on the transverse momentum difference $|p_{\mathrm{T},\alpha} - p_{\mathrm{T},\beta}|$, the average transverse momentum $(p_{\mathrm{T},\alpha} + p_{\mathrm{T},\beta})/2$ and the rapidity separation $\Delta\eta = |\eta_\alpha - \eta_\beta|$ of two charged particles for the centrality $30-40$ % events. These dependencies of the correlation $\langle\cos(\varphi_\alpha + \varphi_\beta - 2\Psi_{RP})\rangle$ are similar to the results observed by the STAR collaboration as shown in Fig. B.6. The difference between same and opposite charge correlations for these three azimuthal correlations are similarly localized within about one unit of rapidity, which is the typical hadronic width, (or may even change sign as a function of $\Delta\eta$) and extend up to the higher $|p_{\mathrm{T},\alpha} - p_{\mathrm{T},\beta}|$ and $(p_{\mathrm{T},\alpha} + p_{\mathrm{T},\beta})/2$. They increase with the increase of $(p_{\mathrm{T},\alpha} + p_{\mathrm{T},\beta})/2$, which is inconsistent to the CME expectations but roughly consistent to the LCC induced correlations because the charge balance width of larger p_{T} pairs is expected to be smaller due to the focusing effect of the boosted charge balance pairs [34]. However, as already discussed, the simple Blast Wave model do not consider the *surface emission* parts, which emits the higher p_{T} particles, the Blast Wave model can not properly used for the predictions of the differential correlations. At the moment, there are no quantitative model calculations based on the CME of the charge dependent differential correlations either.

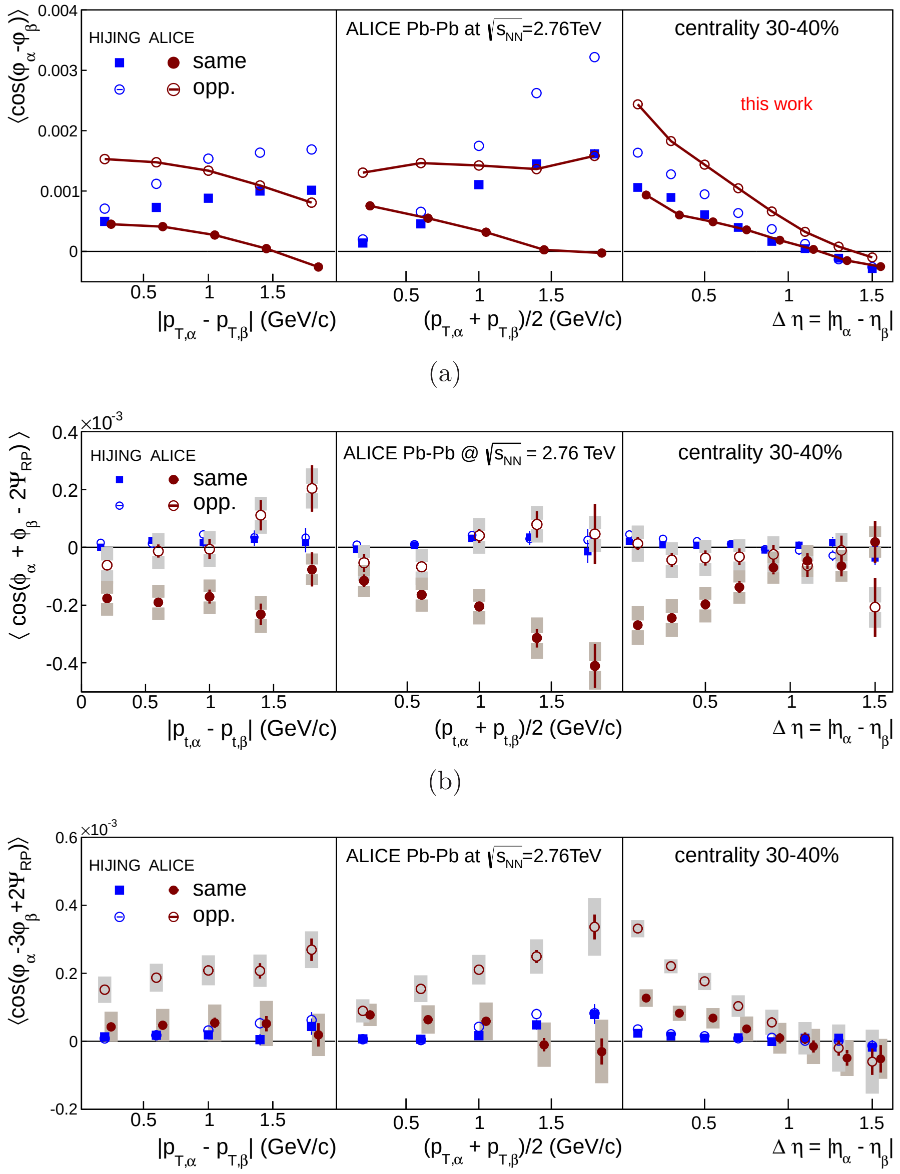

(a)

(b)

(c)

Figure 5.10: The pair differential correlation (a) $\langle \cos(\varphi_\alpha - \varphi_\beta) \rangle$, (b) $\langle \cos(\varphi_\alpha + \varphi_\beta - 2\Psi_{RP}) \rangle$ [92] and (c) $\langle \cos(\varphi_\alpha - 3\varphi_\beta + 2\Psi_{RP}) \rangle$ [81] as a function of (left) the transverse momentum difference $|p_{\mathrm{T},\alpha} - p_{\mathrm{T},\beta}|$, (center) the average transverse momentum $(p_{\mathrm{T},\alpha} + p_{\mathrm{T},\beta})/2$, (right) the rapidity separation $\Delta\eta = |\eta_\alpha - \eta_\beta|$ of the charged particle pair in comparison with the HIJING model.

As a summary of the charge dependent parts, it is found that the simple Blast Wave model incorporating with the LCC on the kinetic freeze-out surface reproduces their main features. This seems to be a strong evidence of the LCC on the kinetic freezeout surface. However, at the same time, the charge dependent correlation $\langle\cos(\varphi_\alpha + \varphi_\beta - 2\Psi_{RP})\rangle$ is consistent with the CME expectation when the LCC effects are ignored. Therefore, both in order to estimate the actual contributions on the correlation $\langle\cos(\varphi_\alpha + \varphi_\beta - 2\Psi_{RP})\rangle$ used for the CME search and study the LCC effects themselves, more precise theoretical works for the predictions of the correlations measured in this thesis are necessary. First results in this direction have been presented in [99, 100] and we expect more studies in the future.

Very importantly, we admit that the phrase “the LCC on the kinetic freeze-out surface” is somehow misleading because the hadrons and anti-hadrons are expected to be created at the hadronization time through the deconfinement phase transition from the partonic to the hadronic phase, which is later than the hadron production at $p + p$ collisions (in this sense it is called delayed hadronization), but earlier than the kinetic freeze-out. The switching from the hydrodynamic to the particle picture on the kinetic freeze-out surface is an artificial procedure but this is a simplest way to describe the collision dynamics in the hydrodynamic model. Therefore, strictly speaking, what we try to test is just the strong spatial and momentum correlations between the hadron and anti-hadrons at the kinetic freeze-out. This correlations may be generated by the elastic and inelastic scattering between hadrons during the hadronic phase. To understand what kind of microscopic mechanisms generate these correlations, the microscopic model beyond the conventional hydrodynamics is mandatory.

In this direction, the models which incorporate the hydrodynamics and the subsequent hadronic rescattering model exists [101]. In these models, the switching from the hydrodynamic to the particle picture implements at some artificial temperature T_{sw}, which is typically chosen to just below the deconfinement phase transition temperature ~ 160 MeV. In practice, T_{sw} is tuned so as to reproduce the particle ratio. After switching the hadronic particle picture, the hadronic rescatterings which include both the elastic and inelastic scatterings between hadrons are taken into considerations. There are mainly three problems in these hydro models with the hadronic rescattering. Firstly, there are no such models incorporating with the LCC at the switching temperature for the moment. But these developments will be rather easily conducted sooner or later. Secondly, in the procedure of the switching, an ideal hadron gas approximation is used to decide the momentum and chemical compositions, which are modified through the hadronic rescattering afterburners. This approximation is still questionable. Lastly, it is still questionable whether or not the particle picture is valid just after the hadronization. It is a very principal problem.

Various models which are no based on the hydrodynamic picture also exist to describe the dynamics of the relativistic heavy-ion collisions and they employ very different charge production mechanisms. In event generators like HIJING [45] and partonic/hadronic cascades such as UrQMD [46] and AMPT [70, 99], the charges are created early by the fragmentation of gluonic strings, which was originally tuned for the hadron production in p+p, e+e- collisions. In the partonic/hadronic cascades such as UrQMD and AMPT, the charge production occurs early like HIJING, but the subsequent interactions contribute on the correlations between the finally produced hardons and anti-hadrons. Therefore, it is also interesting to investigate which microscopic mechanisms, charge creations or the subsequent partonic/hadronic rescatterings, contribute on the finally observed LCC induced correlations using these cascading models.

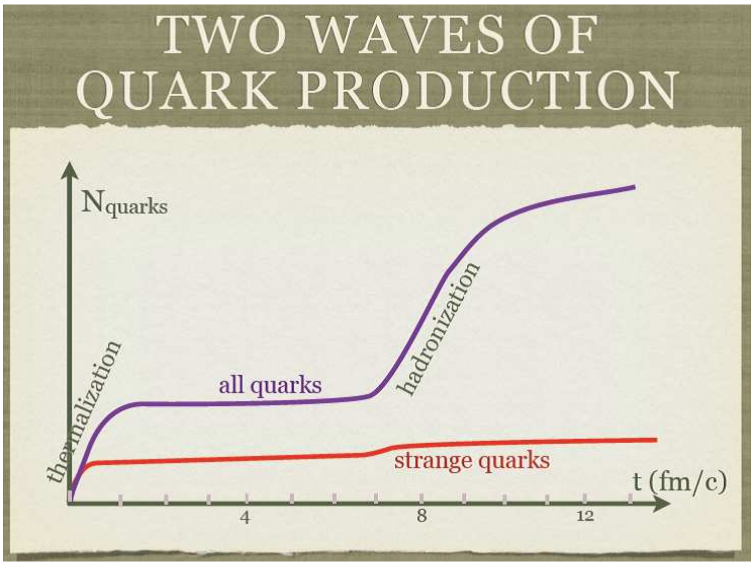

Figure 5.11: The two waves of quark production during system evolution [102]

If correlations generated during the hadronic rescattering are not enough to explain the physics origin of the LCC on the kinetic freeze-out surface, the observed charge parts may have some insight for the microscopic mechanism of the phase transition. It is usually assumed that charge production happens at two different stages of the evolution. The first wave of production is expected to occur during the first fm/c of the collision by initial hard scatterings and during thermalization process to form the quark-gluon plasma phase. After a collective expansion of the system, a second stage of charge production is expected to occur during the transition from the deconfined QGP phase to hadronic matter around $5-10$ fm/c - possible late quark productions as shown in Fig. 5.11. The hadronization with the late quark(and anti-quark) production naturally generates the strong correlation between hadrons and anti-hadrons.

5.2 Charge independent azimuthal correlations associated with the directed flow v_1

In this section, the physics origins of the charge independent multi-particle azimuthal correlations are discussed. As already discussed at the previous section, there is a non-zero charge independent part of the correlation $\langle\cos(\varphi_\alpha+\varphi_\beta-2\Psi_2)\rangle$, which can be regarded as a signature of the quenching effect on the back-to-back opposite charge correlation by the interactions with the QGP medium and parity-odd bubbles from the CME view point. However, it was pointed out that a non-zero charge independent part of this correlation can be explained by the p_T conservation effect or the joint correlation between the directed flow v_1 and the elliptic flow v_2 as shown in Fig. 2.9 (b) [51, 13]. Indeed, nonzero charge independent correlations were generally observed as shown in Fig. 5.6, Fig. 5.8 and Fig. 5.10. It was suggested in [13, 52] that these charge independent correlations can be useful tools to study the directed flow v_1 and the joint correlations between v_1 and the higher harmonic flow, which may originate from the initial density fluctuations and the subsequent hydrodynamic evolution of the system. Naive expectations are provided through the following factorizations as already introduced in Sec.2.3.

$$\langle\cos(\varphi_\alpha-\varphi_\beta)\rangle \sim v_{1,\alpha}\times v_{1,\beta}, \tag{5.10}$$

$$\begin{aligned}\langle\cos[\varphi_\alpha-(m+1)\varphi_\beta+m\Psi_2]\rangle &\sim v_{1,\alpha}\times v_{|m+1|,\beta}\\ &\times \langle\cos[\Psi_1-(m+1)\Psi_{|m+1|}+m\Psi_2]\rangle,\end{aligned} \tag{5.11}$$

where Ψ_1 and $\Psi_{|m+1|}$ denote azimuthal angles of the first and $|m+1|$-th harmonic collision symmetry planes, respectively.

We first estimate the p_T conservation effects on the multi-particle correlations associated with the directed flow v_1 by the semi-analytic way in Sec.5.2.1. It is found that this effect is expected to be suppressed on the three and four-particle correlations compared with on the two-particle correlations. The estimations in this thesis are more accurate than that in Ref. [51]. Then, the possible signatures of the directed flow v_1 in the two-particle correlations and the mixed harmonic correlations, e.g. $\langle\cos(\varphi_\alpha-3\varphi_\beta+2\Psi_2)\rangle$ are studied by comparing with the HIJING model, the AMPT model and the fully (3+1) dimensional ideal hydrodynamic simulations, which was developed in Ref. [101] using the state-of-the-art equation of state from lattice QCD and subsequent hadronic cascadings in the late stage.

As usual in the hydrodynamic simulations, the hydro model used here employs the Cooper-Frye formula to switch the fluid picture to the particle picture. This results in the violation of the global and local momentum conservation and the multi-particle correlations calculated by this model may not reflect the p_T conservation effects correctly. Another problem by the violation of the momentum conservation in this hydro model appears in the non-zero net p_T of the whole system. The simple remedy developed in Ref. [25] is used here and it is confirmed that the results do not change significantly.

A MultiPhase Transport (AMPT) model is a hybrid model with the initial distribution of particles (soft strings and mini-jet partons) generated by the HIJING model of the version 1.383, the partonic cascadings by the Zhangs Parton Cascade (ZPC) model and the final hadronic rescattering including the resonance decays by the ART model [70]. In the default version of the AMPT, the mini-jet partons are recombined with their parent strings when they stop cascade interactions, and the resulting strings are converted to hadrons using the Lund string fragmentation model. In the *string melting* configuration, soft strings produced by the HIJING are melting into partons since we assume the hot QGP matter. After the parton cascadings, the partons combine nearest partons into hadrons, i.e. a quark coalescence model. Here we use the AMPT model with the *string melting* configuration with various parameters tuned according to the measured charged particle distribution and elliptic flow at the LHC energy. The authors of Ref. [70] argued that a parton scattering cross section is one of the important model parameter to reproduce the elliptic flow. At the LHC energy, the AMPT model describes the behavior of both the hard components such as the jet-quenching and the soft components such as the collective flow. Note that this model can not use for the charge dependent correlations since it violates the LCC at the hadronic stage.

Results reported in Sec.5.2.2 can be well explained by the directed flow v_1 and the hydro model works very well. However, the other correlations reported in Sec.5.2.3 are difficult to understand only in terms of the flow effects for the moment. Instead, the remarkable agreements with the AMPT model are found, which indicates that the interplay between the flowing matter and jets is generally important for the understanding of the mixed harmonic multi-particle azimuthal correlations.

5.2.1 Transverse momentum conservation effect

In Ref. [51], the p_{T} conservation effect on the p_{T} weighted azimuthal correlation $\langle p_{\mathrm{T},\alpha} p_{\mathrm{T},\beta} \cos(\varphi_\alpha + \varphi_\beta - 2\Psi_2)\rangle$ was discussed. Here we will discuss more sophisticated way.

According to the discussion in Ref. [22, 23, 103, 104], the two particle distribution can be factorized into the one particle distributions with the correction factor for the global p_{T} conservation induced correlations.

$$\frac{dN_{pairs,\alpha\beta}}{d^2\mathbf{p}_{\mathrm{T},\alpha} d^2\mathbf{p}_{\mathrm{T},\beta}} = \frac{dN}{d^2\mathbf{p}_{\mathrm{T},\alpha}} \frac{dN}{d^2\mathbf{p}_{\mathrm{T},\beta}} \Big(1 - 2\frac{\mathbf{p}_{\mathrm{T},\alpha} \cdot \mathbf{p}_{\mathrm{T},\beta}}{K}\Big), \tag{5.12}$$

where $K = \sum p_{\mathrm{T}}^2$ and is $O(10^4) \sim O(10^5)$ and this sum is over all particles in the events. From this equation, Eq. (2.15) can be derived. In principal, the p_{T} conservation effect can be derived not only the correlation $\langle \cos(\varphi_\alpha - \varphi_\beta)\rangle$ but also all the other mixed harmonic azimuthal correlations.

Following D. Teaney and L. Yan in Ref. [13] we will approximate the two particle correlation with the disconnected component. The yield of particle type α (this label denotes $p_{\mathrm{T},\alpha}$ bins) for a fixed Glauber configuration in a single event is

$$\begin{aligned} \frac{dN_\alpha}{d\varphi_\alpha} = \frac{N_\alpha}{2\pi}\Big[1 &+ 2\frac{v_{1,\alpha}}{\epsilon_1}\epsilon_1 \mathrm{cos}(\varphi_\alpha - \Psi_1) \\ &+ 2\frac{v_{2,\alpha}}{\epsilon_2}\epsilon_2 \mathrm{cos}(2\varphi_\alpha - 2\Psi_2) \\ &+ 2\frac{v_{3,\alpha}}{\epsilon_3}\epsilon_3 \mathrm{cos}(3\varphi_\alpha - 3\Psi_3)\Big], \end{aligned} \tag{5.13}$$

where we have assumed that the response is linearly proportional to the deformation. Then the two particle correlation function with respect to the 2nd harmonic symmetry plane with the consideration of the global p_{T} conservation effects is approximated as

$$\begin{aligned} \Big\langle\Big\langle \frac{dN_{pairs,\alpha\beta}}{d\varphi_\alpha d\varphi_\beta} \Big\rangle\Big\rangle_{\Psi_2} &\sim \Big\langle\Big\langle \frac{dN}{d\varphi_\alpha}\frac{dN}{d\varphi_\beta}\Big(1 - 2\frac{p_{\mathrm{T},\alpha}p_{\mathrm{T},\beta}\mathrm{cos}(\varphi_\alpha - \varphi_\beta)}{K}\Big)\Big\rangle\Big\rangle_{\Psi_2} \\ &\sim \frac{N_\alpha N_\beta}{(2\pi)^2}\Big[1 + \sum_n 2\Big(\frac{v_{n\alpha}v_{n\beta}}{\epsilon_n^2}\Big)\langle\langle\epsilon_n^2\rangle\rangle \mathrm{cos}(n\varphi_\alpha - n\varphi_\beta) \\ &+ 2\frac{v_{2\alpha}}{\epsilon_2}\langle\langle\epsilon_2\rangle\rangle \mathrm{cos}(2\varphi_\alpha - 2\Psi_2) \\ &+ 2\frac{v_{2\alpha}v_{2\beta}}{\epsilon_2^2}\langle\langle\epsilon_2^2\rangle\rangle \mathrm{cos}(2\varphi_\alpha + 2\varphi_\beta - 4\Psi_2) \\ &+ 2\frac{v_{1\alpha}v_{1\beta}}{\epsilon_1^2}\langle\langle\epsilon_1^2 \mathrm{cos}(2\Psi_1 - 2\Psi_2)\rangle\rangle \mathrm{cos}(\varphi_\alpha + \varphi_\beta - 2\Psi_2) \\ &+ 2\frac{v_{1\alpha}v_{3\beta}}{\epsilon_1\epsilon_3}\langle\langle\epsilon_1\epsilon_3 \mathrm{cos}(\Psi_1 - 3\Psi_3 + 2\Psi_2)\rangle\rangle \mathrm{cos}(\varphi_\alpha - 3\varphi_\beta + 2\Psi_2) \\ &+ \alpha \leftrightarrow \beta\Big] \times \Big[1 - 2\frac{p_{\mathrm{T},\alpha}p_{\mathrm{T},\beta}}{K}\mathrm{cos}(\varphi_\alpha - \varphi_\beta)\Big], \end{aligned} \tag{5.14}$$

where double brackets $\langle\langle\ \rangle\rangle_{\Psi_2}$ denotes the average over glauber configurations at fixed N_{part} and fixed Ψ_2 and double brackets $\langle\langle\ \rangle\rangle$ denotes the average over glauber configurations at fixed N_{part}. The observables $\langle\cos(\varphi_\alpha+\varphi_\beta-2\Psi_2)\rangle$ can be calculated by

$$\begin{aligned}
\langle\cos(\varphi_\alpha+\varphi_\beta-2\Psi_2)\rangle &= \frac{1}{2\pi}\int d\Psi_2 d\varphi_\alpha d\varphi_\beta dp_{\mathrm{T},\alpha}dp_{\mathrm{T},\beta}\frac{\cos(\varphi_\alpha+\varphi_\beta-2\Psi_2)}{N_\alpha N_\beta}\Big\langle\Big\langle\frac{dN_{pairs,\alpha\beta}}{d\varphi_\alpha d\varphi_\beta}\Big\rangle\Big\rangle_{\Psi_2} \\
&= \int dp_{\mathrm{T},\alpha}dp_{\mathrm{T},\beta}\frac{v_{1\alpha}v_{1\beta}}{\epsilon_1^2}\langle\langle\epsilon_1^2\cos(2\Psi_1-2\Psi_2)\rangle\rangle \\
&- \frac{2}{K(2\pi)^3}\int dp_{\mathrm{T},\alpha}dp_{\mathrm{T},\beta}p_{\mathrm{T},\alpha}p_{\mathrm{T},\beta}2\frac{v_{2,\beta}}{\epsilon_2}\langle\langle\epsilon_2\rangle\rangle\times \\
&\int d\Psi_2 d\varphi_\alpha d\varphi_\beta\cos(\varphi_\alpha+\varphi_\beta-2\Psi_2)\times\cos(2\varphi_\beta-2\Psi_2)\times\cos(\varphi_\alpha-\varphi_\beta) \\
&- \frac{2}{K(2\pi)^3}\int dp_{\mathrm{T},\alpha}dp_{\mathrm{T},\beta}p_{\mathrm{T},\alpha}p_{\mathrm{T},\beta}2\frac{v_{2,\alpha}}{\epsilon_2}\langle\langle\epsilon_2\rangle\rangle\times \\
&\int d\Psi_2 d\varphi_\alpha d\varphi_\beta\cos(\varphi_\alpha+\varphi_\beta-2\Psi_2)\times\cos(2\varphi_\alpha-2\Psi_2)\times\cos(\varphi_\alpha-\varphi_\beta) \\
&= \int dp_{\mathrm{T},\alpha}dp_{\mathrm{T},\beta}\frac{v_{1\alpha}v_{1\beta}}{\epsilon_1^2}\langle\langle\epsilon_1^2\cos(2\Psi_1-2\Psi_2)\rangle\rangle \\
&- \frac{1}{K}\int dp_{\mathrm{T},\alpha}dp_{\mathrm{T},\beta}p_{\mathrm{T},\alpha}p_{\mathrm{T},\beta}(v_{2,\alpha}+v_{2,\beta}). \qquad (5.15)
\end{aligned}$$

A first term in the last line represents the contribution originated from the spatial correlation of the initial density profile, which may survive (or be altered) through the evolution of the system. A second term in the last line shows the p_{T} conservation effect on the azimuthal correlations, which corresponds to the correction term derived in Ref. [51]. The p_{T} conservation also affects on the correlation $\langle\cos(\varphi_\alpha-3\varphi_\beta+2\Psi_2)\rangle$ as a same way. By this estimation, it was found that the p_{T} conservation effect can be significant in magnitude $O(10^{-4}\sim10^{-3})$ compared with the magnitude of the observed signals.

However, since we do not know the reaction plane angle, the correlations $\langle\cos(\varphi_\alpha+\varphi_\beta-2\Psi_2)\rangle$ and $\langle\cos(\varphi_\alpha-3\varphi_\beta+2\Psi_2)\rangle$ are experimentally estimated by three particle correlations through the following factorization,

$$\langle\cos(\varphi_\alpha+\varphi_\beta-2\Psi_2)\rangle \sim \frac{\langle\cos(\varphi_\alpha+\varphi_\beta-2\varphi_\gamma)\rangle}{v_{2,\gamma}}, \qquad (5.16)$$

$$\langle\cos(\varphi_\alpha-3\varphi_\beta+2\Psi_2)\rangle \sim \frac{\langle\cos(\varphi_\alpha-3\varphi_\beta+2\varphi_\gamma)\rangle}{v_{2,\gamma}}. \qquad (5.17)$$

Therefore, we need to estimate the p_{T} conservation effects not on two particle correlations with respect to the reaction plane but on the three particle correlations.

Again according to the discussion in Ref. [22, 23, 103, 104], the three particle distribution can be factorized into the one particle distributions with the correction factor for the global p_{T} conservation induced correlations.

$$\begin{aligned}
\frac{dN_{\alpha\beta\gamma}}{d^2\mathbf{p}_{\mathrm{T},\alpha}d^2\mathbf{p}_{\mathrm{T},\beta}d^2\mathbf{p}_{\mathrm{T},\gamma}} &= \frac{dN}{d^2\mathbf{p}_{\mathrm{T},\alpha}}\frac{dN}{d^2\mathbf{p}_{\mathrm{T},\beta}}\frac{dN}{d^2\mathbf{p}_{\mathrm{T},\gamma}} \\
&\times \Big[1-\frac{2}{M\cdot K}(\mathbf{p}_{\mathrm{T},\alpha}\cdot\mathbf{p}_{\mathrm{T},\beta}+\mathbf{p}_{\mathrm{T},\alpha}\cdot\mathbf{p}_{\mathrm{T},\gamma}+\mathbf{p}_{\mathrm{T},\beta}\cdot\mathbf{p}_{\mathrm{T},\gamma}) \\
&+ \frac{4}{K^2}\Big((\mathbf{p}_{\mathrm{T},\alpha}\cdot\mathbf{p}_{\mathrm{T},\beta})(\mathbf{p}_{\mathrm{T},\alpha}\cdot\mathbf{p}_{\mathrm{T},\gamma}) \\
&+ (\mathbf{p}_{\mathrm{T},\alpha}\cdot\mathbf{p}_{\mathrm{T},\beta})(\mathbf{p}_{\mathrm{T},\beta}\cdot\mathbf{p}_{\mathrm{T},\gamma}) \\
&+ (\mathbf{p}_{\mathrm{T},\alpha}\cdot\mathbf{p}_{\mathrm{T},\gamma})(\mathbf{p}_{\mathrm{T},\beta}\cdot\mathbf{p}_{\mathrm{T},\gamma})\Big)\Big],
\end{aligned} \tag{5.18}$$

where M denotes the total number of generated particles in the collisions. Then, inserting Eq. (5,13) in Eq. (5.18), we can obtain three particle azimuthal distributions written as

$$\begin{aligned}
\Big\langle\Big\langle\frac{dN_{\alpha\beta\gamma}}{d\varphi_\alpha d\varphi_\beta d\varphi_\gamma}\Big\rangle\Big\rangle &\sim \frac{N_\alpha N_\beta N_\gamma}{(2\pi)^3}\Big[1+\sum_n 2\Big(\frac{v_{n\alpha}v_{n\beta}}{\epsilon_n^2}\Big)\langle\langle\epsilon_n^2\rangle\rangle\cos(n\varphi_\alpha-n\varphi_\beta) \\
&+ \ldots \\
&+ 2\frac{v_{1\alpha}v_{1\beta}v_{2\gamma}}{\epsilon_1^2\epsilon_2}\langle\langle\epsilon_1^2\epsilon_2\cos(2\Psi_1-2\Psi_2)\rangle\rangle\cos(\varphi_\alpha+\varphi_\beta-2\varphi_\gamma) \\
&+ 2\frac{v_{1\alpha}v_{3\beta}v_{2\gamma}}{\epsilon_1\epsilon_3\epsilon_2}\langle\langle\epsilon_1\epsilon_3\epsilon_2\cos(\Psi_1-3\Psi_3+2\Psi_2)\rangle\rangle\cos(\varphi_\alpha-3\varphi_\beta+2\varphi_\gamma) \\
&+ \cdots+\alpha\leftrightarrow\beta\leftrightarrow\gamma\Big] \\
&\times \Big[1-\frac{2p_{\mathrm{T},\alpha}p_{\mathrm{T},\beta}}{M\cdot K}\cos(\varphi_\alpha-\varphi_\beta)-\frac{2p_{\mathrm{T},\alpha}p_{\mathrm{T},\gamma}}{M\cdot K}\cos(\varphi_\alpha-\varphi_\gamma) \\
&- \frac{2p_{\mathrm{T},\beta}p_{\mathrm{T},\gamma}}{M\cdot K}\cos(\varphi_\beta-\varphi_\gamma) \\
&+ \frac{4p_{\mathrm{T},\alpha}^2p_{\mathrm{T},\beta}p_{\mathrm{T},\gamma}}{K^2}\cos(\varphi_\alpha-\varphi_\beta)\cos(\varphi_\alpha-\varphi_\gamma) \\
&+ \frac{4p_{\mathrm{T},\alpha}p_{\mathrm{T},\beta}^2p_{\mathrm{T},\gamma}}{K^2}\cos(\varphi_\alpha-\varphi_\beta)\cos(\varphi_\beta-\varphi_\gamma) \\
&+ \frac{4p_{\mathrm{T},\alpha}p_{\mathrm{T},\beta}p_{\mathrm{T},\gamma}^2}{K^2}\cos(\varphi_\alpha-\varphi_\gamma)\cos(\varphi_\beta-\varphi_\gamma)\Big].
\end{aligned} \tag{5.19}$$

Now we can calculate the correlations $\langle\cos(\varphi_\alpha+\varphi_\beta-2\Psi_2)\rangle$ and $\langle\cos(\varphi_\alpha-3\varphi_\beta+2\Psi_2)\rangle$

by using Eq. (5.16) and Eq. (5.19).

$$
\begin{aligned}
&\langle\cos(\varphi_\alpha+\varphi_\beta-2\Psi_2)\rangle=\int d\varphi_\alpha d\varphi_\beta d\varphi_\gamma dp_{\mathrm{T},\alpha}dp_{\mathrm{T},\beta}dp_{\mathrm{T},\gamma}\frac{\cos(\varphi_\alpha+\varphi_\beta-2\varphi_\gamma)}{v_{2,\gamma}N_\alpha N_\beta N_\gamma}\Big\langle\Big\langle\frac{dN_{\alpha\beta\gamma}}{d\varphi_\alpha d\varphi_\beta d\varphi_\gamma}\Big\rangle\Big\rangle\\
&=\int dp_{\mathrm{T},\alpha}dp_{\mathrm{T},\beta}dp_{\mathrm{T},\gamma}\frac{v_{1\alpha}v_{1\beta}}{\epsilon_1^2\epsilon_2}\langle\langle\epsilon_1^2\epsilon_2\cos(2\Psi_1-2\Psi_2)\rangle\rangle\\
&-\frac{1}{M\cdot K}\int dp_{\mathrm{T},\alpha}dp_{\mathrm{T},\beta}dp_{\mathrm{T},\gamma}p_{\mathrm{T},\alpha}p_{\mathrm{T},\beta}(v_{2,\alpha}+v_{2,\beta})\\
&-\frac{1}{M\cdot K}\int dp_{\mathrm{T},\alpha}dp_{\mathrm{T},\beta}dp_{\mathrm{T},\gamma}\frac{p_{\mathrm{T},\alpha}p_{\mathrm{T},\gamma}v_{1,\beta}v_{1,\gamma}+p_{\mathrm{T},\beta}p_{\mathrm{T},\gamma}v_{1,\alpha}v_{1,\gamma}}{v_{2,\gamma}}\\
&+\frac{1}{K^2}\int dp_{\mathrm{T},\alpha}dp_{\mathrm{T},\beta}dp_{\mathrm{T},\gamma}\frac{p_{\mathrm{T},\alpha}p_{\mathrm{T},\beta}p_{\mathrm{T},\gamma}^2}{v_{2,\gamma}}\\
&+\frac{1}{K^2}\int dp_{\mathrm{T},\alpha}dp_{\mathrm{T},\beta}dp_{\mathrm{T},\gamma}p_{\mathrm{T},\alpha}p_{\mathrm{T},\beta}p_{\mathrm{T},\gamma}(p_{\mathrm{T},\alpha}v_{2,\beta}+p_{\mathrm{T},\beta}v_{2,\alpha})\\
&+\frac{1}{K^2}\int dp_{\mathrm{T},\alpha}dp_{\mathrm{T},\beta}dp_{\mathrm{T},\gamma}\frac{p_{\mathrm{T},\alpha}p_{\mathrm{T},\beta}p_{\mathrm{T},\gamma}}{v_{2,\gamma}}\\
&\qquad\Big(p_{\mathrm{T},\alpha}v_{1,\alpha}v_{1,\gamma}+p_{\mathrm{T},\alpha}v_{3,\alpha}v_{3,\gamma}+p_{\mathrm{T},\beta}v_{1,\beta}v_{1,\gamma}+p_{\mathrm{T},\beta}v_{3,\beta}v_{3,\gamma}\Big).
\end{aligned}
\tag{5.20}
$$

As a same way, we can calculate the p_T conservation effects on the correlation $\langle\cos(\varphi_\alpha-3\varphi_\beta+2\Psi_2)\rangle$ by using Eq. (5.17) and Eq. (5.19).

$$
\begin{aligned}
&\langle\cos(\varphi_\alpha-3\varphi_\beta+2\Psi_2)\rangle=\int d\varphi_\alpha d\varphi_\beta d\varphi_\gamma dp_{\mathrm{T},\alpha}dp_{\mathrm{T},\beta}dp_{\mathrm{T},\gamma}\frac{\cos(\varphi_\alpha-3\varphi_\beta+2\varphi_\gamma)}{v_{2,\gamma}N_\alpha N_\beta N_\gamma}\Big\langle\Big\langle\frac{dN_{\alpha\beta\gamma}}{d\varphi_\alpha d\varphi_\beta d\varphi_\gamma}\Big\rangle\Big\rangle\\
&=\int dp_{\mathrm{T},\alpha}dp_{\mathrm{T},\beta}dp_{\mathrm{T},\gamma}\frac{v_{1\alpha}v_{3\beta}}{\epsilon_1\epsilon_3\epsilon_2}\langle\langle\epsilon_1\epsilon_3\epsilon_2\cos(\Psi_1-3\Psi_3+2\Psi_2)\rangle\rangle\\
&-\frac{1}{M\cdot K}\int dp_{\mathrm{T},\alpha}dp_{\mathrm{T},\beta}dp_{\mathrm{T},\gamma}p_{\mathrm{T},\alpha}(p_{\mathrm{T},\beta}v_{2,\beta}+p_{\mathrm{T},\gamma}\frac{v_{3,\beta}v_{3,\gamma}}{v_{2,\gamma}})\\
&+\frac{1}{K^2}\int dp_{\mathrm{T},\alpha}dp_{\mathrm{T},\beta}dp_{\mathrm{T},\gamma}p_{\mathrm{T},\alpha}p_{\mathrm{T},\beta}p_{\mathrm{T},\gamma}^2(v_{2,\beta}+\frac{v_{2,\alpha}v_{2,\beta}}{v_{2,\gamma}})\\
&+\frac{1}{K^2}\int dp_{\mathrm{T},\alpha}dp_{\mathrm{T},\beta}dp_{\mathrm{T},\gamma}\frac{p_{\mathrm{T},\alpha}p_{\mathrm{T},\beta}^2p_{\mathrm{T},\gamma}}{v_{2,\gamma}}\\
&\qquad\Big(v_{1,\alpha}v_{1,\beta}+v_{3,\alpha}v_{3,\beta}+v_{1,\beta}v_{1,\gamma}+v_{3,\beta}v_{3,\gamma}\Big)\\
&+\frac{1}{K^2}\int dp_{\mathrm{T},\alpha}dp_{\mathrm{T},\beta}dp_{\mathrm{T},\gamma}p_{\mathrm{T},\alpha}p_{\mathrm{T},\beta}p_{\mathrm{T},\gamma}^2\frac{v_{4,\beta}v_{4,\gamma}}{v_{2,\gamma}}.
\end{aligned}
\tag{5.21}
$$

With these estimation, the p_T conservation effect on the correlation $\langle\cos(\varphi_\alpha-3\varphi_\beta+2\Psi_2)\rangle$ differs from that on $\langle\cos(\varphi_\alpha+\varphi_\beta-2\Psi_2)\rangle$. Terms with factor $1/(M\cdot K)$ are suppressed by factor $M\sim O(10^4)$ in comparison with p_T conservation effect on the two-particle correlations. Terms with factor $1/K^2$ are suppressed by factor $p_\mathrm{T}^2/(Kv_2^2)\sim O(10^{-3})$. Therefore, the p_T conservation effects on the multi-particle correlations are in general suppressed than that on the two-particle correlations and it is found that the global p_{T} conservation effect can not explain the non-zero charge independent parts of the experimentally measured correlation $\langle\cos(\varphi_\alpha+\varphi_\beta-2\Psi_2)\rangle$ and $\langle\cos(\varphi_\alpha-3\varphi_\beta+2\Psi_2)\rangle$.

In reality, we can expect that p_{T} conserves somehow locally since the QGP is not any longer dilute system but dense matter. If we use particles only at mid-rapidity regions and sum of the p_{T} in this subsystem is considered to be conserved, a factor K can become smaller and the p_{T} conservation effect can be more significant. Above discussion can be still hold if the number of particles in this subsystem is large enough.

5.2.2 Directed flow v_1 signatures

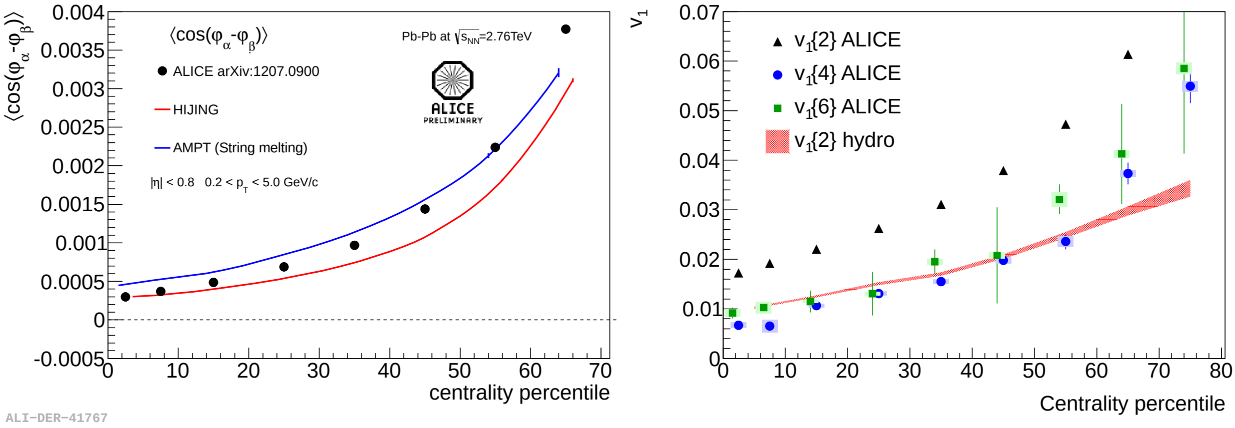

(a)

(b)

Figure 5.12: (a) The centrality dependence of the correlation $\langle\cos(\varphi_\alpha-\varphi_\beta)\rangle$ measured by the ALICE in comparison with AMPT and HIJING calculations [45, 70, 106]. (b) The centrality dependence of the integrated correlation $v_1\{2\}\equiv\sqrt{\langle\cos(\varphi_\alpha-\varphi_\beta)\rangle}$ compared with the experimental results of $v_1\{2\}$, $v_1\{4\}$ and $v_1\{6\}$ by the ALICE collaboration [101, 107].

Figure 5.12 (a) shows the integrated correlation $\langle\cos(\varphi_\alpha-\varphi_\beta)\rangle$ with the AMPT and HIJING model calculations. Here no eta-gap between two particles is required. The HIJING model reproduces most of the observed correlation, which indicates that the dominant physics origin of the integrated correlation $\langle\cos(\varphi_\alpha-\varphi_\beta)\rangle$ without the eta-gaps is a two-particle non-flow effect. On the other hand, $v_1\{2\}\equiv\sqrt{\langle\cos(\varphi_\alpha-\varphi_\beta)\rangle}$ calculated by the hydro model is smaller than measured $v_1\{2\}$ by factor two or more and roughly agrees with $v_1\{4\}$ and $v_1\{6\}$ measured by the ALICE collaboration [101, 107]. Since the statistics of the hydro model data is not enough to calculate the four-particle cumulant, here we compared $v_1\{2\}$ of the hydro model. However, $v_1\{2\}$ of the hydro model can be regarded as the directed flow because the hydro model does not include non-flow effect from jets and $\Delta\eta$ dependence of the correlation $\langle\cos(\varphi_\alpha-\varphi_\beta)\rangle$ of the hydro model is found to be very small as shown in Fig. 5.17 (a). Note that the measured $v_1\{2,4,6\}$ is by definition a positive real number or an imaginary number. If the result is imaginary number, the flow interpretation is completely invalid. Then the agreements between the hydro $v_1\{2\}$, the experimental $v_1\{4\}$ and $v_1\{6\}$ may indicate the directed flow v_1 signatures exists in reality.

Now we notice that a large eta-gap between two particles is important to remove the non-flow effect on the experimental measurement of the directed flow when the two-particle cumulant method is used. We employ the same method used in Ref. [105, 26] so called the Global Fit method (GF) to measure the p_{T} differential directed flow in the hydro model. In the first step of this method, $N \times N$ symmetric matrix consisted of the two-particle correlation $V_{1\Delta}$ as a function of trigger particle p_{T} and associated particle p_{T} bin is calculated,where N denotes the number of p_{T} bins. The requirement $|\eta_t - \eta_a| > 0.8$ between trigger and associated particle is used. Indeed, the ALICE collaboration observed the strong dependence on the eta-gap of the $V_{1\Delta}$ and this dependence converges at $|\Delta\eta| \sim 0.8$. Then the N values of $v_1(p_{\mathrm{T}})$ are extracted by simultaneously fitting this matrix with the right-hand side of Eq. (2.15). Here, we ignore the correction term from p_{T} conservation effect. Figure 5.13 shows the $V_{1\Delta}$ results and the fitting results in comparison with the experimental results by the ALICE collaboration [105]. The fitting works rather well in the low p_{T} region, but the simple factorization seems to be broken in the high p_{T} region both with measured data and the hydro model. The directed flow v_1 as a function of p_{T} is somehow extracted by this method and the measured data by the ALICE collaboration agrees well with the hydro model as shown in Fig. 5.14. A sign of v_1 at the low p_{T} region is opposite to that in the high p_{T} region and a crossing-point with $v_1 \sim 0$ at around $p_{\mathrm{T}} =1.5$ GeV/c exists. This p_{T} dependence of the signal is consistent with the expectations of the directed flow picture.

Figure 5.15 (a) shows the p_{T} differential correlation $\langle\cos(\varphi_\alpha - 3\varphi_\beta + 2\Psi_2)\rangle$ without any eta-gaps measured by the ALICE collaboration for each centrality events [107]. The three-particle cumlant method is used. Contrary to the naive prediction shown in Fig. 2.9 (a), a sign of the correlation does not change at any p_{T} region. Interestingly, Figure 5.15 (b) and (c) show the hydro model calculation and remarkable similarities to the measured correlation are found although the physics origin of this p_{T} dependence is not yet clear. Observed signals in the low p_{T} region might be interpreted as a signature of the directed flow.

In Ref. [26], it was pointed out that the directed flow is rather insensitive to the shear viscosity. But, these results may be sensitive to the initial state model, the EoS of the matter and so on.

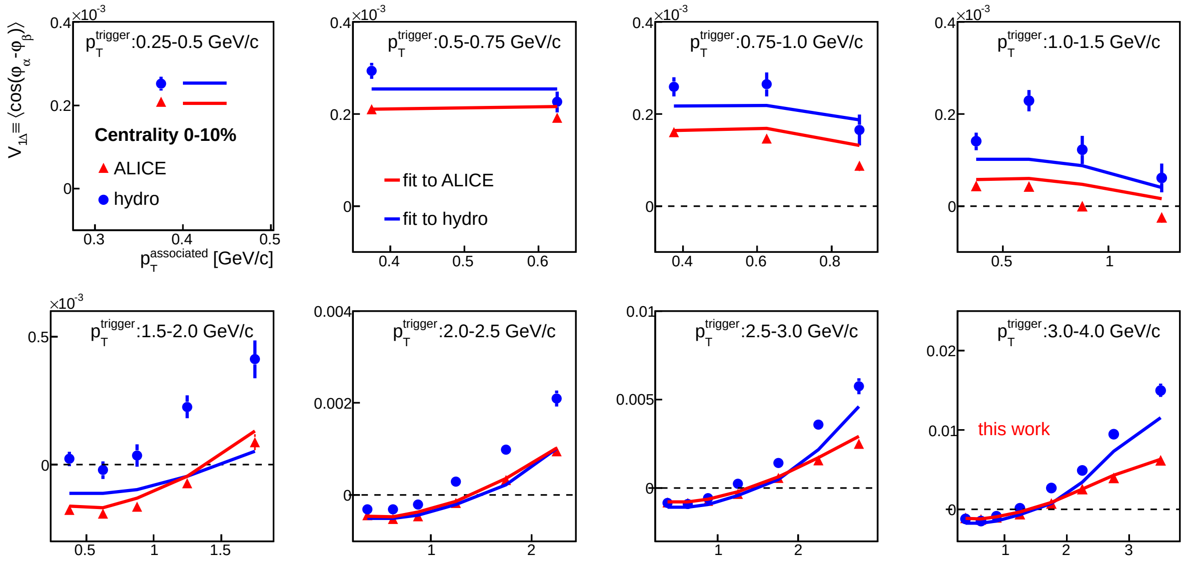

(a) Centrality 0-10%

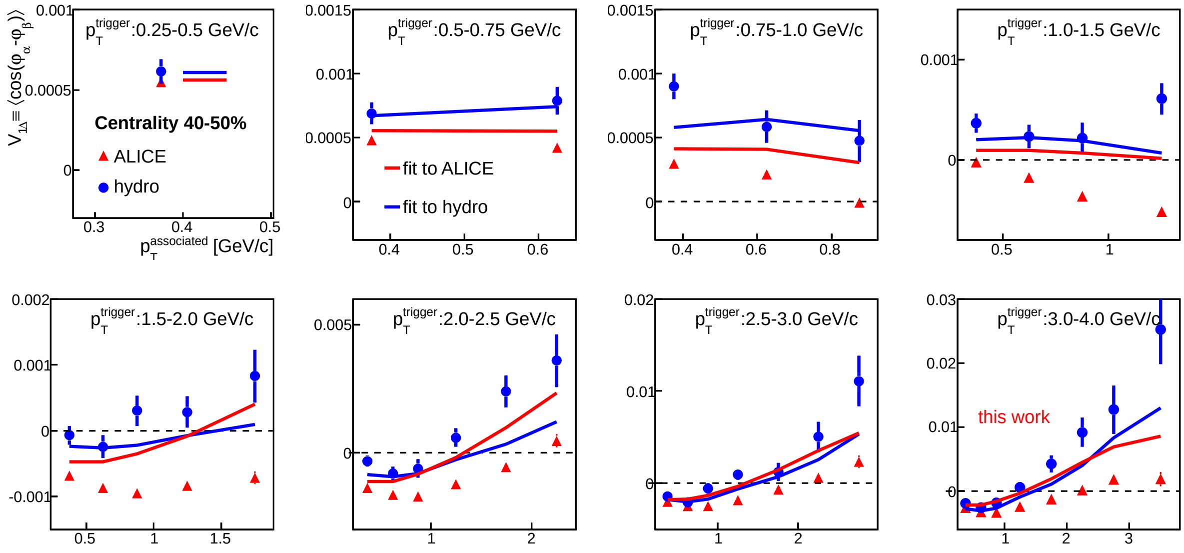

(b) Centrality 40-50%

Figure 5.13: $V_{1\Delta}$ as a function of associated particle $p_{\rm T}$ for each $p_{\rm T}$ bins of trigger particle $p_{\rm T}$ in minimum bias events. A transverse axis indicates associated particle $p_{\rm T}$ [GeV/c] and a longitudinal axis indicates $V_{1\Delta}$. Eta gaps between trigger and associated particle $|\Delta\eta| > 0.8$ are required. Blue points are from event-by-event hydro calculations. Red lines are fitting results [101, 105].

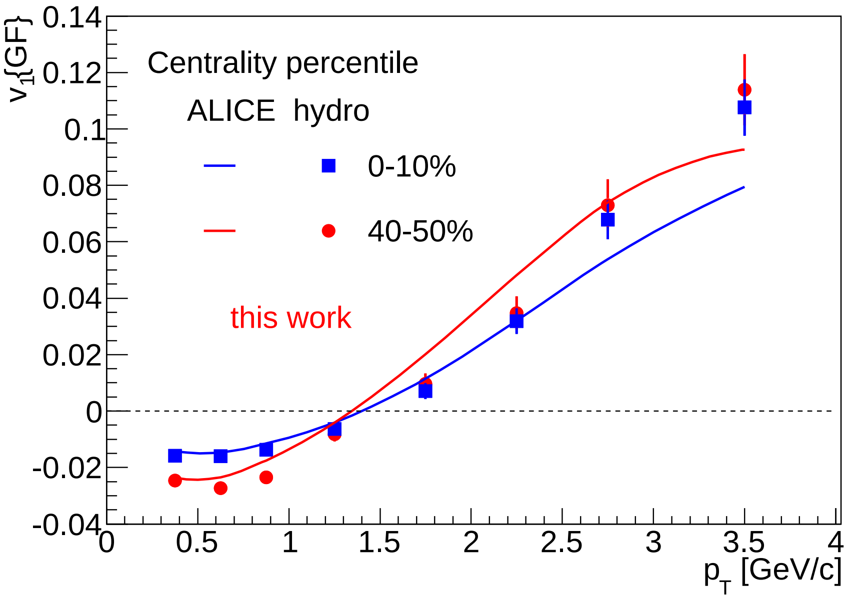

Figure 5.14: p_{T} differential directed flow v_1 measured by the Global Fit method in minimum bias Pb–Pb events at 2.76 TeV from the ideal hydrodynamic simulations [101, 105].

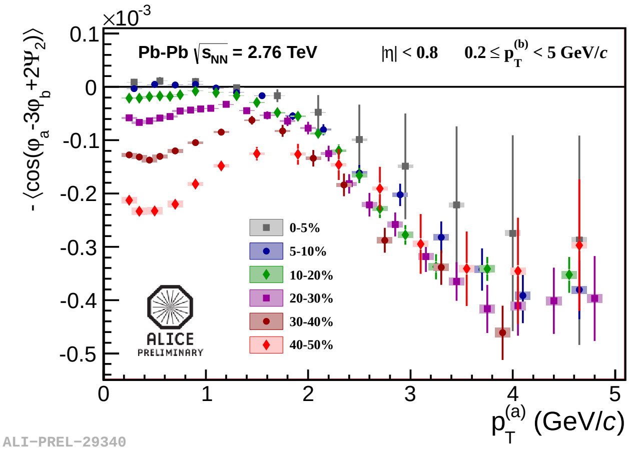

(a)

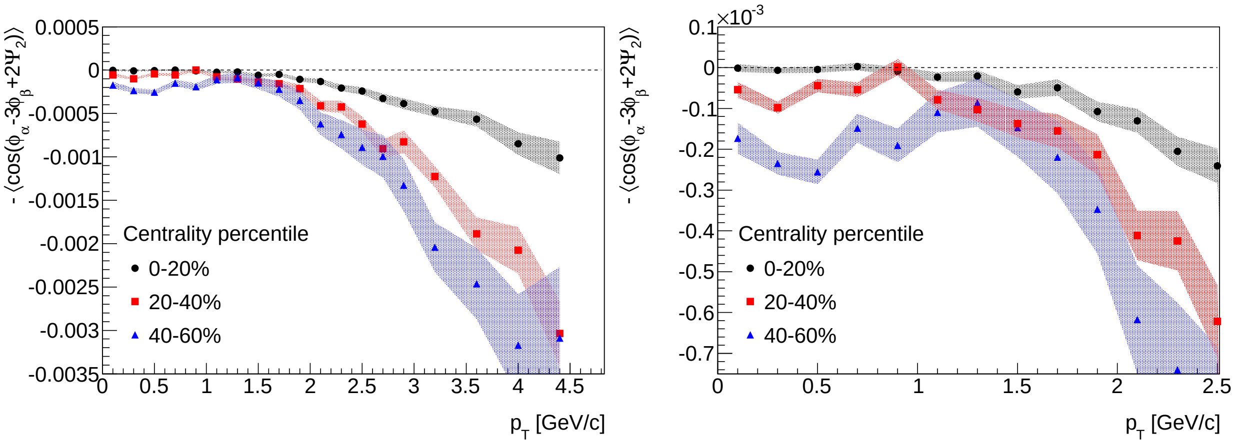

(b) (c)

Figure 5.15: The p_{T} differential correlation $\langle\cos(\varphi_\alpha - 3\varphi_\beta + 2\Psi_2)\rangle$ for each centrality class (a) measured by the ALICE collaboration by the three-particle cumulant method [107], (b)calculated by the hydro model by the event plane method and (c) Zoomed plot.

5.2.3 Further analysis

Figure 5.16 shows the centrality dependence of the charge independent multi-particle correlations in comparison with (a) the HIJING model, (b) the hydro model and (c) the AMPT model calculations. Results from the HIJING model are almost negligible while the hydro model reasonably reproduces them except for the correlation $\langle\cos(\varphi_\alpha+\varphi_\beta-2\Psi_2)\rangle$. Because the measured correlation $\langle\cos(\varphi_\alpha-3\varphi_\beta+2\Psi_2)\rangle$ at the low p_T region agrees with the hydro model as already studied in Fig. 5.15, the p_T integrated results are also in good agreement. The correlation $\langle\cos(\varphi_\alpha+\varphi_\beta-2\Psi_2)\rangle$ calculated with the hydro model disagrees with both the naive expectations shown in Fig. 2.9 (b) and the experimental results, whose reason is difficult to answer for the moment.

What is worse about the hydro model, there is little $\Delta\eta$ dependence of the correlations $\langle\cos(\varphi_\alpha-\varphi_\beta)\rangle$, $\langle\cos(\varphi_\alpha-3\varphi_\beta+2\Psi_2)\rangle$ and $\langle\cos(\varphi_\alpha+\varphi_\beta-2\Psi_2)\rangle$ in the hydro model while the measured results have a strong dependence as shown in Fig. 5.17. Note that since the boost invariance of the initial density profile is roughly assumed and jets are not considered in the hydro model, the little $\Delta\eta$ dependence in this model is reasonable.

Interestingly, the AMPT model reproduces well both all the integrated correlations and their $\Delta\eta$ dependencies as shown in Fig. 5.16 (c) and Fig. 5.17. These results may indicate that the physics origin of the mixed harmonic azimuthal correlations associated with the directed flow is the combined effect of the directed flow and jets. Further theoretical efforts like the development of the hydro+jet model, the detailed study of the dependence on the various parameters in the AMPT model, are necessary.

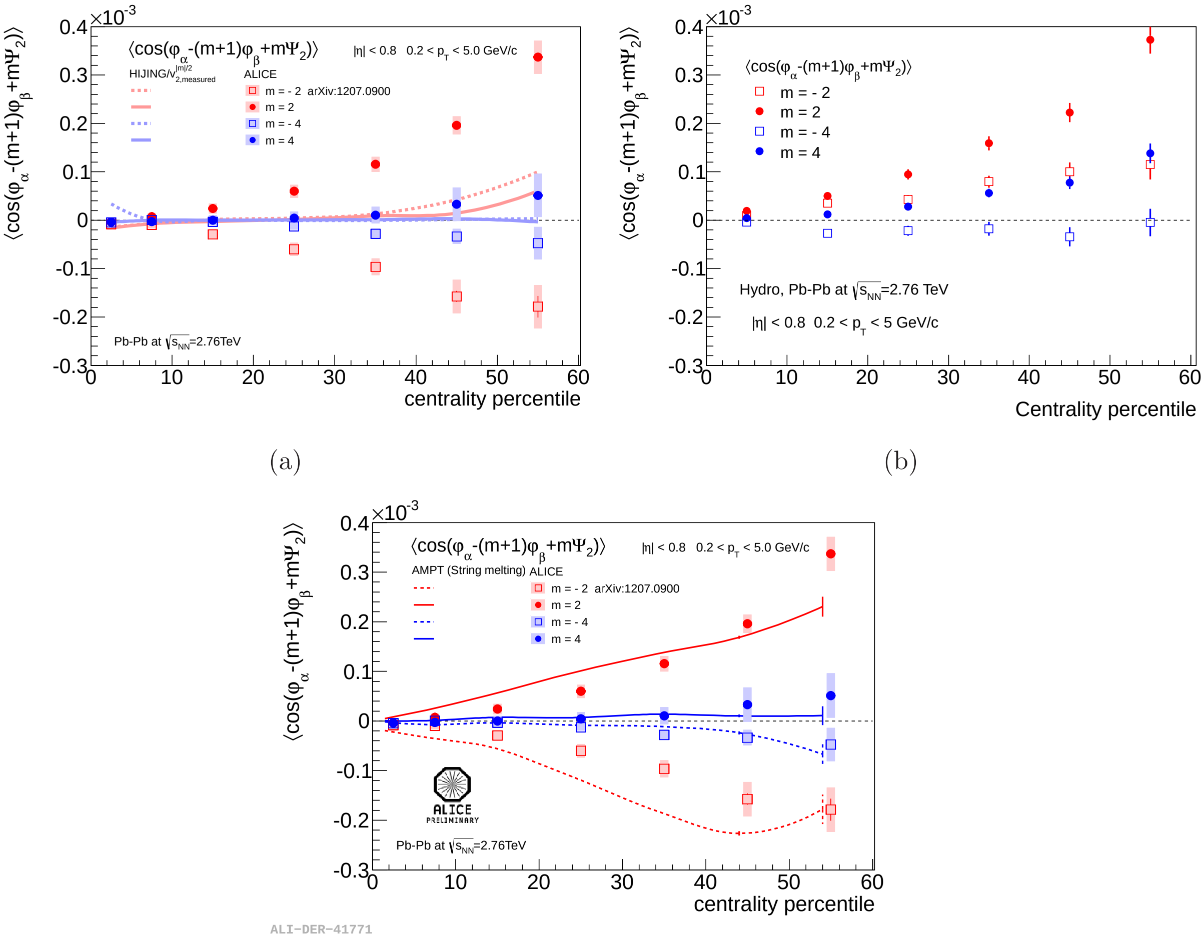

(a)

(b)

(c)

Figure 5.16: The centrality dependence of the correlation $\langle \cos[\varphi_\alpha - (m+1)\varphi_\beta + m\Psi_2] \rangle$ measured by the ALICE in comparison with (a) the HIJING model, (b) the hydro model and (c) the AMPT model calculations [106].

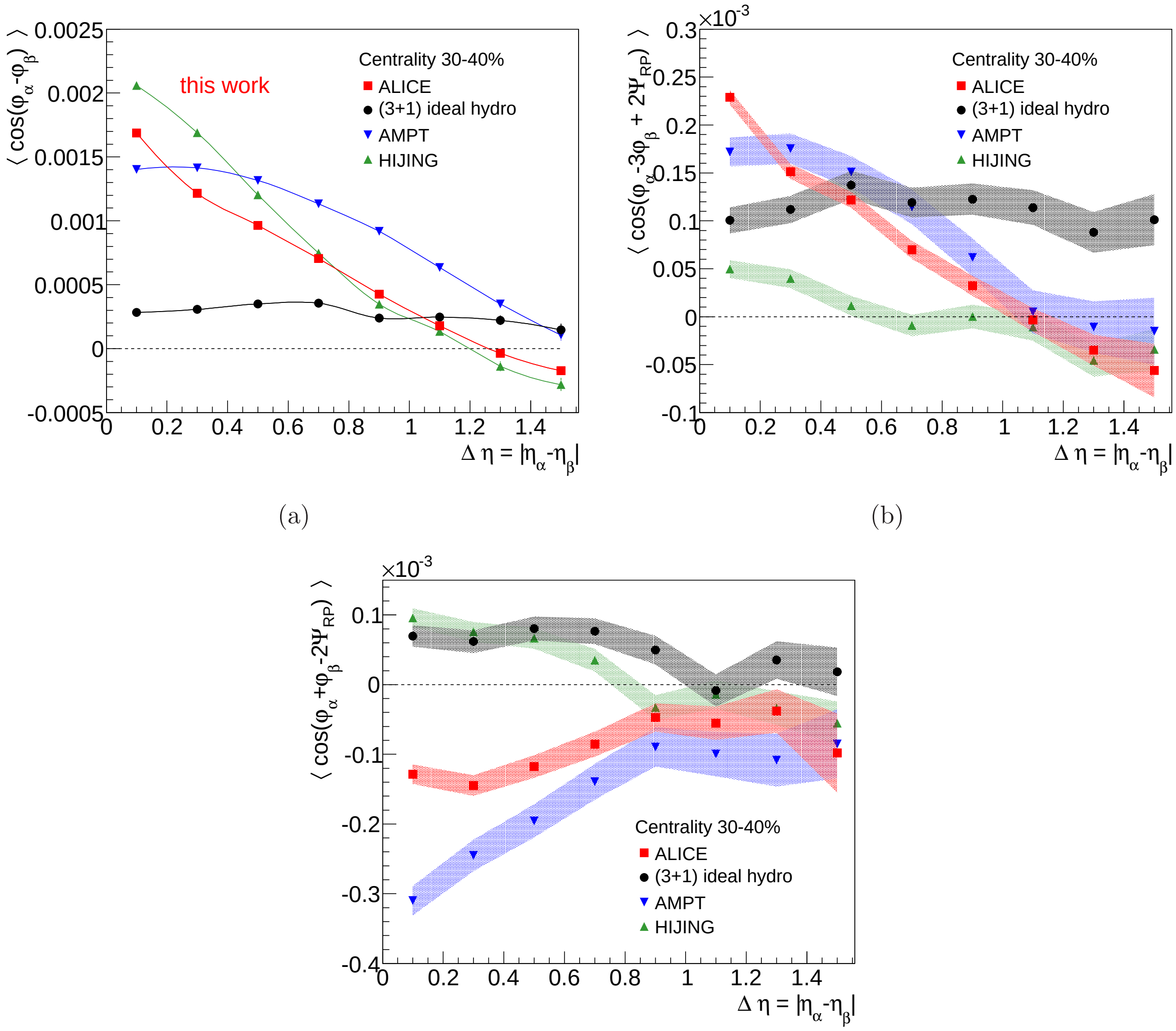

(a)

(b)

(c)

Figure 5.17: The $\Delta\eta = |\eta_\alpha - \eta_\beta|$ differential correlation (a) $\langle\cos(\varphi_\alpha - \varphi_\beta)\rangle$, (b) $\langle\cos(\varphi_\alpha - 3\varphi_\beta + 2\Psi_2)\rangle$ and (c) $\langle\cos(\varphi_\alpha + \varphi_\beta - 2\Psi_2)\rangle$ for centrality 30-40% events in comparison with the HIJING, AMPT and hydro models.

Chapter 6

Summary and Conclusions

In this thesis, the mixed harmonic azimuthal correlations at mid-rapidity in $\sqrt{s_{NN}}$ =2.76 TeV Pb–Pb collisions measured with the ALICE detectors at LHC were reported.

Their charge dependent parts have two competing physics implications: the Local Charge Conservation (LCC) induced correlations and the Chiral Magnetic Effect (CME). In general, charge dependent parts of azimuthal correlations are expected to be induced by the LCC and the azimuthal anisotropic flow. In order to test the "effective" LCC on the kinetic freeze-out surface, charge dependent parts of a series of the mixed harmonic azimuthal correlations $\Delta\langle\cos[n(\varphi_\alpha - \varphi_\beta)]\rangle$ and $\Delta\langle\cos[n\varphi_\alpha + m\varphi_\beta - (n+m)\Psi_k]\rangle$ are proposed. The correlations $\Delta\langle\cos[n(\varphi_\alpha - \varphi_\beta)]\rangle$ can be regarded as the n-th Fourier moments of the relative azimuthal distribution between charge and balancing anti-charge. Especially, $\Delta\langle\cos(\varphi_\alpha - \varphi_\beta)\rangle$ can be interpreted as the inverse width between charge and anti-charge and may be sensitive to the radial flow. The correlations $\Delta\langle\cos[n\varphi_\alpha + m\varphi_\beta - (n+m)\Psi_k]\rangle$ can be regarded as the $|n+m|$-th azimuthal modulations of the n-th Fourier moments with respect to the k-th harmonic symmetry plane. They are expected to be roughly proportional to the $|n+m|$-th harmonic azimuthal flow with respect to the k-th harmonic symmetry plane, i.e. $v_{|n+m|,k}$.

It has been discussed that the local parity P and charge-parity CP violation in QCD occur via the topologically non-trivial gluon field configurations although its direct evidence is not yet experimentally found. In the presence of a large magnetic field generated perpendicularly to the reaction plane in non-central relativistic heavy ion collisions, this local P and CP violation in QCD is expected to result in a charge separation along the direction of the magnetic field. This phenomenon is called the CME. A measurement of a charge dependent azimuthal correlation $\langle\cos(\varphi_\alpha + \varphi_\beta - 2\Psi_{RP})\rangle$ was originally proposed to search the charge separation due to the CME. However, the LCC induced correlations can be a possible background of the CME search in the presence of the elliptic flow.

Firstly, observed $\Delta\langle\cos(\varphi_\alpha - \varphi_\beta)\rangle$ is consistent with the inverse width between charge and anti-charge induced by the "effective" LCC on the large radially expanding kinetic freeze-out surface. On the other hand, since the near-side correlations such as HBT seem to be relevant for the higher moment $\Delta\langle\cos[n(\varphi_\alpha - \varphi_\beta)]\rangle$, the simple Blast Wave model incorporating with the LCC on the kinetic freeze-out fails to describe them.

The Blast Wave model incorporating with the LCC on the kinetic freeze-out can also systematically reproduce $\Delta\langle\cos[\varphi_\alpha-(m+1)\varphi_\beta+m\Psi_2]\rangle$ with $n=2,-2,4$ ans 4 (including $\Delta\langle\cos(\varphi_\alpha+\varphi_\beta-2\Psi_2)\rangle$). Note that this model has the large radial flow, the elliptic flow v_2 and the fourth harmonic flow with respect to the 2nd harmonic symmetry plane $v_{4,2}$. Again, these agreements strongly indicate that the "effective" LCC seems to be realized on the kinetic freeze-out surface. The "effective" LCC on the kinetic freeze-out surface may be originated from the LCC at the hadronization and/or the correlations induced at the highly interacting hadronic matter. Its physics origins must be understood, which may provide insights about the chemical evolution of the QGP such as the information about the charge production mechanism. To this end, theoretical developments of the hydrodynamic + hadron cascade models with the LCC constraint are necessary.

It is found that the charge dependent azimuthal correlation $\langle\cos(\varphi_\alpha+\varphi_\beta-2\Psi_2)\rangle$ is positive or ~ 0 for the opposite charge combinations and negative for the same charge, which is qualitatively consistent with the CME if the background effects are ignored. However, now we know that the LCC induced correlations seem to be realistic and significant, contributions from the LCC effects should be precisely subtracted for the further CME search.

Charge dependent parts of azimuthal correlations with respect to the 3rd and 4th harmonic symmetry planes are also observed. Their magnitudes are again consistent with the naive expectation of the LCC scenario. Furthermore, the dependencies of the charge dependent azimuthal correlations $\langle\cos(\varphi_\alpha-\varphi_\beta)\rangle$, $\langle\cos(\varphi_\alpha+\varphi_\beta-2\Psi_{RP})\rangle$ and $\langle\cos(\varphi_\alpha-3\varphi_\beta+2\Psi_{RP})\rangle$ on the transverse momentum difference $|p_{\mathrm{T},\alpha}-p_{\mathrm{T},\beta}|$, the average transverse momentum $(p_{\mathrm{T},\alpha}+p_{\mathrm{T},\beta})/2$ and the rapidity separation $\Delta\eta=|\eta_\alpha-\eta_\beta|$ of two charged particles were investigated. Their charge dependent parts are similarly localized within about one unit of rapidity, which is the typical hadronic width, (or may even change sign as a function of $\Delta\eta$) and extend up to the higher $|p_{\mathrm{T},\alpha}-p_{\mathrm{T},\beta}|$ and $(p_{\mathrm{T},\alpha}+p_{\mathrm{T},\beta})/2$. They increase with the increase of $(p_{\mathrm{T},\alpha}+p_{\mathrm{T},\beta})/2$, which is inconsistent with the CME expectations but qualitatively consistent with the LCC induced correlations. To quantify these new correlations, the theoretical developments of the event-by-event full hydrodynamic models with the LCC constraint are necessary.

A non-zero charge independent part of the correlation $\langle\cos(\varphi_\alpha+\varphi_\beta-2\Psi_2)\rangle$ is observed. In the context of the CME, it can be understood as a suppression of the opposite charge correlation because the opposite charge correlation is considered to be a back-to-back correlation and modified by the interactions between the parity-odd bubbles and the medium created in the collisions. However, it was pointed out that the global transverse momentum conservation of the system also affects on it. In this thesis, it is found by the semi-analytic way that this effect is not large enough to explain the observed charge independent part.

Charge independent parts of the mixed harmonic azimuthal correlations are originally considered to be useful tools to study the collision dynamics and the collective properties of the QGP. In particular, the directed flow v_1 and joint correlations between v_1 and higher harmonic flow v_n have been recently recognized as a consequence of the initial density fluctuations and subsequent hydrodynamical evolutions. This can be an alternative explanation of the observed non-zero charge independent part of the correlation $\langle \cos(\varphi_\alpha + \varphi_\beta - 2\Psi_2) \rangle$. By comparing the various azimuthal correlations measured by the ALICE collaboration with the results of the ideal event-by-event hydrodynamic simulations, the directed flow v_1 signals are observed with multi-particle azimuthal correlation measurements. However, it is found that the ideal hydrodynamic model used in this thesis can not explain the observed charge independent part of the correlation $\langle \cos(\varphi_\alpha + \varphi_\beta - 2\Psi_2) \rangle$. Remarkably, the AMPT model, which is based on the partonic/hadronic cascade, can reproduce all mixed harmonic azimuthal correlations measured in this thesis. This indicates that the interplay between the hydrodynamic matter and jets is a key ingredient for the comprehensive understanding of their physics origins.

Acknowledgment

First of all, it is a great pleasure to express my science gratitude to Prof. Hideki Hamagaki who has led me to this exciting and interesting field of science. I appreciate him for his continuous encouragement and appropriate teaching. I couldn't accomplish this work at all without his abundant knowledge and many pieces of valuable advices.

I would like to express my sincere thanks to Dr. Taku Gunji for his persevering guidance, advice, discussion, and encouragements. I could learn many things as an experimentalist from his working style.

I wish to acknowledge all the collaborators of the ALICE experiment. I am deeply grateful to the former ALICE spokesperson, Prof. Jurgen Schkraft and the current spokesperson Prof. Paolo Giubellino for their heartful administration of entire collaboration. I also wish to acknowledge the staff of Pt.2 of ALICE experiment. Especially, I would like to thank the Run Coordinator of 2010, Dr. Chilo G Cuadrado. I also would like to thank Dr. Ken Oyama as a great contributor to the ALICE operation.

I appreciate the ALICE-TPC calibration group. I wish to thank Prof. Luciano Musa to accept me to the calibration group. I would like to thank Dr. Stefan Rossegger, Prof. Jim Thomas, Mr. Magnus Mager and Dr. Marian Ivanov for their many teaching and kind introduction to TPC calibrations. Their innovative works were amazing for me.

I would like to acknowledge the Physics Working Group - Correlation and Fluctuation (PWG-CF) in the ALICE collaboration. I'm grateful to the convener of PWG-CF, Prof. Raimond Snellings and Dr. Jan Fiete Grosse-Oetringhaus. Special thanks to Dr. Ilya Selyuzhenkov and Dr. Panos Christakoglou for the intensive discussions and collaborations. Without them, my analysis will never finish. I would like to thanks Prof. Sergei Voloshin and Dr. Ante Bilandzic for giving me their deep knowledge about the flow and CME analysis. I was always surprised by their creative works. I would like to express many thanks to all the other people working with me about the flow and correlation analysis, Prof. Paul Kuijer, Dr. Cristian George Ivan, Mr. Carlos Eugenio Perez Lara, Dr. Alexandru Florin Dobrin, Dr. Francesco Noferini, Mr. You Zou, Mr. Jocelyn Mlynarz, Dr. Mikolaj Krzewicki, Prof. Zhong-Bao Yin, Dr. Michael Weber, Ms. Vera Loggins, Dr. Andrew Adare, Prof. Shinichi Esumi, Ms. Hongyan Yang. etc..

I express my gratitude to Dr. Soeren Schlichting, Prof. Scott Pratt, Prof. Tesufumi Hirano and Mr. Koichi Murase for providing me their results of the theoretical model calculation and fruitful discussions. I enjoyed the model discussions and a paper preparation with Dr. Soeren Schlichting very much. I also would like to thanks Mr. Akihiro Monnai, Prof. Masayuki Asakawa, Prof. Piotr Bozek and Prof. Kenji Fukushima for the discussions.

I would also like to thank all other CNS, University of Tokyo members for their excellent discussions, ideas, help and encouragements. In particular, I would also like to thank the fellow CNS graduate students, past and present, Dr. Hisayuki Torii, Mr. Yuji Tsuchimoto, Dr. Yuhei Morino, Dr. Yorito L. Yamaguchi, Dr. Yoki Aramaki, Dr. Satoshi Sano, Mr. Akihisa Takahara, Mr. Ryoji Akimoto, Mr. Tomoya Tsuji, Mr. Shinichi Hayashi, Mr. Atsushi Nukariya, Ms. Yuko Sekiguchi, Mr. Kohei Terasaki.

I hope to express my thanks to all the staff of the Hiroshima Univ. group. I would like to thank Prof. Tohoru Sugitate to allow me to use the powerful cluster. I also would like to thank members of Sugitate group for their management of the cluster. My analysis was progressed smoothly on their great operation. I would like to thanks Prof. Kenta Sigaki for the discussion at the Heavy Ion Pub hold at the Hiroshima Univ.

I also appreciate other japanese collaborators in the ALICE collaboration, Mr. Masato Sano, Mr. Dousatsu Sakata, Mr. Satoshi Yano, Mr. Daisuke Watanabe, Dr. Shingo Sakai. Espacially, I learned many things about the analysis in the ALICE experiment from Dr. Shingo Sakai.

I appreciate all heartful supports by the CNS secretaries, Ms. Midori Hirano, Ms. Takako Endo, Ms. Ikuko Yamamoto, Ms. Yukino Kishi, Ms. Yuko Soma, Ms. Toshiko Itagaki, Ms. Yuko Asakawa for their supports of the research. I express my appreciation to the ALICE secretaries, Ms. Ulla Tihinen, Ms. Carnita Hervet, Ms. Helena Zerlauth, and Ms. Michelle Connor.

I am grateful to Prof. Ryugo Hayano, Prof. Hidetoshi Yamaguchi, Prof. Tetsuo Hatsuda, Prof. Satoru Yamashita, and Prof. Hiroyoshi Sakurai for their valuable comments and important advice. I would like to express my appreciation to Prof. Ryugo Hayano for his truly relevant advice and proof-readings.

The financial support form JSPS was essential to continue the work.

Finally, I would like to give thanks to my family and my sister's family for their supports and encouragements.

Appendix A

Azimuthal Anisotropic Flow

A.1 Measurement Methods

In the standard event plane method, one experimentally estimates the n-th harmonic symmetry plane angle Ψ_n from the n-th harmonics of the anisotropic particle distribution itself. This experimental estimation is called event plane angle. The event flow vector Q_n in each events is defined as a 2 dimensional vector in the transverse plane:

$$(Q_{n,x}, Q_{n,y}) \;\; = \;\; (\sum_i w_i \mathrm{cos} n\varphi_i, \sum_i w_i \mathrm{sin} n\varphi_i), \tag{A.1}$$

where the sum goes over all particles i. The quantities φ_i and w_i are the azimuthal angle measured in the laboratory frame and weight for particle i. The weight w_i is usually set to unit, p_{T} of the particle, and so on. The event plane is defined as

$$\Psi_{EP_n} \;\; \equiv \;\; \tan^{-1}\left(\frac{Q_{n,y}}{Q_{n,x}}\right)/n. \tag{A.2}$$

Then, with the event plane method, the anisotropic flow is calculated as

$$v_n\{EP_k\} \equiv \frac{\langle \mathrm{cos}[n(\varphi - \Psi_{EP_k})] \rangle}{R}, \tag{A.3}$$

where R is the correction factor for the finite resolution of the event plane angle determination. In order to remove the auto-correlation between φ and Ψ_{EP_k}, the bracket denotes the average over particles which are not used for the event plane angle estimation in all events. For example, the event plane angle is calculated using the forward-rapidity detectors and the the estimation of anisotropic flow uses the central-rapidity detectors. Detailed description for the event plane method is found in Sec.4.5.

In the two-particle cumulant method,$v_n\{2\}$ is obtained from the two-particle azimuthal correlation defined as

$$v_n\{2\} \equiv \sqrt{\langle \mathrm{cos}[n(\varphi_\alpha - \varphi_\beta)] \rangle}, \tag{A.4}$$

where the bracket denotes the average over all pairs in all events. This relation is deduced as follows.

$$\begin{aligned}\langle\cos[n(\varphi_\alpha-\varphi_\beta)]\rangle &= \langle\cos[n(\varphi_\alpha-\Psi_n)-2(\varphi_\beta-\Psi_n)]\rangle \\ &= \langle\cos[n(\varphi_\alpha-\Psi_n)]\times\cos[n(\varphi_\beta-\Psi_n)]\rangle \\ &\quad-\langle\sin[n(\varphi_\alpha-\Psi_n)]\times\sin[n(\varphi_\beta-\Psi_n)]\rangle \\ &\sim \langle\cos[n(\varphi_\alpha-\Psi_n)]\times\cos[n(\varphi_\beta-\Psi_n)]\rangle \\ &\sim \langle\cos[n(\varphi_\alpha-\Psi_n)]\rangle\langle\cos[n(\varphi_\beta-\Psi_n)]\rangle \\ &\sim v_n^2. \end{aligned} \tag{A.5}$$

The sine terms are negligible in case of the perfect azimuthal acceptance. An approximation from the fourth to the fifth line is valid if the particle α and β are correlated with each other only via common correlation to the reaction plane.

In the four-particle cumulant method, $v_n\{4\}$ is defined as

$$\begin{aligned} v_n\{4\} &\equiv (n\langle\cos[n(\varphi_\alpha-\varphi_\beta)]\rangle^2-\langle\cos[n(\varphi_\alpha+\varphi_\beta-\varphi_\gamma-\varphi_\delta)]\rangle)^{\frac{1}{4}} \\ &\sim [2(v_n^2)^2-v_n^4]^{\frac{1}{4}}\sim v_n. \end{aligned} \tag{A.6}$$

The elliptic flow estimations using the six and eight-particle cumulant method, $v_n\{6\}$ and $v_n\{8\}$, are defined similarly. But their definitions are extremely complicated and we omit them here.

The event plane method and the two-particle cumulant method are categorized into the two-particle azimuthal correlations while the four, six and eight-particle cumulant methods are categorized into the multi-particle correlations. Since the azimuthal anisotropic flow is a collective motion of the participant region, it can contribute not only the two-particle correlations but also the multi-particle correlations. It is known that the two-particle correlation method suffers from the intrinsic two-particle correlations induced by the jets and resonances, which are called non-flow correlation, while the non-flow contributions on the multi-particle correlations are negligible. Therefore, the multi-particle correlation method is better than the two-particle correlation method for the flow measurements. On the other hand, the statistical errors of the multi-particle correlations are in general larger than the two-particle correlations. A general definition of the cumulant method is explained in Sec.4.4.

A.2 Physics origin of the elliptic flow

Elliptic flow quantifies how the system responds to the initial spatial ellipsoidal anisotropy. Suppose the two extreme situations. In the case where the mean free path among the produced particles is much larger than the typical size of the system, the azimuthal distribution of the finally emitted particles is flat. In the opposite extreme case, where the mean free path is very small enough to achieve thermalization, then the hydrodynamics can be applied to describe the space-time evolution of the matter. The hydrodymanic flow is generated due to the pressure gradient of the matter. The magnitude of the hydrodynamic flow depends on the azimuthal direction as shown by the arrows in the right picture of Fig. A.1 [74], which results in the azimuthal anisotropy of the collective flow.

The basic equations for the relativistic hydrodynamics are energy-momentum conservation;

$$\partial_\mu T^{\mu\nu} = 0, \tag{A.7}$$

where $T^{\mu\nu}$ is the energy-momentum tensor, and the current conservation;

$$\partial_\mu N^\mu = 0, \tag{A.8}$$

where N^μ is the conserved current. $T^{\mu\nu}$ and N^μ can be represented by the flow vector u^μ as a function of the space-time coordinate x. The two equations above therefore compose a simultaneous differential equation for u^μ, which can be numerically solved with the equation of the state (EoS) of the produced matter.

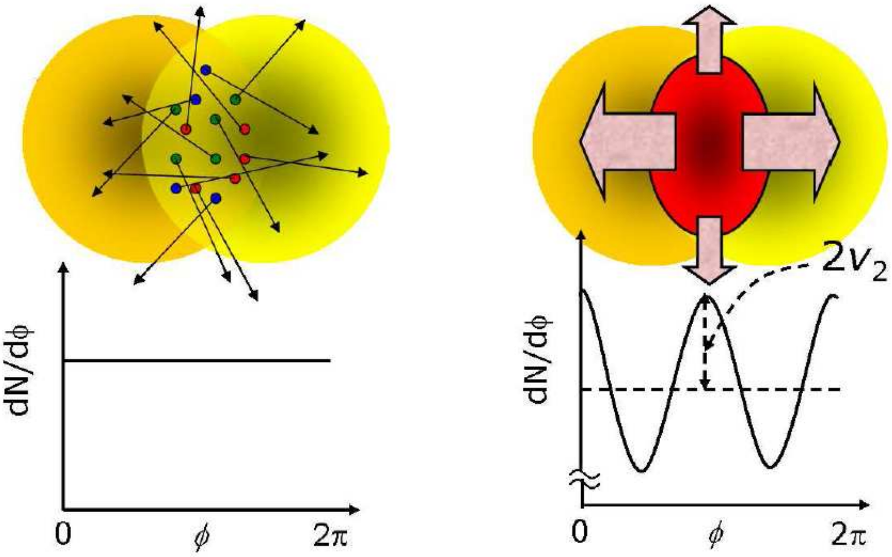

Figure A.1: The illustration of the elliptic flow development in the two extreme case: a large and small mean free path among the produced particles in the left and right pictures respectively. The aizmuthal angle ϕ in these pictures is measured from the reaction plane angle [74].

Figure A.2 (a) shows $\mathrm{N_{part}}$ dependence of the integrated elliptic flow v_2 in $\sqrt{s_{NN}} = 200$ GeV Au–Au collisions measured by the PHOBOS collaboration at RHIC. $\mathrm{N_{part}}$ denotes the number of the participants in the collisions and is correlated to the event centrality. In the hydrodynamic models, the Cooper-Frye formula is used in order to convert the macroscopic variables calculated by the hydrodynamic simulations into the particle distributions. A solid line is a result from a full 3D ideal hydrodynamic simulation both at the QGP and hadronic gas stage while a dashed line is a result from a ideal hydrodynamic simulation and subsequent hadronic rescattering model. The elliptic flow v_2 is small in most central collsions, where $\mathrm{N_{part}}$ is large, because the initial anisotropy is small in most central collisions. The magnitudes of v_2 in non-central collisions are $O(10^{-2} \sim 10^{-1})$, which roughly agree with the results using ideal hydrodynamic models. On the other hand, the prediction by the hadronic cascade model (dash-dotted line) is smaller than the observed result. This is a strong evidence that the matter contains non-hadronic components and its density is high enough to regard it as the hydrodynamic matter.

Figure A.2 (b) shows the p_{T} differential elliptic flow v_2 measurement using the event plane method in $\sqrt{s_{NN}} = 200$ GeV Au–Au collisions by the STAR collaboration [108]. Observed v_2 increases from ~ 0 up to ~ 0.2 at the low p_{T} region and goes constant or down at $p_{\mathrm{T}} \sim 3\mathrm{GeV}/c$. At the low p_{T} region, the elliptic flow v_2 agrees well with the ideal hydrodynamic model shown by a red line. At the high p_{T} region, the hard components like jets become relevant and the agreement to the simple hydrodynamic model becomes worse.

There are two parameters which have to be provided from the comparison with the flow signatures in the hydrodynamic theories: the initial condition for the hydrodynamic simulations and the viscosity of the hydrodynamic matter. There are two-type of the initial conditions - the Glauber models [109] and the models based on the Color Glass Condensate (CGC) picture [110]. Hadronic processes in the heavy ion collisions are described in a simple geometrical picture by the Glauber Model, which assumes straightline nucleon trajectories and $N-N$ cross section independent of the number of collisions the nucleons have undergone before. The nuclear density profile is given by a Woods-Saxon distribution. In the ALICE experiment, a nucleon-nucleon cross section of 64 mb is used and was confirmed by the measurement of the Van der Meer scans [69, 111]. The collision geometry determines the number of nucleons that participate in the reaction, so-called number of participants N_{part}, and the number of independent hard collisions N_{coll}. In the CGC models, the energy density at the center of the participant profile is saturated compared to the Glauber models, which generally results in the large spatial anisotropy. Recently, the relativistic hydrodynamic simulations with the shear viscosity have been available and it was demonstrated that the shear viscosity decreases the anisotropic flow as expected. However, before the estimation of the viscosity and the determination of the initial condition by comparing the models and experimental results, the flow fluctuation effect on the each flow measurement method should be carefully considered as described in the next section.

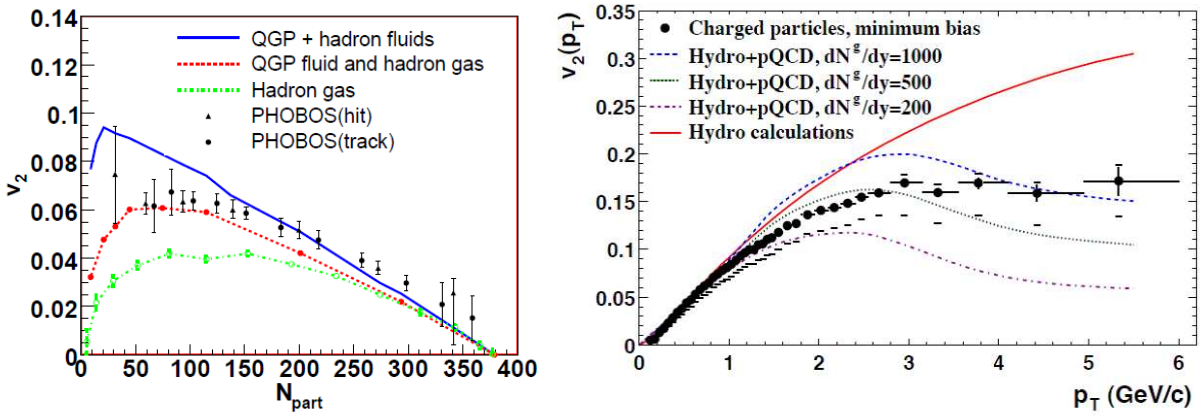

Figure A.2: (a) $N_{\rm part}$ dependence of the integrated elliptic flow v_2 in $\sqrt{s_{NN}}$ = 200 GeV Au–Au collisions measured by the PHOBOS collaboration [112] in comparison with the various models. A solid line is a result from a full 3D ideal hydrodynamic simulation both at the QGP and hadronic gas stage (T_{th} = 100 MeV). A dashed line is a result from a full 3D ideal hydrodynamic simulation at the QGP stage (T_{th} = 160 MeV) and subsequent hadronic cascade model [113]. A dash-dotted line is a result from a hadronic cascade model [114]. (b) The $p_{\rm T}$ differential elliptic flow v_2 in $\sqrt{s_{NN}}$ = 200 GeV Au–Au collisions measured by the STAR collaboration [108] using the event plane method in comparison with the hydrodynamic models. The predicted magnitude of v_2 at higher $p_{\rm T}$ based on energy loss expectations for different values of the gluon density in a static medium [115].

A.3 Flow fluctuation and Higher harmonic flow

The anisotropy fluctuates event-by-event even if the impact parameter is fixed. The magnitude of flow fluctuations is characterized by σ_{v_2}, defined as

$$\sigma_{v_2} \equiv \langle v_2^2 \rangle - \langle v_2 \rangle^2. \tag{A.9}$$

Flow methods involve various functions of v_2, which are also affected by fluctuations. The average value of $f(v_2)$ is obtained by expanding around $\langle v_2 \rangle$ to leading order in $\sigma_{v_2}^2$:

$$\langle f(v_2) \rangle = f(\langle v_2 \rangle) + \frac{\sigma_{v_2}^2}{2} f''(\langle v_2 \rangle). \tag{A.10}$$

Using the definition of $v_2\{2\}$ and $v_2\{4\}$, we have

$$v_2\{2\}^2 = \langle v_2^2 \rangle = \langle v_2 \rangle^2 + \sigma_{v_2}^2 + \delta_2, \tag{A.11}$$

and

$$v_2\{4\}^2 = (2\langle v_2^2 \rangle^2 - \langle v_2^4 \rangle)^{1/2} = \langle v_2 \rangle^2 - \sigma_{v_2}^2, \tag{A.12}$$

where δ_2 denotes the nonflow contributions on the two-particle correlations. Fluctuations represented by σ_{v_2} increase $v_2\{2\}$ and decrease $v_2\{4\}$ compared to v_2. Fluctuations also affect the six and eight-particle cumulant $v_2\{6\}$ and $v_2\{8\}$ as a same way as the $v_2\{4\}$ to leading order in $\sigma_{v_2}^2$ [116]. Fluctuations are considered to affect the elliptic flow measurement in the event plane method by the rather complicated way and detailed descriptions are found in Ref. [116].

Figure A.3 (a) shows the centrality dependence of the integrated elliptic flow for the charged particles in $\sqrt{s_{NN}} = 2.76$ TeV Pb–Pb collisions measured by the ALICE collaboration using the various methods [73]. Magnitudes and centrality dependence of integrated v_2 observed at the LHC energy are roughly consistent to the hydrodynamic model predictions as shown in Fig. A.3 (b) [117]. For two-particle cumulant method, non-flow contributions are suppressed by the larger eta-gaps $|\Delta\eta| > 1$ between two particles for semi-peripheral and peripheral collisions, which is consistent with the expectations. The elliptic flow $v_2\{4, 6, 8\}$ measured with the multi-particle cumulant method agree well each other and the difference between $v_2\{2\}$ and $v_2\{4\}$ can be considered to originate from the flow fluctuations, i.e. $\sigma_{v_2} \sim \sqrt{v_2\{2\}^2 - v_2\{4\}^2}$. Experimentally, there are several sources of flow fluctuations: fluctuations of the impact parameter within the sample of the events and, more importantly, the event-by-event fluctuations of the initial density profile. Figure A.3 (c) shows the centrality dependence of the elliptic flow fluctuations $\sigma_{v_2}/\bar{v}_2$ ($\bar{v}_2 \equiv \sqrt{v_2\{2\}^2 + v_2\{4\}^2/2}$) in comparison with that of the initial eccentricity flucutations calculated using the CGC-type(MC-KLN) and Glauber-type Monte Carlo models. It was found according to this plot that the observed elliptic flow fluctuations can be roughly explained by the fluctuations of the initial geometry.

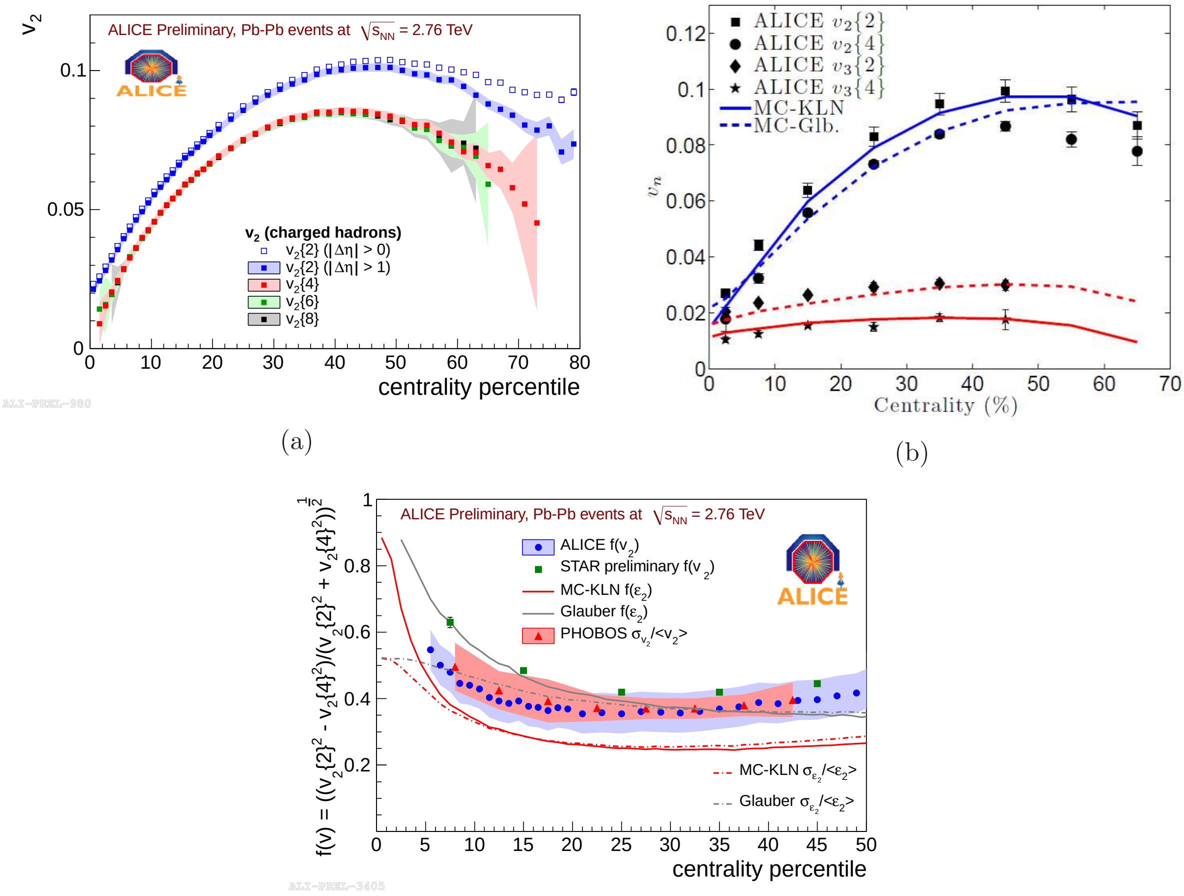

(a)

(b)

(c)

Figure A.3: (a) The centrality dependence of the integrated elliptic flow v_2 for charged hardrons with various methods measured by the ALICE collaboration [73]. (b) The integrated elliptic flow v_2 and triangle flow v_3 measured by the ALICE collaboration in comparison with the viscous hydrodynamic simulations. Solid lines are the results with the Monte Carlo KLN-CGC initial condition with $\eta/s = 0.2$. Dotted lines are the results with the Monte Carlo Glauber initial condition with $\eta/s = 0.08$. For the simultaneous description for v_2 and v_3, the dotted lines are better [117]. (c) The centrality dependence of the elliptic flow fluctuations by ALICE collaboration in comparison with the RHIC results (STAR and PHOBOS) and the Glauber-type and CGC-type (MC-KLN) theoretical calculations

Due to the event-by-event fluctuations of the nucleon positions in nuclei, the initial profile of the energy density is very complex and may also possess higher harmonic anisotropies. Figure A.4 (a) shows the centrality dependence of the integrated higher harmonic anisotropy measured by the ALICE collaboration [15]. The triangle flow $v_3\{2\}$ and $v_3\{4\}$ have finite values and their centrality dependences are smaller than that of the elliptic flow. Note that the difference between $v_3\{2\}$ and $v_3\{4\}$ is larger than that of the elliptic flow. The magnitudes of the fourth harmonic flow $v_4\{2\}$ are compatible to that of the triangle flow $v_3\{4\}$ and again its centrality dependence is small. These magnitudes and centrality dependencies are roughly consistent to the predictions by hydrodynamic models with the event-by-event initial conditions. Therefore, they can be considered to originate from the eccentricities formed by the initial density fluctuations.

The p_{T} differential higher harmonic flow v_n with $n = 3, 4, 5$ measured by the two-particle cumulant method are shown in Fig. A.4 (b) [15]. Their magnitude becomes weaker than the elliptic flow but the p_{T} dependence is similar for all harmonic flow. Observed v_3 clearly prefer to the viscous hydrodynamics with η/s= 0.08 (this value is still small, c.f. superfluid ^{4}He at χ-point $\sim$ 0.8) while the elliptic flow is less sensitive to the viscosity than the triangle flow. Note that these theoretical calculations are based on the Glauber initial conditions because it was pointed out by the PHENIX collaboration a few years ago that the simultaneous comparison of v_2 and v_3 with the model calculations prefer to the Glauber-type initial conditions than the simple CGC models [17]. However, the latest CGC based models such as Ref. [118] can reproduce the ellptic flow as well as the higher harmonic flow. The interpretations of the measured flow signatures will be easily changed by the further theoretical developments, e.g. the inclusion of the quantum fluctuations in the initial stage [119], the thermodynamical fluctuations during the hydrodynamic evolution [120], the temperature dependence of η/s [121] and so on. Therefore, the systematic measurements of the all harmonic flow are expected to play an enssential role to understand the collision dynamics and the matter properties more presicely.

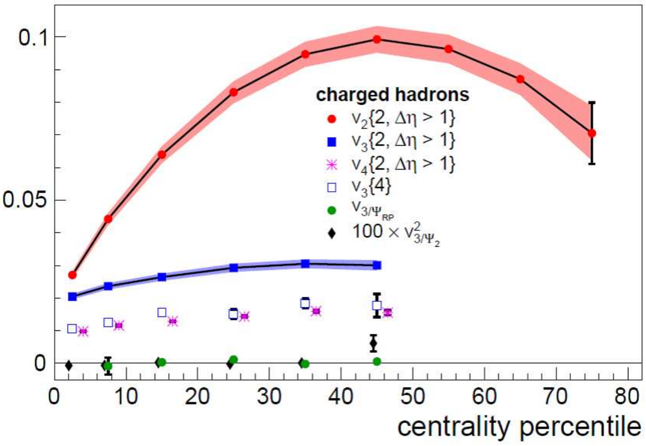

(a)

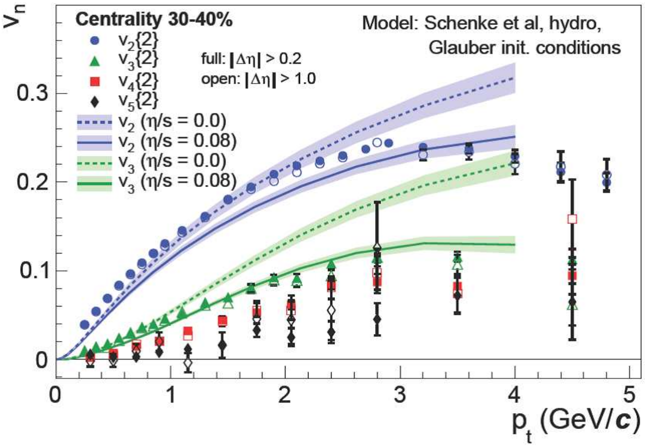

(b)

Figure A.4: (a) The centrality dependence of the integrated flow v_n measured by the ALICE collaboration. $v_n\{2, \Delta\eta > 1\}$ for $n = 2, 3, 4$ is the n-th harmonic flow measured by the two-particle cumulant method with eta-gap between two particles for suppression of the non-flow effects. $v_{3/\Psi_{RP}}$ is the triangle flow with respect to the 2nd harmonic event plane (or the reaction plane) measured by the event plane method. v_{3/Ψ_2} is similar, but measured by the five-particle cumulant method $\langle\cos(3\varphi_\alpha + 3\varphi_\beta - 2\varphi_{\gamma_1} - 2\varphi_{\gamma_2} - 2\varphi_{\gamma_3})\rangle$ [15]. (b) Charged hardron p_{T} differential flow v_n with the two-particle cumulant method measured by the ALICE collaboration in comparison with the Glauber-type initial condition and the viscous hydrodynamic simulations [15].

Appendix B

Chiral Magnetic Effect

B.1 Theoretical Aspects

All gauge field configurations which have finite action can be characterized by a topological invariant, the winding number (Cherm Simons topological charge) Q_w [122]. The winding number is an integer and given as

$$Q_w \equiv \frac{g^2}{32\pi^2} \int d^4x F^a_{\mu\nu} \tilde{F}^{\mu\nu}_a \in \mathbb{Z}, \tag{B.1}$$

where $F^a_{\mu\nu}$ denotes the strength tensor of the gluonic field and $\tilde{F}^{\mu\nu}_a$ is its dual tensor. g denotes the QCD coupling constant with generators normalized as $\mathrm{tr} t_a t_b = \delta_{ab}/2$. In the classical vacuum of QCD the gauge field has to be a pure gauge so that the energy density is minimal. In the temporal gauge ($A_0 = 0$) this implies $A_i(x) = i/gU(x)\partial_i U^\dagger(x)$, where $U(x)$ is an element of the gauge group SU(3). The different classical vacua can be characterized by a topological invariant, the winding number ν which is an integer and given by

$$\nu = \frac{1}{24\pi^2} \int d^3x \epsilon^{ijk} \mathrm{tr}[(U^\dagger \partial_i U)(U^\dagger \partial_j U)(U^\dagger \partial_k U)]. \tag{B.2}$$

Now one can show that if a gauge field configuration goes to a pure gauge at infinity and has nonzero Q_w it induces a transition from one classical vacuum to another, more precisely

$$Q_w = \nu(t = \infty) - \nu(t = -\infty). \tag{B.3}$$

At zero temperature such transition requires tunneling through a potential barrier. A height of the barrier is order the QCD scale Λ_{QCD} over the strong coupling constant α_S, so the transition rate will be suppressed exponentially. In this case the main contribution to the transition rate comes from fluctuations around instantons (which are minima of the classical Euclidean action). The transition rate due to instantons will go down if the temperature is raised.

It was also realized that the QCD contains static solutions which have finite energy and half integer winding number, which is called a sphaleron as shown in Fig. B.1 [123]. Figure B.1 shows a potential of the gluon field, which has a structure like a Bloch crystal. Sphalerons exist on the unstable point of the potential as shown by the red symbol. If the temperature is higher than the energy of the sphaleron it is likely that one can go over the barrier instead of tunneling. It will happen at the high temperature environment in the QGP. The existence of topological gluonic field configurations with non-zero Q_w is one of the intriguing predictions of QCD, but it was not yet directly found experimentally. The relativistic heavy ion collisions are the best place to search the experimental evidence for their existence.

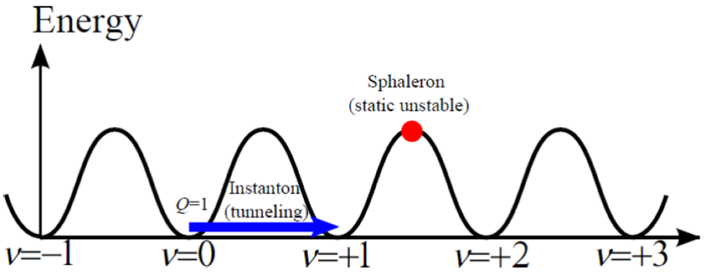

Figure B.1: A classical potential of the gluon field as a Bloch crystal. The minimums of its potential exist at the integer ν. The QCD vacuum is a superposition of states with different topology. The gauge field configurations with $Q_w = 1$ invoke the transition shown by blue arrow [125].

An interesting feature of these transitions is that they involve the parity P and charge-parity CP odd field configurations [125]. Figure B.2 (a) shows the visualization of topological charge density associated with such configurations calculated by QCD lattice simulations. The topological charge density fluctuates like metastable bubbles [124]. We call them the parity-odd bubbles or the bubbles with non-zero topological charge density. Several dynamical scenarios for the production and the decay of the parity-odd bubbles have been considered. It was proposed that in the vicinity of the deconfinement phase transition QCD vacuum can possess metastable parity-odd domains [126]. It was also suggested that they are generated in the initial state of the quark-gluon plasma produced in heavy-ion collisions, i.e. the so-called glasma [127]. In the content of the parity violating phenomena, it was pointed out processes which are normally forbidden, such as $\eta \rightarrow \pi^0\pi^0$, will be allowed in parity odd bubbles. As another promising phenomena, the experimental studied of P- and CP- odd correlations of pion momenta were also proposed and seem to be in principle feasible [126, 128].

In QCD, the probability to generate either a parity-odd bubble with positive or negative winding number is equal. This is because there is no direct P and CP violation in QCD. Importantly, the parity-odd bubbles can transform left- into right-handed quarks

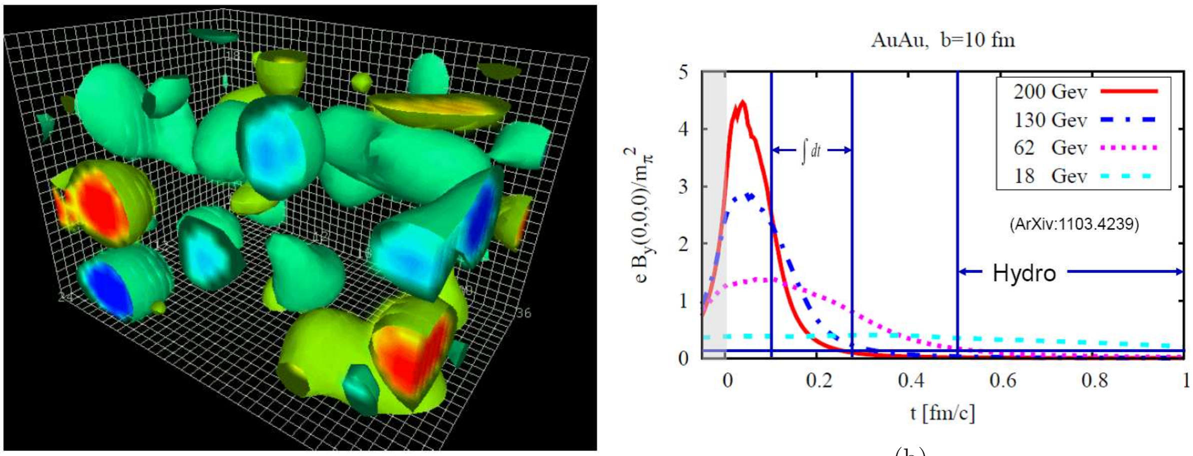

(a)

(b)

Figure B.2: (a) The visualization of the quantum fluctuation of the topological charge density in QCD vacuum calculated by QCD lattice simulation [124]. (b) A magnetic field generated in the Au–Au collisions as a function of time. A large magnetic field at $t \sim 0.05$ generates by the two spectators. One order or more smaller magnetic field than the magnetic field at $t \sim 0.05$ fm/c remains rather long time, which is created by the angular momentum and the charge in the participant region. The metastable bubbles with topological charge can be created at both the beginning of the collisions described by e.g. glasma and the later stage of the hydrodynamic hot matter [129].

or vice versa via the axial anomaly.

$$\frac{d(N_R - N_L)}{dt} = \frac{g^2 N_f}{16\pi^2} \int d^3x F^a_{\mu\nu} \tilde{F}^{\mu\nu}_a, \tag{B.4}$$

where $N_{R,L}$ denotes the net number of quarks (minus antiquarks) with right/left-handed chirality. This equation is derived from the space integral of the axial Ward-identity. As a result of the axial anomaly the interactions between the topological configurations and the quarks locally violate the net chirality conservation and also break P and CP symmetries. Then, the variance of the chirality will be nonzero. Every time events of quark gluon plasma is produced, it will posses a non-zero net chirality.

A large magnetic field ($\sim 10^{15}$ T) is expected to be generated perpendicularly to the reaction plane during the non-central heavy ion collisions as shown in Fig. B.2 (b) [129]. A large magnetic field at $t \sim 0.05$ generates by the two spectators. One order or more smaller magnetic field than the magnetic field at $t \sim 0.05$ fm/c remains rather long time, which is created by the angular momentum and the charge in the participant region. In the presence of this large external magnetic field, the net chirality originated from the existence of the parity-odd bubbles is expected to result in the asymmetric charge emission along the magnetic field, i.e. the charge separation with respect to the reaction plane. This is called Chiral Magnetic Effect (CME) [36, 37, 38]. Figure B.3 illustrates the classical picture of the CME with the time evolution from left panel to the right one. The red and blue arrows denote the direction of momentum and the spin of the quarks respectively. Firstly, due to the large magnetic field up and down quarks are all in the lowest Landau level and can only move along the direction of the magnetic field. Initially there are as many left-handed quarks as right-handed quarks. Then, the quarks interact with the parity-odd bubbles. Assuming $Q_w = -1$, this will convert a left-handed up/down quark into a right-handed up/down quark by reversing the direction of momentum. Finally the right-handed up quarks will move upwards, the right-handed down quarks will move downwards in this picture. A charge difference of $Q = 2e$ will be created between two sides of a plane perpendicular to the magnetic field. Figure B.4 shows that such charge separation is indeed related to the parity violation in QCD.

However, a few hundreds of the parity-odd bubbles can be created in a single heavy ion collision because the typical size of the parity-odd bubble is expected to be ~ 0.3 fm and the typical transverse size of the participant regions in the heavy ion collisions is a few tens fm. Since the probability to generate either a parity-odd bubble with positive or negative winding number is equal, the net charge separation in a single event is not significant.

The CME could be used to determine whether a chirally symmetric phase of matter is created in heavy ion collisions [36, 37]. Deconfinement may not be a necessary requirement for the charge separation to work. This is because the confinement state itself does not conduct electric current but in the presence of strong magnetic field it turns into an anisotropic conductor [130]. On the other hand, chiral symmetry restoration is essential to produce the nonzero net chirality because a chiral condensate will tend to erase any asymmetry between the number of right- and left-handed fermions. Therefore, it is important to consider the time scale of the magnetic field, the production of the parity-odd bubbles and the chiral symmetry restoration to calculate the magnitude of the resulted charge separation.

Recently, the theoretical evidence of the charge separation due to the CME has been found in lattice QCD calculations [131]. Further theoretical studies reveal rich structures related to the local parity violation and the magnetic field in the QGP such as the chiral veortical effect [132], the chiral magnetic spiral [133], the chiral magnetic wave [134] and so on.

B.2 Further experimental results from the STAR collaboration

Figure B.5 shows the charge dependent part of the correlation $\langle\cos(\varphi_\alpha + \varphi_\beta - 2\Psi_{RP})\rangle$ decreases as collision energy decreases from $\sqrt{s_{NN}} = 7.7$ GeV to 200 GeV [136]. This collision energy dependence may be explained by the probability to produce the parity-odd bubbles, the magnitude of the magnetic field and the lifetime of the chiral restoration phase in the collisions in the context of the CME.

Figure B.6 shows the pair differential correlations for centrality 30-50% events measured by the STAR collaboration [39]. The correlation depends on $|p_{T,\alpha} - p_{T,\beta}|$ weakly,

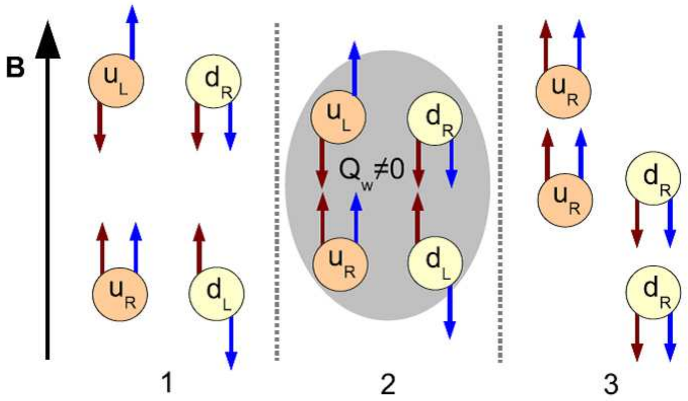

Figure B.3: The classical picture of the Chiral Magnetic effect (CME). A time evolves from left to right (1 → 2 → 3). The red and blue arrows denote the direction of momentum and the spin of the quarks respectively. A grey region represents the parity-odd bubbles with winding number $Q_w \neq 0$. [36]

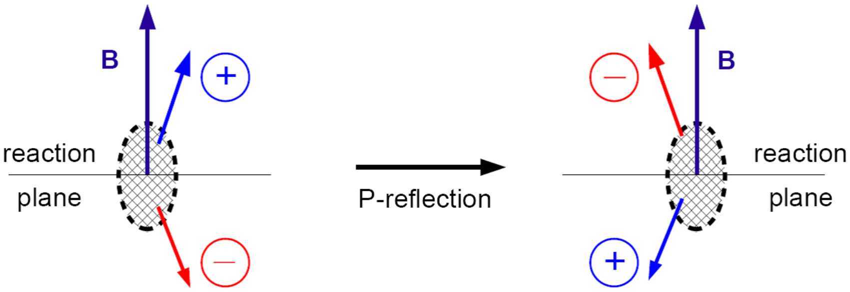

Figure B.4: Parity-violation of the charge separation with respect to the reaction plane [135].

which excludes the short range correlations due to the quantum interference (HBT) and Coulomb effect. The charge dependent part of the correlation increases with $(p_{T,\alpha} + p_{T,\beta})/2$, which contradicts the signal concentration in the low p_{T} region as naively expected with the CME. Finally, the dependence on $\Delta\eta$ has a typical hadronic width of about one unit of pseudo-rapidity as expected with the CME.

In this thesis, the integrated and differential correlations $\langle\cos(\varphi_\alpha+\varphi_\beta-2\Psi_{RP})\rangle$ for the same and opposite charge combinations are measured at the LHC energy by the ALICE collaboration.

The correlated particles are produced in a domain of the order of 1 fm, and it is expected that the correlations should have a width of the order of unity in $\Delta\eta = |\eta_\alpha - \eta_\beta|$, as is typical for hadronic production from clusters.

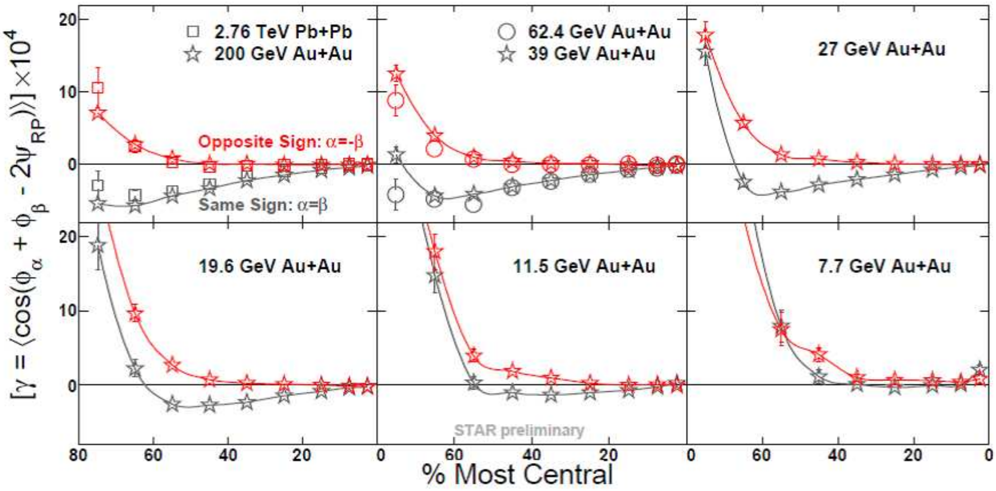

Figure B.5: The centrality dependence of the correlation $\langle\cos(\varphi_\alpha + \varphi_\beta - 2\Psi_{RP})\rangle$ in $\sqrt{s_{NN}}$ =7.7, 11.5, 19.6, 27, 39, 62.4 and 200 GeV Au–Au collisions at RHIC measured by the STAR collaboration [136].

The main contribution to the signal should come from particles with low transverse momentum although the actual dependence might be affected by the radial flow.

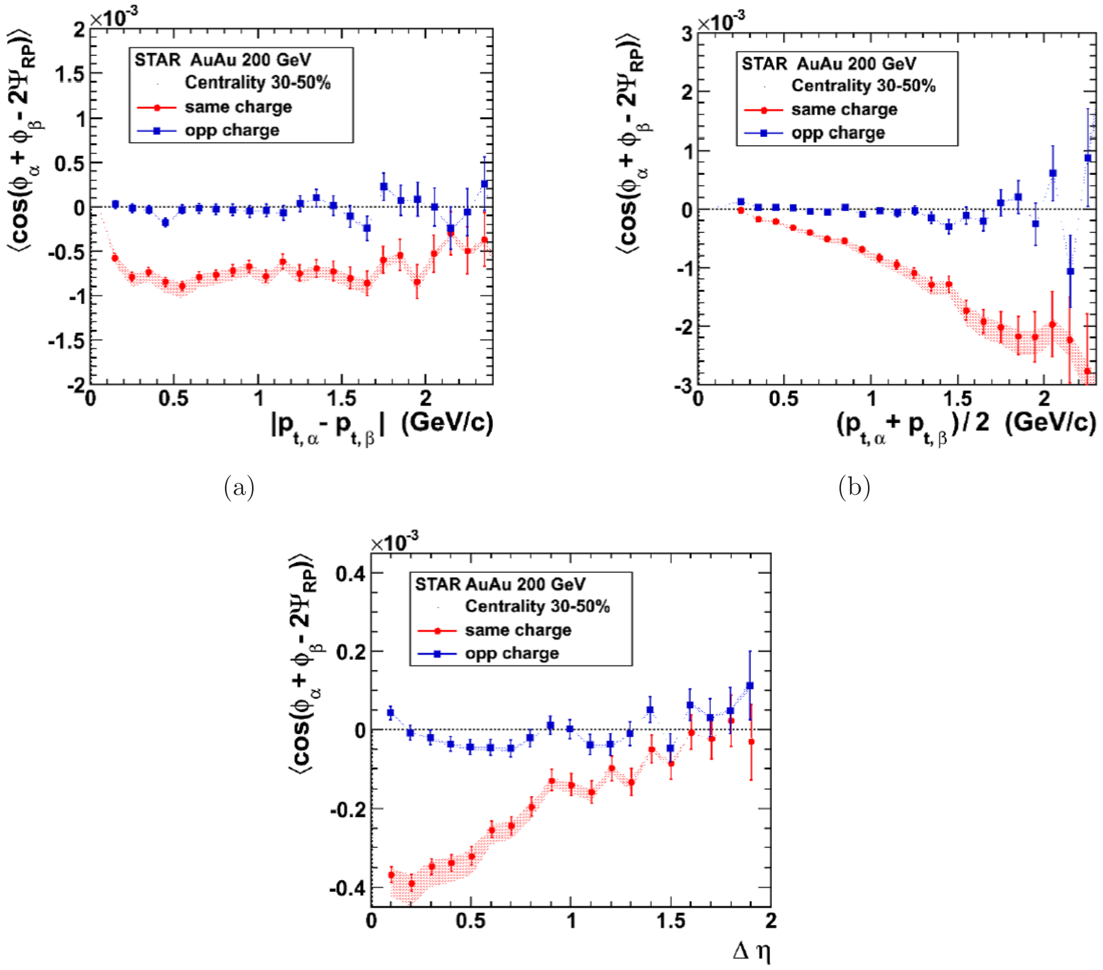

(a)

(b)

(c)

Figure B.6: The pair differential correlation $\langle \cos(\varphi_\alpha + \varphi_\beta - 2\Psi_{RP}) \rangle$ as a function of (a) the transverse momentum difference $|p_{T,\alpha} - p_{T,\beta}|$, (b) the average transverse momentum $(p_{T,\alpha} + p_{T,\beta})/2$, (c) the rapidity separation $\Delta\eta = |\eta_\alpha - \eta_\beta|$ of the charged particle pair for centrality 30-50% events measured by the STAR collaboration [39].

Appendix C

Figures for the systematic uncertainty study of the differential correlations

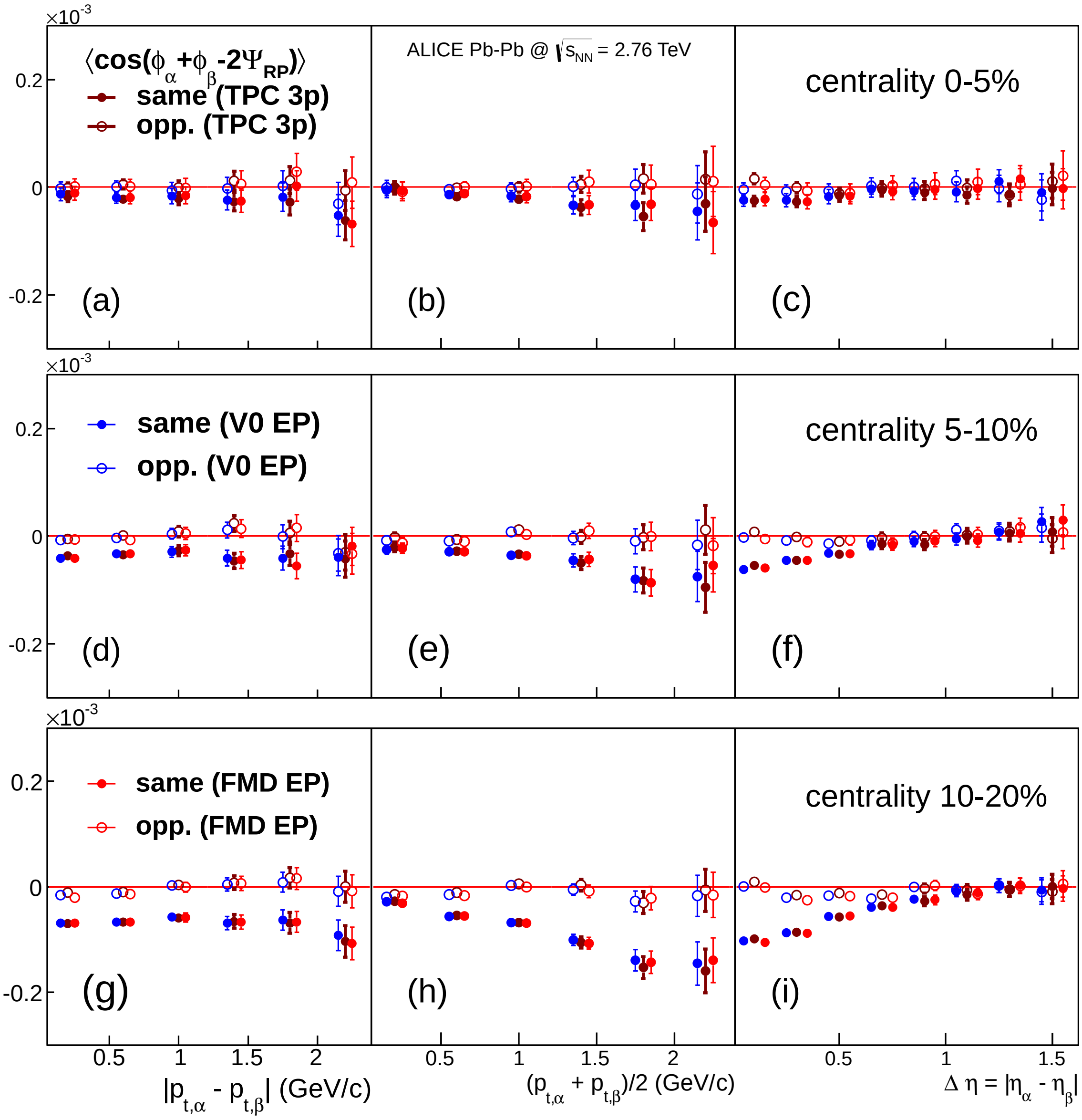

Figure C.1: The pair differential 3-particle correlator $\langle \cos(\varphi_\alpha + \varphi_\beta - 2\Psi_{RP}) \rangle$ with the different methods. Top: centrality 0-5%, Center: centrality 5-10%, Bottom: centrality 10-20%.

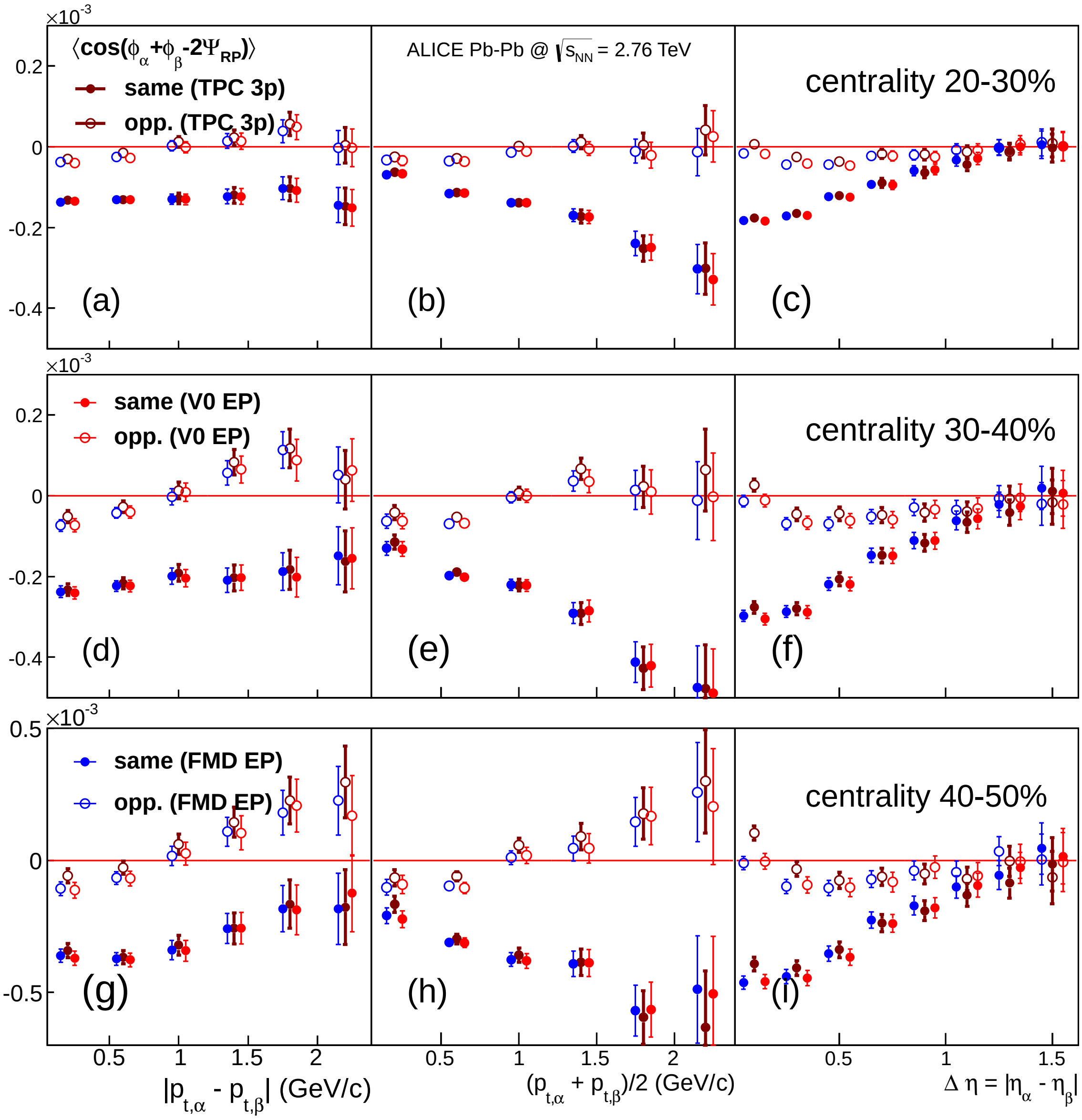

Figure C.2: The pair differential 3-particle correlator $\langle \cos(\varphi_\alpha + \varphi_\beta - 2\Psi_{RP}) \rangle$ with the different methods. Top: centrality 20-30%, Center: centrality 30-40%, Bottom: centrality 40-50%.

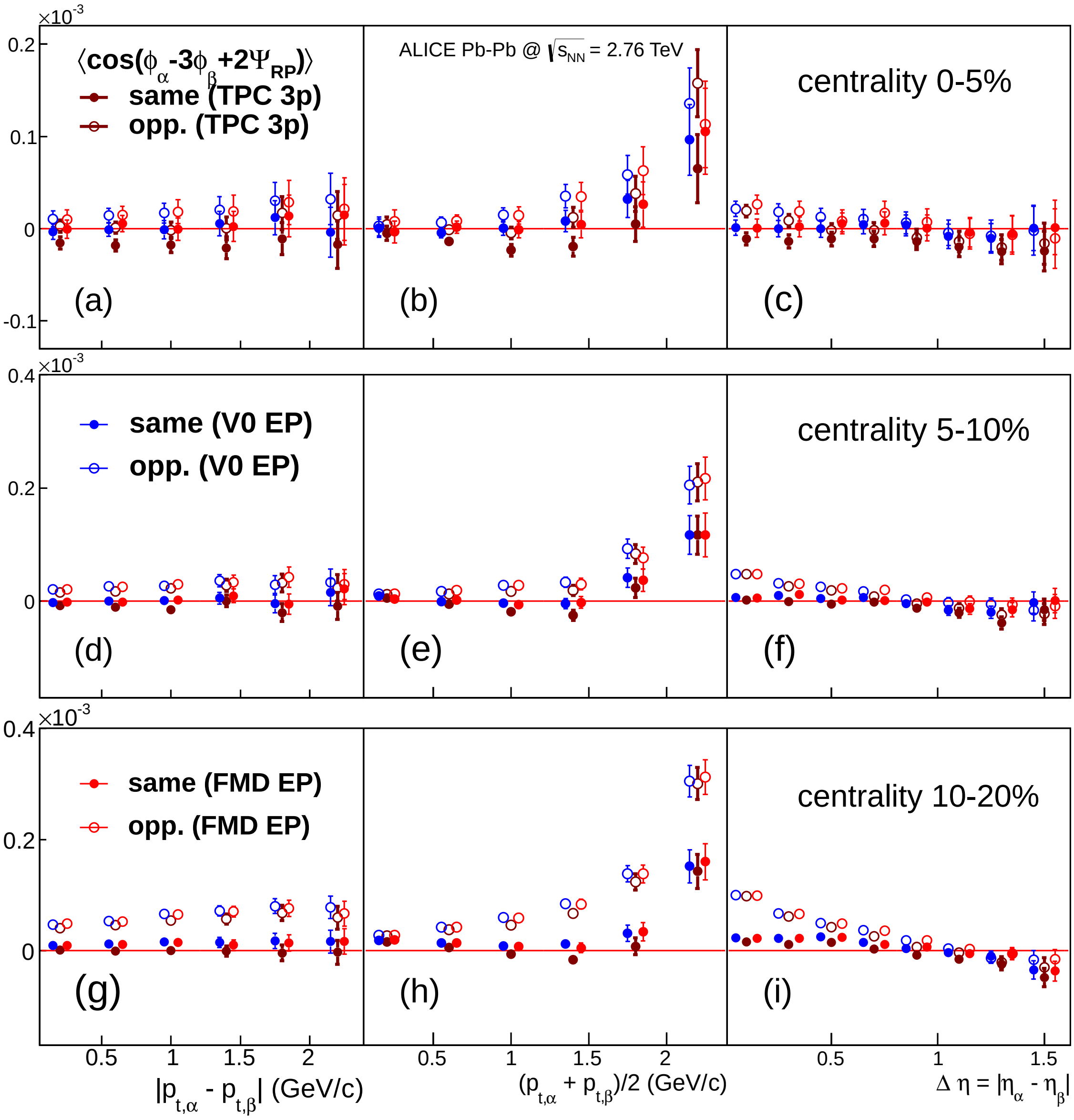

Figure C.3: The pair differential 3-particle correlator $\langle\cos(\varphi_\alpha - 3\varphi_\beta + 2\Psi_{RP})\rangle$ with the different methods. Top: centrality 0-5%, Center: centrality 5-10%, Bottom: centrality 10-20%.

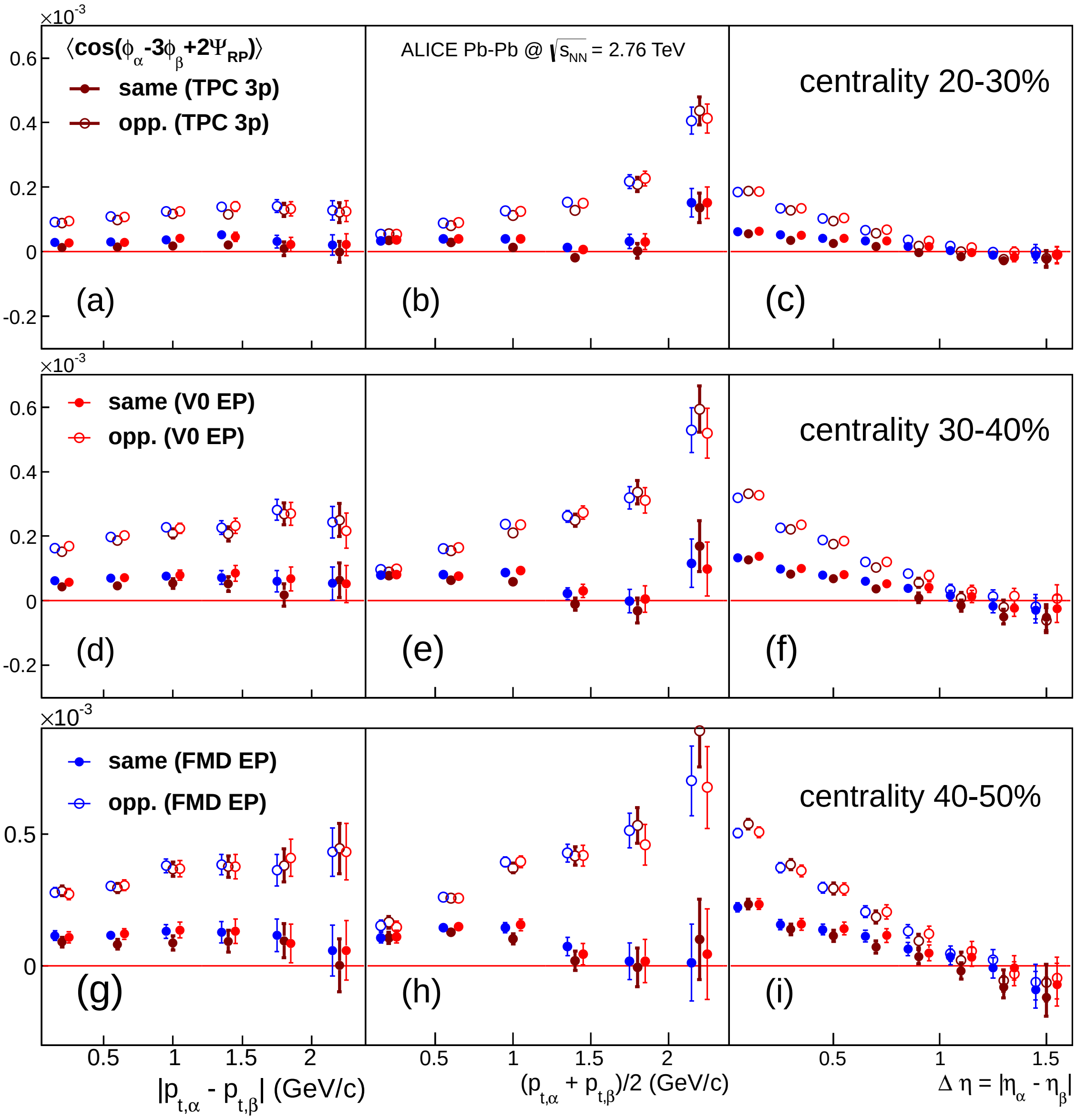

Figure C.4: The pair differential 3-particle correlator $\langle \cos(\varphi_\alpha - 3\varphi_\beta + 2\Psi_{RP}) \rangle$ with the different methods. Top: centrality 20-30%, Center: centrality 30-40%, Bottom: centrality 40-50%.

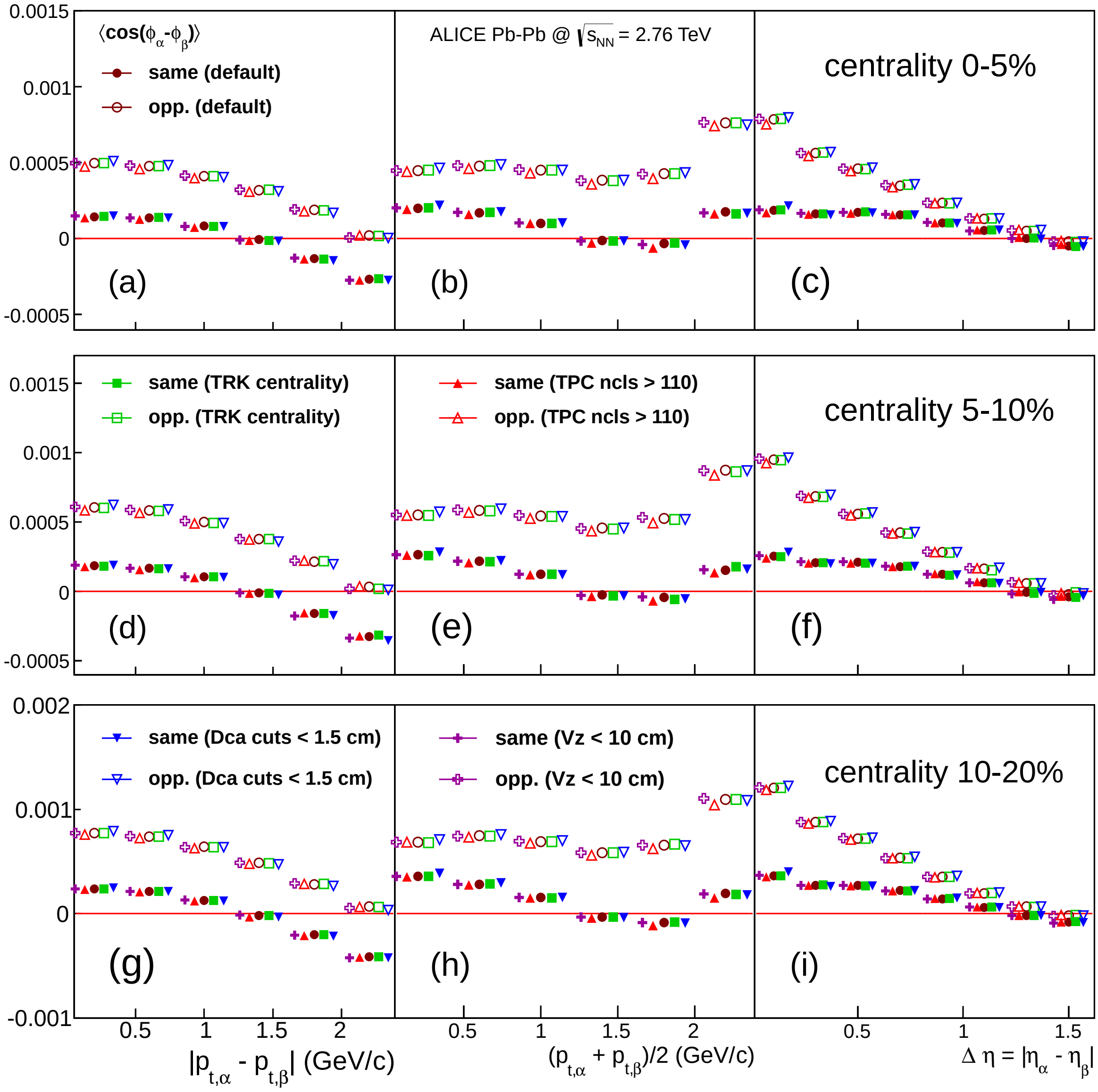

Figure C.5: The pair differential 3-particle correlator $\langle\cos(\varphi_\alpha - \varphi_\beta)\rangle$ with the various event and track cuts. Top: centrality 0-5%, Center: centrality 5-10%, Bottom: centrality 10-20%.

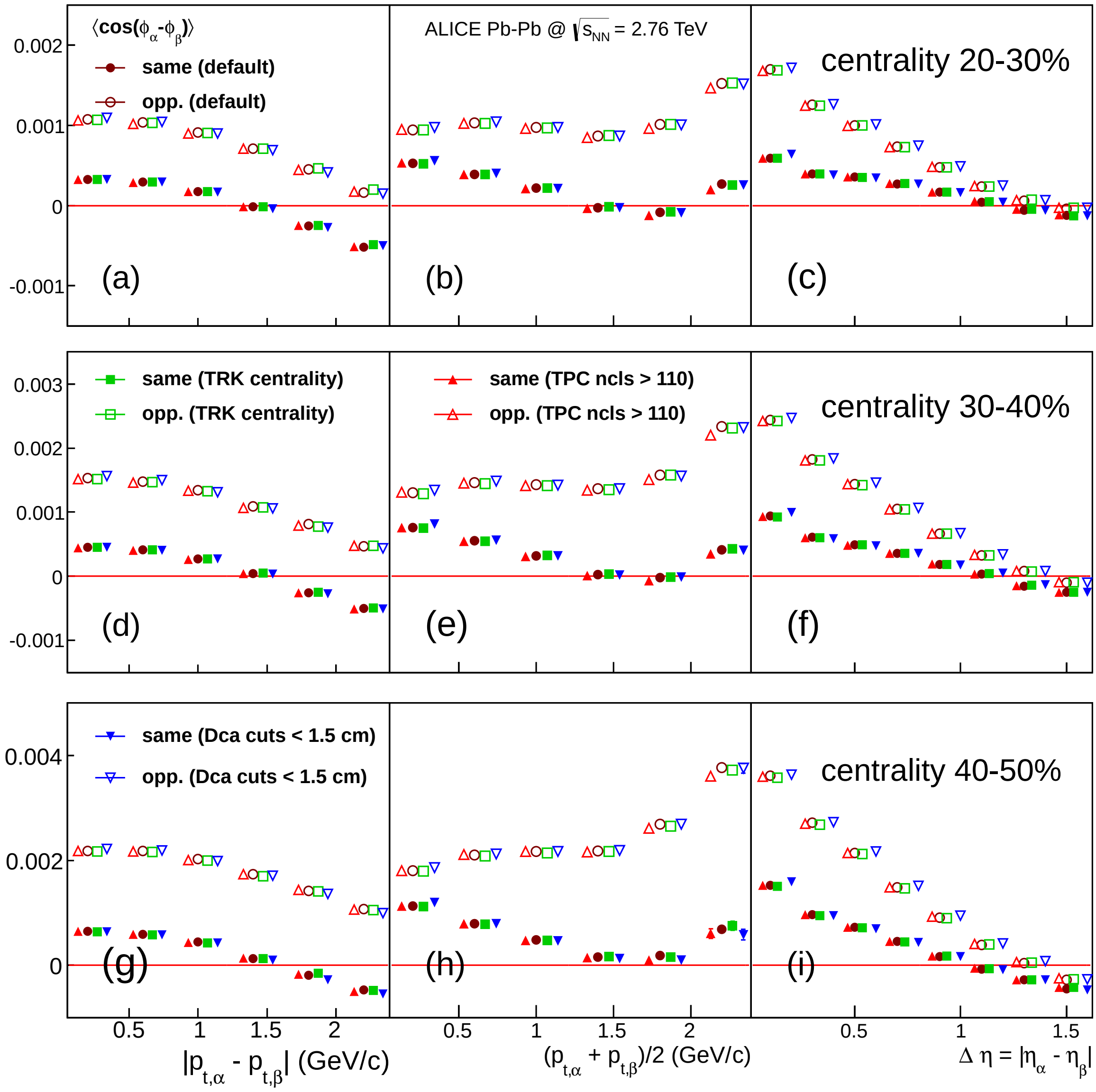

Figure C.6: The pair differential 3-particle correlator $\langle\cos(\varphi_\alpha - \varphi_\beta)\rangle$ with the various event and track cuts. Top: centrality 20-30%, Center: centrality 30-40%, Bottom: centrality 40-50%.

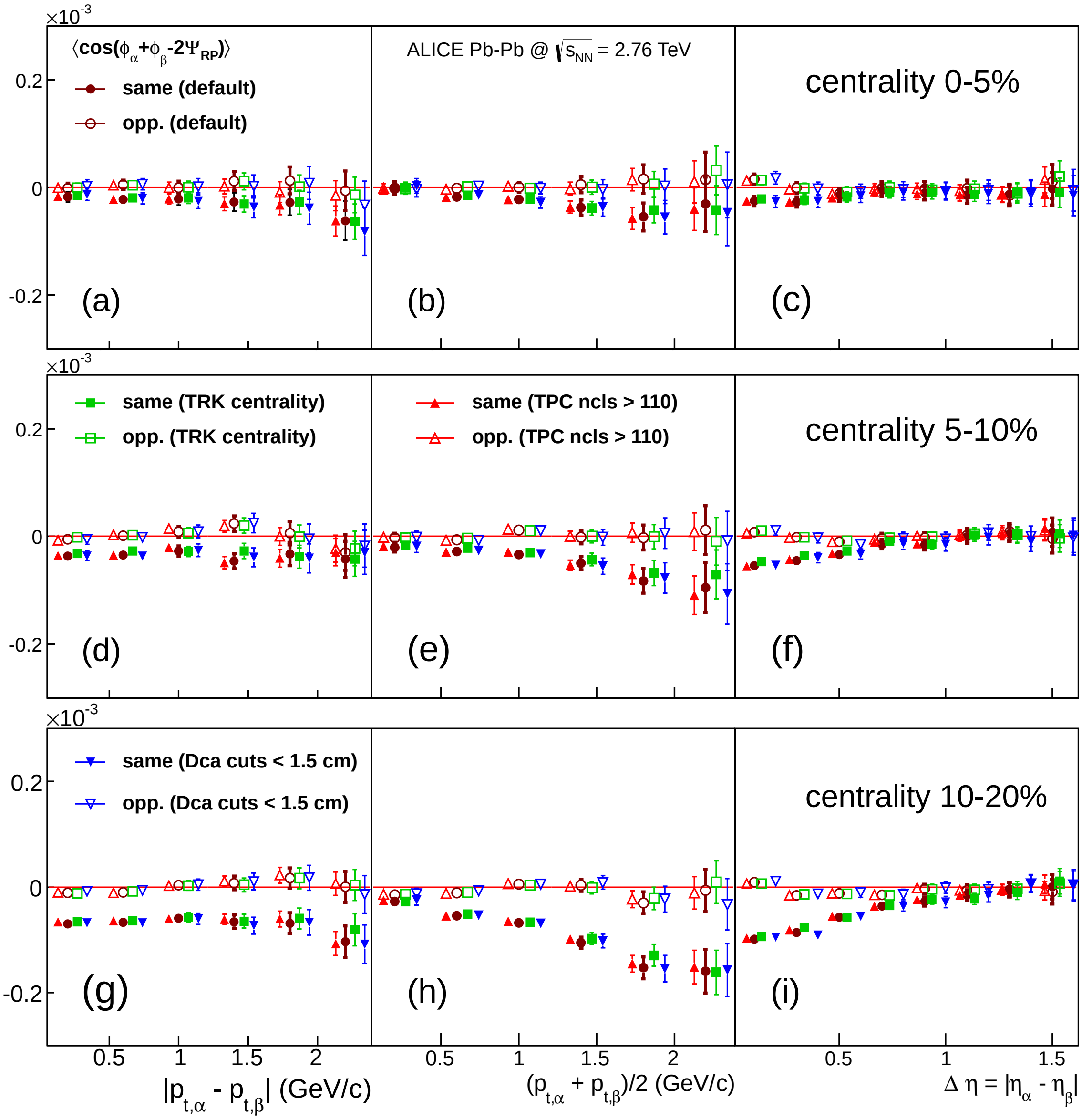

Figure C.7: The pair differential 3-particle correlator $\langle\cos(\varphi_\alpha + \varphi_\beta - 2\Psi_{RP})\rangle$ with the various event and track cuts. Top: centrality 0-5%, Center: centrality 5-10%, Bottom: centrality 10-20%.

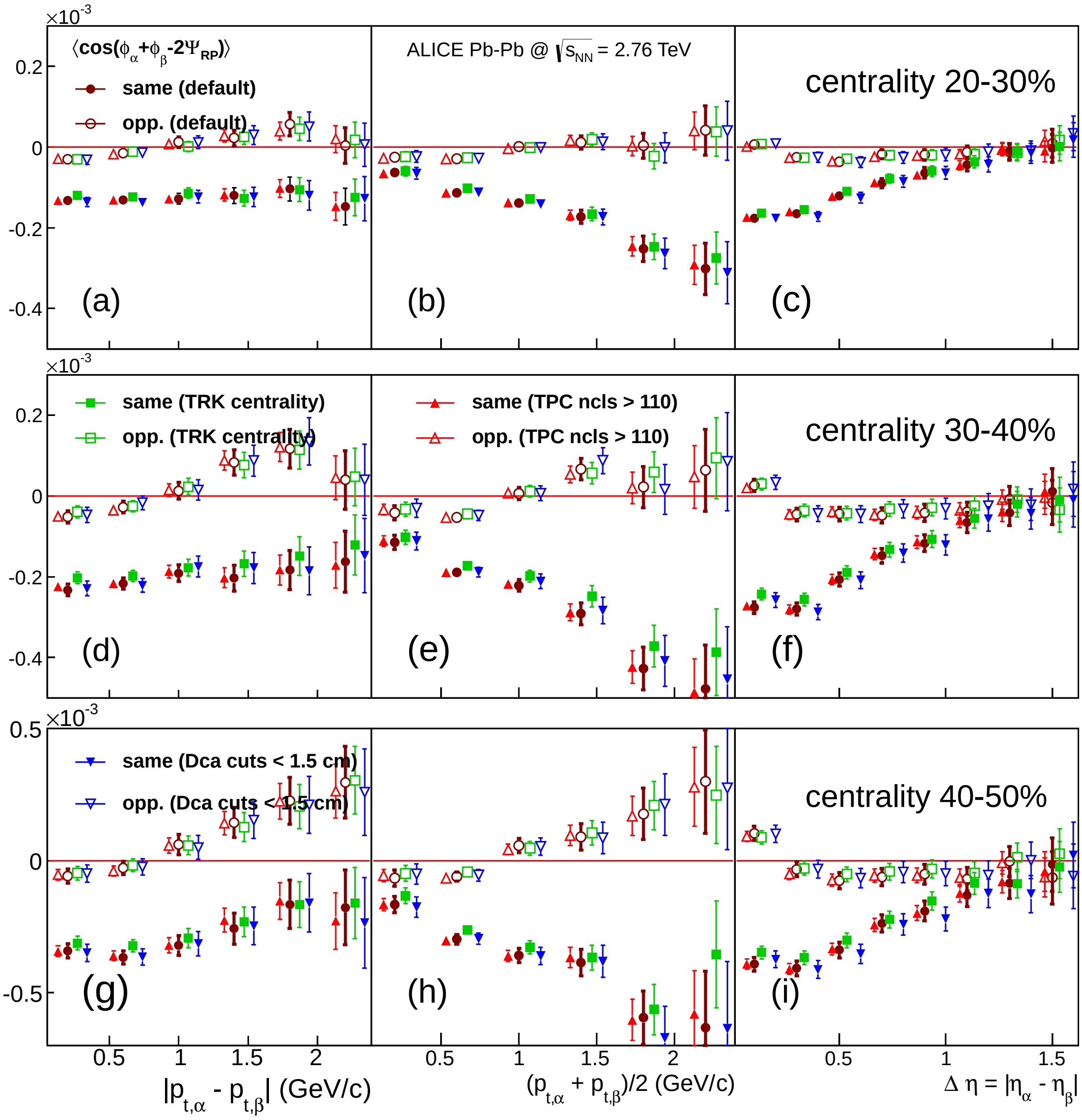

Figure C.8: The pair differential 3-particle correlator $\langle \cos(\varphi_\alpha + \varphi_\beta - 2\Psi_{RP}) \rangle$ with the various event and track cuts. Top: centrality 20-30%, Center: centrality 30-40%, Bottom: centrality 40-50%.

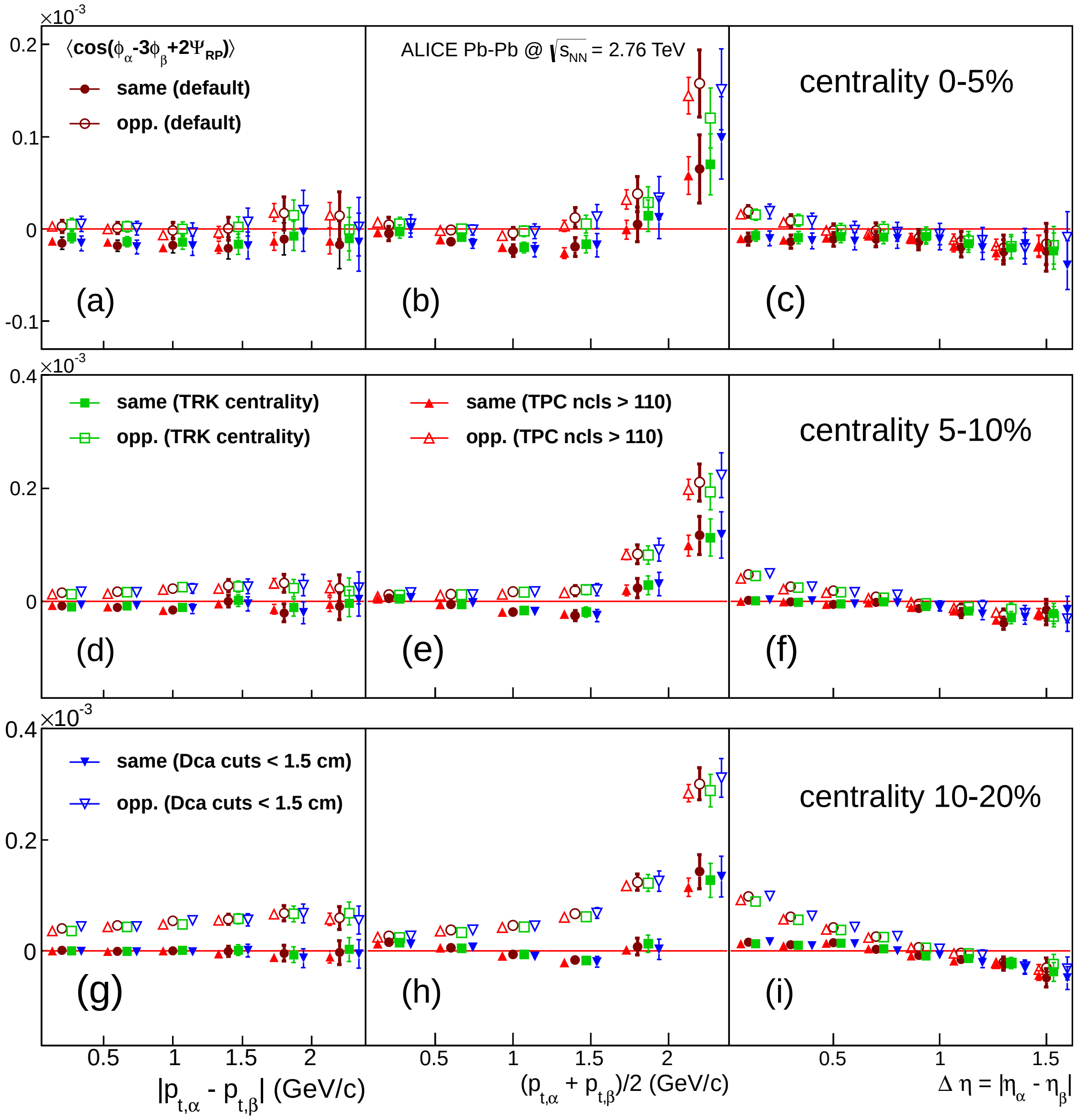

Figure C.9: The pair differential 3-particle correlator $\langle\cos(\varphi_\alpha - 3\varphi_\beta + 2\Psi_{RP})\rangle$ with the various event and track cuts. Top: centrality 0-5%, Center: centrality 5-10%, Bottom: centrality 10-20%.

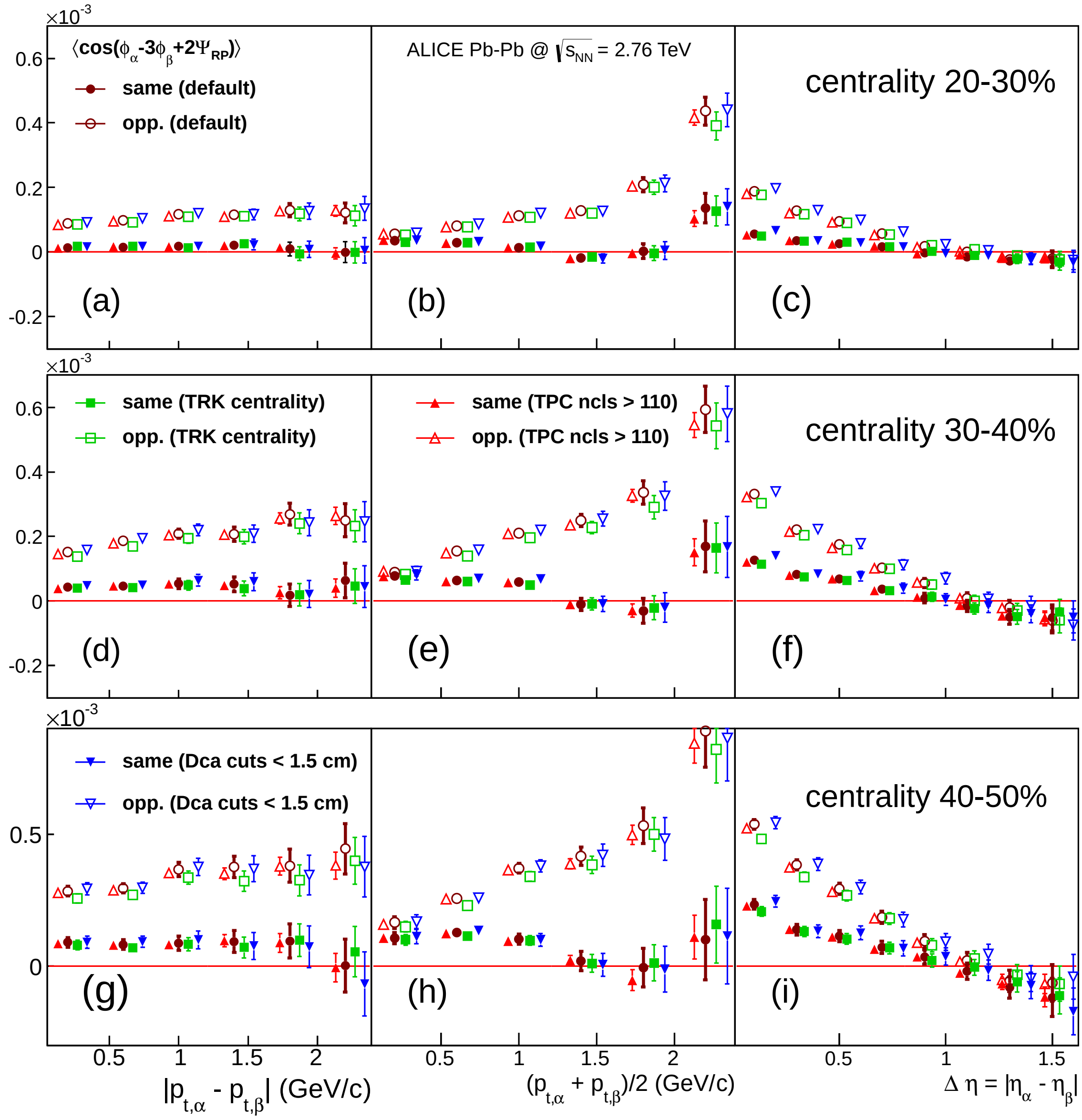

Figure C.10: The pair differential 3-particle correlator $\langle\cos(\varphi_\alpha - 3\varphi_\beta + 2\Psi_{RP})\rangle$ with the various event and track cuts. Top: centrality 20-30%, Center: centrality 30-40%, Bottom: centrality 40-50%.

Appendix D

Tracking algorithm and Calibration of the TPC

Kalman filter has advantages in tracking:

- It takes into account multiple scattering, magnetic field inhomogeneity.
- It has possibility to take into account mean energy losses
- It is the efficient way to match tracks between several detectors

The reconstruction begins with cluster finding in all of the ALICE detectors. After the determination of the position of each clusters is determined, tracking procedure are executed with Kalman Filter [137].

Kalman filter is quite a general and powerful method for statistical estimations and predictions. The conditions for its applicability are the following. A certain system is determined at any moment in time t_k by a state vector x_k In the tracking of ALICE detectors, k corresponds to the ID number of the cluster, and a state vector x_k corresponds to the track parameter. The state vector varies with time according to an evolution equation:

$$x_k = f_k(x_{k-1}) + \epsilon_k. \tag{D.1}$$

It is supposed that f_k is a know deterministic function and ϵ_k is a random vector of intrinsic process noise which has a zero mean value ($\epsilon_k = 0$) and known covariance matrix (cov(δ_k=V_k)). In many cases, the measurement function h_k can be represented by a certain matrix H_k:

$$m_k = H_k x_k + \delta_k. \tag{D.2}$$

If, at certain time t_{k-1}, we are given some estimates of the state vector $\tilde{x}_{k-1}$ and of its covariance matrix $\tilde{C}_{k-1} = cov(\tilde{x}_{k-1} - x_{k-1})$, these estimates can be extrapolated to the next time slot t_k by means of formulas (this is called prediction):

$$\tilde{x}_k^{k-1} = f_k(\tilde{x}_{k-1}), \tilde{C}_k^{k-1} = F_k \tilde{C}_{k-1} F_k^T + Q_k,\ F_k = \frac{\partial f_k}{\partial x_{k-1}}. \tag{D.3}$$

The value of the prediction χ^2 increment can be also calculated:

$$(\chi^2)_k^{k-1} = (r_k^{k-1})^T (R_k^{k-1})^{-1} r_k^{k-1}, r_k^{k-1} = m_k - H_k \tilde{x}_k^{k-1}, \\ R_k^{k-1} = V_k + H_k \tilde{C}_k^{k-1} H_k^T. \tag{D.4}$$

The number of degrees of freedom is equal to the dimension of the vector m_k.

If at the time t_k, together with the results of predictions, we also have the results of the state vector measurement, this additional information can be combined with the prediction results (this is called filtering). As a consequence, the estimation of the state vector improves:

$$\tilde{x}_k = \tilde{x}_k^{k-1} + K_k(m_k - H_k \tilde{x}_k^{k-1}),\ \tilde{C}_k = \tilde{C}_k^{k-1} - K_k H_k \tilde{C}_k^{k-1}, \tag{D.5}$$

where K_k is the Kalman gain matrix $K_k = \tilde{C}_k^{k-1} H_k^T (V_k + H_k \tilde{C}_k^{k-1} H_k^T)^{-1}$.

Finally, the next formula gives us the value of the filtered χ^2 increment:

$$\chi^2 = (r_k)^T (R_k)^{-1} r_k,\ r_k = m_k - H_k \tilde{x}_k,\ R_k = V_k - H_k \tilde{C}_k H_k^T. \tag{D.6}$$

It can be shown that the predicted χ^2 value is equal to the filtered one:

$$(\chi^2)_k^{k-1} = \chi_k^2. \tag{D.7}$$

The prediction and filtering steps are repeated as many times as we have measurements of the state vector. In the case of tracking in ALICE, the number of steps corresponds to the number of clusters for the track.

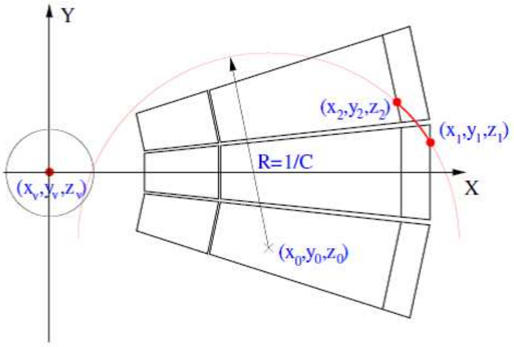

Figure D.1: Track finding coordinate system, track parameters and the schematic view of seeding with the vertex constraint.

The reconstructed TPC tracks and clusters are expressed in the local coordinate system. y and z coordinates for the intersection point of a track at a pad row of a given x coordinate are then given by the equations:

$$\begin{aligned} y(x) &= y_0 - \frac{1}{C} - \sqrt{1-(Cx-\eta)^2}, \\ z(x) &= z_0 - \frac{\tan\lambda}{C}\arcsin(Cx-\eta),\ \eta \equiv Cx_0, \end{aligned} \tag{D.8}$$

where C is the curvature of the track projection on the pad plane, λ is the dip angle between the track and the pad plane, (x_0,y_0) are the coordinates of the center of the curvature of the track projection on the pad plane, and $z_0 \equiv z(x_0)$ as shown in Fig. D.1.

The track state vector $\mathbf{x}^T$ used in the Kalman filter calculation is then chose as

$$\mathbf{x}^T = (y, z, \sin\phi, \tan\lambda, C). \tag{D.9}$$

With this track parametrization, only three of the five components of the state vector (the local track position y,z and $\sin\phi$) change as the track is propagated from one pad row to another as followings:

$$\begin{aligned} y_{k+1} &= y_k + dx \cdot (c_1 + c_2)/(r_1 + r_2), \\ z_{k+1} &= z_k + dx \cdot (c_1 + c_2)/(c_1 r_1 + c_2 r_2) \cdot \tan\lambda, \\ \sin\phi_{k+1} &= \sin\phi_k - c_1 + c_2, \end{aligned} \tag{D.10}$$

where $dx = x_{k+1} - x_k$, $c_1 = Cx_k - Cx_0$, $c_2 = Cx_{k+1} - Cx_0$, $r_1 = 1 - c_1^2$, and $r_2 = 1 - c_2^2$. Detail descriptions for $F_k\tilde{C}_{k-1}F^T$, Q_k due to the multiple scattering and the update of the parameter C due to the energy loss are found in Ref. [137]. These calculations are done 159 times (number of TPC pad rows) per a track. When a track is leaving one sector and is entering another, the coordinate system is rotated, then three components (y, z and $\sin\phi$) have to be changed.

A first estimation of the primary vertex position is performed using pairs of hits in the SPD (tracklets) and it is used as a starting point for the track finding. The track finding algorithm is ran starting from the hits at the outer radius of the TPC where the track density is low and prolonging the trajectories towards the inside. The outermost TPC pad rows and the primary vertex position are used as seeds. When tracks are prolonged to the inner radius of the TPC, the algorithm is called for the ITS. TPC tracks are matched to points in the outermost SSD layer and then prolonged to inner ITS layers until the first SPD layer. Next step is back propagation and refit of the tracks outward in the ITS and then in the TPC. Once the outer radius of TPC is reached, tracks are prolonged and matched to the TRD at first and then to the other detectors of the central barrel (TOF, HMPID, PHOS, EMCAL) for particle identification. At this point the tracks are again propagated inward down to the ITS and to the primary vertex as computed in the first step. Finally the final position of the primary vertex is computed from the reconstructed tracks to obtain the optimal resolution. Each tracks *dca* to this final primary vertex are calculated [55, 56].

The basic calibration program for the TPC can be separated into three types as followings [138, 139].

- Correction for the readout circuit
  The pedestal and noise for each pads are taken during the pedestal runs and their values are transfer ed to the ALTRO chip for zero suppression and baseline correction.

The length of the lines on the readout board for each channel is different and there are timing differences of the charge signals between readout pads typically 200μm (7 ns). This correction is applied before the installation of the TPC in the ALICE site. The timing for each channel is measured with induction charge made by input of pulse signals into the cathode wires of the readout chambers. This pulser system can be also used for the electronics gain calibration and the detection of the dead electronics.

- Correction of the Drift velocity
  Since the E field of the TPC is not high enough for the gas drift velocity to be saturated with E/P, the drift velocity in the ALICE TPC is sensitive to the E field, temperature, pressure and gas composition variations. Dedicated temperature and pressure sensors are situated within and around the TPC. The gas composition is monitored by the GOOFIE system. All measured environmental properties are handled by DCA system and transported via the Suttle system into the OCDB, where all important reconstruction parameters are stored. After the reconstruction, the drift velocity can be checked using the matching between the ITS hits and the TPC tracks and the laser system.

- Correction of the Gas gain amplification
  For the absolute gas gain calibration, a radioactive Krypton-gas is used during the special calibration run. Another approach uses electrons from the central electrode illumination by the laser light.

Appendix E

Calibration of the TPC $E \times B$ space point distortions

Time Projection Chamber (TPC) is a main central tracking device in ALICE detector at LHC. TPC is cylindrical shape and operated in 0.5 T solenoidal B field parallel to the E field axis. A central HV electrode divides TPC into two volumes, which are called A side and C side. The direction of E field at A side is opposite to that of C side. For each side, a maximum drift length is $L \sim 2.5$ m.

The direction of electron drift is same as that of E field if $E \times B$ is perfectly zero. However, many imperfect structures lead to E and B field distortions listed below, which in turn lead to space point distortions in the pad plane [140].

- B field non-uniformity
  B field can be precisely measured, so the correction for them is done rather well.
- $E \times B$ twist
  It occurs when global axis of E and B field are not precisely parallel each other.
- E field non-uniformity
  E field distortions are caused by the imperfect structures of the TPC and often difficult to identify. In particular, E field non-uniformity due to the space charge will be important for the future high luminosity experiment.

E.1 Equation to correct TPC $E \times B$ space point distortions

The solution of the steady-state Langevin equation to describe the motion of the drift electron under E and B fields is

$$\overrightarrow{u} = \frac{\mu|\overrightarrow{E}|}{(1+\omega^2\tau^2)}\Big[\hat{E} + \omega\tau(\hat{E} \times \hat{B}) + \omega^2\tau^2(\hat{E} \cdot \hat{B})\hat{B}\Big], \tag{E.1}$$

where $\overrightarrow{u}$ is the drift velocity and μ is the scalar mobility of the electron [141]. τ denotes the mean time between collisions of the drift electron with atom in the gas and ω is the cyclotron frequency:

$$\omega\tau = q\mu B = \frac{-10B\nu_0}{||E||}\frac{[kGauss][cm/\mu sec]}{[V/cm]}, \tag{E.2}$$

where $\nu_0(=\mu|E|)$ strongly depends on the temperature and in the case of ALICE TPC its fluctuation is expected to be $\sim 2\%$. Lets's assume that E and B fields are nearly parallel $|\overrightarrow{E}| \sim E_z \sim E_0$ and $|\overrightarrow{B}| \sim B_z \sim B_0$. Furthermore, we assume the small perturbations $E_x \sim E_y \ll E_z$ and $B_x \sim B_y \ll B_z$. Then we have the following simplifications with 2nd order approximations:

$$\begin{aligned}
\hat{E}_x = \frac{E_x}{E_z} \quad &\text{and} \quad \hat{E}_y = \frac{E_y}{E_z}, \\
\hat{B}_x = \frac{B_x}{B_z} \quad &\text{and} \quad \hat{B}_y = \frac{B_y}{B_z}, \\
\hat{E}_z = (1 - \frac{1}{2}\hat{E}_x{}^2 - \frac{1}{2}\hat{E}_y{}^2) \quad &\text{and} \quad \hat{B}_z = (1 - \frac{1}{2}\hat{B}_x{}^2 - \frac{1}{2}\hat{B}_y{}^2).
\end{aligned} \tag{E.3}$$

This means that

$$\hat{E}\cdot\hat{B} = (1 + \hat{E}_x\hat{B}_x + \hat{E}_y\hat{B}_y - \frac{1}{2}\hat{E}_x{}^2 - \frac{1}{2}\hat{E}_y{}^2 - \frac{1}{2}\hat{B}_x{}^2 - \frac{1}{2}\hat{B}_y{}^2). \tag{E.4}$$

Continuing the algebra and neglecting all 3rd order terms, we find that

$$\begin{aligned}
(\hat{E}\cdot\hat{B})\hat{B}_x &= \hat{B}_x, \\
(\hat{E}\cdot\hat{B})\hat{B}_y &= \hat{B}_y, \\
(\hat{E}\cdot\hat{B})\hat{B}_z &= (1 + \hat{E}_x\hat{B}_x + \hat{E}_y\hat{B}_y - \frac{1}{2}\hat{E}_x{}^2 - \frac{1}{2}\hat{E}_y{}^2 - \hat{B}_x{}^2 - \hat{B}_y{}^2).
\end{aligned} \tag{E.5}$$

Returning to the Langevin equation, we find

$$\begin{aligned}
\frac{u_x}{u_z} &= \frac{\hat{E}_x + \omega\tau(\hat{E}_y\hat{B}_z - \hat{E}_z\hat{B}_y) + \omega^2\tau^2\hat{B}_x}{\hat{E}_z + \omega\tau(\hat{E}_x\hat{B}_y - \hat{E}_y\hat{B}_x) + \omega^2\tau^2(\hat{E}\hat{B})\hat{B}_z} \\
&= \frac{\frac{E_x}{E_z} + \omega\tau\left(\frac{E_y}{E_z} - \frac{B_y}{B_z}\right) + \omega^2\tau^2\frac{B_x}{B_z}}{(1 - O(2)) + \omega\tau O(2) + \omega^2\tau^2(1 + O(2))}.
\end{aligned} \tag{E.6}$$

Therefore, the complete 2nd order distortion equations in the transverse plane in cartesian coordinates is

$$\begin{pmatrix}\delta x \\ \delta y\end{pmatrix} = \begin{pmatrix} c_0 & c_1 \\ -c_1 & c_0 \end{pmatrix}\begin{pmatrix}\int \frac{E_x}{E_z}dz \\ \int \frac{E_y}{E_z}dz\end{pmatrix} + \begin{pmatrix} c_2 & -c_1 \\ c_1 & c_2 \end{pmatrix}\begin{pmatrix}\int \frac{B_x}{B_z}dz \\ \int \frac{B_y}{B_z}dz\end{pmatrix}, \tag{E.7}$$

in cylindrical coordinates

$$\begin{pmatrix} \delta r \\ r\delta\phi \end{pmatrix} = \begin{pmatrix} c_0 & c_1 \\ -c_1 & c_0 \end{pmatrix} \begin{pmatrix} \int \frac{E_r}{E_z} dz \\ \int \frac{E_\phi}{E_z} dz \end{pmatrix} + \begin{pmatrix} c_2 & -c_1 \\ c_1 & c_2 \end{pmatrix} \begin{pmatrix} \int \frac{B_r}{B_z} dz \\ \int \frac{B_\phi}{B_z} dz \end{pmatrix}, \tag{E.8}$$

$$\text{with } \mathrm{c}_0 = \frac{1}{1+\mathrm{T}_2^2\omega^2\tau^2},\ \mathrm{c}_1 = \frac{\mathrm{T}_1\omega\tau}{1+\mathrm{T}_1^2\omega^2\tau^2} \text{ and } \mathrm{c}_2 = \frac{\mathrm{T}_{2^2}\omega^2\tau^2}{1+\mathrm{T}_2^2\omega^2\tau^2}, \tag{E.9}$$

where T_1 and T_2 parameters depend on B and E field configuration. In full microscopic theory, the drift velocity is a tensor and the drift velocity in the transverse plane are slightly different from that along the z axis. T_1 and T_2 parameters are introduced in order to take into account this effect. Measured T_1 and T_2 for P9 (P10) gas by the STAR Collaboration are $T_1 = 1.34$ and $T_2 = 1.11$ ($T_1 = 1.36$ and $T_2 = 1.11$) since they are one of the hot gases [142]. MagBolz simulation indicates that both T_1 and T_2 are equal to 1 in case of the cold gases such as Ar-CO$_2$ or Ne-CO$_2$. E_r and E_ϕ are calculated by a poisson relaxation method with the TPC geometry [143] or an analytic method. B_r and B_ϕ are obtained from the B field map parametrized with Chebyshev polynomials, which is based on precise B field measurement.

B field variations is as large as 2% (0.5 T±0.01 T). The largest radial components of the field are ±0.01 T at the outer radius of the TPC and the ϕ components of the field are ±0.005 T. Thus, 2nd order approximation described above are 0.04%. For example, the non-uniformity of the B field give rise to 1 cm scale distortions at maximum and the 2nd order calculations should be good to 4 μm.

E.2 Laser track distortions with the gating grid voltage mismatch

Distortions can arise from incorrect matching of the end cap potential with the field cage cylinder. The effective position of the ground plane depends on the amount of field leakage from the anode wires and its compensation with the gating grid plane bias in the ReadOut Chamber (ROC) of TPC. The ground end of the field cage cylinder can be biased to achieve the correct matching. The following calculation shows the E field distortion when this matching bias is incorrect [144].

The first step is to write down the solution to Laplace equation for the error potential in cylindrical coordinate (ρ, ϕ, z). Laplace equation with the separation of variables (there is no ϕ dependence in this problem)

$$\Phi(\rho, z) \equiv R(\rho) \cdot Z(z), \tag{E.10}$$

is

$$\frac{d^2}{d\rho^2}R + \frac{1}{\rho}\frac{d}{d\rho}R - k^2 R = 0, \tag{E.11}$$

and

$$\frac{d^2}{dz^2}Z + k^2 Z = 0. \tag{E.12}$$

This gives the Z solution $\sin(kz)$ or $\cos(kz)$. This can be used in an expansion of the potential along the inner and outer cylinders. Since the potential must go to 0 at the ends, $z = 0$ and $z = L$, then the sine function is the appropriate solution and the coupling constant, k, must be limited to $k = n\pi/L$ where n is an integer. The linearly independent solutions to the radial equation are the zeroth order modified Bessel functions of the first kind $I_0(n\pi\rho/L)$ and second kind $K_0(n\pi\rho/L)$, where the restricted value of k has been included. The combine solution is:

$$\Phi(\rho, z) = \sum_{n=1}^{infty} \Big(A_n \cdot I_0(\frac{n\pi\rho}{L}) + B_n \cdot K_0(\frac{n\pi\rho}{L})\Big) \cdot \sin(\frac{n\pi\rho}{L}). \tag{E.13}$$

The coefficients A_n and B_n are evaluated using the potentials given on the inner and outer cylinders in the following manner using $\int_0^L \sin(n\pi z/L)\sin(m\pi z/L)dz = L/2\delta_{n,m}$:

$$\begin{aligned}\int_0^L \Phi(\rho_{in}, z) \cdot \sin(\frac{n\pi z}{L})dz &= \frac{L}{2}\Big(A_n \cdot I_0(\frac{n\pi\rho_{in}}{L} + B_n \cdot K_0(\frac{n\pi\rho_{in}}{L})\Big),\\ \int_0^L \Phi(\rho_{out}, z) \cdot \sin(\frac{n\pi z}{L})dz &= \frac{L}{2}\Big(A_n \cdot I_0(\frac{n\pi\rho_{out}}{L} + B_n \cdot K_0(\frac{n\pi\rho_{out}}{L})\Big),\end{aligned} \tag{E.14}$$

where $\rho_{in/out}$ is the inner/outer cylinder radius. These equations are a pair of linear equations which can be solved for A_n and B_n giving

$$\begin{aligned}A_n &= \frac{\mathrm{Sin_n} \cdot K_0(\frac{n\pi\rho_{out}}{L}) - \mathrm{Sout_n} \cdot K_0(\frac{n\pi\rho_{in}}{L})}{I_0(\frac{n\pi\rho_{in}}{L})K_0(\frac{n\pi\rho_{out}}{L}) - I_0(\frac{n\pi\rho_{out}}{L})K_0(\frac{n\pi\rho_{in}}{L})},\\ B_n &= \frac{\mathrm{Sout_n} \cdot K_0(\frac{n\pi\rho_{out}}{L}) - \mathrm{Sin_n} \cdot K_0(\frac{n\pi\rho_{in}}{L})}{I_0(\frac{n\pi\rho_{in}}{L})K_0(\frac{n\pi\rho_{out}}{L}) - I_0(\frac{n\pi\rho_{out}}{L})K_0(\frac{n\pi\rho_{in}}{L})},\end{aligned} \tag{E.15}$$

where

$$\begin{aligned}Sin_n &\equiv \frac{2}{L}\int_0^L \Phi(\rho_{in}, z) \cdot \sin(\frac{n\pi z}{L})dz\\ Sout_n &\equiv \frac{2}{L}\int_0^L \Phi(\rho_{out}, z) \cdot \sin(\frac{n\pi z}{L})dz\end{aligned} \tag{E.16}$$

Now we have an expression for the potential $\Phi(\rho, z)$ and a way to determine the coefficients. It is slightly simpler to switch to a normalized error potential $\phi(\rho, z) \equiv \Phi(\rho, z)/V$ where V is the full voltage on the field cage generating the drift field. This voltage appears in the radial distortion expression in terms of the drift field $E_z = V/L$. Changing to the normalized potential,

$$\Phi(\rho, z) = V \cdot \sum_{n=1}^{infty} \Big(a_n \cdot I_0(\frac{n\pi\rho}{L}) + b_n \cdot K_0(\frac{n\pi\rho}{L})\Big) \cdot \sin(\frac{n\pi\rho}{L}), \tag{E.17}$$

$$\begin{aligned} a_n &= \frac{\hat{\mathrm{Sin}}_\mathrm{n} \cdot K_0(\frac{n\pi\rho_{out}}{L}) - \hat{\mathrm{Sout}}_\mathrm{n} \cdot K_0(\frac{n\pi\rho_{in}}{L})}{I_0(\frac{n\pi\rho_{in}}{L})K_0(\frac{n\pi\rho_{out}}{L}) - I_0(\frac{n\pi\rho_{out}}{L})K_0(\frac{n\pi\rho_{in}}{L})}, \\ b_n &= \frac{\hat{\mathrm{Sout}}_\mathrm{n} \cdot K_0(\frac{n\pi\rho_{out}}{L}) - \hat{\mathrm{Sin}}_\mathrm{n} \cdot K_0(\frac{n\pi\rho_{in}}{L})}{I_0(\frac{n\pi\rho_{in}}{L})K_0(\frac{n\pi\rho_{out}}{L}) - I_0(\frac{n\pi\rho_{out}}{L})K_0(\frac{n\pi\rho_{in}}{L})}, \end{aligned} \tag{E.18}$$

$$\begin{aligned} \hat{Sin}_n &\equiv \frac{2}{L}\int_0^L \phi(\rho_{in}, z) \cdot \sin(\frac{n\pi z}{L})dz, \\ \hat{Sout}_n &\equiv \frac{2}{L}\int_0^L \phi(\rho_{out}, z) \cdot \sin(\frac{n\pi z}{L})dz. \end{aligned} \tag{E.19}$$

In the radial distortion expression, using $d/dxI_0(x) = I_1(x)$ and $d/dxK_0(x) = K_1(x)$

$$\begin{aligned} E_\rho(\rho, z) &= \frac{d}{d\rho}\Phi(\rho, z) \\ &= V \cdot \sum_{n=1}^{\infty} \frac{n\pi\rho}{L}\Big(a_n I_1(\frac{n\pi\rho}{L}) - b_n K_1(\frac{n\pi\rho}{L})\Big) \cdot \sin(\frac{n\pi z}{L}), \end{aligned} \tag{E.20}$$

where I_1 and K_1 are the first order modified Bessel functions of the first and second kind. We represent the voltage mismatch with the gating grid plane as the following error potential on the inner and outer cylinder boundaries

$$\phi(z) = \delta V \frac{L - z}{L}, \tag{E.21}$$

where δV is the potential mismatch at the endcap expressed as a fraction of the total potential on the field cage. Figure E.1 shows the space point distortions due to the endcap voltage mismatch. The space point distortion is almost independent on the z-position.

The absolute position of the laser track is not known, so the distortion of the laser track is not measurable. But, the difference between measured positions of the laser track with different gating grid voltage can be compared with the model calculations.

$$\delta Y_{V_2} - \delta Y_{V_1} = Y_{V_2} - Y_{V_1}, \tag{E.22}$$

where Y_V denotes a measured local Y-position of the laser track as a function of local X-position with gating grid voltage V and $\delta Y_V = Y_V - Y_{V_{ideal}}$. A default gating grid voltage V_{ideal} is set to 70 V. The left-hand side of this equation can be calculated by the analytic formula (C.20) and the 2nd order approximation of the Langevin equation (C.8). The right-hand side of this equation can be measured with gating grid voltage scan. By comparing the relative distortions, the other distortion effects can be minimized in these measurements. Fig. E.1 (a) shows the measured $Y_{70\,V} - Y_{40\,V}$ as a function of the local X-position of the readout pad in comparison with the model calculations of $\delta Y_{70\,V} - \delta Y_{40\,V}$ for $B = 0$ T. The measured data points clearly prefer to model calculation with $c_0 = 1$ and $c_1 = 1$. Note the effective voltage at the gating grid plane is not same as the setting

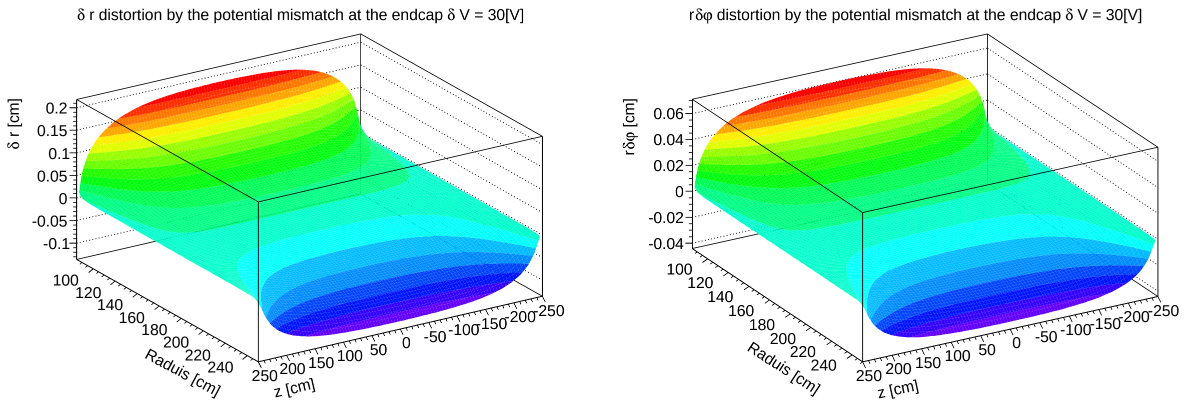

(a)

(b)

Figure E.1: The space point distortions by the potential mismatch δV = 20 [V] at the endcap in the (a) δr and (b) $r\delta\varphi$ directions.

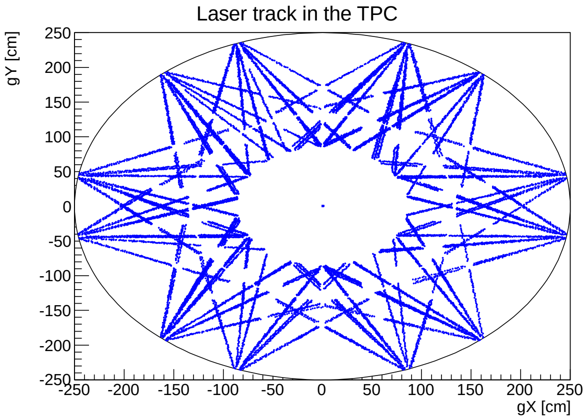

Figure E.2: A view of the laser tracks from A side endcap.

of the gating grid voltage. Therefore, the Garfield simulations [145] are necessary to calculate δV, which is an input for the calculations of the space point distortions. The measured data points have zigzag patterns of order 100 μm around the model lines due to the pad geometries, which is larger than the precision of the 2nd order approximation of the Langevin equation.

Fig. E.4 shows χ^2 distribution of the comparison between data points at B=0.5 T and model calculations with various T_1, T_2 values. A best value of T_1, T_2 is 1.0±0.1 and 1.0±0.3. These values agree with MagBolz simulation results [145].

E.3 B field non-uniformity

Using Eq. (E.8) with the extracted values of T_1 and T_2 parameters and the measured B field map, the space point distortions due to the B field non-uniformity can be calculated.

Fig. E.5 shows the $E \times B$ space point distortion map due to the B field non-uniformity. The distortion maps are not axial symmetrical since the TPC is not positioned in the center of the L3 magnet. The maximum magnitude of the distortion is $\sim$ 3 mm at the outer radius of the TPC and these distortions significantly degrade the TPC tracking performance. Therefore, in the reconstruction procedures, the reconstructed space points are corrected according to these distortion maps.

E.4 $E \times B$ twist distortions and A-C vertex shift

The space point distortions due to an angular mismatch between global axis of E and B field can be significant even if TPC is slightly inclined in the L3 magnet. This $E \times B$ twist distortion can be calculated in a compact form:

$$\begin{pmatrix} \delta x \\ \delta y \end{pmatrix} = \begin{pmatrix} c_2 & -c_1 \\ c_1 & c_2 \end{pmatrix} \begin{pmatrix} \theta_x z_{drift} \\ \theta_y z_{drift} \end{pmatrix},$$

where z_{drift} is a drift length of electron, $\theta_{x,y}$ are the angles between x, y axis and twist vector. Figure E.6 shows the map of the space point distortions when E and B axis are inclined by 3 mrad. The direction of the space point distortions at the TPC A side is opposite to that at the TPC C side because E field direction at the A side is opposite to that at the C side while B field direction is same at the A and C side.

Roughly speaking, the track distortion is a parallel shift and the direction of the shift is opposite at the A and C side each other as shown in Fig. E.7 (a). Therefore, the effect of $E \times B$ twist distortions can be observed by the measurement of the shift between the collision vertex reconstructed with the A side tracks and that of the C side tracks, which is called the A-C vertex shift.

Figure E.7 (b) shows that A-C vertex shift is proportional to $E \times B$ twist angle if twist angle is small enough by using the full and fast Monte Carlo simulation studies.

The A-C vertex shift was found in p+p collision data as shown in Fig. E.8. Primary vertex is reconstructed with all ITS-TPC tracks and is positioned in the middle of A and C side vertex. Positions of A and C side vertex are swapped with the negative and positive B field polarities. Observed A-C vertex shift is $\sim$ 0.33 cm while the A-C vertex shift at $B = 0$ T p+p run is below 0.004 cm. This results in $\theta_x = -1.7$ mrad, $\theta_y = -0.94$ mrad if this A-C vertex shift is only from $E \times B$ twist distortions. It is confirmed that possible E field distortions can not cause A-C vertex shift by the Monte Carlo simulations as shown in Fig. E.9. To calculate the E field distortions due to the defects on the boundary conditions, the poisson relaxation method is used [143]. The data obtained from the survey of the chamber misalignment is used for the calculation of the E field distortions due to the TPC ROC misalignment. The other possible E field distortions due to the TPC conical deformations and the shifted rods or strips of the TPC field cage are also considered.

The A-C vertex shift is reduced to $\sim$300μm with correction of $E \times B$ twist distortions according to the extracted twist values.

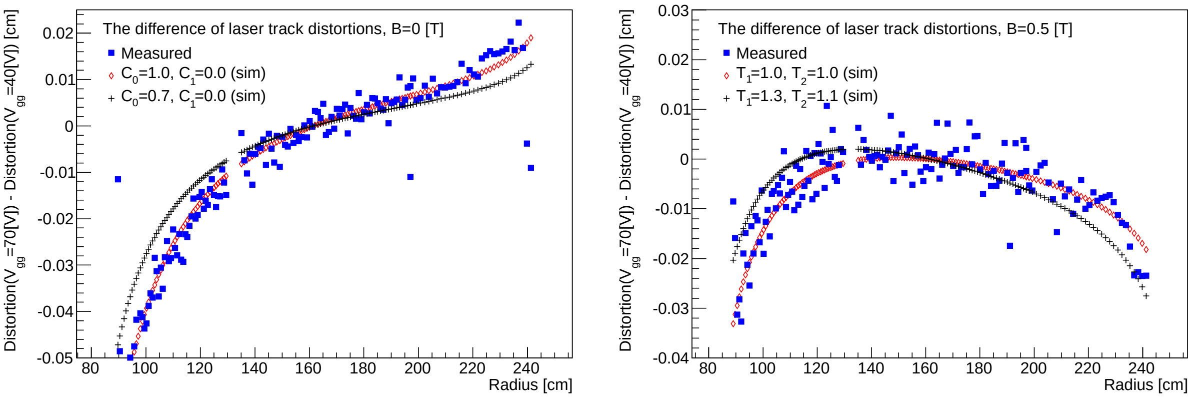

(a) (b)

Figure E.3: A difference of measured laser track $r\phi$ with the gating grid voltage scan vs. radial position of space point (a) B=0 T, (b) B = 0.5 T.

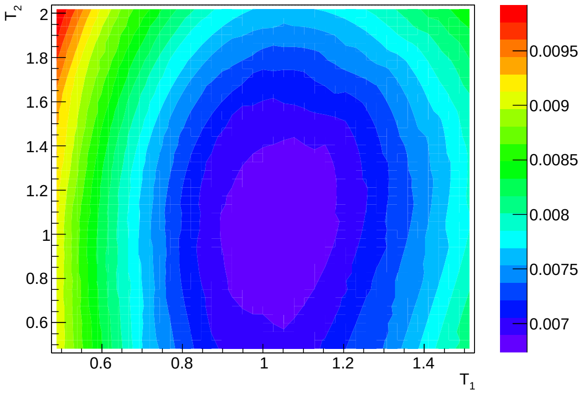

Figure E.4: Contour plot for T_1, T_2 optimization with the gating grid scan data at B = 0.5 T

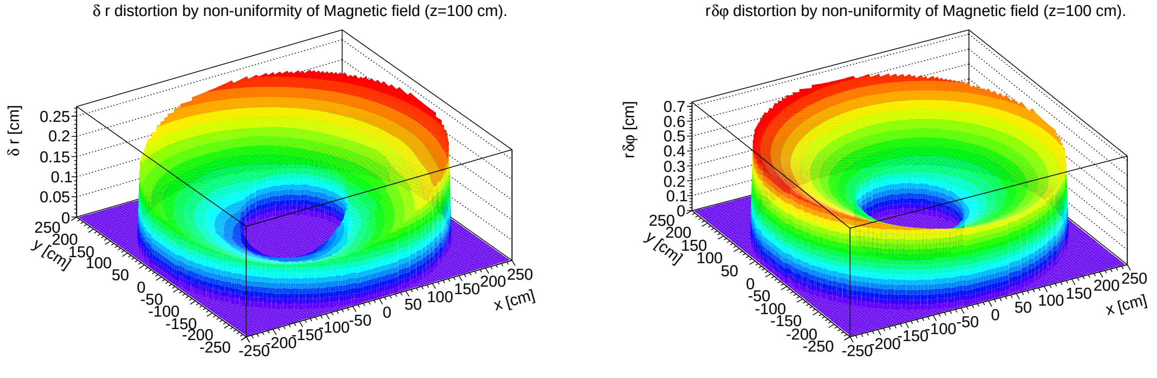

(a) (b)

Figure E.5: $E \times B$ space point distortion map due to the B field non-uniformity in the (a) δr and (b) $r\delta\varphi$ directions.

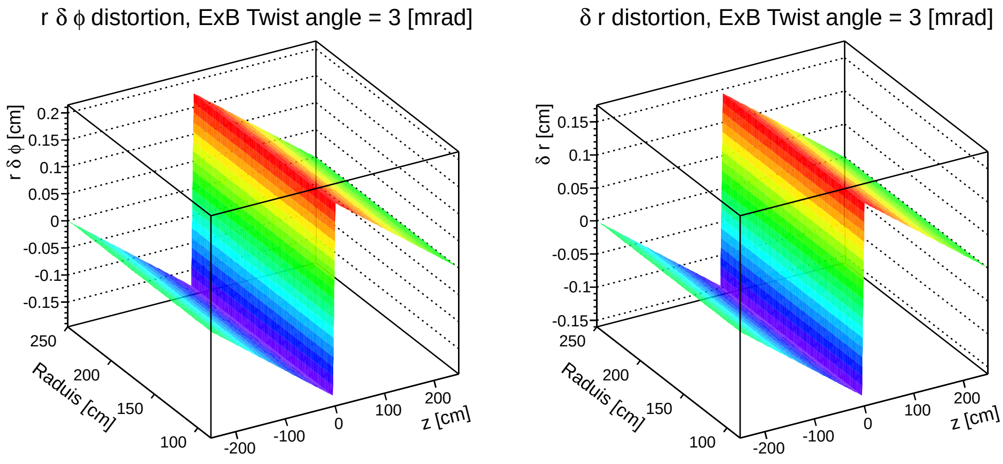

Figure E.6: $E \times B$ twist distortion map with twist angle = 3 mrad in the (a) δr and (b) $r\delta\varphi$ directions. The sign of δr and $r\delta\varphi$ is changed at $z = 0$ cm.

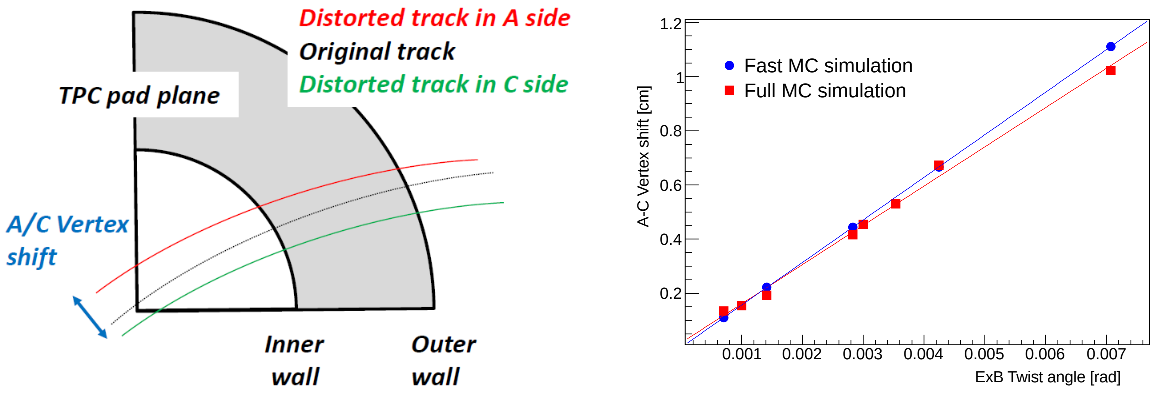

(a)

(b)

Figure E.7: (a) A schematic view of the TPC $E \times B$ twist distortions of the tracks in the A and C side. (b) Relation between twist angle and A-C vertex shift calculated by the full and fast Monte Carlo simulations.

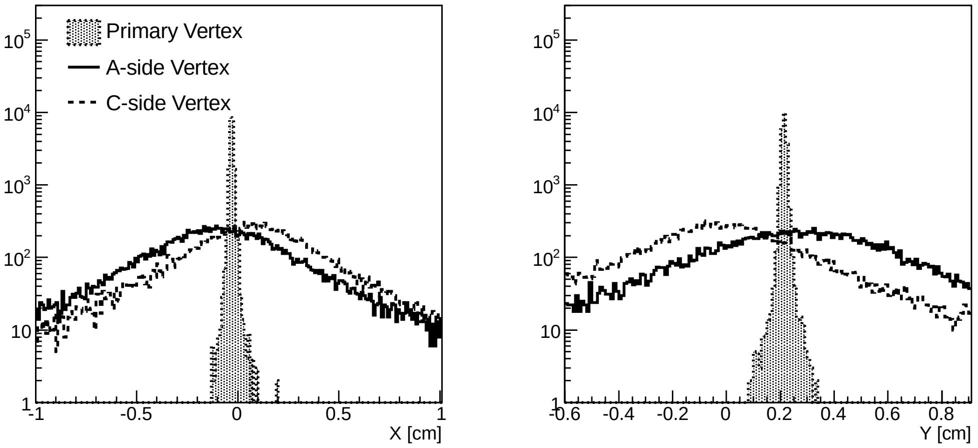

Figure E.8: A-C vertex shift measured in p+p collision data. The resolution of the primary vertex is much better than the A- and C-side vertex because the primary vertex uses the ITS information.

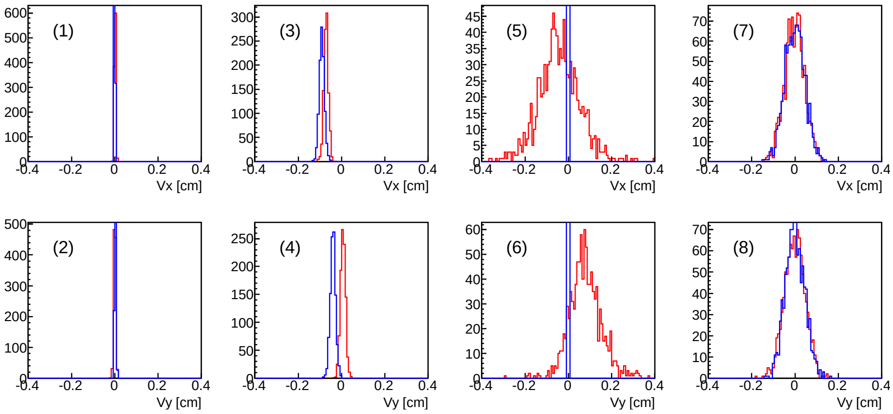

(a) Magnetic polarity + +

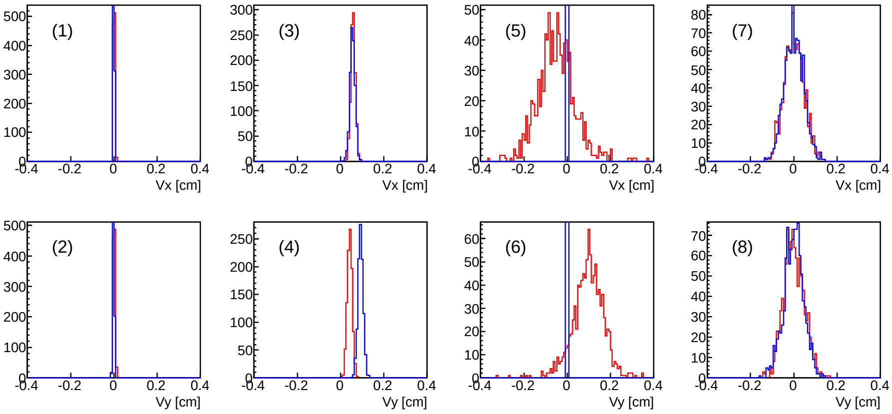

(b) Magnetic polarity - -

Figure E.9: A-C vertex shift fast simulations. The top (bottom) columns are the x (y) position distributions of the A-side (red line) and C-side (blue line) vertexes. (1)(2): The TPC ROC misalignment. (3)(4): B field non-uniformity. (5)(6) The shifted rods or strips of the TPC field cage. (7)(8) The TPC conical deformations.

Appendix F

Measurement of the identified particle elliptic flow in $\sqrt{s_{NN}} = 2.76$ TeV Pb–Pb collisions

An important test of the hydrodynamic description of the QGP is an interplay between the radial flow (azimuthally symmetric radial expansion, which can be indirectly measured by a slope of the p_{mT} spectra) and anisotropic flow [7]. It is expected that this interplay results in the particle mass dependence of the identified particle elliptic flow at small transverse momenta.

A scalar product method (SP) [8] is one of the two-particle correlation method and the differential flow in SP is defined as:

$$v_n(p_{\mathrm{T}}, \eta) = \frac{\langle Q_n \cdot u_{n,i}^*(p_{\mathrm{T}}, \eta) \rangle}{2\sqrt{\langle Q_n^a \cdot Q_n^{b*} \rangle}}, \tag{F.1}$$

where $\langle\rangle$ denotes the average over all particles in all events. $u_{n,i} \equiv \exp(in\varphi_i)$ is the unit vector of the i-th particle and $Q_n \equiv \sum \exp(in\varphi)$ is the event flow vector. In this analysis, $u_{n,i}$ is calculated by TPC tracks at $|\eta|$ <0.8 and Q_n^a and Q_n^b are calculated by the VZERO detectors at $-3.1 < \eta < -1.7$ and $2.8 < \eta < 5.1$, respectively. $(Q_n = Q_n^a + Q_n^b)$. It is empirically known that non-flow effects on the two-particle correlations can be removed by introducing η gaps between $u_{n,i}$, Q_n^a and Q_n^b. The detector effect can be removed by the similar way to the two-particle cumulant method.

Pions, kaons and protons/antiprotons are identified using dE/dx and time information measured by the TPC and the TOF detector [146]. For K_s^0, $\Lambda/\bar{\Lambda}$ and ϕ, an invariant mass method of the two daughter candidates is used for identification and reconstruction [147].

If the reconstruction efficiency strongly depends on the local particle density at the detector, this results in the decrease (increase) of the positive (negative) elliptic flow. We conducted Monte Carlo simulation study in order to estimate this effect and assigned a few % systematic error for this effect.

F.1 Results of identified particle elliptic flow

Figure F.1 shows the results of identified particle elliptic flow in $\sqrt{s_{NN}} = 2.76$ TeV Pb–Pb collisions at centrality 10-20% and 40-50% measured by the ALICE experiment [148]. As expected by the hydrodynamics, v_2 values of the heavier particles shift toward to higher p_T direction at the low p_T region. This can be regarded as a sign of hydrodynamic pressure on particles by large radial flow at the LHC energy. The mass dependence of v_2 in p_T <2.5 GeV/c, is reasonably reproduced by viscous hydrodynamic model calculations shown by solid lines. Models considering the hadronic cascade phase can better describe the data, particularly heavier particles.

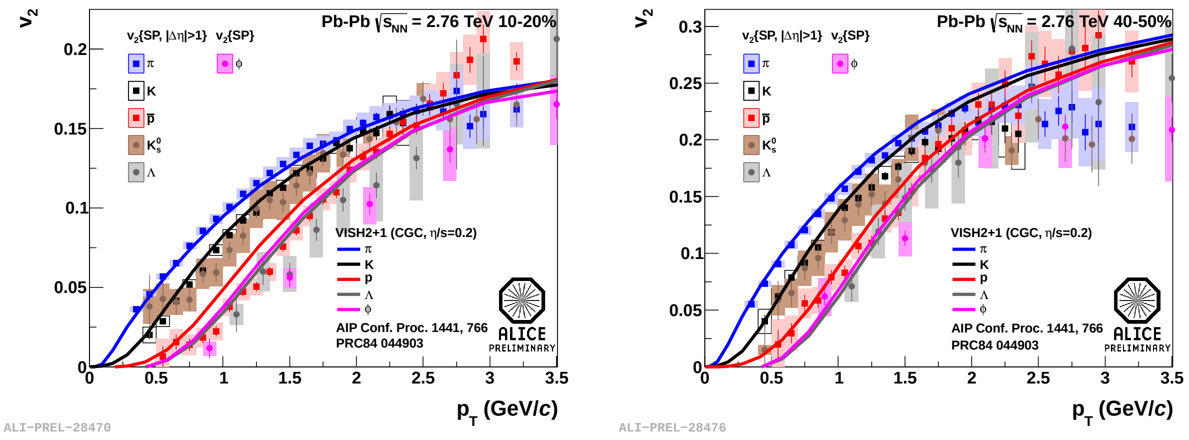

(a) (b)

Figure F.1: The p_T differential elliptic flow v_2 of π, k, $\bar{p}$, K_s^0, Λ and ϕ with theoretical prediction VISH2+1 (CGC, η/s = 0.2) at centrality (a) 10-20% and (b) 40-50% [148].

F.2 Kaon elliptic flow via decay topological identification

In Fig. F.1, the elliptic flow of the K_s^0 is systematically lower than that of TOF-TPC Kaon although the discrepancy is within systematic errors. We also measured kaons by the kink topology method as an alternative identification method [137, 149]. Kaons have two main decay modes, K $\rightarrow \mu\nu$ (Branching ratio 63.55%) and K $\rightarrow \pi\pi^0$ (Branching ratio 20.66%). These decay modes have a large $c\tau \sim 371.3$ cm and hence can be recognized as a kink topology in the ALICE TPC active area as shown in Fig. F.2. Kaon can be identified at wider range of p_T with the kink topology than TOF-TPC identification method.

The kink finding algorithm proceeds in two main steps. First, it reconstructs the large kink angle decays by associating pairs of tracks that intersect (within some tolerance) in space and have the same charge, then it searches for breakpoints in high p_T track candi-

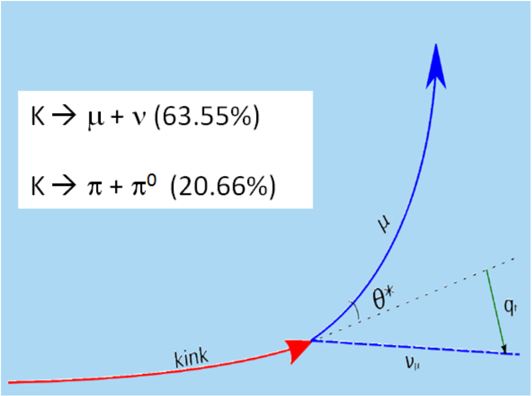

Figure F.2: Kink kaon decays and topological parameter θ and q_{T}

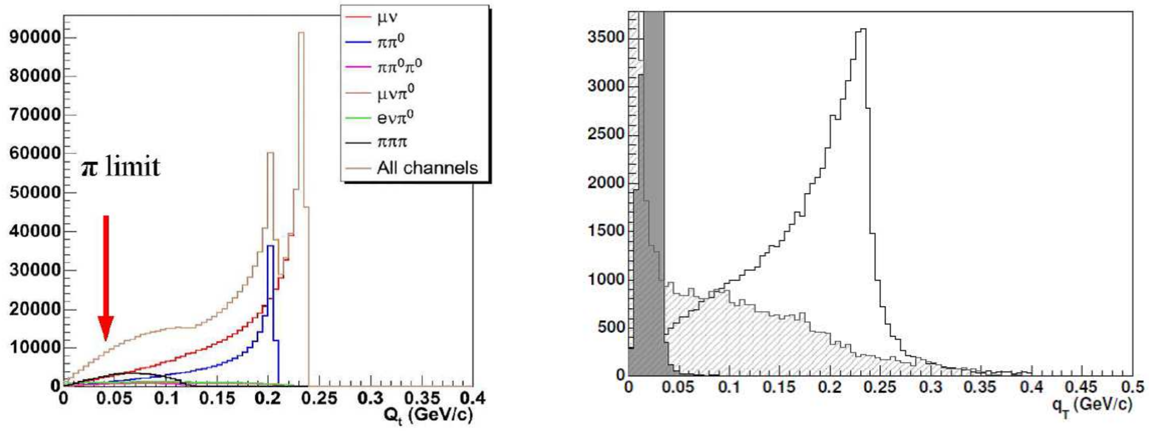

(a) (b)

Figure F.3: (a) q_{T} distribution of Kaon decays. The arrow indicates the limit of the pion decays (30 MeV/c). (b) q_{T} distribution of the reconstructed kinks. The area under the solid line represents the signal (K→ $\mu\nu$), the hashed area the background due to random association of tracks and the grey filled area reconstructed pion kinks [137].

dates to resolve the small kink angle decays. If the decay angle is large enough, the track segments in front of and behind the decay are reconstructed by the tracking algorithm as two distinctive tracks. On the other hand, the track of the decaying particle are misinterpreted by the track search as a single track if the mother particle p_{T} is above 1.4 GeV/c and the charged decay product is emitted at small angle. In this case, kink is nothing else but a sudden change of the state vector, a change both in direction and in momentum (or curvature). The strategy here is to use the wealth of by-product information of the Kalman filter to obtain trial breakpoint fits at every hit away from the ends of the track,

Selection parameter	Cut value
p_T	> 0.2 GeV/c
$\|\eta\|$	< 0.9
Rapidity with Kaon hypothesis	< 0.7
Number of TPC clusters (TPCncls)	> 2
χ^2/TPCncls	< 4.0
Number of ITS clusters	2
dca_{xy}	< 0.3 cm
dca_z	< 0.3 cm
TPC dE/dx	$< 6\sigma_{dE/dx}$

Table F.1: Selections parameters and cut values for mother tracks

Selection parameter	Cut value
kink dca	< 0.1 cm
Radius of decay points (R)	120 cm $< R <$ 220 cm
Decay angle (loose cut)	> 2
q_T (loose cut)	$0.05 < q_T < 0.3$
Decay angle	$1.2 \times MaxPiMu <$ decay angle
	decay angle $< 0.98 \times MaxKmu$
q_T	$0.12 < q_T < 0.24$
Invariant Mass (M)	$0.4 < M < 0.55$

Table F.2: Kink selections parameters and cut values

which we then use to search for and characterize track breakpoints defined as locations where one or more of the track parameters are discontinuous. Clearly, when both the kink angle and q_T are close to zero the chances of detecting the decay are rather small.

The quality and kinematics cuts for mother track are listed in Table F.1.These cuts are standard cuts for the primary tracks except for the TPC dE/dx and number of TPC clusters.

The kink identification cuts in Table F.2 are applied if kink daughters are associated to the mother track by the kink finding algorithm.

Fig. F.4 shows the distribution of the decay points for all kink candidates. Some TPC structures can be recognized in this distribution. Fig. F.5 (a) shows the Distance of Closest Approach (DCA) between the mother and daughter tracks as a function of mother track signed p. Cut value for the DCA parameter is set to 1.5 cm as shown by black arrow in this plot. Fig. F.5 (b) shows the TPC dE/dx distribution as a function of mother track signed p. Red line in this plot represents the Bethe Bloch curve for the kaons. For low momentum region $p < 0.4$ GeV/c, the kaon and pion dE/dx bands are well separated but they are merged at the higher p region. The loose dE/dx cut ($< 6\sigma_{dE/dx}$, $\sigma_{dE/dx} \sim 7\%$)

is reqiured in order to work at low momentum region and avoid to loss signals at high momentum region.

The expected q_{T} distributions for pion and kaon kinks are shown in Fig. F.3. The kaon kinks have two main peaks at $q_T \sim 0.2$ and 0.25 for two main decays K $\rightarrow \mu\nu$ and K $\rightarrow \pi\pi^0$ respectively while q_T for the pion kinks are below 0.05. The large fraction of kinks from pion decays are removed only by loose q_{T} cut (> 0.05). Furthermore, as shown by two lines in Fig. F.6 (a), the pion kinks can be removed also by the decay angle cuts since the maximum decay angle of the kaon kink is larger than maximum decay angle of the pion kink. *MaxKmu* and *MaxPimu* in Table F.2 represents the maximum decay angles for kaon and pion kinks and are calculated by the measured momentum of mother track and the following formula.

$$(\theta^{lab})_{max} = \frac{p}{\gamma E} \frac{1}{\sqrt{\beta^2 - p^2/E^2}}. \tag{F.2}$$

The decay angle distribution as a function of signed momentum is shown in Fig. F.6 (a). After the decay angle cuts, an invariant mass is calculated with the muon daughter assumption. Therefore, the invariant mass distribution has a peak at kaon mass for K $\rightarrow$ $\mu\nu$ and another peak below kaon mass for K $\rightarrow \pi\pi^0$ as shown in Fig. F.7 (b). Fig. F.7 (a) and (b) are projections onto the X-axis and Y-axis of the two dimensional plot in Fig. F.6 (b). The red square in Fig. F.6 (b) represents the region used for kaon kink signals. Because the background due to random associations has rather small q_{T} as shown by the hashed area in Fig. F.3 (b), the final lower q_{T} cut is set to rather large value 0.12.

Since the invariant mass and q_{T} is partially correlated as shown in Fig. F.6 (b), contamination is estimated by extrapolation of the entries in black square in this plot. It is confirmed to be less than 7% for mother track $p_{\mathrm{T}} < 5$ GeV/c. At the low p_{T} region, the contamination can be estimated also by the TPC dE/dx bands and they are consistent.

Figure F.8 shows the p_{T} differential elliptic flow $v_2\{SP\}$ of the kink kaon at centrality 10-20% and 40-50% with various cuts. According to this comparison plots, the systematic uncertainties are estimated.

Figure F.9 shows the comparison between the elliptic flow $v_2\{SP\}$ of the TOF-TPC kaon, K_0^s and kink kaon. They reasonably agree within the systematic errors.

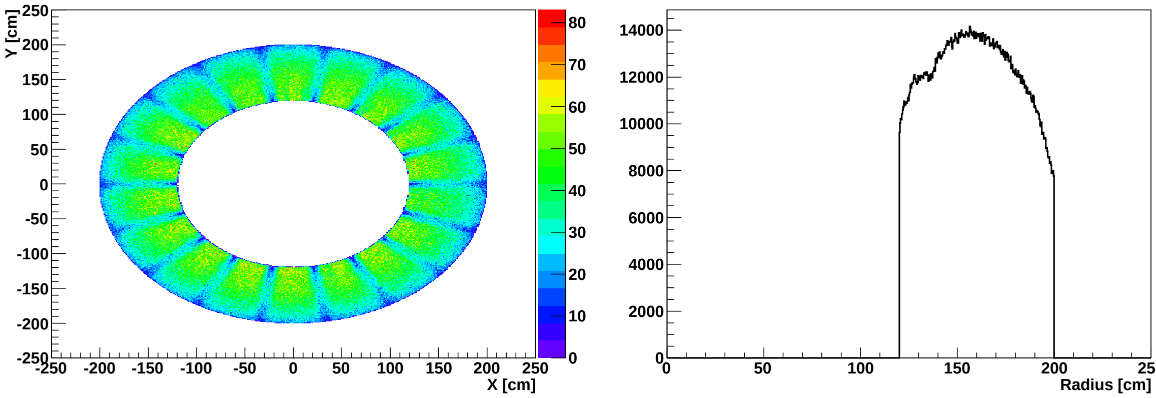

(a) (b)

Figure F.4: (a) X-Y position of kink decay, (b) Radius of kink decay position.

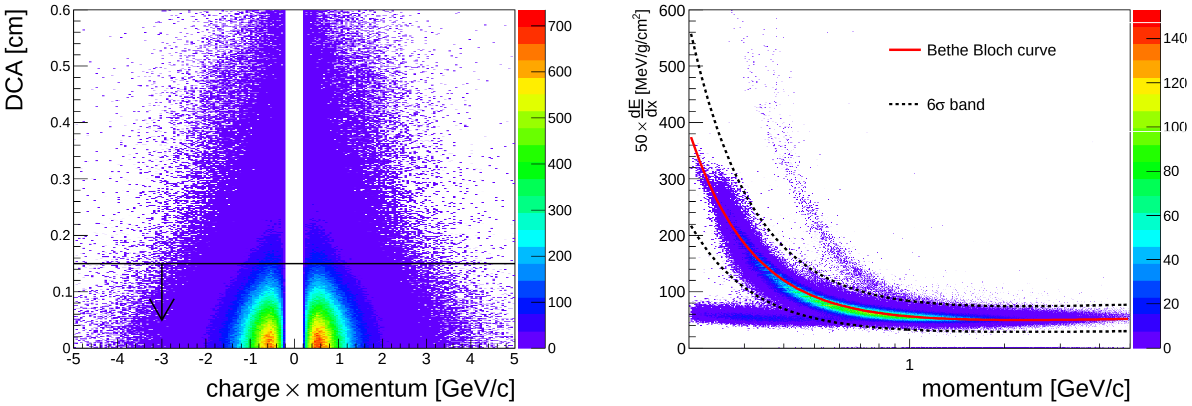

(a) (b)

Figure F.5: (a) Signed p dependence of DCA between mother and daughter tracks. (b) dE/dx [MeV/g/cm^2] as a function of momentum [GeV/c] for kink candidates. Red solid line: Bethe Bloch curve. Black dotted line: 6σ band.

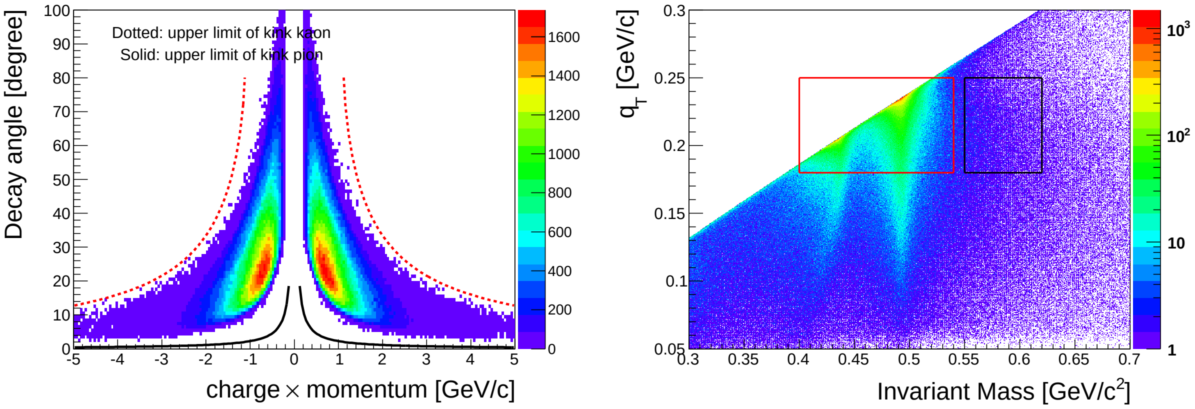

(a)

(b)

Figure F.6: (a) Decay Angle distribution as a function of mother track signed p. Dotted (solid) line represents the maximum decay angle for kaon (pion) kink. (b) Two dimensional distribution of q_{T} and the invariant mass. Red square area is for the signal region. Black square are is used for the background estimation.

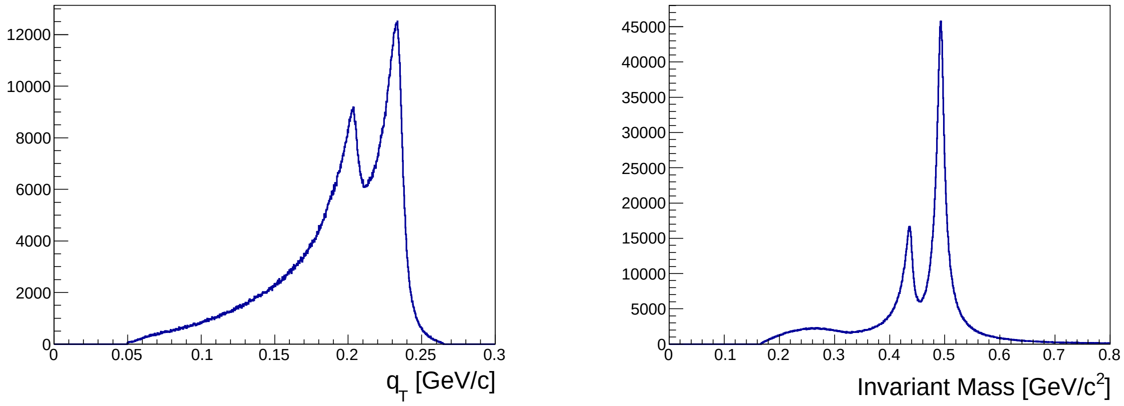

(a)

(b)

Figure F.7: (a) q_{T} and (b) invariant mass distributions, two main peaks correspond to the two main decay modes, K → $\mu\nu$ (Branching ratio 63.55%) and K → $\pi\pi^0$ (Branching ratio 20.66%).

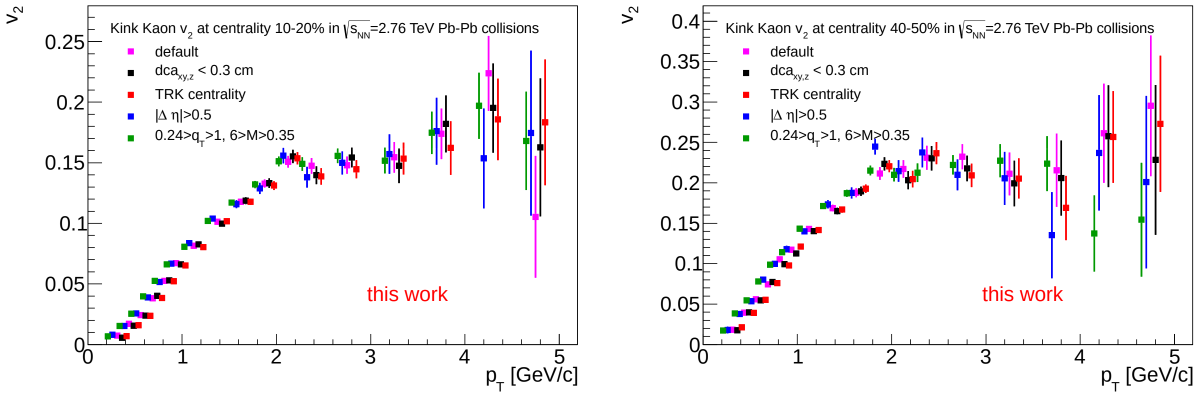

(a)

(b)

Figure F.8: The p_T differential elliptic flow v_2 of kink kaon with various cuts (a) at centrality 10-20% and (b) at centrality 40-50%

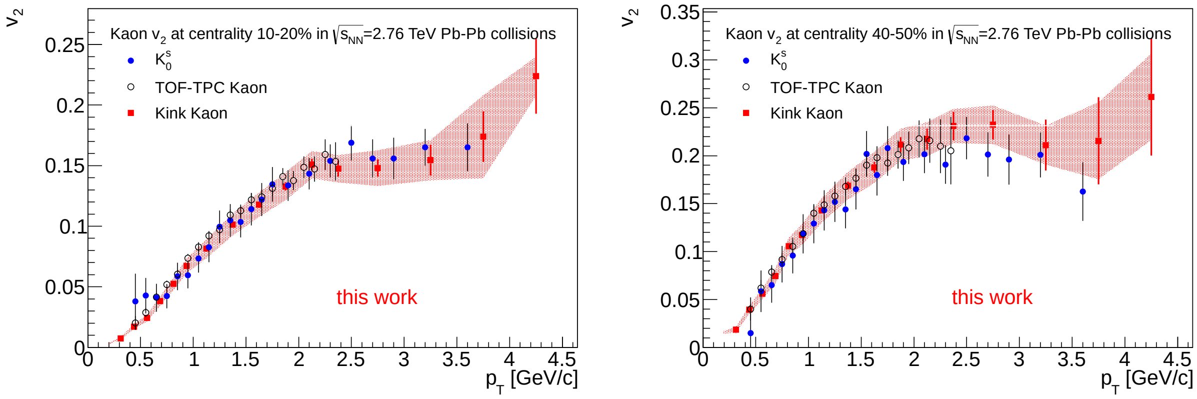

(a)

(b)

Figure F.9: The p_T differential elliptic flow v_2 of kaon identified with TOF-TPC method, K_s^0 invariant mass method and kink kaon method (a) at centrality 10-20% and (b) at centrality 40-50%.

Appendix G

Q-cumulant

In the Q-cumulant method, the estimate of the two-particle correlations in a *single event* are calculated as follows.

$$\begin{aligned}
\sum_{\alpha,\beta} \exp i(n\varphi_\alpha - n\varphi_\beta) &= \sum_{\alpha\neq\beta} \exp i(n\varphi_\alpha - n\varphi_\beta) + M \\
\Leftrightarrow \sum_{\alpha\neq\beta} \exp i(n\varphi_\alpha - n\varphi_\beta) &= |Q_n|^2 - M \\
\Leftrightarrow \{\exp i(n\varphi_\alpha - n\varphi_\beta)\} &= \frac{|Q_n|^2 - M}{M(M-1)} \qquad \text{(G.1)}
\end{aligned}$$

Here we provide a proof of the Eq. (4.13),Eq. (4.14), Eq. (4.15) and Eq. (4.16) in the Q-cumulant method. Eq. (4.13) and Eq. (4.14) are for the three-particle correlations.

$$\begin{aligned}
\sum_{\alpha,\beta,\gamma} \exp i(\varphi_\alpha + \varphi_\beta - 2\varphi_\gamma) &= \sum_{\alpha\neq\beta\neq\gamma} \exp i(\varphi_\alpha + \varphi_\beta - 2\varphi_\gamma) \\
&\quad + \sum_{\alpha\neq\beta} \exp i(\varphi_\alpha - \varphi_\beta) + \sum_{\alpha\neq\beta} \exp i(-\varphi_\alpha + \varphi_\beta) \\
&\quad + \sum_{\alpha\neq\gamma} \exp i(2\varphi_\alpha - 2\varphi_\gamma) + M \\
&= M(M-1)(M-2)\{\exp i(\varphi_\alpha + \varphi_\beta - 2\varphi_\gamma)\} \\
&\quad + 2(|Q_1|^2 - M) + (|Q_2|^2 - M) + M \\
\Leftrightarrow \{\exp i(\varphi_\alpha + \varphi_\beta - 2\varphi_\gamma)\} &= \frac{Q_1^2 Q_2^* - |Q_2|^2 - 2|Q_1|^2 + 2M}{M(M-1)(M-2)}. \qquad \text{(G.2)}
\end{aligned}$$

$$
\begin{aligned}
\sum_{\alpha,\beta,\gamma} \exp i(\varphi_\alpha - 3\varphi_\beta + 2\varphi_\gamma) &= \sum_{\alpha\neq\beta\neq\gamma} \exp i(\varphi_\alpha - 3\varphi_\beta + 2\varphi_\gamma) \\
&\quad + \sum_{\alpha\neq\beta} \exp i(\varphi_\alpha - \varphi_\beta) + \sum_{\alpha\neq\beta} \exp i(3\varphi_\alpha - 3\varphi_\beta) \\
&\quad + \sum_{\alpha\neq\gamma} \exp i(-2\varphi_\alpha + 2\varphi_\gamma) + M \\
&= M(M-1)(M-2)\{\exp i(\varphi_\alpha - 3\varphi_\beta + 2\varphi_\gamma)\} \\
&\quad +(|Q_1|^2 - M) + (|Q_3|^2 - M) + (|Q_2|^2 - M) + M \\
\Leftrightarrow \{\exp i(\varphi_\alpha - 3\varphi_\beta + 2\varphi_\gamma)\} &= \frac{Q_1 Q_3^* Q_2 - |Q_3|^2 - |Q_2|^2 - |Q_1|^2 + 2M}{M(M-1)(M-2)}. \qquad \text{(G.3)}
\end{aligned}
$$

Eq. (4.15) and Eq. (4.16) are for the four-particle correlations.

$$
\begin{aligned}
&\sum_{\alpha,\beta,\gamma_1,\gamma_2} \exp i(\varphi_\alpha + 3\varphi_\beta - 2\varphi_{\gamma_1} - 2\varphi_{\gamma_2}) = \sum_{\alpha\neq\beta\neq\gamma_1\neq\gamma_2} \exp i(\varphi_\alpha + 3\varphi_\beta - 2\varphi_{\gamma_1} - 2\varphi_{\gamma_2}) \\
&+ \sum_{\alpha\neq\beta\neq\gamma_1} \exp i(-\varphi_\alpha + 3\varphi_\beta - 2\varphi_{\gamma_1}) + \sum_{\alpha\neq\beta\neq\gamma_1} \exp i(\varphi_\alpha + \varphi_\beta - 2\varphi_{\gamma_1}) \\
&+ \sum_{\alpha\neq\beta\neq\gamma_1} \exp i(\varphi_\alpha + 3\varphi_\beta - 4\varphi_{\gamma_1}) + \sum_{\alpha\neq\beta\neq\gamma_2} \exp i(-\varphi_\alpha + 3\varphi_\beta - 2\varphi_{\gamma_2}) \\
&+ \sum_{\alpha\neq\beta\neq\gamma_2} \exp i(\varphi_\alpha + \varphi_\beta - 2\varphi_{\gamma_2}) + \sum_{\alpha\neq\gamma_1\neq\gamma_2} \exp i(4\varphi_\alpha - 2\varphi_{\gamma_1} - 2\varphi_{\gamma_2}) \\
&+ \sum_{\alpha\neq\gamma_1} \exp i(4\varphi_\alpha - 4\varphi_{\gamma_1}) + \sum_{\alpha\neq\beta} \exp i(-\varphi_\alpha + \varphi_\beta) + \sum_{\alpha\neq\beta} \exp i(-\varphi_\alpha + \varphi_\beta) \\
&+ \sum_{\alpha\neq\beta} \exp i(-3\varphi_\alpha + 3\varphi_\beta) + \sum_{\alpha\neq\gamma_1} \exp i(2\varphi_\alpha - 2\varphi_{\gamma_1}) \\
&+ \sum_{\alpha\neq\gamma_2} \exp i(2\varphi_\alpha - 2\varphi_{\gamma_2}) + \sum_{\alpha\neq\beta} \exp i(\varphi_\alpha - \varphi_\beta) + M \\
\Leftrightarrow\ & M(M-1)(M-2)(M-3)\{\exp i(\varphi_\alpha + 3\varphi_\beta - 2\varphi_{\gamma_1} - 2\varphi_{\gamma_2})\} \\
&= Q_1 Q_3 (Q_2^*)^2 - 2\Big(Q_1^* Q_3 Q_2^* - |Q_3|^2 - |Q_2|^2 - |Q_1|^2 + 2M\Big) \\
&-2\Big(Q_1^2 Q_2^* - |Q_2|^2 - 2|Q_1|^2 + 2M\Big) - \Big(Q_1 Q_3 Q_4^* - |Q_4|^2 - |Q_3|^2 - |Q_1|^2 + 2M\Big) \\
&-\Big(Q_4 (Q_2^*)^2 - |Q_4|^2 - 2|Q_2|^2 + 2M\Big) - (|Q_4|^2 - M) \\
&-(|Q_3|^2 - M) - 2(|Q_2|^2 - M) - 3(|Q_1|^2 - M) - M
\end{aligned}
$$

$$\begin{aligned}
\Leftrightarrow\quad & \{\cos(\varphi_\alpha + 3\varphi_\beta - 2\varphi_{\gamma_1} - 2\varphi_{\gamma_2})\} = \Big(Q_1 Q_3 (Q_2^*)^2 - Q_1 Q_3 Q_4^* - Q_4 (Q_2^*)^2 \\
& -2Q_1^* Q_3 Q_2^* - 2(Q_1)^2 Q_2^* \\
& +|Q_4|^2 + 2|Q_3|^2 + 4|Q_2|^2 + 4|Q_1|^2 \\
& -6M\Big)/(M(M-1)(M-2)(M-3)).
\end{aligned} \tag{G.4}$$

$$\begin{aligned}
& \sum_{\alpha,\beta,\gamma_1,\gamma_2} \exp i(\varphi_\alpha - 5\varphi_\beta + 2\varphi_{\gamma_1} + 2\varphi_{\gamma_2}) = \sum_{\alpha\neq\beta\neq\gamma_1\neq\gamma_2} \exp i(\varphi_\alpha - 5\varphi_\beta + 2\varphi_{\gamma_1} + 2\varphi_{\gamma_2}) \\
& + \sum_{\alpha\neq\beta\neq\gamma_1} \exp i(3\varphi_\alpha - 5\varphi_\beta + 2\varphi_{\gamma_1}) + \sum_{\alpha\neq\beta\neq\gamma_1} \exp i(\varphi_\alpha - 3\varphi_\beta + 2\varphi_{\gamma_1}) \\
& + \sum_{\alpha\neq\beta\neq\gamma_1} \exp i(\varphi_\alpha - 5\varphi_\beta + 4\varphi_{\gamma_1}) + \sum_{\alpha\neq\beta\neq\gamma_2} \exp i(3\varphi_\alpha - 5\varphi_\beta + 2\varphi_{\gamma_2}) \\
& + \sum_{\alpha\neq\beta\neq\gamma_2} \exp i(\varphi_\alpha - 3\varphi_\beta + 2\varphi_{\gamma_2}) + \sum_{\alpha\neq\gamma_1\neq\gamma_2} \exp i(-4\varphi_\alpha + 2\varphi_{\gamma_1} + 2\varphi_{\gamma_2}) \\
& + \sum_{\alpha\neq\gamma_1} \exp i(-4\varphi_\alpha + 4\varphi_{\gamma_1}) + \sum_{\alpha\neq\beta} \exp i(3\varphi_\alpha - 3\varphi_\beta) + \sum_{\alpha\neq\beta} \exp i(3\varphi_\alpha - 3\varphi_\beta) \\
& + \sum_{\alpha\neq\beta} \exp i(5\varphi_\alpha - 5\varphi_\beta) + \sum_{\alpha\neq\gamma_1} \exp i(-2\varphi_\alpha + 2\varphi_{\gamma_1}) \\
& + \sum_{\alpha\neq\gamma_2} \exp i(-2\varphi_\alpha + 2\varphi_{\gamma_2}) + \sum_{\alpha\neq\beta} \exp i(\varphi_\alpha - \varphi_\beta) + M \\
\Leftrightarrow\quad & M(M-1)(M-2)(M-3)\{\exp i(\varphi_\alpha - 5\varphi_\beta + 2\varphi_{\gamma_1} + 2\varphi_{\gamma_2})\} \\
& = Q_1 Q_5^* Q_2^2 - 2\Big(Q_3^* Q_5 Q_2 - |Q_5|^2 - |Q_3|^2 - |Q_2|^2 + 2M\Big) \\
& -2\Big(Q_1 Q_3^* Q_2 - |Q_3|^2 - |Q_2|^2 - |Q_1|^2 + 2M\Big) - \Big(Q_1 Q_5^* Q_4 - |Q_5|^2 - |Q_4|^2 - |Q_1|^2 + 2M\Big) \\
& -\Big(Q_4^* Q_2^2 - |Q_4|^2 - 2|Q_2|^2 + 2M\Big) - (|Q_5|^2 - M) - (|Q_4|^2 - M) \\
& -2(|Q_3|^2 - M) - 2(|Q_2|^2 - M) - (|Q_1|^2 - M) - M \\
\Leftrightarrow\quad & \{\cos(\varphi_\alpha - 5\varphi_\beta + 2\varphi_{\gamma_1} + 2\varphi_{\gamma_2})\} = \Big(Q_1 Q_5^* (Q_2)^2 - Q_1 Q_5^* Q_4 - Q_4^* (Q_2)^2 \\
& -2Q_5^* Q_3 Q_2 - 2Q_1 Q_3^* Q_2 + 2|Q_5|^2 \\
& +|Q_4|^2 + 2|Q_3|^2 + 4|Q_2|^2 + 2|Q_1|^2 \\
& -6M\Big)/(M(M-1)(M-2)(M-3)).
\end{aligned} \tag{G.5}$$

Appendix H

Q-cumulant for the pair differential correlations

Two nested track-loops are necessary to calculate the pair differential correlations

$$
\begin{aligned}
&\sum_{i\neq j}^{pair\ sel.} \exp i(\varphi_i - \varphi_j), \\
&\sum_{i\neq j}^{pair\ sel.} \exp i(\varphi_i + \varphi_j), \\
&\sum_{i\neq j}^{pair\ sel.} \exp i(3\varphi_i - 3\varphi_j), \\
&\sum_{i\neq j}^{pair\ sel.} \exp i(\varphi_i - 3\varphi_j),
\end{aligned}
\tag{H.1}
$$

where $\sum_{i\neq j}^{pair\ sel.}$ denotes the sum over the pairs which consist of the i-th and $j(\neq i)$-th particles and pass the $(i,\ j)$ symmetric selection criteria such as $0.1 < |\eta_i - \eta_j| < 0.2$. Then we can calculate the pair differential three-particle correlations without any extra nested track-loops as the follows:

$$\begin{aligned}
&\sum_{k}\sum_{i\neq j}^{\textit{pair sel.}} \exp i(\varphi_i+\varphi_j-2\varphi_k)\\
&=\sum_{k(\neq i\neq j)}\sum_{i\neq j}^{\textit{pair sel.}} \exp i(\varphi_i+\varphi_j-2\varphi_k)+2\sum_{i\neq j}^{\textit{pair sel.}} \exp i(\varphi_i-\varphi_j)\\
&\Leftrightarrow \sum_{k(\neq i\neq j)}\sum_{i\neq j}^{\textit{pair sel.}} \exp i(\varphi_i+\varphi_j-2\varphi_k)\\
&=\sum_{i\neq j}^{\textit{pair sel.}} \exp i(\varphi_i+\varphi_j)\times\sum_{k}\exp i(-2\varphi_k)-2\sum_{i\neq j}^{\textit{pair sel.}} \exp i(\varphi_i-\varphi_j). \qquad \text{(H.2)}
\end{aligned}$$

$$\begin{aligned}
&\sum_{k}\sum_{i\neq j}^{\textit{pair sel.}} \exp i(\varphi_i-3\varphi_j+2\varphi_k)=\sum_{k(\neq i\neq j)}\sum_{i\neq j}^{\textit{pair sel.}} \exp i(\varphi_i-3\varphi_j+2\varphi_k)\\
&+\sum_{i\neq j}^{\textit{pair sel.}} \exp i(\varphi_i-\varphi_j)+\sum_{i\neq j}^{\textit{pair sel.}} \exp i(3\varphi_i-3\varphi_j)\\
&\Leftrightarrow \sum_{k(\neq i\neq j)}\sum_{i\neq j}^{\textit{pair sel.}} \exp i(\varphi_i-3\varphi_j+2\varphi_k)=\sum_{i\neq j}^{\textit{pair sel.}} \exp i(\varphi_i-3\varphi_j)\times\sum_{k}\exp i(2\varphi_k)\\
&-\sum_{i\neq j}^{\textit{pair sel.}} \exp i(\varphi_i-\varphi_j)-\sum_{i\neq j}^{\textit{pair sel.}} \exp i(3\varphi_i-3\varphi_j). \qquad \text{(H.3)}
\end{aligned}$$

Appendix I

Proof of Eq. (2.8)

Here we give the definitions of the charge balance function $B(\tilde{\varphi}_k, \Delta\varphi)$, which can be implemented in the analysis of experimental data and provide a proof of the Eq. (2.8). While the expressions presented in the main sections of the paper were based on continuous distributions, we will work with discrete variables here. The multiplicities of positive and negative charged particles in a single event are then given by

$$M_+ = \sum_{\alpha \in +} , \qquad M_- = \sum_{\alpha \in -} , \tag{I.1}$$

and the total charged particle multiplicity is

$$M = M_+ + M_- \ . \tag{I.2}$$

Here $\sum_{\alpha \in +/-}$ denotes the sum over positive and negative charged particles respectively. Similarly the differential charged particle multiplicities dM/dp_α can be calculated by dividing the momentum space into a complete set of disjunct bins and counting the number of particles in each bin. This procedure can formally be expressed as

$$dM/dp_\alpha = \frac{1}{\mathrm{BinSize}(p)} \sum_{\gamma \in C} \mathrm{In}(p_\gamma, p_\alpha), \tag{I.3}$$

where $\mathrm{In}(p_\gamma, p_\alpha)$ is one if p_γ is in the p_α momentum bin and zero otherwise. Here $\mathrm{BinSize}(p)$ denotes the size of the momentum bins and we assumed for simplicity that different bins have equal size. The number of pairs $N_{cd}(p_\beta|p_\alpha)$, where $c, d = +, -$ which appear in the definition of the balance function are defined as

$$N_{cd}(p_\beta|p_\alpha) = \frac{1}{\mathrm{BinSize}^2(p)} \sum_{\gamma \in c} \sum_{\delta \in d}^{\gamma \neq \delta} \mathrm{In}(p_\gamma, p_\alpha) \mathrm{In}(p_\delta, p_\beta) \ , \tag{I.4}$$

where the terms with $\gamma = \delta$ are excluded from the sum. With these definitions, the balance function can then be calculated according to Eq. (2.9). In particular for the balance function $B(\tilde{\varphi}_k, \Delta\varphi)$ in azimuthal angle and with respect to the k-th harmonic symmetry plane, one obtains the relation

$$B(\tilde{\varphi}_k, \Delta\varphi) = \frac{2\langle \Delta N(\tilde{\varphi}_k | \tilde{\varphi}_k + \Delta\varphi)\rangle}{\langle dM/d\tilde{\varphi}_k\rangle}, \tag{I.5}$$

where we abbreviated the charge dependent part according to

$$\Delta N = \frac{1}{2}\left[N_{+-} + N_{-+} - N_{++} - N_{--}\right], \tag{I.6}$$

as previously and $\langle . \rangle$ denotes averages over different events. With the above expressions for the balance function and the charged particle multiplicities, we can now prove Eq. (2.8). The starting point is the right hand side of the identity, which in the continuum takes the form

$$\begin{aligned} RHS &= \frac{2}{\langle M\rangle}\int d\tilde{\varphi}_k \; d\Delta\varphi \; \left\langle \frac{dM}{d\tilde{\varphi}_k}\right\rangle B(\tilde{\varphi}_k, \Delta\varphi) \\ &\qquad \times \cos[n\Delta\varphi + (n+m)\tilde{\varphi}_k] \; . \end{aligned} \tag{I.7}$$

We can then rewrite the above expressions in the discrete version, by replacing all integrals by sums yielding

$$\begin{aligned} RHS &= \frac{4}{\langle M\rangle}\sum_{\Delta\varphi}^{bins}\sum_{\tilde{\varphi}_k}^{bins} \mathrm{BinSize}(\tilde{\varphi}_k)\mathrm{BinSize}(\Delta\varphi) \\ &\qquad \times \Delta N(\tilde{\varphi}_k | \tilde{\varphi}_k + \Delta\varphi) \; \cos[n\Delta\varphi + (n+m)\tilde{\varphi}_k] \; , \end{aligned} \tag{I.8}$$

where the factor $dM/d\tilde{\varphi}_k$ cancels with the denominator of the balance function. Since the number of particle pairs $N_{cd}(\tilde{\varphi}_k | \tilde{\varphi}_k + \Delta\varphi)$ are given by

$$\begin{aligned} N_{cd}(\tilde{\varphi}_k | \tilde{\varphi}_k + \Delta\varphi) &= \frac{1}{\mathrm{BinSize}(\Delta\varphi)}\frac{1}{\mathrm{BinSize}(\tilde{\varphi}_k)} \\ &\qquad \sum_{\alpha\in c}\sum_{\beta\in d}^{\beta\neq\alpha} \mathrm{In}(\varphi_\alpha - \varphi_\beta, \Delta\varphi)\mathrm{In}(\varphi_\beta - \Psi_k, \tilde{\varphi}_k) \; , \end{aligned} \tag{I.9}$$

we can use this expression and individually evaluate the c, d components of the right hand side yielding

$$\begin{aligned} RHS(c,d) &= \frac{4}{\langle M\rangle}\sum_{\Delta\varphi}^{bins}\sum_{\tilde{\varphi}_k}^{bins}\frac{1}{N_{Ev}}\sum_{Events}\sum_{\alpha\in c}\sum_{\beta\in d}^{\beta\neq\alpha} \mathrm{In}(\varphi_\alpha - \varphi_\beta, \Delta\varphi)\mathrm{In}(\varphi_\beta - \Psi_k, \tilde{\varphi}_k) \\ &\qquad \cos[n\Delta\varphi + (n+m)\tilde{\varphi}_k] \\ &= \frac{4}{\langle M\rangle}\frac{1}{N_{Ev}}\sum_{Events}\sum_{\alpha\in c}\sum_{\beta\in d}^{\beta\neq\alpha} \\ &\qquad \cos[n(\varphi_\alpha - \varphi_\beta) + (n+m)(\varphi_\beta - \Psi_k)] \; , \end{aligned} \tag{I.10}$$

where in the last step we first performed the summations over bins and used the fact that

$$\sum_{\Delta\varphi}^{bins}\sum_{\tilde{\varphi}_k}^{bins}\mathrm{In}(X,\Delta\varphi)\mathrm{In}(Y,\tilde{\varphi}_k)\ f(\Delta\varphi,\tilde{\varphi}_k) = f(X,Y)\ , \tag{I.11}$$

for continuous functions $f(X,Y)$ in the limit of small bin sizes. With the assumption that particle number multiplicities are the same for positive and negative charged particles in each event, such that $M^2 = 4M_cM_d$ for $c,d = +,-$ the right hand side expression can be rewritten as

$$RHS(c,d) \;=\; \frac{1}{\langle M\rangle}\frac{1}{N_{Ev}}\sum_{Events}\frac{M^2}{M_cM_d}\sum_{\alpha\in c}\sum_{\beta\in d}^{\beta\neq\alpha}\ \cos[n(\varphi_\alpha-\varphi_\beta)+(n+m)(\phi_\beta-\Psi_k)])\ , \tag{I.12}$$

such that performing the sum over the different charge dependent components $RHS(c,d)$ yields

$$RHS \;=\; \frac{\Delta\left\langle M^2\cos[n\varphi_\alpha+m\varphi_\beta-(n+m)\Psi_k]\right\rangle}{\langle M\rangle}\ , \tag{I.13}$$

which completes our proof.

Appendix J

Calculation of Eq. (5.20 - 21)

We define $X \equiv \varphi_\alpha - \varphi_\beta$ and $Y \equiv \varphi_\beta - \varphi_\gamma$. Then, we have $X + Y = \varphi_\alpha - \varphi_\gamma$, $\cos(\varphi_\alpha + \varphi_\beta - 2\varphi_\gamma) = \cos(X + 2Y)$ and $\cos(\varphi_\alpha - 3\varphi_\beta + 2\varphi_\gamma) = \cos(X - 2Y)$. Eq. (5.19) can be written as:

$$\begin{aligned}
\Big\langle\Big\langle \frac{dN_{\alpha\beta\gamma}}{d\varphi_\alpha d\varphi_\beta d\varphi_\gamma} \Big\rangle\Big\rangle &\sim \frac{N_\alpha N_\beta N_\gamma}{(2\pi)^3}\Big[1 + \sum_{n=1}^{4} 2\Big(\frac{v_{n\alpha}v_{n\beta}}{\epsilon_n^2}\Big)\langle\langle\epsilon_n^2\rangle\rangle\cos(nX) \\
&+ \ldots \\
&+ 2\frac{v_{1\alpha}v_{1\beta}v_{2\gamma}}{\epsilon_1^2\epsilon_2}\langle\langle\epsilon_1^2\epsilon_2\cos(2\Psi_1 - 2\Psi_2)\rangle\rangle\cos(X + 2Y) \\
&+ 2\frac{v_{1\alpha}v_{3\beta}v_{2\gamma}}{\epsilon_1\epsilon_3\epsilon_2}\langle\langle\epsilon_1\epsilon_3\epsilon_2\cos(\Psi_1 - 3\Psi_3 + 2\Psi_2)\rangle\rangle\cos(X - 2Y) \\
&+ \cdots + \alpha \leftrightarrow \beta \leftrightarrow \gamma\Big] \\
&\times \Big[1 - \frac{2p_{\mathrm{T},\alpha}p_{\mathrm{T},\beta}}{M \cdot K}\cos(X) - \frac{2p_{\mathrm{T},\alpha}p_{\mathrm{T},\gamma}}{M \cdot K}\cos(X + Y) \\
&- \frac{2p_{\mathrm{T},\beta}p_{\mathrm{T},\gamma}}{M \cdot K}\cos(Y) \\
&+ \frac{4p_{\mathrm{T},\alpha}^2 p_{\mathrm{T},\beta}p_{\mathrm{T},\gamma}}{K^2}\cos(X)\cos(X + Y) \\
&+ \frac{4p_{\mathrm{T},\alpha}p_{\mathrm{T},\beta}^2 p_{\mathrm{T},\gamma}}{K^2}\cos(X)\cos(Y) \\
&+ \frac{4p_{\mathrm{T},\alpha}p_{\mathrm{T},\beta}p_{\mathrm{T},\gamma}^2}{K^2}\cos(X + Y)\cos(Y)\Big].
\end{aligned} \tag{J.1}$$

There are 7 kinds of terms proportional to 1, $\cos(X)$, $\cos(Y)$, $\cos(X+Y)$, $\cos(X)\cos(Y)$, $\cos(X)\cos(X+Y)$ and $\cos(Y)\cos(X+Y)$ in the factor from the p_{T} conservation effect. In the factor $dN/d^2\mathbf{p}_{\mathrm{T},\alpha} \cdot dN/d^2\mathbf{p}_{\mathrm{T},\beta} \cdot dN/d^2\mathbf{p}_{\mathrm{T},\gamma}$, there are 4 kinds of terms proportional to 1, cos(nX), cos(nY) and cos[n(X + Y)] for $n = 1, 2, 3, 4$ which we need to consider here.

Therefore, we need to calculate $4 \times 7 + 1 = 29$ kinds of integrals.

$$
\begin{aligned}
& v_{2,\gamma}\langle\cos(\varphi_\alpha+\varphi_\beta-2\Psi_2)\rangle \\
&= \int d\varphi_\alpha d\varphi_\beta d\varphi_\gamma dp_{\mathrm{T},\alpha} dp_{\mathrm{T},\beta} dp_{\mathrm{T},\gamma} \frac{\cos(\varphi_\alpha+\varphi_\beta-2\varphi_\gamma)}{N_\alpha N_\beta N_\gamma} \left\langle\left\langle \frac{dN_{\alpha\beta\gamma}}{d\varphi_\alpha d\varphi_\beta d\varphi_\gamma} \right\rangle\right\rangle \\
&= \int dXdY \cos^2(X+2Y) \\
&+ \int dXdY \cos(X+2Y)\cdot 1\cdot 1 \\
&+ (-2p_{\mathrm{T},\alpha}p_{\mathrm{T},\beta})/(M\cdot K) \int dXdY \cos(X+2Y)\cdot 1\cdot \cos(X) \\
&+ (-2p_{\mathrm{T},\beta}p_{\mathrm{T},\gamma})/(M\cdot K) \int dXdY \cos(X+2Y)\cdot 1\cdot \cos(Y) \\
&+ (-2p_{\mathrm{T},\alpha}p_{\mathrm{T},\gamma})/(M\cdot K) \int dXdY \cos(X+2Y)\cdot 1\cdot \cos(X+Y) \\
&+ (+4p_{\mathrm{T},\alpha}p^2_{\mathrm{T},\beta}p_{\mathrm{T},\gamma})/(K^2) \int dXdY \cos(X+2Y)\cdot 1\cdot \cos(X)\cos(Y) \\
&+ (+4p^2_{\mathrm{T},\alpha}p_{\mathrm{T},\beta}p_{\mathrm{T},\gamma})/(K^2) \int dXdY \cos(X+2Y)\cdot 1\cdot \cos(X)\cos(X+Y) \\
&+ (+4p_{\mathrm{T},\alpha}p_{\mathrm{T},\beta}p^2_{\mathrm{T},\gamma})/(K^2) \int dXdY \cos(X+2Y)\cdot 1\cdot \cos(Y)\cos(X+Y) \\
&+ \int dXdY \cos(X+2Y)\cdot \cos(\mathrm{nX})\cdot 1 \\
&+ v_{n,\alpha}v_{n,\beta}(-2p_{\mathrm{T},\alpha}p_{\mathrm{T},\beta})/(M\cdot K) \int dXdY \cos(X+2Y)\cdot \cos(\mathrm{nX})\cdot \cos(X) \\
&+ v_{n,\alpha}v_{n,\beta}(-2p_{\mathrm{T},\beta}p_{\mathrm{T},\gamma})/(M\cdot K) \int dXdY \cos(X+2Y)\cdot \cos(\mathrm{nX})\cdot \cos(Y) \\
&+ v_{n,\alpha}v_{n,\beta}(-2p_{\mathrm{T},\alpha}p_{\mathrm{T},\gamma})/(M\cdot K) \int dXdY \cos(X+2Y)\cdot \cos(\mathrm{nX})\cdot \cos(X+Y) \\
&+ v_{n,\alpha}v_{n,\beta}(+4p_{\mathrm{T},\alpha}p^2_{\mathrm{T},\beta}p_{\mathrm{T},\gamma})/(K^2) \int dXdY \cos(X+2Y)\cdot \cos(\mathrm{nX})\cdot \cos(X)\cos(Y) \\
&+ v_{n,\alpha}v_{n,\beta}(+4p^2_{\mathrm{T},\alpha}p_{\mathrm{T},\beta}p_{\mathrm{T},\gamma})/(K^2) \int dXdY \cos(X+2Y)\cdot \cos(\mathrm{nX})\cdot \cos(X)\cos(X+Y) \\
&+ v_{n,\alpha}v_{n,\beta}(+4p_{\mathrm{T},\alpha}p_{\mathrm{T},\beta}p^2_{\mathrm{T},\gamma})/(K^2) \int dXdY \cos(X+2Y)\cdot \cos(\mathrm{nX})\cdot \cos(Y)\cos(X+Y) \\
&+ \int dXdY \cos(X+2Y)\cdot \cos(\mathrm{nY})\cdot 1 \\
&+ v_{n,\beta}v_{n,\gamma}(-2p_{\mathrm{T},\alpha}p_{\mathrm{T},\beta})/(M\cdot K) \int dXdY \cos(X+2Y)\cdot \cos(\mathrm{nY})\cdot \cos(X)
\end{aligned}
$$

$$
\begin{aligned}
&+v_{n,\beta}v_{n,\gamma}(-2p_{\mathrm{T},\beta}p_{\mathrm{T},\gamma})/(M\cdot K)\int dXdY\cos(X+2Y)\cdot\cos(\mathrm{nY})\cdot\cos(Y)\\
&+v_{n,\beta}v_{n,\gamma}(-2p_{\mathrm{T},\alpha}p_{\mathrm{T},\gamma})/(M\cdot K)\int dXdY\cos(X+2Y)\cdot\cos(\mathrm{nY})\cdot\cos(X+Y)\\
&+v_{n,\beta}v_{n,\gamma}(+4p_{\mathrm{T},\alpha}p^2_{\mathrm{T},\beta}p_{\mathrm{T},\gamma})/(K^2)\int dXdY\cos(X+2Y)\cdot\cos(\mathrm{nY})\cdot\cos(X)\cos(Y)\\
&+v_{n,\beta}v_{n,\gamma}(+4p^2_{\mathrm{T},\alpha}p_{\mathrm{T},\beta}p_{\mathrm{T},\gamma})/(K^2)\int dXdY\cos(X+2Y)\cdot\cos(\mathrm{nY})\cdot\cos(X)\cos(X+Y)\\
&+v_{n,\beta}v_{n,\gamma}(+4p_{\mathrm{T},\alpha}p_{\mathrm{T},\beta}p^2_{\mathrm{T},\gamma})/(K^2)\int dXdY\cos(X+2Y)\cdot\cos(\mathrm{nY})\cdot\cos(Y)\cos(X+Y)\\
&+\int dXdY\cos(X+2Y)\cdot\cos[\mathrm{n(X+Y)}]\cdot 1\\
&+v_{n,\alpha}v_{n,\gamma}(-2p_{\mathrm{T},\alpha}p_{\mathrm{T},\beta})/(M\cdot K)\int dXdY\cos(X+2Y)\cdot\cos[\mathrm{n(X+Y)}]\cdot\cos(X)\\
&+v_{n,\alpha}v_{n,\gamma}(-2p_{\mathrm{T},\beta}p_{\mathrm{T},\gamma})/(M\cdot K)\int dXdY\cos(X+2Y)\cdot\cos[\mathrm{n(X+Y)}]\cdot\cos(Y)\\
&+v_{n,\alpha}v_{n,\gamma}(-2p_{\mathrm{T},\alpha}p_{\mathrm{T},\gamma})/(M\cdot K)\int dXdY\cos(X+2Y)\cdot\cos[\mathrm{n(X+Y)}]\cdot\cos(X+Y)\\
&+v_{n,\alpha}v_{n,\gamma}(+4p_{\mathrm{T},\alpha}p^2_{\mathrm{T},\beta}p_{\mathrm{T},\gamma})/(K^2)\int dXdY\cos(X+2Y)\cdot\cos[\mathrm{n(X+Y)}]\cdot\cos(X)\cos(Y)\\
&+v_{n,\alpha}v_{n,\gamma}(+4p^2_{\mathrm{T},\alpha}p_{\mathrm{T},\beta}p_{\mathrm{T},\gamma})/(K^2)\int dXdY\cos(X+2Y)\cdot\cos[\mathrm{n(X+Y)}]\cdot\cos(X)\cos(X+Y)\\
&+v_{n,\alpha}v_{n,\gamma}(+4p_{\mathrm{T},\alpha}p_{\mathrm{T},\beta}p^2_{\mathrm{T},\gamma})/(K^2)\int dXdY\cos(X+2Y)\cdot\cos[\mathrm{n(X+Y)}]\cdot\cos(Y)\cos(X+Y)
\end{aligned}
$$

$$
\begin{aligned}
= \quad &\int dp_{\mathrm{T},\alpha}dp_{\mathrm{T},\beta}dp_{\mathrm{T},\gamma}\Big[\frac{v_{1\alpha}v_{1\beta}v_{2,\gamma}}{\epsilon_1^2\epsilon_2}\langle\langle\epsilon_1^2\epsilon_2\cos(2\Psi_1-2\Psi_2)\rangle\rangle\\
&+0+0+0+0+0+0+\frac{4}{K^2}p_{\mathrm{T},\alpha}p_{\mathrm{T},\beta}p^2_{\mathrm{T},\gamma}\\
&+0+0+0+0+0+0+0\\
&+0+v_{2,\beta}v_{2,\gamma}\frac{2p_{\mathrm{T},\alpha}p_{\mathrm{T},\beta}}{M\cdot K}+0+v_{1,\beta}v_{1,\gamma}\frac{2p_{\mathrm{T},\alpha}p_{\mathrm{T},\gamma}}{M\cdot K}+\Big(v_{1,\beta}v_{1,\gamma}+v_{3,\beta}v_{3,\gamma}\Big)\frac{4}{K^2}p_{\mathrm{T},\alpha}p^2_{\mathrm{T},\beta}p_{\mathrm{T},\gamma}\\
&\qquad+0+v_{2,\beta}v_{2,\gamma}\frac{4}{K^2}p_{\mathrm{T},\alpha}p_{\mathrm{T},\beta}p^2_{\mathrm{T},\gamma}\\
&+0+v_{2,\alpha}v_{2,\gamma}\frac{2p_{\mathrm{T},\alpha}p_{\mathrm{T},\beta}}{M\cdot K}+v_{1,\alpha}v_{1,\gamma}\frac{2p_{\mathrm{T},\beta}p_{\mathrm{T},\gamma}}{M\cdot K}+0+0+\Big(v_{1,\alpha}v_{1,\gamma}+v_{3,\alpha}v_{3,\gamma}\Big)\frac{4}{K^2}p^2_{\mathrm{T},\alpha}p_{\mathrm{T},\beta}p_{\mathrm{T},\gamma}\\
&\qquad+v_{2,\alpha}v_{2,\gamma}\frac{4}{K^2}p_{\mathrm{T},\alpha}p_{\mathrm{T},\beta}p^2_{\mathrm{T},\gamma}\Big].
\end{aligned}
\tag{J.2}
$$

As a same way, we can calculate them for the correlation $\langle\cos(\varphi_\alpha - 3\varphi_\beta + 2\Psi_2)\rangle$.

$$
\begin{aligned}
&v_{2,\gamma}\langle\cos(\varphi_\alpha - 3\varphi_\beta + 2\Psi_2)\rangle\\
&= \int d\varphi_\alpha d\varphi_\beta d\varphi_\gamma dp_{\mathrm{T},\alpha} dp_{\mathrm{T},\beta} dp_{\mathrm{T},\gamma} \frac{\cos(\varphi_\alpha - 3\varphi_\beta + 2\varphi_\gamma)}{N_\alpha N_\beta N_\gamma} \Big\langle\Big\langle \frac{dN_{\alpha\beta\gamma}}{d\varphi_\alpha d\varphi_\beta d\varphi_\gamma} \Big\rangle\Big\rangle\\
&= \int dX dY \cos^2(X-2Y)\\
&+ \int dX dY \cos(X-2Y)\cdot 1\cdot 1\\
&+ (-2p_{\mathrm{T},\alpha}p_{\mathrm{T},\beta})/(M\cdot K) \int dX dY \cos(X-2Y)\cdot 1\cdot \cos(X)\\
&+ (-2p_{\mathrm{T},\beta}p_{\mathrm{T},\gamma})/(M\cdot K) \int dX dY \cos(X-2Y)\cdot 1\cdot \cos(Y)\\
&+ (-2p_{\mathrm{T},\alpha}p_{\mathrm{T},\gamma})/(M\cdot K) \int dX dY \cos(X-2Y)\cdot 1\cdot \cos(X+Y)\\
&+ (+4p_{\mathrm{T},\alpha}p^2_{\mathrm{T},\beta}p_{\mathrm{T},\gamma})/(K^2) \int dX dY \cos(X-2Y)\cdot 1\cdot \cos(X)\cos(Y)\\
&+ (+4p^2_{\mathrm{T},\alpha}p_{\mathrm{T},\beta}p_{\mathrm{T},\gamma})/(K^2) \int dX dY \cos(X-2Y)\cdot 1\cdot \cos(X)\cos(X+Y)\\
&+ (+4p_{\mathrm{T},\alpha}p_{\mathrm{T},\beta}p^2_{\mathrm{T},\gamma})/(K^2) \int dX dY \cos(X-2Y)\cdot 1\cdot \cos(Y)\cos(X+Y)\\
&+ \int dX dY \cos(X-2Y)\cdot \cos(\mathrm{nX})\cdot 1\\
&+ v_{n,\alpha}v_{n,\beta}(-2p_{\mathrm{T},\alpha}p_{\mathrm{T},\beta})/(M\cdot K) \int dX dY \cos(X-2Y)\cdot \cos(\mathrm{nX})\cdot \cos(X)\\
&+ v_{n,\alpha}v_{n,\beta}(-2p_{\mathrm{T},\beta}p_{\mathrm{T},\gamma})/(M\cdot K) \int dX dY \cos(X-2Y)\cdot \cos(\mathrm{nX})\cdot \cos(Y)\\
&+ v_{n,\alpha}v_{n,\beta}(-2p_{\mathrm{T},\alpha}p_{\mathrm{T},\gamma})/(M\cdot K) \int dX dY \cos(X-2Y)\cdot \cos(\mathrm{nX})\cdot \cos(X+Y)\\
&+ v_{n,\alpha}v_{n,\beta}(+4p_{\mathrm{T},\alpha}p^2_{\mathrm{T},\beta}p_{\mathrm{T},\gamma})/(K^2) \int dX dY \cos(X-2Y)\cdot \cos(\mathrm{nX})\cdot \cos(X)\cos(Y)\\
&+ v_{n,\alpha}v_{n,\beta}(+4p^2_{\mathrm{T},\alpha}p_{\mathrm{T},\beta}p_{\mathrm{T},\gamma})/(K^2) \int dX dY \cos(X-2Y)\cdot \cos(\mathrm{nX})\cdot \cos(X)\cos(X+Y)\\
&+ v_{n,\alpha}v_{n,\beta}(+4p_{\mathrm{T},\alpha}p_{\mathrm{T},\beta}p^2_{\mathrm{T},\gamma})/(K^2) \int dX dY \cos(X-2Y)\cdot \cos(\mathrm{nX})\cdot \cos(Y)\cos(X+Y)\\
&+ \int dX dY \cos(X-2Y)\cdot \cos(\mathrm{nY})\cdot 1\\
&+ v_{n,\beta}v_{n,\gamma}(-2p_{\mathrm{T},\alpha}p_{\mathrm{T},\beta})/(M\cdot K) \int dX dY \cos(X-2Y)\cdot \cos(\mathrm{nY})\cdot \cos(X)
\end{aligned}
$$

$$
\begin{aligned}
&+v_{n,\beta}v_{n,\gamma}(-2p_{\mathrm{T},\beta}p_{\mathrm{T},\gamma})/(M\cdot K)\int dXdY\cos(X-2Y)\cdot\cos(\mathrm{nY})\cdot\cos(Y)\\
&+v_{n,\beta}v_{n,\gamma}(-2p_{\mathrm{T},\alpha}p_{\mathrm{T},\gamma})/(M\cdot K)\int dXdY\cos(X-2Y)\cdot\cos(\mathrm{nY})\cdot\cos(X+Y)\\
&+v_{n,\beta}v_{n,\gamma}(+4p_{\mathrm{T},\alpha}p_{\mathrm{T},\beta}^{2}p_{\mathrm{T},\gamma})/(K^2)\int dXdY\cos(X-2Y)\cdot\cos(\mathrm{nY})\cdot\cos(X)\cos(Y)\\
&+v_{n,\beta}v_{n,\gamma}(+4p_{\mathrm{T},\alpha}^{2}p_{\mathrm{T},\beta}p_{\mathrm{T},\gamma})/(K^2)\int dXdY\cos(X-2Y)\cdot\cos(\mathrm{nY})\cdot\cos(X)\cos(X+Y)\\
&+v_{n,\beta}v_{n,\gamma}(+4p_{\mathrm{T},\alpha}p_{\mathrm{T},\beta}p_{\mathrm{T},\gamma}^{2})/(K^2)\int dXdY\cos(X-2Y)\cdot\cos(\mathrm{nY})\cdot\cos(Y)\cos(X+Y)\\
&+\int dXdY\cos(X-2Y)\cdot\cos[\mathrm{n(X+Y)}]\cdot 1\\
&+v_{n,\alpha}v_{n,\gamma}(-2p_{\mathrm{T},\alpha}p_{\mathrm{T},\beta})/(M\cdot K)\int dXdY\cos(X-2Y)\cdot\cos[\mathrm{n(X+Y)}]\cdot\cos(X)\\
&+v_{n,\alpha}v_{n,\gamma}(-2p_{\mathrm{T},\beta}p_{\mathrm{T},\gamma})/(M\cdot K)\int dXdY\cos(X-2Y)\cdot\cos[\mathrm{n(X+Y)}]\cdot\cos(Y)\\
&+v_{n,\alpha}v_{n,\gamma}(-2p_{\mathrm{T},\alpha}p_{\mathrm{T},\gamma})/(M\cdot K)\int dXdY\cos(X-2Y)\cdot\cos[\mathrm{n(X+Y)}]\cdot\cos(X+Y)\\
&+v_{n,\alpha}v_{n,\gamma}(+4p_{\mathrm{T},\alpha}p_{\mathrm{T},\beta}^{2}p_{\mathrm{T},\gamma})/(K^2)\int dXdY\cos(X-2Y)\cdot\cos[\mathrm{n(X+Y)}]\cdot\cos(X)\cos(Y)\\
&+v_{n,\alpha}v_{n,\gamma}(+4p_{\mathrm{T},\alpha}^{2}p_{\mathrm{T},\beta}p_{\mathrm{T},\gamma})/(K^2)\int dXdY\cos(X-2Y)\cdot\cos[\mathrm{n(X+Y)}]\cdot\cos(X)\cos(X+Y)\\
&+v_{n,\alpha}v_{n,\gamma}(+4p_{\mathrm{T},\alpha}p_{\mathrm{T},\beta}p_{\mathrm{T},\gamma}^{2})/(K^2)\int dXdY\cos(X-2Y)\cdot\cos[\mathrm{n(X+Y)}]\cdot\cos(Y)\cos(X+Y)
\end{aligned}
$$

$$
\begin{aligned}
&=\int dp_{\mathrm{T},\alpha}dp_{\mathrm{T},\beta}dp_{\mathrm{T},\gamma}\Big[\frac{v_{1\alpha}v_{3\beta}v_{2,\gamma}}{\epsilon_1\epsilon_3\epsilon_2}\langle\langle\epsilon_1\epsilon_3\epsilon_2\cos(\Psi_1-3\Psi_3+2\Psi_2)\rangle\rangle\\
&+0+0+0+0+0+0+0\\
&+0+0+0+0+\Big(v_{1,\alpha}v_{1,\beta}+v_{3,\alpha}v_{3,\beta}\Big)\frac{4}{K^2}p_{\mathrm{T},\alpha}p_{\mathrm{T},\beta}^{2}p_{\mathrm{T},\gamma}+0+v_{2,\alpha}v_{2,\beta}\frac{4}{K^2}p_{\mathrm{T},\alpha}p_{\mathrm{T},\beta}p_{\mathrm{T},\gamma}^{2}\\
&+0+v_{2,\beta}v_{2,\gamma}\frac{2}{M\cdot K}p_{\mathrm{T},\alpha}p_{\mathrm{T},\beta}+0+v_{3,\beta}v_{3,\gamma}\frac{2}{M\cdot K}p_{\mathrm{T},\alpha}p_{\mathrm{T},\gamma}\\
&\quad+\Big(v_{1,\beta}v_{1,\gamma}+v_{3,\beta}v_{3,\gamma}\Big)\frac{4}{K^2}p_{\mathrm{T},\alpha}p_{\mathrm{T},\beta}^{2}p_{\mathrm{T},\gamma}+0+\Big(v_{2,\beta}v_{2,\gamma}+v_{4,\beta}v_{4,\gamma}\Big)\frac{4}{K^2}p_{\mathrm{T},\alpha}p_{\mathrm{T},\beta}p_{\mathrm{T},\gamma}^{2}\\
&+0+0+0+0+0+0+0\Big].
\end{aligned}
\tag{J.3}
$$

Bibliography

[1] D.J. Gross, F. Wilczek, Phys. Rev. Lett. **30**, 1343 (1973),
H.D. Politzer, Phys. Rev. Lett. **30**, 1346 (1973).

[2] N. Cabibbo, G. Parisi, Phys. Lett. B **59**, 67 (1975),
J.C. Collins and M.J. Perry, Phys. Rev. lett. **30**, 1353 (1975).

[3] F. Karsch, PoSCPOD **07**, 026 (2007).

[4] K. Rajagopal, They overview. Quark Matter 2011 plenary talk.

[5] J.D. Bjorken, Phys. Rev. D **27**, 140 (1983).

[6] P.F. Kolb, Heavy Ion Phys. **21**, 243 (2004).

[7] Chun Shen, Ulrich W. Heinz, Pasi Huovinen, Huichao Song, Phys. Rev. C **84**, 044903 (2011).

[8] S. Voloshin, A. M. Poskanzer, and R. Snellings, in Relativistic Heavy Ion Physics, Landolt-Bornstein Vol. 1(Springer-Verlag, Berlin, 2010), pp. 554.

[9] A. M. Poskanzer, S. A. Voloshin, Phys. Rev. C **58**, 1671-1678 (1998).

[10] B. Alver and G. Roland, Phys. Rev. C **81**, 054905 (2010) [Erratum-ibid. C 82, 039903 (2010)] [arXiv:1003.0194 nucl-th]].

[11] R. Snellings, Elliptic Flow: A Brief Review, 2011.

[12] M. L. Miller, K. Reygers, S. J. Sanders, and P. Steinberg, Ann. Rev. Nucl. Part. Sci., vol.57, pp.205-243, 2007.

[13] D. Teaney and L. Yan, Phys. Rev. C **83**, 064904 (2011).

[14] B. Abelev *et al.* [The ALICE Collaboration], arXiv:1205.5761 [nucl-ex].

[15] C. A. Loizides *et al.* [ALICE Collaboration], Phys. Rev. Lett. **107**, 032301 (2011) [arXiv:1105.3865 [nucl-ex]].

[16] J. Y. Ollitrault, Phys. Rev. D **46**, 229 (1992).

[17] A. Adare *et al.* [PHENIX Collaboration], Phys. Rev. Lett. **107**, 252301 (2011) [arXiv:1105.3928 [nucl-ex]].

[18] K. Aamodt *et al.* [ALICE Collaboration], Phys. Lett. B **708**, 249 (2012) [arXiv:1109.2501 [nucl-ex]].

[19] J. Jia [ATLAS Collaboration], J. Phys. G **38**, 124012 (2011) [arXiv:1107.1468 [nucl-ex]].

[20] S. Chatrchyan *et al.* [CMS Collaboration], Eur. Phys. J. C **72**, 2012 (2012) [arXiv:1201.3158 [nucl-ex]].

[21] P. Sorensen [STAR Collaboration], J. Phys. G **38**, 124029 (2011) [arXiv:1110.0737 [nucl-ex]].

[22] N. Borghini, P. M. Dinh and J. Y. Ollitrault, Phys. Rev. C **62**, 034902 (2000) [arXiv:nucl-th/0004026].

[23] N. Borghini, P. M. Dinh, J. Y. Ollitrault, A. M. Poskanzer and S. A. Voloshin, Phys. Rev. C **66**, 014901 (2002) [arXiv:nucl-th/0202013].

[24] M. Luzum and J. Y. Ollitrault, Phys. Rev. Lett. **106**, 102301 (2011) [arXiv:1011.6361 [nucl-ex]].

[25] F. G. Gardim, F. Grassi, Y. Hama, M. Luzum and J. Y. Ollitrault, Phys. Rev. C **83**, 064901 (2011) [arXiv:1103.4605 [nucl-th]].

[26] Ekaterina Retinskaya, Matthew Luzum, Jean-Yves Ollitrault, Phys. Rev. Lett. **108**, 252302 (2012)

[27] S. A. Bass, P. Danielewicz and S. Pratt, Phys. Rev. Lett. **85**, 2689 (2000).

[28] S. Cheng, S. Petriconi, S. Pratt, M. Skoby, C. Gale, S. Jeon, V.Topor Pop ad Q.-H. Zhang, Phys. Rev. C **69** 054906 (2004).

[29] S. Pratt, Phys. Rev. C **85**, 014904 (2012).

[30] S. Pratt, Phys. Rev. Lett. **108**, 212301 (2012).

[31] J. Song, F. -l. Shao and Z. -t. Liang, arXiv:1203.0921 [nucl-th].

[32] M. M. Aggarwal *et al.* [STAR Collaboration], Phys. Rev. C **82**, 024905 (2010) [arXiv:1005.2307 [nucl-ex]].

[33] P. Bozek, Phys. Lett. B **609**, 247 (2005) [nucl-th/0412076].

[34] S. Schlichting and S. Pratt, arXiv:1005.5341 [nucl-th].
S. Schlichting and S. Pratt, Phys. Rev. C **83** 014913 (2010).

[35] Y. Hori, T. Gunji, H. Hamagaki and S. Schlichting arXiv:1208.0603 [nucl-th].

[36] D. Kharzeev, Phys. Lett. B **633**, 260 (2006).

[37] K. Fukushima, D. E. Kharzeev and H. J.Warringa, Phys. Rev. D **78**, 074033 (2008).

[38] D. Kharzeev, L. D. McLerran and H. J. Warringa, Nucl. Phys. A **803**, 227 (2008).

[39] B. I. Abelev et al. [STAR Collaboration], Phys. Rev. Lett. **103**, 251601 (2009).
B. I. Abelev et al. [STAR Collaboration], Phys. Rev. C **81**, 54908 (2010).

[40] S. A. Voloshin, Phys. Rev. C **70**, 057901 (2004).

[41] S. Pratt, arXiv:1002.1758 [nucl-th].

[42] H. Wang [STAR Collaboration], J. Phys. G G **38**, 124188 (2011) [J. Phys. A G **38**, 124188 (2011)] [arXiv:1201.0392 [nucl-ex], arXiv:1201.0392 [nucl-ex]].

[43] S. Voloshin and Y. Zhang, Z. Phys. C **70**, 665 (1996). A. M. Poskanzer and S. Voloshin, Phys. Rev. C **58**, 1671 (1998).

[44] Yuji Hirono, Masaru Hongo, Tetsufumi Hirano, [arXiv:1211.1114 [nucl-th]].

[45] M. Gyulassy and X. N. Wang, Comput. Phys. Commun. **83**, 307 (1994).
X. N. Wang and M. Gyulassy, Phys. Rev. D **44**, 3501 (1991).

[46] S. A. Bass et al., Prog. Part. Nucl. Phys. **41**, 255 (1998).

[47] R. L. Ray and R. S. Longacre, arXiv:nucl-ex/0008009.

[48] A. Bzdak, V. Koch and J. Liao, Phys. Rev. C **81**, 031901 (2010) [arXiv:0912.5050 [nucl-th]].

[49] J. Liao, V. Koch and A. Bzdak, Phys. Rev. C **82**, 054902 (2010) [arXiv:1005.5380 [nucl-th]].

[50] A. Bzdak, arXiv:1112.4066 [nucl-th].

[51] S. Pratt, S. Schlichting and S. Gavin, Phys. Rev. C **84**, 024909 (2011).

[52] Fernando G. Gardim, Frederique Grassi, Matthew Luzum, Jean-Yves Ollitrault, Phys. Rev. C **85**, 024908 (2012).
Rajeev S. Bhalerao, Matthew Luzum, Jean-Yves Ollitrault, Phys. Rev. C **84**, 054901 (2011).
Rajeev S. Bhalerao, Matthew Luzum, Jean-Yves Ollitrault, J. Phys. G: Nucl. Part. Phys. **38** 124055 (2011).
Rajeev S. Bhalerao, Matthew Luzum, Jean-Yves Ollitrault, Phys. Rev. C **84**, 034910 (2011).

[53] "The CERN Large Hadron Collider:Accelerator and Experiments, LHC Machine",JINST **3**, S08001 (2008).

[54] K. Aamodt *et al.* [ALICE Collaboration], JINST **3**, S08002 (2008).

[55] K. Aamodt *et al.* [ALICE Collaboration], "Physics Performance Report, Volume I", J. Phys. G **30**, 1517 (2004).

[56] K. Aamodt *et al.* [ALICE Collaboration], "Physics Performance Report, Volume II", J. Phys. G **32**, 1295 (2006).

[57] ALICE Collaboration. "ALICE ITS Technical Resign Report"

[58] ALICE Collaboration. "ALICE TPC Technical Resign Report"

[59] J. Alme *et al.* [ALICE Collaboration], Nucl. Instrum. Meth. A **622**, 316 (2010).

[60] Hans. Hjersing. Dalsgaard, "Pseudorapidity Densities in p+p and Pb+Pb collisions at LHC measured with the ALICE experiment", Doctoral thesis.

[61] Y. Zoccarato *et al.*, Nucl. Instrum. Meth. A, 626-627 (2011) 90-96.

[62] C. H. Christensen *et al.*, Int. J. Mod. Phys. E16: 2432-2437 (2007).

[63] J.F. Grose-Oetringhaus, "Measurement of the Charged-Particle Multiplicity in Proton-Proton Collisions with the ALICE Detector", Doctoral thesis.

[64] ALICE Offline Project $http://aliceinfo.cern.ch/Offline/$

[65] The ALICE Collaboration, $TheALICEOfflineBibble$

[66] ALICE Monitoring system with MonALISA $http://pcalimonitor.cern.ch$

[67] LHC Programme Coordination web pages, $http://lpc.web.cern.ch/lpc/$

[68] K. Aamodt *et al.* [ALICE Collaboration], Phys. Rev. Lett. **105**, 252301 (2010).
K. Aamodt *et al.* [ALICE Collaboration], Phys. Rev. Lett. **106**, 032301 (2011).

[69] A. Toia, [ALICE Collaboration], J. Phys. G: Nucl. Part. Phys. **38**, 124007 (2011), [arXiv:1107.1973 [nucl-ex]].

[70] Jun Xu, Che Ming Ko, Phys. Rev. C **83**, 034904 (2011).

[71] R. Brun *et al.*, GEANT3 User Guide (CERN Data Handling Division DD/EE/841)

[72] R. Brun *et al.*, CERN. Program Library Long Write-up, W5013, GEANT Detector Description and Simulation Tool.

[73] K. Aamodt *et al.* [The ALICE Collaboration], Phys. Rev. Lett. **105**, 252302 (2010) [arXiv:1011.3914 [nucl-ex]].

[74] A. Bliandzic, “Anisotropic Flow Measurements in ALICE at the Large Hadron Collider”, Doctoral thesis.

[75] N. Borghini, P. M. Dinh, J. -Y. Ollitrault, Phys. Rev. C **63**, 054906 (2001).
N. Borghini, P. M. Dinh, J. -Y. Ollitrault, Phys. Rev. C **64**, 054901 (2001).
N. Borghini, P. M. Dinh, J. -Y. Ollitrault, [nucl-ex/0110016].

[76] R. Kubo, “Generalized Cumulant Expansion Method”, Journal of the Physical Society of Japan, Vol. 17, No. 7, (1962).

[77] A. Bilandzic, R. Snellings and S. Voloshin, Phys. Rev. C **83**, 044913 (2011).

[78] G. Cowan, “Statistical data analysis”, Oxford, UK: Clarendon (1998) 197 p.

[79] Ilya Selyuzhenkov, Sergei Voloshin, Phys. Rev. C **77**, 034904 (2008).

[80] A. Adare *et al.* [PHNIEX Collaboration], Phys. Rev. Lett. **105**, 062301 (2010).

[81] Y. Hori [ALICE Collaboration], arXiv:1211.0890 [nucl-ex].

[82] S. A. Voloshin [ALICE Collaboration], arXiv:1211.5680 [nucl-ex].

[83] J. Adams *et al.* [STAR Collaboration], Phys. Rev. C **72**, 14904 (2005).

[84] R. Preghenella (for the ALICE Collaboration) Acta Phys. Pol. B **43**, 555 (2012).

[85] S. Pratt and S. Cheng, Phys. Rev. C **68**, 014907 (2003) [nucl-th/0303025].

[86] B. Abelev *et al.* [ALICE Collaboration], arXiv:1205.5761 [nucl-ex].

[87] K. Aamodt *et al.* [ALICE Collaboration], Phys. Lett. B **696**, 30-39 (2011).

[88] M. Weber [for the ALICE Collaboration], arXiv:1210.5851 [nucl-ex].

[89] Adam Kisiel, Wojciech Broniowski, Mikolaj Chojnacki, Wojciech Florkowski, Phys. Rev. C **79**, 014902 (2009).

[90] K. Aamodt *et al.* [ALICE Collaboration], Phys. Lett. B **696** (4): 328-337, (2011).

[91] C. Markert, R. Bellwied, I. Vitev, Phys. Lett. B **669**, 92-97 (2008).

[92] P. Christakoglou (for the ALICE Collaboration) J. Phys. G:Nucl. Part. Phys. **38**, 124165 (2011).
B. Abelev *et al.* [ALICE Collaboration], arXiv:1207.0900 [nucl-ex].

[93] B. Muller and A. Schafer, Phys. Rev. C **82**, 057902 (2010) [arXiv:1009.1053 [hep-ph]].

[94] A. Bzdak, V. Koch and J. Liao, Phys. Rev. C **81**, 031901 (2010).
A. Bzdak, V. Koch and J. Liao, Phys. Rev. C **83**, 014905 (2011).

[95] A. R. Zhitnitsky, Nucl. Phys. A **853**, 135 (2011).
A. R. Zhitnitsky, Nucl. Phys. A **886**, 18 (2012).

[96] V. D. Toneev and V. Voronyuk, arXiv:1012.1508 [nucl-th].

[97] J. Adams *et al.* [STAR Collaboration], Phys. Rev. Lett. **92**, 062301 (2004).

[98] S. A. Voloshin, arXiv:1111.7241 [nucl-ex].

[99] G. -L. Ma and B. Zhang, Phys. Lett. B **700**, 39 (2011) [arXiv:1101.1701 [nucl-th]].

[100] P. Bozek and W. Broniowski, arXiv:1204.3580 [nucl-th].

[101] Tetsufumi Hirano, Pasi Huovinen, Koichi Murase, Yasushi Nara, arXiv:1204.5814 [nucl-th].

[102] S. Pratt, WPCF 2011 talk.

[103] N. Borghini, Phys. Rev. C **75**, 021904 (2007) [nucl-th/0612093].

[104] Z. Chajecki and M. Lisa, Phys. Rev. C **79**, 034908 (2009) [arXiv:0807.3569 [nucl-th]].

[105] K. Aamodt *et al.* [ALICE Collaboration], Phys. Lett. B **708** 249-264 (2012).

[106] Y. Hori [ALICE Collaboration], arXiv:1301.7126 [nucl-ex].

[107] A. Bilandzic [ALICE Collaboration], arXiv:1210.6222 [nucl-ex].

[108] C. Adler *et al.* [STAR Collaboration], Phys. Rev. Lett.**90**, 032301 (2003), [arXiv:nucl-ex/0206006].

[109] R.J.Glauber, Lectures in Theoretical Physics, ed. WE Brittin, LG Dunham, 1-315. New York: Interscience (1959).

[110] L. V. Gribov, E.M. Levin and M. G. Ryskin, Phys. Rept. **100**, 1 (1983).
A. H. Mueller and J.-W. Qiu, Nucl. Phys. B **268**, 427 (1986).
A. H. Mueller, Nucl. Phys. B **558**, 285 (1999). L. D. McLerran and R. Venugopalan, Phys. Rev. D **49**, 2233 (1994).
L. D. McLerran and R. Venugopalan, Phys. Rev. D **49**, 3352 (1994).
A. Dumitru, D. E. Kharzeev, E. M. Levin and Y. Nara, Phys. Rev. C **85**, 044920 (2012).

[111] K. Oyama, [ALICE Collaboration], J. Phys. G: Nucl. Part. Phys. **38**, 124131 (2011), [arXiv:1107.0692 [nucl-ex]].

[112] B. B. Back *et al.* [PHOBOS Collaboration], Phys. Rev. C **72**, 051901 (2005).

[113] T. Hirano *et al.*, Phys. Lett. B **636**, 299 (2006),
T. Hirano, Phys. Rev. C **65**, 011901 (2001),
T. Hirano and K. Tsuda, Phys. Rev. C **66**, 054905 (2002).

[114] M. Bleicher and H. Stocker, Phys. Lett. B **526**, 309 (2002),
E. L. Bratkovskaya, W. Cassing and H. Stocker, Phys. Rev. C **67**, 054905 (2003),
W. Cassing, K. Gallmeister and C. Greiner, Nucl. Phys. A **735**, 277 (2004).

[115] M. Gyulassy, I. Vitev and X. N. Wang, Phys. Rev. Lett. **86**, 2537 (2001), [arXiv:nucl-th/0012092].

[116] Jean-Yves Ollitrault, Arthur M. Poskanzer, Sergei A. Voloshin, Phys. Rev. C **80**, 014904 (2009).

[117] Zhi Qiu, Chun Shen, Ulrich W. Heinz, Phys. Lett. B **707**, 151 (2012).

[118] Charles Gale, Sangyong Jeon, Bjoern Schenke, Prithwish Tribedy, Raju Venugopalan, arXiv:1209.6330 [nucl-th].

[119] J. Berges, S. Schlichting, arXiv:1209.0817 [hep-ph],
Soeren Schlichting, arXiv:1207.1450 [hep-ph],
J. Berges, S. Schlichting, D. Sexty, arXiv:1203.4646 [hep-ph],
Jurgen Berges, Kirill Boguslavski, Soeren Schlichting, arXiv:1201.3582v1 [hep-ph],
J. Berges, S. Scheffler, S. Schlichting, D. Sexty, arXiv:1111.2751 [hep-ph].

[120] J. I. Kapusta, B. Muller, M. Stephanov, arXiv:1211.3370 [nucl-th],
Todd Springer, Mikhail Stephanov, arXiv:1210.5179 [nucl-th],
Joseph Kapusta, Berndt Mueller, Misha Stephanov, arXiv:1201.3405 [nucl-th],
J. I. Kapusta, B. Muller, M. Stephanov, Phys. Rev. C **85**, 054906 (2012).

[121] A K Chaudhuri, J. Phys. G: Nucl. Part. Phys. **39** 125102 (2012).

[122] S. S. Chern, J. Simons, Ann. Math. **99**, 48 (1974).

[123] T. Schafer and E. V. Shuryak, Rev. Mod. Phys. **70**, 323 (1998).

[124] Derek Leinweber, http://www.physics.adelaide.edu.au/theory/staff/leinweber/VisualQCD/QCD

[125] T. D. Lee, Phys. Rev. D **8**, 1226 (1973).
T. D. Lee and G. C. Wick, Phys. Rev. D **9**, 2291 (1974).

[126] P. D. Morley and I. A. Schmidt, Z. Phys. C **26**, 627 (1985).

[127] D. Kharzeev, A. Krasnitz, R. Venugopalan, Phys. Lett. B **545**, 298-306 (2002).

[128] D. Kharzeev, R. D. Pisarski and M. H. G. Tytgat, Phys. Rev. Lett. **81**, 512 (1998).
D. Kharzeev and R. D. Pisarski, Phys. Rev. D **61**, 111901 (2000).

[129] V. Voronyuk, V.D Toneev, W. Cassing, E.L. Bratkovskaya, V.P. Konchakovski, S.A. Voloshin, Phys. Rev. C **83**, 054911 (2011).

[130] P.V. Buividovich, M. N. Chernodub, D.E. Kharzeev, T. Kalaydzhyan, E.V. Luschevskaya, M.I. Polikarpov, Phys. Rev. Lett. **105**, 132001 (2010), [arXiv:1003.2180 [hep-lat]].

[131] P.V. Buividovich, M.N. Chernodub, E.V. Luschevskaya, M.I. Polikarpov, Phys. Rev. D **80**, 054503 (2009) [arXiv:0907.0494 [hep-lat]],
M. Abramczyk, T. Blum, G. Petropoulos, R. Zhou, PoS LAT 181 (2009), [arXiv:0911.1348 [hep-lat]],
Arata Yamamoto, Phys. Rev. Lett. **107**, 031601 (2011), [arXiv:1105.0385 [hep-lat]].

[132] Dam T. Son, Piotr Surowka, arXiv:0906.5044 [hep-th].

[133] Gokce Basar, Gerald V. Dunne, Dmitri E. Kharzeev, Phys. Rev. Lett. **104**, 232301 (2010).

[134] Dmitri E. Kharzeev, Ho-Ung Yee, Phys. Rev. D **83**, 085007 (2011).

[135] Ilya Selyuzhenkov, WPCF 2011 talk.

[136] Gang Wang [for the STAR Collaboration], arXiv:1210.5498 [nucl-ex].

[137] M. Bondila, "Detection of charged kaons using the decay topology in ALICE TPC", Doctoral thesis.

[138] L. Bozyk, "Spatial Resolution Calibration of the ALICE Time Projection Chamber and Calibration Visulaization", Diploma thesis.

[139] J. Wiechula, "Commissioning and Calibration of ALICE-TPC", Doctoral thesis.

[140] S. Rossegger, "Simulation and Calibration of the ALICE TPC including innovative space charge calculations", Doctoral thesis.
J. Thomas, M. Mager, S. Rossegger, Alice Internal Note, 2010, ALICE-INT-2010-018.

[141] W. Blum and I. Rolandi, Particle Detection with Drift Chambers. Springer, Berlin, 1998.

[142] J. Thomas, M. Mager, S. Rossegger, Alice Internal Note, 2010, ALICE-INT-2010-016.

[143] R. V. Southwell, *Relaxation methods*, Oxford engineering science series (Oxford Univ. Press, Oxford, 1940).

[144] H. Wieman, STAR Note 253.

[145] R. Veenhof, *Garfield, Version 9*, 2009.

[146] B. Abelev *et al.* [ALICE Collaboration], arXiv:1208.1974 [nucl-ex].

[147] K. Aamodt *et al.* [ALICE Collaboration], Eur. Phys. J. C **71** (3), 1594 (2011).

[148] F. Noferini *et al.* [ALICE Collaboration], arXiv:1212.1292 [nucl-ex].

[149] K. Aamodt *et al.* [ALICE Collaboration], Eur. Phys. J. C **71**(6), 1655 (2011).